




Universitat Autònoma de Barcelona

**ADVERTIMENT.** L'accés als continguts d'aquesta tesi queda condicionat a l'acceptació de les condicions d'ús establertes per la següent llicència Creative Commons:  [http://cat.creativecommons.org/?page\\_id=184](http://cat.creativecommons.org/?page_id=184)

**ADVERTENCIA.** El acceso a los contenidos de esta tesis queda condicionado a la aceptación de las condiciones de uso establecidas por la siguiente licencia Creative Commons:  <http://es.creativecommons.org/blog/licencias/>

**WARNING.** The access to the contents of this doctoral thesis it is limited to the acceptance of the use conditions set by the following Creative Commons license:  <https://creativecommons.org/licenses/?lang=en>

# Novel bacterial cellulose materials:

Structuration, functional  
nanocomposites and  
photocurable hydrogels

**Soledad Roig Sánchez**

**Doctoral thesis**

**2021**





Novel bacterial cellulose materials:  
structuration, functional nanocomposites and  
photocurable hydrogels

Soledad Roig Sánchez

Doctoral thesis

Doctoral studies in Materials Science

Supervisors: Dr. Anna Roig Serra and Dr. Anna Laromaine Sagué

Tutor: Dr. Eva Maria Pellicer Vilà

2021

Departament de Química, Facultat de Ciències

Universitat Autònoma de Barcelona

Institut de Ciència de Materials de Barcelona



La **Dra. Anna Roig Serra**, professora d'investigació del CSIC, la **Dra. Anna Laromaine Sagué**, científica titular del CSIC i la **Dra. Eva Maria Pellicer Vilà**, professora titular a la UAB,

CERTIFIQUEN:

Que **Soledad Roig Sánchez**, graduada en Química per la Universitat de València i amb un màster en Nanotecnologia per la Universitat Rovira i Virgili, ha dut a terme aquesta tesi doctoral sota la seva direcció i que queda recollida en aquesta memòria que porta per títol "*Novel bacterial cellulose materials: structuration, functional nanocomposites and photocurable hydrogels*" per optar al títol de Doctora en Ciència de Materials per la Universitat Autònoma de Barcelona amb menció de Doctorat Internacional.

I perquè així consti, signen el present certificat:

Dra. Anna Roig Serra    Dra. Anna Laromaine Sagué    Dra. Eva Maria Pellicer Vilà

Bellaterra, 03 de setembre de 2021



*“By believing passionately in something that  
still does not exist, we create it.  
The nonexistent is whatever we have  
not sufficient desired”*

– Franz Kafka





A mis padres, Juan y Sole,  
mi tío, Pepe, y mi compañero de vida, Jose.  
Y a todo aquel que disfrute de esta lectura.



To my parents, Juan and Sole,  
my uncle, Pepe, and my soulmate, Jose.  
And everyone who enjoys the reading.



## Acknowledgements

It all started one morning when I got on my stool and my mother explained to me how the water suddenly boils when you place it inside the microwave. That experience, to my five-old self, was pure magic. Thank you mum, for teaching me that wondering how things happen and looking for explanations could be so entertaining. Thank you dad, for teaching me that magic is much funnier when you shared it. And so, at that early age stage, I knew I wanted to be an inventor. I graduated in chemistry. Curiosity makes me touch many fields and I specialized myself in Nanochemistry, mainly dedicated to inorganic synthesis, but still there was something that did not fit, until I found the *Nanoparticles and Nanocomposites* (N&N) *group* and its bacterial cellulose project. An interdisciplinary, multicultural and highly active group that combined nanoparticle synthesis with supramolecular chemistry and biology. I discovered what material science was, and I loved it. Looking back, I could not be more grateful to my supervisors for the tremendous opportunity. It has been a long and intense journey where I have grown both personally and professionally. Thank you both, for the advice but also the support and guidance offered over these years. Thank you Anna Roig for training me in the balance between results, efficiency and outreach. Thank you Anna Laromaine for teaching me to squeeze my imagination, because there is where the best outcomes come from, and to trust in my ideas.

I also want to express my gratitude towards my lab colleagues, the new ones and those who have already left. Deyaa, my microbiology mentor; Irene, Amanda and Sumi, who have listened attentively to my wildest ideas about a bio world completely unknown to me. Jan and Ma and their particular sense of humor. Martí and Yajie with their uncountable questions that make you doubt everything and set yourself new goals. Miquel, Luo and Jordi, little I can add that you do not know; I already miss you. Carlos, whose advice has prepared me for the next scientific stage. Anna May and her smile and contagious joy. Oriol, Gerrit, Thomas, Wenchao, Nerea, Andrea and the new incorporations, Wid, Nico, Vinod, Aurna, Nanthilde and someone else I would surely forget to mention. Without you, the *NN group* would not be the same.

I would like to thank the ICMABers for made me feel at home during these five years. The atmosphere and the camaraderie inside the institute are incredible, no matter how

many pandemics come our way. Special thanks to the “third-floor” group, whose debates during lunch have helped me to solve more than one problem and where I have established friendship bonds that I hope will last for a lifetime. David Piña, joy personified. The JPhD2019 commission, no matter where we end, we will conquer the world.

I would also like to acknowledge our collaborators which make possible to present this thesis. Jordi Faraudo, David Malaspina, Dino Tonti and Wenhai and the discussions in rooms and corridors about cellulose that expanded my field of knowledge. To Lars and his group, for hosting me for a month in a beautiful snowy Sweden, and especially to Erik, for teaching me the basics of material’s mechanical studies. Pau, Christine and Kamelia, B.Braun researchers, for eagerly collaborate with us and take the bacterial cellulose one step closer to its industrial implementation. To Shlomo, for accepting me into his group for a short stay with the crazy project of 3D printing bacterial cellulose, it has turned out to be much more difficult than expected. To his group, for making my life much easier there, and especially to Doron, for his availability and for continuing the experiments after I returned to ICMAB.

Thanks to my family, my husband and my friends, those close by and those who are far away and I see less often; they endure all my eccentricities, good and bad days and made me the person I am nowadays: Pepe, M<sup>a</sup> Jesús, Paula, German, vilabellas (all of them), denienses (only with hot weather), Sandra, Andreu, Rubén, Valle, Raquel, Toni, Dani, Cristian, Greta, Astrid and Joel. And thanks to all my mentors, teachers and supervisors.

Finally, I would like to acknowledge the financial support provided during these years: the Spanish Ministry of Science and Innovation through the RTI2018-096273-B-I00 and MAT2015-64442-R projects and my FPI doctoral scholarship (BES-2016-077533), the ‘Severo Ochoa’ Programme for Centers of Excellence in R&D (SEV-2015-0496 and CEX2019-000917-S) and the Generalitat de Catalunya, (2017SGR765).

## Agradecimientos

Todo empezó una mañana yo subida en mi taburete y mi madre explicándome como el agua de repente hervía al meterla en el microondas. Aquello, a mis cinco años, era magia. Gracias mamá, por enseñarme que preguntarse como suceden las cosas y buscar explicaciones es algo de lo más entretenido. Gracias papá, por enseñarme que esa magia es mucho más divertida cuando se comparte. Y así, a esa temprana edad tenía claro que quería ser inventora. Estudié Química. La curiosidad me hizo tocar muchos campos y me especialicé en Nanoquímica, principalmente dedicada a síntesis inorgánica, pero aun así había algo que no encajaba, hasta que encontré al *Nanoparticles and Nanocomposites (N&N) group* y su proyecto de celulosa bacteriana. Un grupo interdisciplinar, multicultural y muy activo que aunaba lo mejor de la síntesis y caracterización de nanopartículas con la química supramolecular y la biología. Descubrí lo que era la ciencia de materiales, y me ha encantado. Echando la vista atrás, no puedo estar más agradecida a mis supervisoras por tremenda oportunidad. Ha sido un viaje largo e intenso donde he crecido tanto personal como profesionalmente. Gracias a ambas, gracias por los consejos, pero también por el soporte y la guía ofrecida durante estos años. Anna Roig por enseñarme el equilibrio entre resultados, eficacia y transmisión de ideas. Gracias Anna Laromaine por enseñarme a expresar la imaginación, porque de ahí es donde salen los logros, y a confiar en mis ideas.

También quiero agradecer a mis compañeros de laboratorio, los nuevos y los que ya se han ido. Deyaa, mi mentor en microbiología; Irene, Amanda y Sumi, quienes han escuchado con atención mis ideas más locas sobre un mundo bio completamente desconocido para mí. Dani Beltrán, mi primer café, por el cual te estaré siempre agradecida. Jan y Ma, y su especial sentido del humor. Martí y Yajie con sus innumerables preguntas que te hacen dudar de todo y plantearte objetivos nuevos. Miquel, Luo y Jordi, poco puedo añadir que no sepáis; os echo de menos ya. Carlos, cuyos consejos me han preparado para mi próxima etapa científica. Anna May y su sonrisa y alegría contagiosa. Oriol, Gerrit, Thomas, Wenchao, Nerea, Andrea y las más nuevas incorporaciones, Wid, Nico, Vinod, Aurna, Nanthilde y alguno más que me dejaré en el tintero. Sin vosotros el *NN group* no sería lo que es.

También quiero agradecer al resto de ICMABers que han hecho que estos cinco años me sintiera como en casa, es increíble la atmosfera y compañerismo que se respira en el centro, no importa las pandemias que se nos pongan por en medio. Especiales agradecimientos al grupo de “la tercera planta”, cuyas charlas durante la comida resolviendo dudas me han solventado más de un problema y de donde me llevo unas amistades que espero perduren para toda la vida. David Piña, la alegría personificada. La comisión del JPhD2019, acabemos donde acabemos sé que nos comeremos el mundo.

También quiero agradecer a nuestros colaboradores que han hecho posible esta tesis. Jordi Farauo, David Malaspina, Dino Tonti y Wenhai y las discusiones en salas y pasillos sobre celulosa que hacían expandir mi campo de conocimiento. A Lars y su grupo, por acogerme durante un mes en una Suecia nevada preciosa, y muy especialmente a Erik, por enseñarme las bases de los estudios mecánicos en materiales. A Pau, Christine y Kamelia, investigadores en B.Braun, por aceptar colaborar con nosotros y llevar la celulosa bacteriana un pasito más cerca de su implantación industrial. A Shlomo, por aceptarme en su grupo para una estancia breve con la idea loca de imprimir celulosa en 3D, ha resultado ser mucho más difícil de lo que esperábamos. A su grupo, por hacerme la vida allí mucho más fácil, y en especial a Doron, por su disponibilidad y por continuar con los experimentos después de que volviera al ICMAB.

Quisiera agradecer a mi familia, mi marido y amigos; los lejanos, los cercanos, los que veo mucho y los que veo un poco menos pero que están ahí y aguantan cada una de mis excentricidades y me han hecho ser la persona que soy ahora: Pepe, M<sup>a</sup> Jesús, Paula, German, vilabellas (todas ellas), denienses (pero solo cuando hace calor), Sandra, Andreu, Rubén, Valle, Raquel, Toni, Dani, Cristian, Greta, Astrid y Joel. También quiero dar las gracias a todos mis mentores y profesores.

Finalmente, quisiera agradecer la financiación recibida durante estos años: el Ministerio de Ciencia e Innovación de España a través de los proyectos RTI2018-096273-B-I00 y MAT2015-64442-R y mi beca doctoral FPI (BES-2016-077533), el Programa ‘Severo Ochoa’ para Centros de Excelencia en I&D (SEV-2015-0496 and CEX2019-000917-S) y los proyectos de la Generalitat de Catalunya (2017SGR765).

## Attributions

I would like to thank the people that contributed to the thesis:

- Dr. Deeya Yousef established the bacterial growth protocol.
- Dr. Jordi Faraudo and Dr. David. C. Malaspina from the *Materials simulation and theory research group* at ICMAB performed the adhesion simulation analysis between two cellulose crystals in wet and dry environment.
- The ICMAB technical services: Dr. Judit Oro performed the TEM visualization of nanoparticles and cellulose nanofibers. Ana Esther Carrilo instructed me in the SEM images acquisition. Dr. Vega Lloveras trained me in spectrophotometric techniques. Roberta Ceravola executed the thermal gravimetric analysis of bacterial cellulose with and without nanoparticles. David Piña taught me to use the supercritical plant. José Amable Bernabé helped me with the titration analysis of bacterial cellulose. Dr. Bernat Bozzo (ICMAB-CSIC) carried out the magnetometry experiments. Maite Simon carried out the AFM measurements.
- Kamelia Treger from B.Braun performed the mechanical tests of pristine layers and multilayers of bacterial cellulose.
- *Nanoquim platform* technicians (Dr. Neus Romá, Oriol Sabater, Luigi Morrone and Marta Gerbolés), who teach me how to use the microwave-assisted reactor and support me through their optimization towards scalable productions.
- Dr. Anna May, Dr. Muling Zheng and bachelor student Jordi Floriach established the first synthesis protocol of gold, silver, titania and SPIONs on bacterial cellulose through microwave-assisted reaction.
- Marcos Rosado from the *Electron Microscopy Unit* from ICN2 helped me with the acquisition of high-resolution SEM images and EDAX analysis of the nanocomposites multilaminates.
- *Prof. Lars Berglund's research group*, which taught me how to measure mechanical properties and granted me their facilities to perform the mechanical studies.



- *Prof. Pavel A. Levkin research group* provided the superhydrophobic surfaces for bacterial cellulose sphere production.
- The master student Oriol Torrecilla performed the confocal images of the magnetic spheres and helped to establish the protocol for their synthesis in stirring and static conditions during his master thesis.
- *Prof. Cesar Fernández's research group* helped me to fabricate the silicon wafer and the polydimethylsiloxane (PDMS) stamps used for the structuration of bacterial cellulose surface.
- The *NANOPTO group* from ICMAB provides the sub-micron patterned stamp of polydimethylsiloxane.
- Dr. Irene Anton-Sales performed the confocal microscopy acquisition and the prelaminar cell seeding studies in structured bacterial cellulose films.
- *Prof. Shlomo Magdassi's research group*, and especially Ph.D. student Doron Kam, who collaborate in the production and analysis of polyacrylic acid hydrogels.
- Website platform Patternizer, which helped me to create the cover page design of the thesis.

## Glossary

	3D	Three dimensions
A	AFM	Atomic force microscopy
B	BA	Benzyl alcohol
	BC	Bacterial cellulose
	BCf	Bacterial cellulose nanofibers
	BCD	Bacterial cellulose dome-like shape
	BCS	Bacterial cellulose spheres
	f-BCS	Filled bacterial cellulose sphere
	f-BCS-SP	Filled bacterial cellulose sphere with SPIONs
	h-BCS	Hollow bacterial cellulose spheres
	h-BCS-SP	Hollow bacterial cellulose spheres with SPIONs
C	CNC	Cellulose nanocrystals
	CNF	Cellulose nanofibrils/nanofibers
	CNW	Cellulose nanowhiskers
D	DI	Deionized water
	DMA	Dynamic mechanical analysis
	DMSO	Dimethyl Sulfoxide
	DP	Degree of polymerization
E	ECM	Extra cellular matrix
F	FD	Freeze-dried
	F <sub>max</sub>	Resistance to tearing
	FTIR	Fourier transform infrared spectroscopy
H	H <sub>2</sub> O <sub>up</sub>	Water uptake
	HS	Hestrin-Schramm

I	ICMAB	Institut de Ciència de Materials de Barcelona
	ICP-OES	Inductively coupled plasma – optical emission spectroscopy
K	kN	Kilo Newtons
	<i>K. xylinus</i>	<i>Komagataeibacter xylinus</i>
L	LED	Light-emitting diode
M	M	Metals
	MD	Molecular dynamics
	$m_d$	Weight of the dry sample before hydration
	MQ	Milli-Q water
	MRI	Magnetic resonance image
	$m_w$	Weight of the wet sample after hydration
	MW	Microwave
N	NP	Nanoparticle
O	OD	Oven dried
	OA	Oleyamine
	OH	Hydroxyl group
P	P-BC	Patterned bacterial cellulose
	PAA	Polyacrylic acid
	PEGDA	Poly(ethylene glycol) diacrylate
	PET	Polyethylene terephthalate
	PGA	Polyglycolic acid
	PLA	Poly(lactic acid)
	pN	Pico Newtons
	PP	Polypropylene
	PTFE	Polytetrafluoroethylene
	PU	Polyurethane
	PVP	Polyvinylpyrrolidone

R	rms	Root mean square
	Sc	Semiconductor
	SCD	Supercritical dried
	SDS	Sodium dodecyl sulfate
	SEM	Scanning electron microscopy
S	SERS	Surface-enhanced Raman spectroscopy
	SQUID	Superconducting quantum interference device
	SPIONs	Superparamagnetic iron oxide
	SPR	Surface plasmon resonance
	TBOT	Titanium(IV) butoxide
	TEM	Transmission electron microscopy
T	TGA	Thermogravimetric analysis
	TPO	Diphenyl(2,4,6-trimethylbenzoyl) phosphine oxide
	UAB	Universitat Autònoma de Barcelona
U	UV	Ultraviolet
	UV-Vis	Ultraviolet-visible light spectroscopy
V	VMD	Visual molecular dynamics
W	WAC	Water absorption capacity
X	XRD	X-ray diffraction



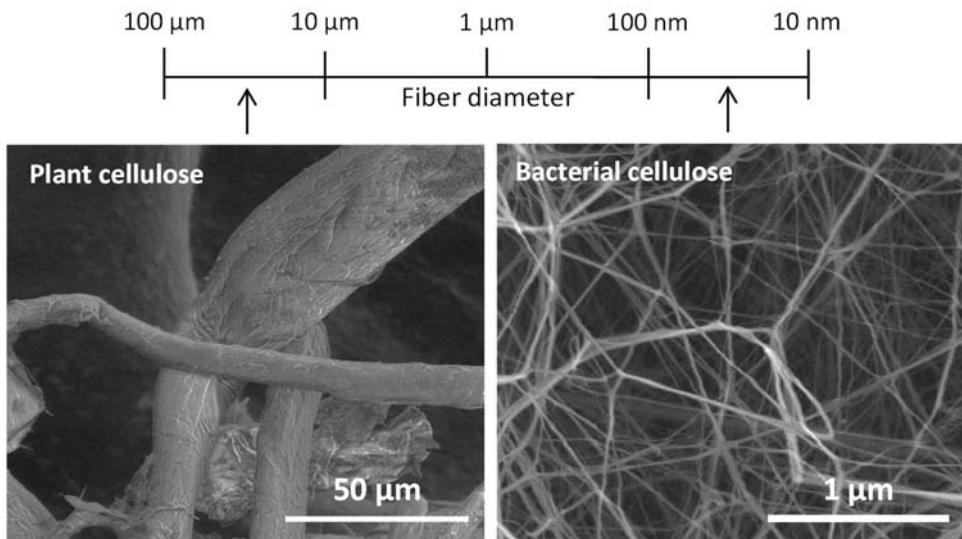
## List of content

Acknowledgements.....	xi
Agradecimientos .....	ix
Attributions .....	xiii
Glossary .....	xv
<b>CHAPTER 1: Bacterial cellulose – state of the art, motivation and objectives of the thesis .....</b>	<b>- 1 -</b>
Chapter summary.....	- 3 -
1.1 Biopolymers.....	- 5 -
1.2 Cellulose: morphology, structure and sources .....	- 6 -
1.3 Bacterial cellulose.....	- 9 -
1.4 Motivation and objectives of the thesis.....	- 16 -
1.5 References.....	- 20 -
<b>CHAPTER 2: Production of bacterial cellulose films, fibers and 3D structures - 27 -</b>	
Chapter summary.....	- 29 -
2.1 Bacterial cellulose culture parameters .....	- 31 -
2.2 Bacteria activation and proliferation.....	- 33 -
2.3 Bacterial cellulose films.....	- 35 -
2.4 Bacterial cellulose nanofibers .....	- 49 -
2.5 Bacterial cellulose spheres.....	- 50 -
2.6 Conclusions.....	- 53 -
2.7 References.....	- 55 -
<b>CHAPTER 3: Surface structuration of bacterial cellulose films .....</b>	<b>- 59 -</b>
Chapter summary.....	- 61 -
3.1 Bacterial cellulose film lithography.....	- 63 -
3.2 Bio-lithography.....	- 66 -

3.3 Soft-imprint lithography .....	- 74 -
3.4 Conclusions.....	- 77 -
3.5 References.....	- 80 -
CHAPTER 4: Engineering bacterial cellulose nanocomposites .....	- 83 -
Chapter summary.....	- 85 -
4.1 Bacterial cellulose functionalization mechanisms .....	- 87 -
4.2 Bacterial cellulose/nanoparticles films by microwave-assisted reaction .....	- 91 -
4.3 Characterization of bacterial cellulose/nanoparticles films .....	- 93 -
4.4 Multilayered bacterial cellulose nanocomposite.....	- 101 -
4.5 Bacterial cellulose nanofibers decorated with magnetic nanoparticles.....	- 106 -
4.6 Functionalization of bacterial cellulose spheres .....	- 108 -
4.7 Conclusions.....	- 119 -
4.8 References.....	- 123 -
CHAPTER 5: Bacterial cellulose nanofibers to reinforce photocurable polyacrylic acid hydrogels .....	- 127 -
Chapter summary.....	- 129 -
5.1 Hydrogels for tissue engineering .....	- 131 -
5.2 Bacterial cellulose nanofibers/polyacrylic acid hydrogel synthesis.....	- 137 -
5.3 Bacterial cellulose nanofibers/polyacrylic acid double network hydrogel characterization .....	- 139 -
5.4 Functionalized bacterial cellulose nanofibers/polyacrylic acid hydrogel .....	- 149 -
5.5 Conclusions.....	- 150 -
5.6 References.....	- 152 -
CHAPTER 6: Summary and prospects.....	- 157 -
ANNEX I: Technical details.....	- 167 -
ANNEX II : <i>Curriculum vitae</i> and publications .....	- 183 -

# Chapter 1

**Bacterial cellulose: state of the art,  
motivation and objectives of the thesis**







## CHAPTER SUMMARY

Chapter 1 introduces cellulose from a macroscopic to a molecular level. Particular attention is given to nanocelluloses and how bacterial cellulose is obtained, its characteristics and the comparison to other cellulose sources. The overall framework is followed by the motivation and objectives of the Ph.D. thesis.

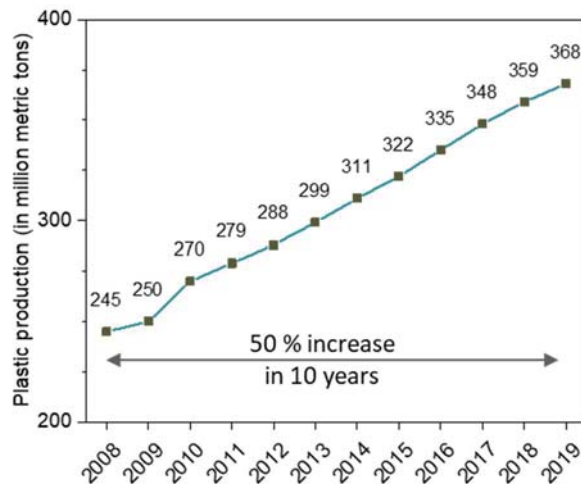
## CHAPTER INDEX

CHAPTER SUMMARY .....	- 3 -
1.1 Biopolymers .....	- 5 -
1.2 Cellulose: morphology, structure and sources .....	- 6 -
1.2.1 Cellulose crystal structures .....	- 8 -
1.3 Bacterial cellulose .....	- 9 -
1.3.1 Biosynthesis .....	- 10 -
1.3.2 Culture Media .....	- 11 -
1.3.3 Bacterial cellulose biosynthesis methods .....	- 13 -
1.3.4 Properties .....	- 14 -
1.3.5 Applications .....	- 15 -
<b>1.4 Motivation and objectives of the thesis .....</b>	<b>- 16 -</b>
1.5 References .....	- 20 -



## 1.1 Biopolymers

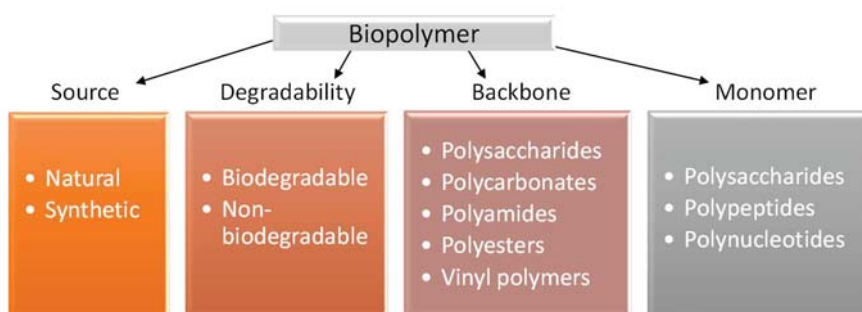
Plastics are made from synthetic or semi-synthetic polymers and their facility to be molded with the desired shape, their durability, lightweight and inexpensive production has made them the most employed material during the past century, with a production in 2019 of 368 million tons (Figure 1), 50 % more than 10 years before. Due to its durability and extended degradability ratio (hundreds of years), recent studies showed that about 60% of the plastics being produced end up in a landfill or the natural environment<sup>1</sup> and are finally released to the ecosystem as microplastics<sup>2-4</sup>. Therefore, serious concerns about their environmental impact are rising, especially after the identification of huge garbage patches with plastic debris in the ocean gyres.<sup>5</sup> Efforts have been made during the past decades to improve waste management, reuse products and reduce the production of non-degradable plastic by substituting them with other materials,<sup>6</sup> however it is still a worldwide problem. One of the candidates to replace non-degradable fuel-based polymers which are arising attention are biopolymers.



**Figure 1:** Worldwide production of plastics in million metric tons. Source: Plastic Europe (PEMRG), Statista 2021.

Biopolymers comprise polymers produced from living organisms, for instance, plants, animals or bacteria (*i.e.*, natural biopolymers such as leather, cotton, chitin or starch) or produced synthetically from biological resources, like polylactic acid (PLA), which monomer (lactic acid) is obtained from bacterial fermentation. As shown in Figure 2, they can be classified following different criteria. For example,

they can be sorted as biodegradable and non-biodegradable. Biodegradable polymers are materials easy to break down upon exposure to sunlight, water, bacteria or enzymes. Examples of biodegradable biopolymers would be chitosan, casein or silk, while polyethylene terephthalate (PET), polyglycolic acid (PGA) or polyurethane (PU) are non-biodegradable. Depending on the molecular backbone polysaccharides, polycarbonates polyamides, polyesters and vinyl polymers can be found. By the repeating unit, biopolymers can be assorted into three big groups: polysaccharides (made from sugars), as cellulose; polypeptides and proteins (made from amino acids), as collagen; or polynucleotides (made from nucleotides), as DNA.<sup>7</sup>

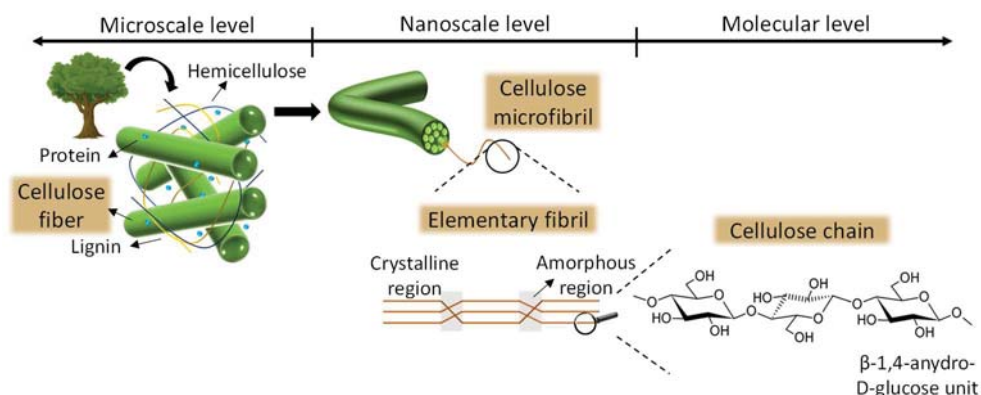


**Figure 2:** Biopolymer classification routes.

## 1.2 Cellulose: morphology, structure and sources

Among natural biopolymers, cellulose is the most abundant one on Earth and constitutes one of the principal renewable resources. To give a more precise picture, in 2018 cellulose had a worldwide production above 187 million tons only in pulp.<sup>8</sup> This natural polysaccharide was discovered in 1838 when Anselme Payen isolated a fibrous material from plant tissues after an acidic and ammonia treatment<sup>7</sup>, although the elucidation of its polymeric structure is attributed to Hermann Staudinger<sup>9</sup>. Cellulose is mainly obtained through the digestion of wood. In plants, cellulose fibers are found in the wall of plant cells physically and chemically bonded to other compounds such as lignin, hemicelluloses and pectin as depicted in Figure 3.<sup>10,11</sup> These cellulose fibers possess a diameter of 10-50  $\mu\text{m}$  and are composed of cellulose fibrils with a diameter in the nanometric range. Those fibrils are formed by glucose chains with crystalline (ordered) and amorphous (disordered) disposal. From a molecular point of view, cellulose is a linear homopolymer composed of linked  $\beta$ -1,4-anhydro-D-glucose units at a  $180^\circ$  rotation and with 3 hydroxyl groups in each

anhydroglucose unit.<sup>12,13</sup> This structure confers to the material hydrophilicity and chirality. In addition, it can be degraded by enzymes and is chemically modifiable due to the high quantity of hydroxyl (OH) groups prone to react and create hydrogen bonds. However, the final properties of the cellulose are determined by the supramolecular order and organization.

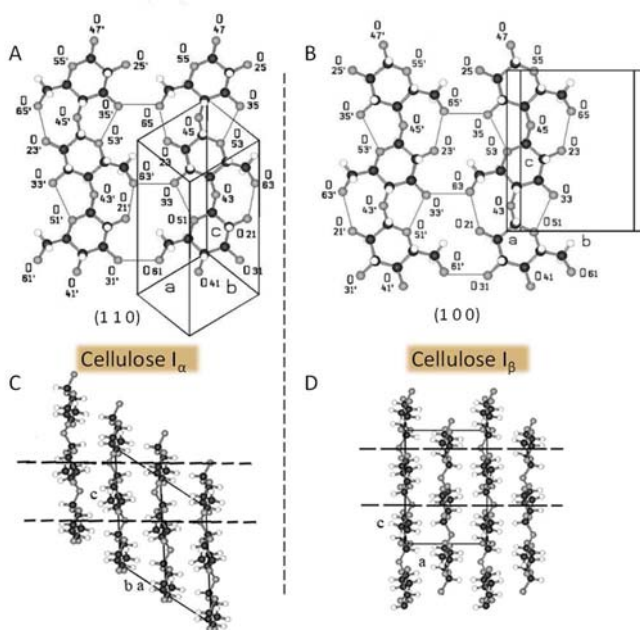


**Figure 3:** Top-down scheme of the cellulose structure: from the composition of the plant cell wall to the molecular entity.

Cellulose with one dimension into the nanometric range is called nanocellulose and encompasses the properties of the cellulose combined with the features of nanometric materials derived from the increased surface area. During the past decade, nanocelluloses such as cellulose nanofibrils/nanofibers (CNF), cellulose nanocrystals (CNC) or cellulose nanowhiskers (CNW), their isolation and uses as the main matrix material or as reinforcement have generated a great amount of research activity.<sup>10,14</sup> For the extraction of nanocelluloses, plant native semicrystalline cellulose is broken down and the amorphous part is removed, obtaining the elementary crystalline structures. During the process, two steps are needed: first and alkali (usually sodium or potassium hydroxide) or acid-chlorite (a combination of sodium chlorite and glacial acetic acid) treatment. Then, acids, enzymes, oxidizers, mechanical steps or combinations of all of them are used to remove the non-cellulosic components.<sup>15–20</sup> However, nanocelluloses can be also attained by changing the cellulose source, reducing or avoiding processing steps and chemical treatments. That is the case of several nanocellulose-producer microorganisms such as bacteria or tunicates.

## 1.2.1 Cellulose crystal structures

The cellulose source and the applied chemical modifications during the digestion determine the crystalline structure of cellulose. That structure provides general information about the reactivity and stability of the cellulose as the hydroxyl groups' interaction between chains differs. Up to four crystal structures have been identified so far: I, II, III and IV. Cellulose I is the native structure that can be found in nature. It can present a triclinic crystallographic space group ( $I_\alpha$ ) or a monoclinic one ( $I_\beta$ ).<sup>21,22</sup> While the first one is identified in most algae and bacteria, the second one is found in higher plants and is thermodynamically more stable, although both structures can be found coexisting in native cellulose.<sup>23</sup> These allomorphs can be distinguished by the chain distances and orientations, containing different hydrogen networks as shown in Figure 4, where both structures are displayed. As it can be observed, the main difference resides in the sheet displacement.  $I_\alpha$  presents the two  $\beta$ -1,4-anhydro-D-glucose units with a  $180^\circ$  rotation between them as the structural unit (*i.e.*, a cellobiose) while  $I_\beta$  exhibits two symmetry related glucoses as structural unit.



**Figure 4:** A,B) Projection of a sheet of cellulose  $I_\alpha$  on the (110) plane (A) and  $I_\beta$  on the (100) plane (B) showing the hydrogen bonds. C,D) Chain arrangement of cellulose  $I_\alpha$  in [1 -1 0] direction and (C) and  $I_\beta$  in [010] direction (D) showing the sheet displacement Adapted from 24.

The other cellulose polymorphs are obtained by chemical treatments of cellulose I. Cellulose II is prepared via regeneration (dissolution and precipitation) or mercerization (alkaline treatment) of cellulose I and is considered the most stable structure. Depending on the alkali concentration and mercerization time, the complex can return to the original cellulose I configuration or irreversible transform into cellulose II.<sup>25</sup> Cellulose III allomorphs are obtained after an ammonia treatment of cellulose I and cellulose II, obtaining cellulose III<sub>I</sub> and cellulose III<sub>II</sub> respectively. Both allomorphs are reversible upon heating in water and possess a monoclinic unit cell, although the chain arrangement differs (parallel in cellulose III<sub>I</sub> and antiparallel in cellulose III<sub>II</sub>).<sup>26</sup> Cellulose IV is obtained through thermal treatments of cellulose III.

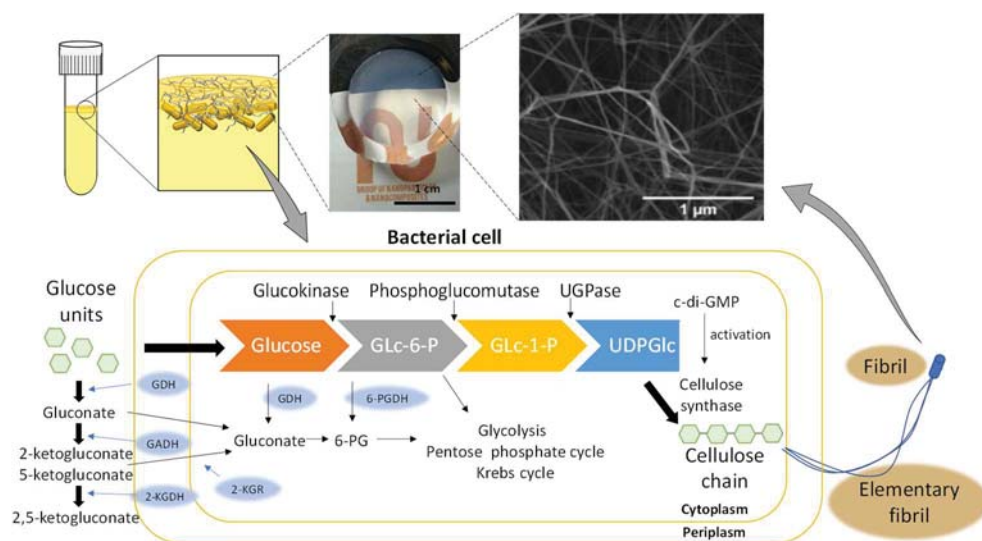
### 1.3 Bacterial cellulose

It is expected that the regulatory requirements to reduce disposable plastic products and replace them with biodegradable materials will increase the cellulose demand in the future. However, there is a need to purpose more reasonable use of forest resources and plantations (the principal source of cellulose)<sup>27</sup> as the uncontrolled deforestation is producing habitat and biodiversity changes<sup>28,29</sup>, increasing the environmental temperature and climate changing<sup>30,31</sup>. Among the possibilities considered, bacterial cellulose arises as a good candidate for an alternative source of renewable cellulosic-based materials.

Bacterial cellulose (BC) was first described by Brown when a jelly-like translucent membrane was found in the mother of vinegar when cultivated in a medium with fructose. He named the microorganism producing the pellicle *Acetobacter xylinus*.<sup>32</sup> Among bacteria, several other species can excrete cellulose, such as *Agrobacterium*, *Aerobacter*, *Sarcina*, *Azobacter*, *Pseudomonas* or *Salmonella*. Acetic acid bacteria of the genus *Komagataeibacter* (formerly *Gluconacetobacter* or *Acetobacter*) is a gram-negative, rodlike shaped (0.6-0.8  $\mu\text{m}$  in diameter and 1-3  $\mu\text{m}$  in length), aerobic bacteria that can be found during the fermentation of sugars (damaged fruits, juice, beer, wine or vinegar).<sup>33</sup> *Komagataeibacter xylinus* (*K. xylinus*) in particular, the strain employed during this thesis, is commercially available and has been widely studied due to its ability to produce cellulose from a wide range of carbon and nitrogen sources, being one of the strains with the highest production of cellulose.<sup>34,35</sup> A single bacterial cell can polymerize up to 200.000 glucose molecules per second.<sup>36</sup>



Bacterial cellulose, as presented in Figure 5 (upper panel), is found at the interface between air and the liquid media which supplies the nutrients for the bacterial cells to live and grow. While growing, the cells secrete cellulose nanofibers creating a transparent pellicle of interwoven fibers. That pellicle acts as a self-defense mechanism towards UV light and dehydration while, at the same time, prevent potential competitors' access to the nutrients and enhance colonization as serves as support to properly access to the oxygen supply.<sup>37</sup>



**Figure 5:** Upper panel: Scheme of the bacterial cellulose growth and obtention of a transparent pellicle with a structure of interwoven nanocellulose fibrils (TEM image). Bottom panel: scheme adapted from <sup>38</sup> to present the major cellulose metabolic pathway of *K.xylinus* and the assembly of the polymer into fibrils.

### 1.3.1 Biosynthesis

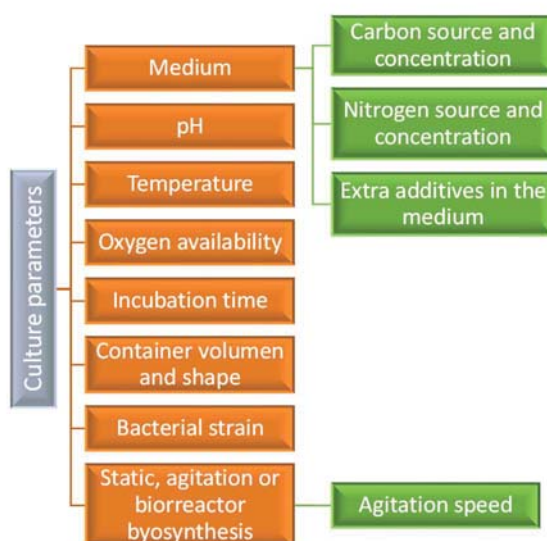
Bacterial cellulose biosynthesis is depicted in Figure 5 and consists of a complex two-step process that involves enzymes, catalytic complexes and regulatory proteins and which full comprehension is still under study. First, the polymerization of  $\beta$ -1,4-glucan chains to cellulose takes place in the cytoplasm of the bacterial cell and then the chain assembly and crystallization occurs on the periplasm membrane.<sup>35,38-40</sup>

- 1) When glucose is used as the main carbon source, first glucose is phosphorylated by glucokinase. Then glucose-6-phosphate (Glc-6-P) isomerizes to glucose-1-phosphate (Glc-1-P) by phosphoglucomutase. Next, uridine diphosphoglucose (UDPGlc) is synthesized by UDPGlc-pyrophosphorylase (UGPase) and finally, cellulose synthase reaction takes place and polymerizes the glucose units creating  $\beta$ -1,4-glucan chains. This reaction is enhanced by the presence of a cyclic dinucleotide molecule, cyclic diguanylic acid (c-di-GMP). In their absence, the enzyme (UGPase) remains inactive or with low activity.
- 2) The cellulose molecules synthesized inside the bacteria are spun together creating protofibrils (or elementary fibrils) of 2-4 nm in diameter. These protofibrils ( $\beta$ -1,4-glucan chains) are extruded from the bacteria cell wall and combined in entangled ribbon-like structures creating fibrils of 10-100 nm diameter size and 1-9  $\mu$ m length. Those fibrils remain associated with the bacterial cells even during cell division, producing the interwoven network with a branching structure known as bacterial cellulose pellicle. That branching structure was described in more detail by Yamaka et al.<sup>41</sup> If the cellulose extrusion continues beyond cell generation, each daughter cell will extrude a fibril of smaller diameter, creating a branching point, and those fibrils would recover the original diameter as the cells mature.

### 1.3.2 Culture Media

The composition of the culture media is a key factor for the proper growth of the bacteria and BC production. Among the culture media components, the carbon and nitrogen sources and their concentration are crucial. While carbon is described as the bacteria food and constitutes the bone of the cellulosic chain, nitrogen is necessary for cell metabolism and comprises between 8-14 % of the dry mass of the bacteria. In an effort to obtain the highest BC production ratio at the lower cost, monosaccharides, oligosaccharides<sup>42,43</sup>, alcohols<sup>44</sup> organic acids<sup>34</sup> and more recently agricultural wastes<sup>45,46</sup> have been studied as carbon sources. Yeast extract, polypeptone or corn steep liquor among others are examples of tested nitrogen sources.<sup>47-49</sup> The highest cellulose production yield has been observed when the carbon concentration is abundant and the nitrogen concentration is minimal. In other cases, extra supplies as amino acids, inorganic salts, vitamins or oil have been added to increase the cellulose yield.<sup>50-52</sup>

Further environmental parameters can also affect the production of BC, namely pH, temperature, dissolved oxygen, rotation speed, culture days<sup>42,53</sup> or container volume and shape<sup>54,55</sup>. Bacteria can grow in media with pHs ranging between 4 and 7<sup>36</sup>, although the highest BC production rates have been observed at pH values between 4 and 5. In addition, as bacteria grow the fermentation process produces an accumulation of gluconic, acetic and lactic acids<sup>34</sup> and the addition of a buffer to the medium is needed to maintain the pH in the optimal range. Temperature is reported to influence the crystallinity of BC and bacteria growth. In general, optimal yields have been obtained for temperatures between 28 and 30 °C. The dissolved oxygen concentration in the media is affected by the container shape and it is also important as high concentrations reduce BC production while low concentrations impede the bacteria growth and thereof BC production is reduced. Besides, long incubation periods and large accessibility to nutrients lead to thicker films and higher production ratios.

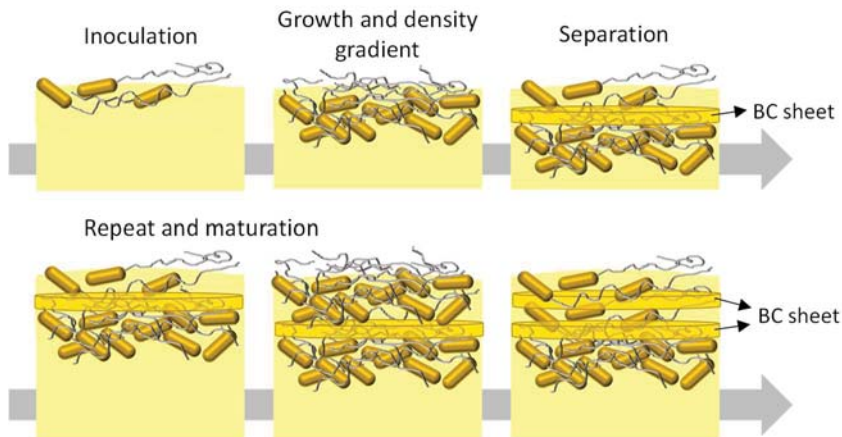


**Figure 6:** Bacterial culture conditions to be considered for an optimal BC production yield.

Additionally, the strain used and how is manipulated are relevant. It has been noted that bacteria mutate spontaneously when it is subcultured repeatedly or agitated.<sup>36,44,55</sup> Those mutations can produce non-cellulose producer cells reducing the cellulose yield.

### 1.3.3 Bacterial cellulose biosynthesis methods

Current methods to produce BC are in static or agitated conditions or within a bioreactor with a continuous or semicontinuous fermentation. The selection of the method will depend on the final morphological, physical and mechanical properties of the resulting BC.



**Figure 7:** Scheme of layer-by-layer BC production in static conditions. Upon inoculation, bacterial cells grow protruding cellulose nanofibers until a critical density point is achieved and two independent populations appear. The process is repeated until oxygen or nutrient availability reaches critical points.

The static culture method is the traditional and more widely used approach to synthesize BC at a laboratory scale. A container is filled with fresh medium inoculated with bacteria and incubated between 1-14 days at a suitable temperature (28-30 °C) and pH (between 4 - 7). After the culturing time, a pellicle at the interface air-liquid medium is created. Recently Gromovykh et al.<sup>56</sup> proposed a multistep layer-by-layer process to explain how bacteria expand and BC is obtained under static conditions. As Figure 7 illustrates, during the first stage the cells expand and grow excreting cellulose nanofibers during the process and produce a thin film that covers the surface. As bacterial cells number grow, more fibers are spread and the film thickens and becomes denser. At some point, the density is high enough to impede the cells to penetrate and two different areas with two bacteria populations appear, developing independently. Bacteria allocated in the top part cannot go to the bottom area and continue growing and excreting cellulose nanofibers, producing a new layer. After some time, the density increases and the situation repeats. Bacteria on the top area continue thickening the pellicle while the trapped bacteria connect the different

---

sheets and make them thicker. In the case of the deeper bacteria, as the oxygen availability decreases, the synthesis slows down until the oxygen availability reached critical points, the synthesis stops and the cells switch to the dormant state.

Similarly, as the BC growth is highly dependent on the liquid-air interface surface area, acquiring the shape of such interface, more intricated configurations such as tubes can be obtained by molding it.<sup>57</sup> Indeed, BC hollow cylindrical tubes have been obtained where the first layer is formed near a silicone tube surface, where the oxygen availability is higher. More evidence of the layer-by-layer process has been reported when colorful additives are added to the media, seeing vertical phase segregation.<sup>58</sup> Even so, the precise mechanism of BC growth is still unknown and the bacterial cells could also employ the pellicles created just as a platform to settle near the oxygen supply (the interface), stopping the production with the expiration of nutrients.

In an attempt to increase the yield production of BC up to a commercial scale while reducing the culture days other biosynthesis methods, such as agitation or the use of bioreactors, have been investigated.<sup>59</sup> Agitation takes place at the same conditions as the static culture method with the extra characteristic of a continuous stirring which supplies spare oxygen to the bacteria. With agitation, cellulose is synthesized inside the medium as fibrous suspensions, spheres, or irregular masses and extra parameters such as strain instability, rotation speed, non-Newtonian mixing behavior or the correct oxygen supply have to be taken into account.<sup>60,61</sup> However, a non-significant increase in BC production is observed, probably due to the appearance of non-cellulosic mutants. In addition, BC produced under agitation has a lower degree of polymerization, slightly lower crystallinity, lower Young's modulus and higher viscosity and emulsion stability.<sup>62</sup> The bioreactor culture, on the other hand, consists of the constant supply of nutrients and oxygen to increase the cellulose production efficiency and overcome some limitations of the static and agitation culture, however, the large energy consumption to support the bacteria cell growth highlight the need of more economical approaches.

### **1.3.4 Properties**

BC produces a 3D porous hydrogel pellicle with a reticulated network of fibers three orders of magnitude thinner than the one from as-obtained plant-cellulose fibers.

Those fibers are chemically pure, free of lignin and hemicelluloses and have some properties that differ from those of wood-derived cellulose due to the differentiated size. However, for a proper comparison, BC should be compared to other nanocelluloses such as CNF and CNC.<sup>33</sup>

BC is endowed with high crystallinity, up to 90% compared to the 40-70% reported for CNF,<sup>59</sup> a higher degree of polymerization (up to 8000) than CNC and high surface area, as it possesses a higher aspect ratio (667-6000). It also possesses a high water content (more than 90% of its weight) which is attributed to the native hydrophilicity of cellulose, the porous structure and the high aspect ratio. Besides, BC sheets display a higher mechanical performance (Young modulus of 15-35 GPa and tensile strength of 150-300 MPa) compared to their CNF counterparts.<sup>41,63</sup> It is mainly composed of  $I_{\alpha}$  (70-80%) with a small ratio of  $I_{\beta}$ , although the varying composition depends on the culture conditions, in comparison to CNF and CNC, which are mainly composed of  $I_{\beta}$ . Compared to the wood pulp or microcrystalline cellulose, BC presents 150 °C lower activation energy to start the first thermal degradation stage.

Furthermore, some of those properties such as the crystallinity, porosity and mechanical properties of the film can be changed and tuned by the addition of additives to the culture media.<sup>64-67</sup> Finally, the surface chemistry of BC opens a wide range of possibilities. Due to the high concentration of available hydroxyl groups, BC can be oxidated with ammonium persulfate<sup>16</sup> or TEMPO (2,2,6,6-tetramethylpiperidine-1-oxyl)<sup>68</sup> to increase its reactivity, or through their esterification with organic acids, higher hydrophobic BC films are obtained.<sup>69</sup> BC can also be modified by the incorporation of, for instance, polymers, metal nanoparticles or ceramics, creating composite materials which combine properties of both components.

### 1.3.5 Applications

The most extended application of BC is its distribution as a popular Philippine dessert called *Nata de coco*. In this particular case, BC is obtained from the fermentation of coconut water. However, due to its outstanding properties and easy chemical modifications (such as esterification, TEMPO oxidation, additive incorporation,...), BC has found applicability in different industrial and medical fields for food packing,

---

coating films, battery separators, adsorbents, cosmetics, wound dressing and scaffolds for tissue engineering. BC pellicles have huge potential in tissue engineering and biomedical applications as the fibrous structure resembles the extracellular matrix of tissues maintaining a high rate of humidity.<sup>70,71</sup> In fact, commercially available BC films for wound dressing can already be found.<sup>72</sup> Examples are JaNaCell®, Suprasorb® or BioFill®. BC also allows stable emulsions not affected by changes in pH, temperature or ionic strength which can be used in food and cosmetics.<sup>73,74</sup> In addition, the attainment process of BC allows its modification during the biosynthesis (*in-situ*) or afterward (*ex-situ*). During the *in-situ* approach additives incorporated into the media allow tuning the final properties, shape and structure. For example, wax microspheres or sacrificial templates can be added to create films with microporous structures with applicability as biofilms or vascular scaffolds<sup>75,76</sup> or, it has demonstrated to be a good candidate as thermoelectric paper when combined with carbon nanotubes.<sup>58</sup> Moreover, the ability to modulate the shape of the BC material by controlling the interface made possible the production of more intricate 3D shapes such as tubes, spheres or even allow 3D imprint, compelling in the biotechnology and tissue engineering field.<sup>77-79</sup> Products derived from agitation culture has been used as drug carriers or heavy metal adsorbents.<sup>80-82</sup>

After the bioprocess, the pellicles can be coated with polymers, other chemical compounds or NPs being used as bactericidal,<sup>83</sup> for wound dressing<sup>64</sup> or drug delivery<sup>84</sup>. BC has been also used as a reinforcement or matrix for nanocomposites<sup>85</sup> or as optical sensors for human albumin serum monitoring.<sup>86</sup>

## **1.4 Motivation and objectives of the thesis**

The huge worldwide year production of plastics and their environmental impact are demanding efforts to the society, and especially to the researchers, to investigate ways to reduce waste, reuse products and create biodegradable materials. Cellulose arises as a good substitute for petroleum-based materials as it is the most abundant natural renewable resource. Specifically, nanocelluloses allow expanding the scope of sustainable materials and nanocomposites as they encompass the cellulose characteristics with the properties of the nanomaterials. Among them, BC outstands as it is not produced from plants and no hazardous chemical processing steps are needed to afford the nanometric cellulosic fibers, as they are natively obtained

through bacteria excretion. This was one of the main reasons I was first attracted to the project. I come from an area dedicated principally to orchards with a lacking of forest areas and an alternative cellulosic source to plants seemed fascinating. BC presents specific structure and properties such as the nanometric dimensions of the fibers, the high surface area, the porosity or the high concentration of available hydroxyl groups which allows powerful interactions with their surroundings (water, inorganic compounds, other polymers or living cells) with applicability in fields such as tissue engineering, bioremediation or cosmetics that make it interesting. In addition, the versatility to tune its properties and functionalize it opens a wide new range of future applications of these materials.

In our group we have previous expertise in synthesizing bacterial cellulose films, control their properties through drying and even magnetically functionalize them. Besides this background, the recent findings published in the literature and the material limitations detected raised new questions. Although its outstanding properties, the industrialization of BC is still far away as the plant-cellulose manufacture is well established and economic, however, is there a way to produce new BC structures with a simple and fast approach appealing for the industry? On the other hand, BC has been proposed for several applications, especially in the biomedical sector. Can we structure the bacterial cellulose by simulating a sensor or a microfluidic device to extend the application of BC to other areas? If so, to what extent? Could we be able to include multiple functionalizations on BC with other inorganic systems and avoiding the leaching of the nanoparticles to afford new properties and renewable advanced materials based on nanocellulose?

**Therefore, the main objective of this thesis was to control cellulose morphologies and to endow the bacterial cellulose with new functionalities showing the versatility of the material.** For that, I present several strategies *in-situ*, during the biosynthesis of the BC, and *ex-situ*, obtaining complex BC materials that we hope would be one step closer to provide bioresource-based materials to society.

The specific objectives pursued during these years have been:

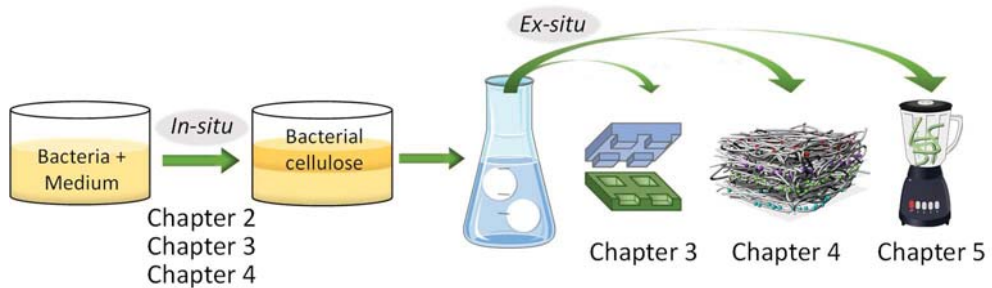


- 
1. Production of several BC configurations applying different culture methods and structuration of them through two soft-imprint approaches.
  2. Synthesis of inorganic nanoparticles and functionalization and characterization of the BC configurations previously synthesized, creating on-demand arrangements with multiple functionalities.
  3. Applicability of BC nanofibers as reinforcement of other polymeric matrices.

The thesis is organized in 6 chapters detailed below and schematically presented in Figure 8:

- Chapter 1 introduces the worldwide plastic emergency, the need to explore renewable materials and how cellulose, and in particular nanocellulose, stands out due to its exceptional properties. Special attention is provided to bacterial cellulose production and applications.
- Production and optimization of bacterial cellulose structures under different cultures methods and with different sizes are presented in chapter 2. Drying effects on BC films are also presented from a macro to microscopic point of view, as well as a protocol to produce multilaminated materials with enhanced mechanical properties.
- Chapter 3 contains the surface structuration of BC films during the biosynthesis (*in-situ*) or after it (*ex-situ*) using polydimethylsiloxane molds with motifs of different shapes and sizes and the effect of the drying method on the fidelity of the pattern motifs.
- Nanoparticle synthesis of four inorganic systems along with the *in-situ* and *ex-situ* functionalization of BC under different culture conditions are described in Chapter 4. An *ad libitum* multilaminated films and Janus spheres synthesis protocol and characterization would also be detailed.
- Chapter 5 includes a particular case where BC is used as a nanofiber additive for synthetic hydrogel production. The mechanical performance of the hydrogel while controlling the swelling behavior due to the presence of BC is explored.

- The main findings and conclusions of the thesis together with future prospects are summarized in Chapter 6.
- Annex I compile the material description, synthesis production and characterization technical details used during the thesis.
- Annex II includes the CV of the author and the publications resulted from this thesis.



**Figure 8:** Scheme of the aspects treated during this thesis in each chapter.

---

## 1.5 References

- (1) Geyer, R.; Jambeck, J. R.; Law, K. L. Production, Use, and Fate of All Plastics Ever Made. *Sci. Adv.* **2017**, *3* (7), e1700782. <https://doi.org/10.1126/sciadv.1700782>.
- (2) Rhodes, C. J. Plastic Pollution and Potential Solutions. *Sci. Prog.* **2018**, *101* (3), 207–260. <https://doi.org/10.3184/003685018X15294876706211>.
- (3) Petersen, F.; Hubbart, J. A. The Occurrence and Transport of Microplastics: The State of the Science. *Sci. Total Environ.* **2021**, *758*, 143936. <https://doi.org/10.1016/j.scitotenv.2020.143936>.
- (4) Ali, M. U.; Lin, S.; Yousaf, B.; Abbas, Q.; Munir, M. A. M.; Ali, M. U.; Rasihd, A.; Zheng, C.; Kuang, X.; Wong, M. H. Environmental Emission, Fate and Transformation of Microplastics in Biotic and Abiotic Compartments: Global Status, Recent Advances and Future Perspectives. *Sci. Total Environ.* **2021**, *791*, 148422. <https://doi.org/10.1016/j.scitotenv.2021.148422>.
- (5) Lebreton, L.; Slat, B.; Ferrari, F.; Sainte-Rose, B.; Aitken, J.; Marthouse, R.; Hajbane, S.; Cunsolo, S.; Schwarz, A.; Levivier, A.; et al. Evidence That the Great Pacific Garbage Patch Is Rapidly Accumulating Plastic. *Sci. Rep.* **2018**, *8* (1), 4666. <https://doi.org/10.1038/s41598-018-22939-w>.
- (6) Ferdous, W.; Manalo, A.; Siddique, R.; Mendis, P.; Zhuge, Y.; Wong, H. S.; Lokuge, W.; Aravinthan, T.; Schubel, P. Recycling of Landfill Wastes (Tyres, Plastics and Glass) in Construction – A Review on Global Waste Generation, Performance, Application and Future Opportunities. *Resour. Conserv. Recycl.* **2021**, *173*, 105745. <https://doi.org/10.1016/j.resconrec.2021.105745>.
- (7) Mohan, S.; Oluwafemi, O. S.; Nandakumar, K.; Thomas, S.; Songca, S. P. Biopolymers – Application in Nanoscience and Nanotechnology. *Recent advances in biopolymers*; Perveen, F. K., Ed.; InTech, **2016**. <https://doi.org/10.5772/62225>.
- (8) Confederation of European Paper Industries. Cepi Key Statistics 2019. <https://www.cepi.org/key-statistics-2019>.
- (9) Staudinger, H. Viscosity Investigations for the Examination of the Constitution of Natural Products of High Molecular Weight and of Rubber and Cellulose. *Trans. Faraday Soc.* **1933**, *29* (140), 18–32. <https://doi.org/10.1039/tf9332900018>.
- (10) Zhu, H.; Luo, W.; Ciesielski, P. N.; Fang, Z.; Zhu, J. Y.; Henriksson, G.; Himmel, M. E.; Hu, L. Wood-Derived Materials for Green Electronics, Biological Devices, and Energy Applications. *Chem. Rev.* **2016**, *116* (16), 9305–9374. <https://doi.org/10.1021/acs.chemrev.6b00225>.
- (11) Gigli-Bisceglia, N.; Engelsdorf, T.; Hamann, T. Plant Cell Wall Integrity Maintenance in Model Plants and Crop Species-Relevant Cell Wall Components and Underlying Guiding Principles. *Cell. Mol. Life Sci.* **2020**, *77* (11), 2049–2077. <https://doi.org/10.1007/s00018-019-03388-8>.
- (12) Ververis, C.; Georghiou, K.; Christodoulakis, N.; Santas, P.; Santas, R. Fiber Dimensions, Lignin and Cellulose Content of Various Plant Materials and Their Suitability for Paper Production. *Ind. Crops Prod.* **2004**, *19* (3), 245–254. <https://doi.org/10.1016/j.indcrop.2003.10.006>.

- (13) Chinga-Carrasco, G. Cellulose Fibres, Nanofibrils and Microfibrils: The Morphological Sequence of MFC Components from a Plant Physiology and Fibre Technology Point of View. *Nanoscale Res. Lett.* **2011**, *6* (1), 417. <https://doi.org/10.1186/1556-276X-6-417>.
- (14) Klemm, D.; Kramer, F.; Moritz, S.; Lindström, T.; Ankerfors, M.; Gray, D.; Dorris, A. Nanocelluloses: A New Family of Nature-Based Materials. *Angew. Chemie - Int. Ed.* **2011**, *50* (24), 5438–5466. <https://doi.org/10.1002/anie.201001273>.
- (15) Cao, X.; Dong, H.; Li, C. M. New Nanocomposite Materials Reinforced with Flax Cellulose Nanocrystals in Waterbone Polyurethane. *Biomacromolecules* **2007**, *8*, 899–904. <https://doi.org/10.1021/bm0610368>.
- (16) Leung, A. C. W.; Hrapovic, S.; Lam, E.; Liu, Y.; Male, K. B.; Mahmoud, K. A.; Luong, J. H. T. Characteristics and Properties of Carboxylated Cellulose Nanocrystals Prepared from a Novel One-Step Procedure. *Small* **2011**, 302–305. <https://doi.org/10.1002/sml.201001715>.
- (17) Ding, S.-Y.; Liu, Y.-S.; Zeng, Y.; Himmel, M. E.; Baker, J. O.; Bayer, E. A. How Does Plant Cell Wall Nanoscale Architecture Correlate with Enzymatic Digestibility? *Science* **2012**, *338* (2), 1055–1060. <https://doi.org/10.1007/s12155-015-9703-1>.
- (18) Morán, J. I.; Alvarez, V. A.; Cyras, V. P.; Vázquez, A. Extraction of Cellulose and Preparation of Nanocellulose from Sisal Fibers. *Cellulose* **2008**, *15* (1), 149–159. <https://doi.org/10.1007/s10570-007-9145-9>.
- (19) Montanari, S.; Roumani, M.; Heux, L.; Vignon, M. R. Topochemistry of Carboxylated Cellulose Nanocrystals Resulting from TEMPO-Mediated Oxidation. *Macromolecules* **2005**, *38* (5), 1665–1671. <https://doi.org/10.1021/ma048396c>.
- (20) Hendriks, A. T. W. M.; Zeeman, G. Pretreatments to Enhance the Digestibility of Lignocellulosic Biomass. *Bioresour. Technol.* **2009**, *100* (1), 10–18. <https://doi.org/10.1016/j.biortech.2008.05.027>.
- (21) Nishiyama, Y.; Sugiyama, J.; Chanzy, H.; Langan, P. Crystal Structure and Hydrogen Bonding System in Cellulose I $\alpha$  from Synchrotron X-Ray and Neutron Fiber Diffraction. *J. Am. Chem. Soc.* **2003**, *125* (47), 14300–14306. <https://doi.org/10.1021/ja037055w>.
- (22) Nishiyama, Y.; Langan, P.; Chanzy, H. Crystal Structure and Hydrogen Bonding System in Cellulose I $\beta$  from Synchrotron X-Ray and Neutron Fiber Diffraction. *J. Am. Chem. Soc.* **2002**, *124*, 9074–9082. <https://doi.org/10.1021/ja0257319>.
- (23) Atalla, R. H.; VanderHart, D. L. Native Cellulose: A Composite of Two Distinct-Crystalline Forms. *Science* **1984**, *223* (4633), 283–285. <https://doi.org/10.1126/science.223.4633.283>.
- (24) Zugenmaier, P. Order in Cellulosics: Historical Review of Crystal Structure Research on Cellulose. *Carbohydr. Polym.* **2021**, *254*, 117417. <https://doi.org/10.1016/j.carbpol.2020.117417>.
- (25) Okano, T.; Sarko, A. Meerization of Cellulose. II. Alkali-Cellulose Intermediates and a Possible Mercerization Mechanism. *J. Appl. Polym. Sci.* **1985**, *30* (1), 325–332. <https://doi.org/10.1002/app.1985.070300128>.
- (26) Sarko, A.; Southwick, J.; Hayashi, J. Packing Analysis of Aarbohydrates and Polysaccharides. 7. Crystal Structure of Cellulose III1 and Its Relationship to Other Cellulose Polymorphs. *Macromolecules* **1976**, *9* (5), 857–863. <https://doi.org/10.1021/ma60053a028>.

- 
- (27) Mohan, M.; Rue, H. A.; Bajaj, S.; Galgamuwa, G. A. P.; Adrah, E.; Aghai, M. M.; Broadbent, E. N.; Khadamkar, O.; Sasmito, S. D.; Roise, J.; et al. Afforestation, Reforestation and New Challenges from COVID-19: Thirty-Three Recommendations to Support Civil Society Organizations (CSOs). *J. Environ. Manage.* **2021**, *287*, 112277. <https://doi.org/10.1016/j.jenvman.2021.112277>.
- (28) Miranda, E. B. P.; Peres, C. A.; Carvalho-Rocha, V.; Miguel, B. V.; Lormand, N.; Huizinga, N.; Munn, C. A.; Semedo, T. B. F.; Ferreira, T. V.; Pinho, J. B.; et al. Tropical Deforestation Induces Thresholds of Reproductive Viability and Habitat Suitability in Earth's Largest Eagles. *Sci. Rep.* **2021**, *11* (1), 13048. <https://doi.org/10.1038/s41598-021-92372-z>.
- (29) Kaupper, T.; Hetz, S.; Kolb, S.; Yoon, S.; Horn, M. A.; Ho, A. Deforestation for Oil Palm: Impact on Microbially Mediated Methane and Nitrous Oxide Emissions, and Soil Bacterial Communities. *Biol. Fertil. Soils* **2020**, *56* (3), 287–298. <https://doi.org/10.1007/s00374-019-01421-3>.
- (30) Lawrence, D.; Vandecar, K. Effects of Tropical Deforestation on Climate and Agriculture. *Nat. Clim. Chang.* **2015**, *5* (1), 27–36. <https://doi.org/10.1038/nclimate2430>.
- (31) Masuda, Y. J.; Garg, T.; Anggraeni, I.; Ebi, K.; Krenz, J.; Game, E. T.; Wolff, N. H.; Spector, J. T. Warming from Tropical Deforestation Reduces Worker Productivity in Rural Communities. *Nat. Commun.* **2021**, *12*, 1601. <https://doi.org/10.1038/s41467-021-21779-z>.
- (32) Brown, A. J. On an Acetic Ferment Which Form Cellulose. *J. Chem. Soc., Trans.* **1886**, *49*, 432–439. <https://doi.org/10.1039/CT8864900432>.
- (33) Campano, C.; Balea, A.; Blanco, A.; Negro, C. Enhancement of the Fermentation Process and Properties of Bacterial Cellulose: A Review. *Cellulose* **2016**, *23* (1), 57–91. <https://doi.org/10.1007/s10570-015-0802-0>.
- (34) Masaoka, S.; Ohe, T.; Sakota, N. Production of Cellulose from Glucose by *Acetobacter Xylinum*. *J. Ferment. Bioeng.* **1993**, *75* (1), 18–22. [https://doi.org/10.1016/0922-338X\(93\)90171-4](https://doi.org/10.1016/0922-338X(93)90171-4).
- (35) Chawla, P. R.; Bajaj, I. B.; Survase, S. A.; Singhal, R. S. Microbial Cellulose: Fermentative Production and Applications. *Food Technol. Biotechnol.* **2009**, *47* (2), 107–124.
- (36) Hestrin, S.; Schramm, M. Synthesis of Cellulose by *Acetobacter Xylinum*. II. Preparation of Freeze-Dried Cells Capable of Polymerizing Glucose to Cellulose. *Biochem. J.* **1954**, *58* (2), 345–352. <https://doi.org/10.1042/bj0580345>.
- (37) Scott Williams, W. S.; Cannon, R. E. Alternative Environmental Roles for Cellulose Produced by *Acetobacter Xylinum*. *Appl. Environ. Microbiol.* **1989**, *55* (10), 2448–2452. <https://doi.org/10.1128/aem.55.10.2448-2452.1989>.
- (38) Lee, K.-Y.; Buldum, G.; Mantalaris, A.; Bismarck, A. More than Meets the Eye in Bacterial Cellulose: Biosynthesis, Bioprocessing, and Applications in Advanced Fiber Composites. *Macromol. Biosci.* **2014**, 10–32. <https://doi.org/10.1002/mabi.201300298>.
- (39) Morgan, J. L. W.; Strumillo, J.; Zimmer, J. Crystallographic Snapshot of Cellulose Synthesis and Membrane Translocation. *Nature* **2013**, *493* (7431), 181–186. <https://doi.org/10.1038/nature11744>.
- (40) Salgado, L.; Blank, S.; Esfahani, R. A. M.; Strap, J. L.; Bonetta, D. Missense Mutations in a Transmembrane Domain of the *Komagataeibacter Xylinus* BcsA Lead to Changes in Cellulose Synthesis. *BMC Microbiol.* **2019**, *19*, 216. <https://doi.org/10.1186/s12866-019-1577-5>.

- (41) Yamanaka, S.; Watanabe, K.; Kitamura, N.; Iguchi, M.; Mitsuhashi, S.; Nishi, Y.; Uryu, M. The Structure and Mechanical Properties of Sheets Prepared from Bacterial Cellulose. *J. Mater. Sci.* **1989**, *24* (9), 3141–3145. <https://doi.org/10.1007/BF01139032>.
- (42) Ruka, D. R.; Simon, G. P.; Dean, K. M. Altering the Growth Conditions of *Gluconacetobacter Xylinus* to Maximize the Yield of Bacterial Cellulose. *Carbohydr. Polym.* **2012**, *89* (2), 613–622. <https://doi.org/10.1016/j.carbpol.2012.03.059>.
- (43) Mikkelsen, D.; Flanagan, B. M.; Dykes, G. A.; Gidley, M. J. Influence of Different Carbon Sources on Bacterial Cellulose Production by *Gluconacetobacter Xylinus* Strain ATCC 53524. *J. Appl. Microbiol.* **2009**, *107* (2), 576–583. <https://doi.org/10.1111/j.1365-2672.2009.04226.x>.
- (44) Park, J. K.; Jung, J. Y.; Park, Y. H. Cellulose Production by *Gluconacetobacter Hansenii* in a Medium Containing Ethanol. *Biotechnol. Lett.* **2003**, *25*, 2055–2059. <https://doi.org/10.1023/b:bile.0000007065.63682.18>.
- (45) Sperotto, G.; Stasiak, L. G.; Godoi, J. P. M. G.; Gabiatti, N. C.; De Souza, S. S. A Review of Culture Media for Bacterial Cellulose Production: Complex, Chemically Defined and Minimal Media Modulations. *Cellulose* **2021**, *5*. <https://doi.org/10.1007/s10570-021-03754-5>.
- (46) Abol-Fotouh, D.; Hassan, M. A.; Shokry, H.; Roig, A.; Azab, M. S.; Kashyout, A. E. H. B. Bacterial Nanocellulose from Agro-Industrial Wastes: Low-Cost and Enhanced Production by *Komagataeibacter Saccharivorans* MD1. *Sci. Rep.* **2020**, *10*, 3491. <https://doi.org/10.1038/s41598-020-60315-9>.
- (47) Santos, S. M.; Carbajo, J. M.; Villar, J. C. The Effect of Carbon and Nitrogen Sources on Bacterial Cellulose Production and Properties from *Gluconacetobacter Sucofermentans* CECT 7291 Focused on Its Use in Degraded Paper Restoration. *BioResources* **2013**, *8* (3), 3630–3645. <https://doi.org/10.15376/biores.8.3.3630-3645>.
- (48) Costa, A. F. S.; Almeida, F. C. G.; Vinhas, G. M.; Sarubbo, L. A. Production of Bacterial Cellulose by *Gluconacetobacter Hansenii* Using Corn Steep Liquor as Nutrient Sources. *Front. Microbiol.* **2017**, *8*, 1–12. <https://doi.org/10.3389/fmicb.2017.02027>.
- (49) Ramana, K. V.; Tomar, A.; Singh, L. Effect of Various Carbon and Nitrogen Sources on Cellulose Synthesis by *Acetobacter Xylinum*. *World J. Microbiol. Biotechnol.* **2000**, *16* (3), 245–248. <https://doi.org/10.1023/A:1008958014270>.
- (50) Son, H. J.; Kim, H. G.; Kim, K. K.; Kim, H. S.; Kim, Y. G.; Lee, S. J. Increased Production of Bacterial Cellulose by *Acetobacter* Sp. V6 in Synthetic Media under Shaking Culture Conditions. *Bioresour. Technol.* **2003**, *86* (3), 215–219. [https://doi.org/10.1016/S0960-8524\(02\)00176-1](https://doi.org/10.1016/S0960-8524(02)00176-1).
- (51) Tian, D.; Shen, F.; Hu, J.; Rennecker, S.; Saddler, J. N. Enhancing Bacterial Cellulose Production via Adding Mesoporous Halloysite Nanotubes in the Culture Medium. *Carbohydr. Polym.* **2018**, *198*, 191–196. <https://doi.org/10.1016/j.carbpol.2018.06.026>.
- (52) Żywicka, A.; Junka, A. F.; Szymczyk, P.; Chodaczek, G.; Grzesiak, J.; Sedghizadeh, P. P.; Fijałkowski, K. Bacterial Cellulose Yield Increased over 500% by Supplementation of Medium with Vegetable Oil. *Carbohydr. Polym.* **2018**, *199*, 294–303. <https://doi.org/10.1016/j.carbpol.2018.06.126>.
- (53) Gerrard, A. M.; Hornung, M.; Ludwig, M.; Gerrard, A. M.; Schmauder, H.-P. Optimizing the Production of Bacterial Cellulose in Surface Culture: Evaluation of Substrate Mass Transfer Influences on the Bioreaction (Part 1). *Eng. Life Sci.* **2006**, *6* (6), 537–545. <https://doi.org/10.1002/elsc.200620162>.

- 
- (54) Hornung, M.; Ludwig, M.; Gerrard, A. M.; Schmauder, H.-P. Optimizing the Production of Bacterial Cellulose in Surface Culture: Evaluation of Product Movement Influences on the Bioreaction (Part 2). *Eng. Life Sci.* **2006**, *6* (6), 546–551. <https://doi.org/10.1002/elsc.200620163>.
- (55) Krystynowicz, A.; Czaja, W.; Wiktorowska-Jeziarska, A.; Gonçalves-Miśkiewicz, M.; Turkiewicz, M.; Bielecki, S. Factors Affecting the Yield and Properties of Bacterial Cellulose. *J. Ind. Microbiol. Biotechnol.* **2002**, *29* (4), 189–195. <https://doi.org/10.1038/sj.jim.7000303>.
- (56) Gromovykh, T. I.; Pigaleva, M. A.; Gallyamov, M. O.; Ivanenko, I. P.; Ozerova, K. E.; Kharitonova, E. P.; Bahman, M.; Feldman, N. B.; Lutsenko, S. V.; Kiselyova, O. I. Structural Organization of Bacterial Cellulose: The Origin of Anisotropy and Layered Structures. *Carbohydr. Polym.* **2020**, *237*, 116140. <https://doi.org/10.1016/j.carbpol.2020.116140>.
- (57) Rahman, M. M.; Netravali, A. N. High-Performance Green Nanocomposites Using Aligned Bacterial Cellulose and Soy Protein. *Compos. Sci. Technol.* **2017**, *146*, 183–190. <https://doi.org/10.1016/j.compscitech.2017.04.027>.
- (58) Abol-Fotouh, D.; Dörling, B.; Zapata-Arteaga, O.; Rodríguez-Martínez, X.; Gómez, A.; Reparaz, J. S.; Laromaine, A.; Roig, A.; Campoy-Quiles, M. Farming Thermoelectric Paper. *Energy Environ. Sci.* **2019**, *12*, 716–726. <https://doi.org/10.1039/c8ee03112f>.
- (59) Wang, J.; Tavakoli, J.; Tang, Y. Bacterial Cellulose Production, Properties and Applications with Different Culture Methods – A Review. *Carbohydr. Polym.* **2019**, *219*, 63–76. <https://doi.org/10.1016/j.carbpol.2019.05.008>.
- (60) Czaja, W.; Romanovicz, D.; Brown, R. M. Structural Investigations of Microbial Cellulose Produced in Stationary and Agitated Culture. *Cellulose* **2004**, *11*, 403–411. <https://doi.org/10.1023/b:cell.0000046412.11983.61>.
- (61) Kouda, T.; Yano, H.; Yoshinaga, F.; Kaminoyama, M.; Kamiwano, M. Characterization of Non-Newtonian Behavior during Mixing of Bacterial Cellulose in a Bioreactor. *J. Ferment. Bioeng.* **1996**, *82* (4), 382–386. [https://doi.org/10.1016/0922-338X\(96\)89155-0](https://doi.org/10.1016/0922-338X(96)89155-0).
- (62) Watanabe, K.; Tabuchi, M.; Morinaga, Y.; Yoshinaga, F. Structural Features and Properties of Bacterial Cellulose Produced in Agitated Culture. *Cellulose* **1998**, *5* (3), 187–200. <https://doi.org/10.1023/A:1009272904582>.
- (63) Hervy, M.; Santmarti, A.; Lahtinen, P.; Tammelin, T.; Lee, K. Sample Geometry Dependency on the Measured Tensile Properties of Cellulose Nanopapers. *Mater. Des.* **2017**, *121*, 421–429. <https://doi.org/10.1016/j.matdes.2017.02.081>.
- (64) Chang, W. S.; Chen, H. H. Physical Properties of Bacterial Cellulose Composites for Wound Dressings. *Food Hydrocoll.* **2016**, *53*, 75–83. <https://doi.org/10.1016/j.foodhyd.2014.12.009>.
- (65) Cheng, K. C.; Catchmark, J. M.; Demirci, A. Effect of Different Additives on Bacterial Cellulose Production by *Acetobacter Xylinum* and Analysis of Material Property. *Cellulose* **2009**, *16* (6), 1033–1045. <https://doi.org/10.1007/s10570-009-9346-5>.
- (66) Kim, J. H.; Park, S.; Kim, H.; Kim, H. J.; Yang, Y. H.; Kim, Y. H.; Jung, S. K.; Kan, E.; Lee, S. H. Alginate/Bacterial Cellulose Nanocomposite Beads Prepared Using *Gluconacetobacter Xylinus* and Their Application in Lipase Immobilization. *Carbohydr. Polym.* **2017**, *157*, 137–145. <https://doi.org/10.1016/j.carbpol.2016.09.074>.

- (67) Butchosa, N.; Brown, C.; Larsson, P. T.; Berglund, L. A.; Bulone, V.; Zhou, Q. Nanocomposites of Bacterial Cellulose Nanofibers and Chitin Nanocrystals: Fabrication, Characterization and Bactericidal Activity. *Green Chem.* **2013**, *15* (12), 3404–3413. <https://doi.org/10.1039/c3gc41700j>.
- (68) Luo, H.; Xiong, G.; Hu, D.; Ren, K.; Yao, F.; Zhu, Y.; Gao, C.; Wan, Y. Characterization of TEMPO-Oxidized Bacterial Cellulose Scaffolds for Tissue Engineering Applications. *Mater. Chem. Phys.* **2013**, *143* (1), 373–379. <https://doi.org/10.1016/j.matchemphys.2013.09.012>.
- (69) Lee, K.-Y.; Quero, F.; Blaker, J. J.; Hill, C. A. S.; Eichhorn, S. J.; Bismarck, A. Surface Only Modification of Bacterial Cellulose Nanofibres with Organic Acids. *Cellulose* **2011**, *18*, 595–605. <https://doi.org/10.1007/s10570-011-9525-z>.
- (70) Fey, C.; Betz, J.; Rosenbaum, C.; Kralisch, D.; Vielreicher, M.; Friedrich, O.; Metzger, M.; Zdziebło, D. Bacterial Nanocellulose as Novel Carrier for Intestinal Epithelial Cells in Drug Delivery Studies. *Mater. Sci. Eng. C* **2020**, *109*, 110613. <https://doi.org/10.1016/j.msec.2019.110613>.
- (71) Anton-Sales, I.; D’Antin, J. C.; Fernández-Engroba, J.; Charoenrook, V.; Laromaine, A.; Roig, A.; Michael, R. Bacterial Nanocellulose as a Corneal Bandage Material: A Comparison with Amniotic Membrane. *Biomater. Sci.* **2020**, *8*, 2921–2930. <https://doi.org/10.1039/d0bm00083c>.
- (72) Zhong, C. Industrial-Scale Production and Applications of Bacterial Cellulose. *Front. Bioeng. Biotechnol.* **2020**, *8*, 605374. <https://doi.org/10.3389/fbioe.2020.605374>.
- (73) Ougiya, H.; Watanabe, K.; Morinaga, Y.; Yoshinaga, F. Emulsion-Stabilizing Effect of Bacterial Cellulose. *Biosci. Biotechnol. Biochem.* **1997**, *61* (9), 1541–1545. <https://doi.org/10.1271/bbb.61.1541>.
- (74) Paximada, P.; Tsouko, E.; Kopsahelis, N.; Koutinas, A. A.; Mandala, I. Food Hydrocolloids Bacterial Cellulose as Stabilizer of o/w Emulsions. *Food Hydrocoll.* **2016**, *53*, 225–232. <https://doi.org/10.1016/j.foodhyd.2014.12.003>.
- (75) Rühls, P. A.; Storz, F.; López Gómez, Y. A.; Haug, M.; Fischer, P. 3D Bacterial Cellulose Biofilms Formed by Foam Templating. *npj Biofilms Microbiomes* **2018**, *4*, 21. <https://doi.org/10.1038/s41522-018-0064-3>.
- (76) Sämfors, S.; Karlsson, K.; Sundberg, J.; Markstedt, K.; Gatenholm, P. Biofabrication of Bacterial Nanocellulose Scaffolds with Complex Vascular Structure. *Biofabrication* **2019**, *11*, 045010. <https://doi.org/10.1088/1758-5090/ab2b4f>.
- (77) Schaffner, M.; Rühls, P. A.; Coulter, F.; Kilcher, S.; Studart, A. R. 3D Printing of Bacteria into Functional Complex Materials. *Sci. Adv.* **2017**, *3* (12), eaa06804. <https://doi.org/10.1126/sciadv.aao6804>.
- (78) Shin, S.; Kwak, H.; Shin, D.; Hyun, J. Solid Matrix-Assisted Printing for Three-Dimensional Structuring of a Viscoelastic Medium Surface. *Nat. Commun.* **2019**, *10* (1), 4650. <https://doi.org/10.1038/s41467-019-12585-9>.
- (79) Rühls, P. A.; Malollari, K. G.; Binelli, M. R.; Crockett, R.; Balkenende, D. W. R.; Studart, A. R.; Messersmith, P. B. Conformal Bacterial Cellulose Coatings as Lubricious Surfaces. *ACS Nano* **2020**, *14* (4), 3885–3895. <https://doi.org/10.1021/acsnano.9b09956>.



- 
- (80) Zhu, H.; Jia, S.; Wan, T.; Jia, Y.; Yang, H.; Li, J.; Yan, L.; Zhong, C. Biosynthesis of Spherical Fe<sub>3</sub>O<sub>4</sub>/Bacterial Cellulose Nanocomposites as Adsorbents for Heavy Metal Ions. *Carbohydr. Polym.* **2011**, *86* (4), 1558–1564. <https://doi.org/10.1016/j.carbpol.2011.06.061>.
- (81) Drozd, R.; Szymańska, M.; Rakoczy, R.; Junka, A.; Szymczyk, P.; Fijałkowski, K. Functionalized Magnetic Bacterial Cellulose Beads as Carrier for Lecitase® Ultra Immobilization. *Appl. Biochem. Biotechnol.* **2019**, *187* (1), 176–193. <https://doi.org/10.1007/s12010-018-2816-1>.
- (82) Meng, C.; Hu, J.; Gourlay, K.; Yu, C.; Saddler, J. N. Controllable Synthesis Uniform Spherical Bacterial Cellulose and Their Potential Applications. *Cellulose* **2019**, *26* (15), 8325–8336. <https://doi.org/10.1007/s10570-019-02446-5>.
- (83) Pal, S.; Nisi, R.; Stoppa, M.; Licciulli, A. Silver-Functionalized Bacterial Cellulose as Antibacterial Membrane for Wound-Healing Applications. *ACS Omega* **2017**, *2*, 3632–3639. <https://doi.org/10.1021/acsomega.7b00442>.
- (84) Tsai, Y.; Yang, Y.; Ho, Y.; Tsai, M. Drug Release and Antioxidant/Antibacterial Activities of Silymarin-Zein Nanoparticle/Bacterial Cellulose Nanofiber Composite Films. *Carbohydr. Polym.* **2018**, *180*, 286–296. <https://doi.org/10.1016/j.carbpol.2017.09.100>.
- (85) Qian, C.; Asoh, T. A.; Uyama, H. Osmotic Squat Actuation in Stiffness Adjustable Bacterial Cellulose Composite Hydrogels. *J. Mater. Chem. B* **2020**, *8* (12), 2400–2409. <https://doi.org/10.1039/c9tb02880c>.
- (86) Maneerung, T.; Tokura, S.; Rujiravanit, R. Impregnation of Silver Nanoparticles into Bacterial Cellulose for Antimicrobial Wound Dressing. *Carbohydr. Polym.* **2008**, *72* (1), 43–51. <https://doi.org/10.1016/j.carbpol.2007.07.025>.

# Chapter 2

Production of bacterial cellulose films,  
fibers and 3D structures





## CHAPTER SUMMARY

Chapter 2 describes the production of bacterial cellulose films and includes a description of the final properties of the material acquired through different drying routes, introducing the formation of multilayered films. Other structures such as fibers and spheres are also analyzed, emphasizing the versatility of the material.

## CHAPTER INDEX



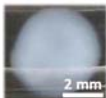

CHAPTER SUMMARY .....	- 29 -
2.1 Bacterial cellulose culture parameters .....	- 31 -
2.2 Bacteria activation and proliferation.....	- 33 -
2.3 Bacterial cellulose films.....	- 35 -
2.3.1 Increasing film production.....	- 37 -
2.3.2 Drying processes.....	- 37 -
2.3.3 Bacterial cellulose single-film characterization .....	- 40 -
2.3.4 Film self-adherence.....	- 41 -
2.3.5 Tensile properties.....	- 45 -
2.4 Bacterial cellulose nanofibers .....	- 49 -
2.5 Bacterial cellulose spheres.....	- 50 -
2.6 Conclusions.....	- 53 -
2.7 References.....	- 55 -



## 2.1 Bacterial cellulose culture parameters

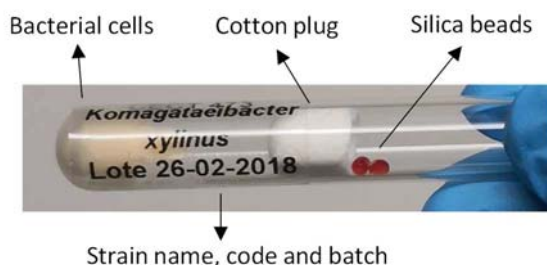
In the previous chapter, I mentioned that several parameters such as the cultivation method, time, temperature and culture medium affect bacterial cell growth and bacterial cellulose yield production. In this chapter, I present the principal conditions I have used during this thesis and the nanocellulosic materials obtained. Two main cultivation approaches were used. Thereof variations in addition to a blending post-processing step of the material resulted in different sizes and shapes that could be useful in different applications. As compiled in Table 1, by modifying the biosynthesis process from static to agitation conditions, BC films or full BC spheres were obtained. Static biosynthesis upon superhydrophobic surfaces allowed achieving hollow BC spheres. At the same time, the films could be dried crafting multilayered materials or could be blended to produce fibers that will be later used as reinforcement in hydrogels.

**Table 1:** Summary of the points and BC materials treated in this chapter.

		Static		Agitation
Biosynthesis		Films 	Spheres 	Spheres 
	Blending 			

Important to mention that during the thesis, bacterial cellulose production was performed under sterile conditions inside a laminar flow cabinet and the material used was previously sterilized by autoclave (120 °C, 20 min) or through 15 min UV radiation. A more detailed technical description of the materials and methods used during this thesis can be found in Annex I. In addition, bacteria strain, the culture media or the subculture process were maintained without alterations:

1) The bacteria strain employed was *Komagataeibacter xylinus* (*K. xylinus*) (NCIMB 5346), purchased in its lyophilized format from CECT (Valencia, Spain) as shown in Figure 1. The bacterial cells were delivered inside a sealed crystal vial, protected with a cotton plug and silica beads to absorb the humidity.



**Figure 1:** Freeze-dried bacterial cells inside a sealed crystal vial.

2) Although Hestrin-Schramm (HS) medium generates lower cellulose yield ratios than others culture media, the  $I_{\alpha}$  content is higher (approx. 80 %) <sup>1</sup>, and therefore, this media was selected for our study. It was prepared as indicated in Table 2. Dextrose solution was done separately to avoid a reaction between the monosaccharides and proteins and the caramelization of sugar during autoclaving. After sterilization (autoclave for 20 min at 121 °C), both solutions were mixed, cooled down and preserved in a fridge until further use. For solid medium, a final volume of 100 mL was prepared and, after autoclaving and before cooling, 33 mL were dispensed in Petri dishes (9 x 1.5 cm, 60 mL vol) previously sterilized with 15 min of UV light.

**Table 2:** Component description for 1L of HS medium.

Bottle A	Bottle B
20 g dextrose (D-glucose)	1.15 g citric acid
	6.8 g Na <sub>2</sub> HPO <sub>4</sub> ·12H <sub>2</sub> O
	5 g peptone
	5 g yeast extract
	15 g agar*
200 mL MQ water	800 mL MQ water

\* Only when solid medium is prepared.

- 3) Repetitive subculturing of bacteria makes each generation weaker, increasing the probability of genetic mutations. Those mutations can lead to abnormal or non-growth of bacterial cells and a decrease, or even lack of production, of bacterial cellulose. To avoid these problems a seed lot system is usually applied, which consists of the increment of the number of bacterial cells by making passages. A passage is described as the transference of small volumes of viable bacteria from a previous bacterial culture to a large number of containers with a fresh growth medium. By this process we can, on one hand, extend the freshness of the strain without affecting its viability as the different containers can be frozen until its use, and on the other, produce higher amounts of cellulose to work with.

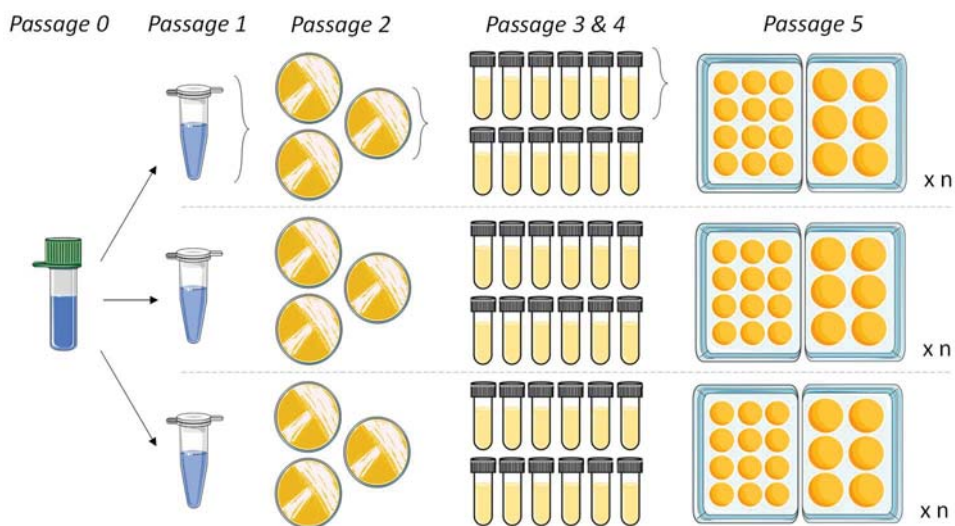
## 2.2 Bacteria activation and proliferation

When buying lyophilized bacteria, a recondition is needed prior to its use. This step was done following the CECT instructions<sup>2</sup>. After carefully opened the sealed vial and removed the silica beads and the cotton plug, 4 mL of HS liquid medium were added to the bacterial cells drop by drop. The suspension was then mixed by a pipette several times and incubated for 30 min at 30 °C to let the cells rehydrate. Afterward, 1 mL of the suspension was dispensed on two agar plates, whereas the remaining 2 mL were transferred to a 100 mL capacity Erlenmeyer with 30 mL of HS liquid medium and everything was incubated at 30 °C for 15 days to enable bacteria to proliferate. While the solution would be used in further steps, the plates would allow controlling the proper growth of bacteria without associated species. This culture is considered *passage 0*. Then, several subculturing steps were performed and are schematically described in Figure 2.

After 15 days, bacteria grew on the bacterial liquid broth and a pellicle of cellulose could be observed at the surface. The film was removed with gentle agitation and ampoules were filled with the broth and frozen, using glycerol as a cryoprotectant (*passage 1*). A cryoprotectant is a chemical compound (such as glycerol or dimethyl sulfoxide (DMSO)) that is mixed with the bacterial culture before freezing the bacterial cells to protect them from damage and death, as it minimizes the formation of water crystals. 500 µL of the bacterial broth were mixed with 500 µL of sterile 50% glycerol solution by repetitive sucking with a pipette avoiding air bubble

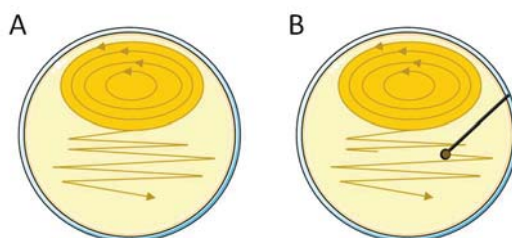


formation. Finally, the ampoules were labeled and stored in a box inside a -80 °C freezer.



**Figure 2:** Bacteria proliferation scheme.

Every 3 months one of the ampoules was thaw inside the biohood (or laminar flow cabinet) at room temperature. 330  $\mu\text{L}$  were dispensed in an HS agar plate and with a sterile loop a rotating distribution through the plate was done, finishing with a zigzag movement (Figure 3A). The plates were dried for approx. 10 min inside the hood to evaporate the excess of liquid, closed with parafilm and incubated in an inverted position for 15 days at 30 °C. With this protocol, *passage 2* is defined by the three agar plates made from each ampoule. After the incubation period, bacterial culture colonies appeared on the agar surface and the plates were transferred to a fridge at 4 °C.



**Figure 3:** HS agar plates showing: A) how to inoculate the bacteria and B) how to pick several bacterial cells.

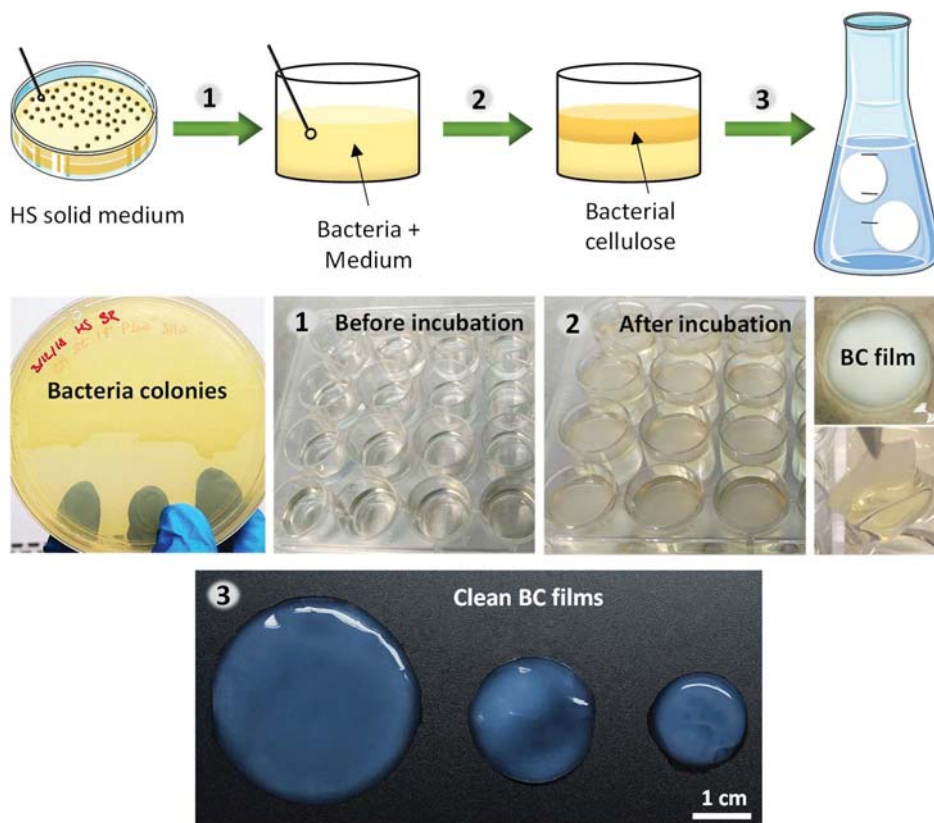
*Passage 3* was formed every month by mixing 6 mL of fresh HS media with an aggregate of bacterial cells in a sterile tube. To pick the bacterial cells, the surface of a *passage 2* agar plate was touched with a sterile loop. Then, it was shifted softly through the surface to fill the loop ring with bacteria (Figure 3B) and transferred to the liquid media where was gently shaken to disperse the cells over the media. This step could be repeated to prepare as many tubes as needed, then the tubes were incubated at 30 °C for 7 days and relocated into a fridge at 4 °C until further use. This relocation was done to avoid logging the death phase of the bacteria and the accumulation of the dead cells, which is appreciable as the color of the media changes from light yellow to dark orange-brown.

The called working passages are the range from *passage 3* to *passage 5* and differ depending on the user and the final application of the bacterial cellulose produced. Usually, *passage 4* is a bacterial cell expansion of *passage 3* and *passage 5* consists of the dispensation of a diluted bacterial solution into different shaped containers (as well-plates with different sizes) to obtain BC films of various shapes or dimensions. *Passage 3* to above would be described in detail in each BC production section.

### 2.3 Bacterial cellulose films

*K. xylinus* bacteria were grown in HS solid medium. As shown in Figure 4, an aggregate of bacterial cells was expanded in 6 mL of the same liquid medium (*i.e.*, without agar) for 7 days at 30 °C. Then, 0.5 mL were inoculated into 4.5 mL of fresh medium and incubated for another three days. Finally, a dilution of the bacterial solution with fresh medium was done in a 1:14 ratio and transferred into 24 well-plates (step 1). After 3 days inside the incubator, BC pellicles were produced at the top of the liquid (well diameter  $\approx$  1.5 cm) and could be harvested (step 2). Those films presented a yellowish color, originated by the absorption of the media (yellow *per se*), and a mucous appearance at the bottom section due to cell proliferation. Harvested BC films were cleaned first with a 50% ethanol solution for 10 min, twice with boiling water and then other two times with a 0.1M sodium hydroxide solution for 20 min at 90 °C to lyse the bacterial cells. Then, the pellicles were washed with Milli-Q (MQ) water until neutral pH and were stored in water at room temperature. Stronger alkali solutions (above 6%), longer times or higher temperatures can cause deformation and shrinkage and transform cellulose I into cellulose II.<sup>3-5</sup> Therefore, during this thesis, mild mercerization conditions (1.6% alkali concentration and short

times) were used and the same cleaning protocol was maintained for all BC productions.

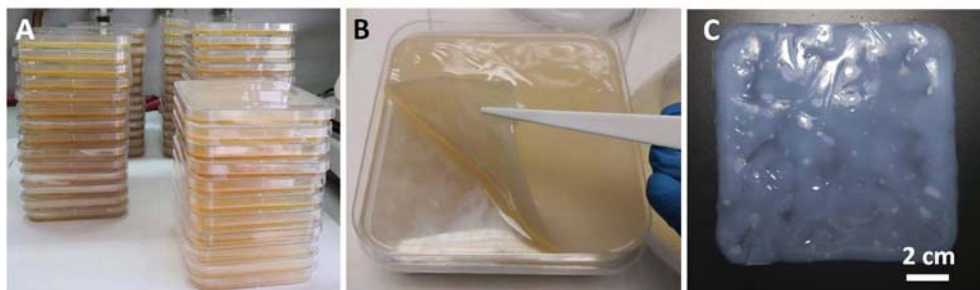


**Figure 4:** Scheme of BC film production. Step 1) Expansion of a bacterial colony in liquid HS. Image: HS agar plate with bacterial cells and 24-well plate before incubation. Step 2) Production of a BC film on top of the liquid medium. Image: 24-well plate after incubation and a harvested film from top and cross-section view. Step 3) Cleaning of BC to remove organic residues. Image: Clean BC films of different sizes.

After cleaning (step 3), the films turned to transparent pellicles although, in the image, the black background enhances a whitish coloring on the films produced by the light scattering of the fibers and the pores. Besides, as BC grows at the interface between air and liquid bacterial broth, by changing the well-plate size the dimensions of the obtained BC films could be controlled, being able to produce circular pellicles of 3.5, 2.5 and 1.5 cm in diameter, as depicted in the image.

### 2.3.1 Increasing film production

In addition to the well-plates, higher BC production was attained employing bigger containers as a first step towards obtaining increased amounts of BC at a laboratory level. The films were synthesized and cleaned as previously described with some additional changes. In brief, 4.5 mL of fresh HS medium were inoculated with 0.5 mL of bacteria and incubated for 3 days at 30 °C. After the dilution in a proportion 1:14 ratio bacteria inoculum:HS fresh medium, 65 mL of the bacterial broth were poured on 12x12 cm plates, which were distributed in columns of 5 and cultivated for 6 days. Next, the films were harvested and soaked in 1:1 EtOH:deionized (DI) water for 10 min, autoclaved twice and immersed two times, for 20 min each, in NaOH 0.1 M solution at 90 °C. The samples were washed with DI water until neutralization and autoclaved again. The number of plates in each column is relevant as a larger stacking does not allow the proper oxygen diffusion to the lower plates and the cellulose growth was not adequate. In addition, when using larger surfaces containers, culture periods of 6 days were needed instead of the usual three days. Figure 5A displays the simultaneous production of seventy-two films adding up more than 1 m<sup>2</sup> of BC. Those films presented a yellowish color when harvested that disappears after cleaning, as observed for the smaller pellicles.



**Figure 5:** A) Image showing a numbering up production of BC at a laboratory scale level using 12x12 cm plates. B) Harvested BC film showing a yellowish color due to the media compounds. C) BC film after the cleaning process where the yellow color has vanished.

### 2.3.2 Drying processes

BC thickness and microstructure of pellicles of 1.5 cm diameter before and after drying was studied. It is reported that ~ 98% of the weight of as-obtained BC pellicles corresponds to entrapped water.<sup>6-8</sup> Therefore, the technique used to dry those films will have an impact on their final microstructure. In fact, the effect of three drying

routes - oven drying (OD), freeze-drying (FD), and supercritically drying (SCD) - on the porosity, water absorption capacity and mechanical properties of the films was previously reported by our group.<sup>9</sup> Throughout the thesis, those three drying processes were also used and the study of their influence on the BC materials was expanded.

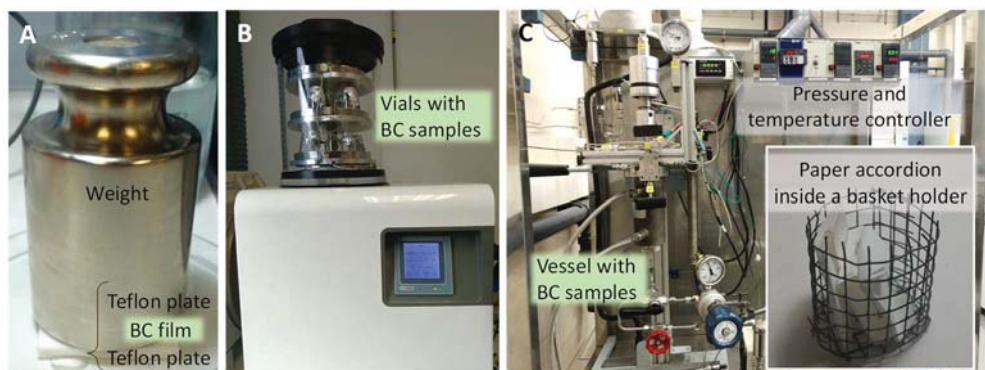
The drying method set-ups are depicted in Figure 6 and they are also described in Annex I for an easier review during the next chapters whenever required. They consisted of:

### **Oven drying (OD):**

BC films were placed between two PTFE (polytetrafluoroethylene or Teflon) plates and dried for 12 h at 60 °C with a 1-2 kg weight on top to flatten the sample.

### **Freeze-drying (FD):**

Each BC film was placed inside a vial and covered by the smallest amount of MQ water needed. Then, the vial was sealed with pierced aluminum foil and was placed inside the lyophilizer at -80 °C and 0.05 mbar for 48 h until complete sublimation of water.



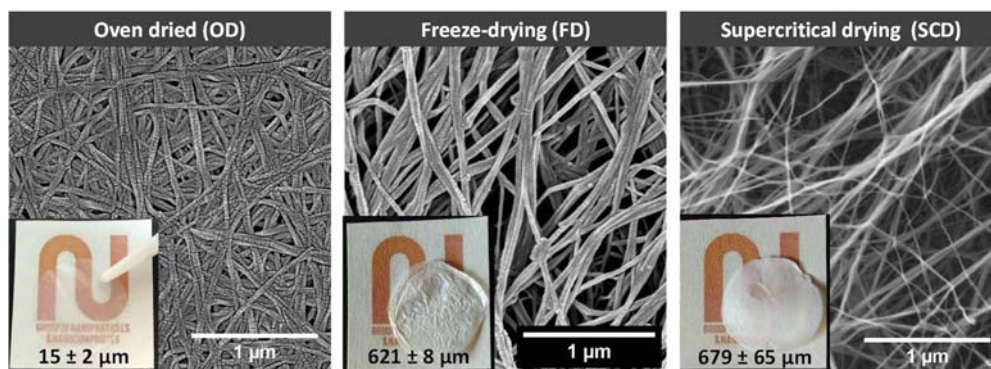
**Figure 6:** Set-up of the drying routes applied. A) Oven drying (OD), B) Freeze-drying (FD), C) Supercritical drying (SCD) plant. Inset: Three paper accordions containing BC films samples. The metallic basket with the paper accordions is placed inside the vessel for drying.

### **Supercritical drying (SCD):**

Samples were distributed on a paper accordion, each fold containing one film, and were subjected to a water-to-ethanol solvent exchange. Firstly, the accordion was

soaked twice in absolute ethanol for 3h and then another 12 h in fresh ethanol. The resulting alcogel was placed on a 300 mL capacity autoclave vessel filled with ethanol and the system was pressurized to 100 bars at room temperature. Ethanol was exchanged with liquid CO<sub>2</sub> at a flow rate of 1500 mL/h for 1.5 hours. Then, the reactor was heated up to 45 °C to reach supercritical conditions, and supercritical CO<sub>2</sub> was dispensed with the same flow rate for 1h. Finally, the vessel was slowly depressurized to avoid pore collapse and BC aerogels were obtained.

Figure 7 shows a macro and microscopical comparison of the films after the different drying processes. The thickness was measured by placing the pellicles between two cover glass and calculating with a micrometer the mean of five points. In the case of never-dried (as-obtained) BC, samples were deposited first on a filter paper to blot the excess of water. In addition, the plunger of the micrometer was lifted and lowered three times and the thickness was obtained when the value was stable for more than 2 s during the third time. The thickness measurement (displayed in the inset pictures) revealed a decrease of 98% when the BC films were subjected to an OD process (from  $733 \pm 45 \mu\text{m}$  wet film; to  $15 \pm 2 \mu\text{m}$  dry film) correlated to the evaporation of water. FD and SCD, on the other hand, maintained better the initial thickness ( $621 \pm 8$  and  $679 \pm 65 \mu\text{m}$  for FD and SCD respectively).



**Figure 7:** Micro (SEM image) and macroscopic (optical inset picture) comparison of the films subjected to three drying processes. Film thickness after drying is also indicated (n=3).

OD and FD samples were coated with 5 nm Pt, and the three different samples were analyzed by a high-resolution scanning electron microscope to image the cellulose nanofibers. It was noticed that the nanofibers were highly packed after OD and less dense when FD or SCD were used. In addition, the transparency observed for OD

---

films vanishes for the other drying processes, acquiring the pellicle a whitish color. OD films presented the smallest thickness values (41 to 45 times smaller than the other drying approaches) which imply higher fiber compaction, a lower scattering of the visible light and, thereof, higher transparent or rather translucent films. However, this decrease of porosity has been reported to affect other parameters such as the mechanical and electrochemical properties or the capacity to fully rehydrate.<sup>8-11</sup> Never-dried samples were not possible to measure under high resolution microscope conditions due to the presence of water. Still, the similar thickness between wet and SCD films made us argue that SCD process best maintained the initial microstructure and porosity of the never-dried BC film.

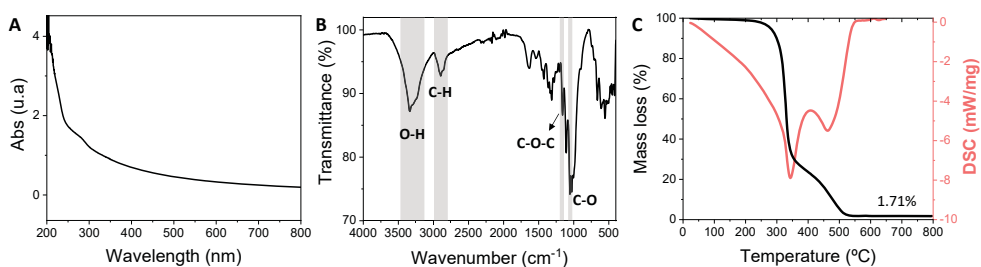
### **2.3.3 Bacterial cellulose single-film characterization**

As mentioned, the group previously reported the properties of BC films after each drying route.<sup>9</sup> Therefore, in this section the principal characteristics of BC film after OD process will be presented, as it is the main material investigated in the thesis.

The transparency of the films was analyzed through optical spectroscopy (UV-Vis). The pellicles were placed within an opaque holder with an aperture in the middle and a cover glass, which was fixed with tape to the holder to immobilize the film, and the absorbance spectrum was acquired. Figure 8A shows a high transmittance (absorbance values near 0) in the visible spectra region with an absorption band at the UV range (200 nm).

Fourier transform infrared spectroscopy (FTIR) was acquired by folding 4 times the BC film and averaging 32 scans in a range between 400 and 4000  $\text{cm}^{-1}$  with a resolution of 4.0  $\text{cm}^{-1}$ . The spectrum obtained is depicted in Figure 8B. The most representative peaks of BC are highlighted in grey. The broad band at 3350 $\text{cm}^{-1}$  corresponds to hydrogen bonding (stretching vibration of O-H). The presence of a peak at 3240  $\text{cm}^{-1}$  is representative of  $I_{\alpha}$  cellulose while a shoulder near 3400  $\text{cm}^{-1}$  would be expected for higher concentrations of  $I_{\beta}$ .<sup>12</sup> The strong peak at 2895  $\text{cm}^{-1}$  corresponds to C-H stretching from  $\text{CH}_2$  and CH groups. The peak around 1158  $\text{cm}^{-1}$  corresponds to stretching vibrations of C-O-C from the  $\beta$ -1.4-glucoside units and peaks from 1070 to 1050  $\text{cm}^{-1}$  can be attributed to C-O oscillations.<sup>13,14</sup> The detailed peak association to the vibrational modes is described in Annex I.

Thermogravimetric studies were performed with a TGA-DSC/DTA analyzer with a heating rate of  $10\text{ }^{\circ}\text{C min}^{-1}$  from 25 to  $800\text{ }^{\circ}\text{C}$  in air to evaluate the carbon mass fraction of BC after carbonization. The profile acquired (Figure 8C) can be described in three sections: first, water evaporation from 50 to  $150\text{ }^{\circ}\text{C}$ , then a thermal degradation which starts at  $280^{\circ}\text{C}$  and is complete at  $340\text{ }^{\circ}\text{C}$  and can be associated with the decomposition and dissociation of glycoside units. Finally, the third step from  $350$  to  $540\text{ }^{\circ}\text{C}$  is correlated to the oxidation and breakdown of carbonaceous residues into gaseous products of low molecular weight.<sup>15,16</sup> The final yield of residual mass corresponds to  $1.71 \pm 0.06\%$  of the initial mass.



**Figure 8:** A) UV-Vis spectra showing the high transparency of the BC film on the visible range after OD. (n= 3) B) FTIR spectra of a BC film after OD drying highlighting in grey the principal peaks of the material. (n= 3) C) TGA of a BC film showing a 2-step decomposition. (n=3)

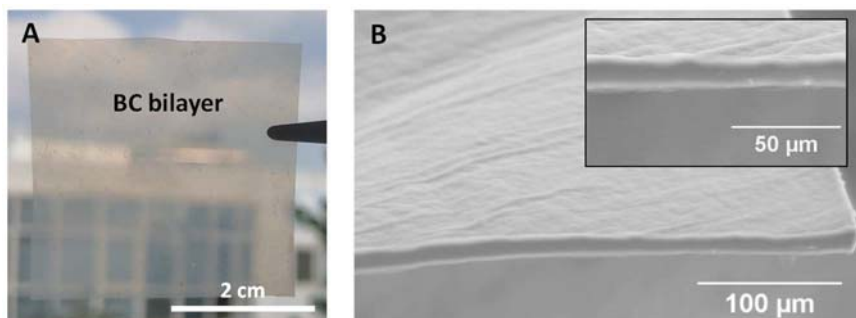
### 2.3.4 Film self-adherence

Bacterial cellulose presents high adhesion to surfaces such as glass. This characteristic mainly results from the large surface area of the nanofibers and the elevated presence of accessible hydroxyl groups, which interact with other surfaces by hydrogen bonding.<sup>17,18</sup> However, the adherence mechanism between cellulose fibers is more complex and other mechanisms could also promote the adhesion, including the mechanical interlocking produced by irregular surfaces or other chemical interactions besides the hydrogen bonding, such as van der Waals or electrostatic forces.<sup>19,20</sup> Hence, we investigated the interfacial adhesion between two wet BC films upon OD drying when we piled them.

Two BC pellicles were placed one above the other between two Teflon plates and dried for 12 h at  $60\text{ }^{\circ}\text{C}$  with a 1-2 kg weight on top. After drying, as shown in Figure 9A, a bilayer was created with the appearance and behavior of a single translucent



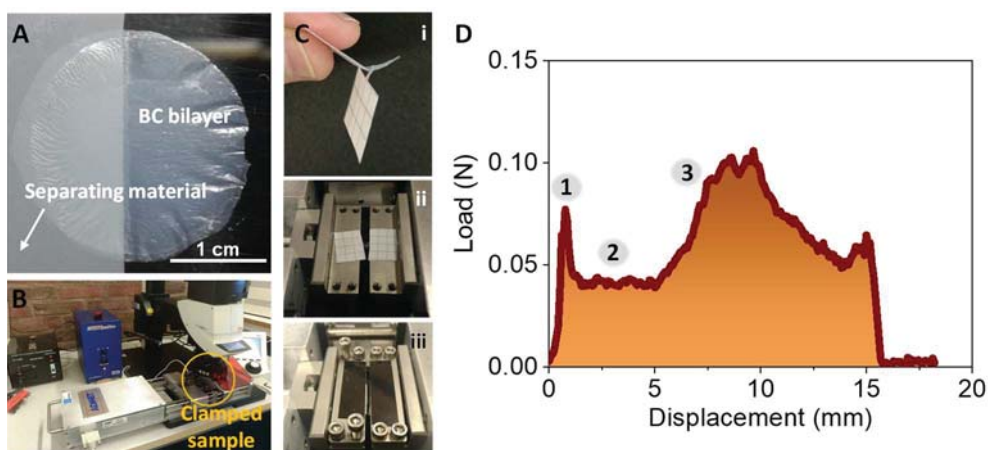
film without appreciable macroscopic air bubbles trapped in the interface. The cross-section was studied under SEM by cutting a section with a stainless-steel blade coated with Teflon and placing the sample with adhesive carbon tape over an aluminum holder tilted 80°. Figure 9B shows a smooth and continuous film where the two layers are not differentiated even in an enlargement of the cross-section (inset image), concluding that a homogeneous adhesion between the two films occurred.



**Figure 9:** A) BC bilayer created after OD two piled BC films. B) SEM image and magnification (inset) of the bilayer cross-section. In both cases, the interface between films is not visible.

The interfacial adhesion energy of the bilayer was then evaluated by a T-peeling test using a dynamic mechanical analysis (DMA) instrument. This study was performed at *Prof. Lars Berglund research group* facilities at KTH, Sweden. As displayed in Figure 10A, half of the film was dried with a Teflon paper between the wet BC layers to prevent adhesion in this region. The samples were cut using a blade and rectangle-shaped BC bilayers were obtained with one of the ends with the layers isolated and with final dimensions of the sticking area of 5 x 7.5 mm. Finally, the tests were conducted using a linear variable differential transformer, a displacement sensor to move both ends at a constant speed of 0.7 mm/s and an ADMET load cell of 100 N under controlled temperature and humidity conditions ( $23\pm 1$  °C and  $25\pm 1$  % humidity) and monitoring the peeling with a microscope. The complete setup is shown in Figure 10B. The two not-adherent ends of the strip were each glued in between two 1.5 x 1.5 cm pieces of paper and placed between clamps. This was done to avoid damage to the BC film close to the gripping area due to the clamps (Figure 10C). Besides, extra care was needed when clamping to avoid applying additional tension to the strip, which would conceal the results. Figure 10D depicts a representative curve of the peeling force needed to separate both layers recorded as a function of the displacement and three regimes (marked with numbers on the graph)

can be discerned. First, the curve presents an increased peak load to achieve the initial displacement. Then, a lower and more constant load is appreciated while the displacement increase as the layers are peeled apart. Finally, upon higher displacements, a second load peak is observed just before the bilayer is completely separated. We hypothesized two possible scenarios for the behavior observed. On one hand, the drying process could facilitate a better adhesion at the edges of the films, more exposed to the air. A second explanation, and a more likely scenario, would be that a crack resulting from the peeling grows inside one of the layers rather than at the bilayer interface. In fact, this event was clearly observed when the films were decorated with nanoparticles (Chapter 4).



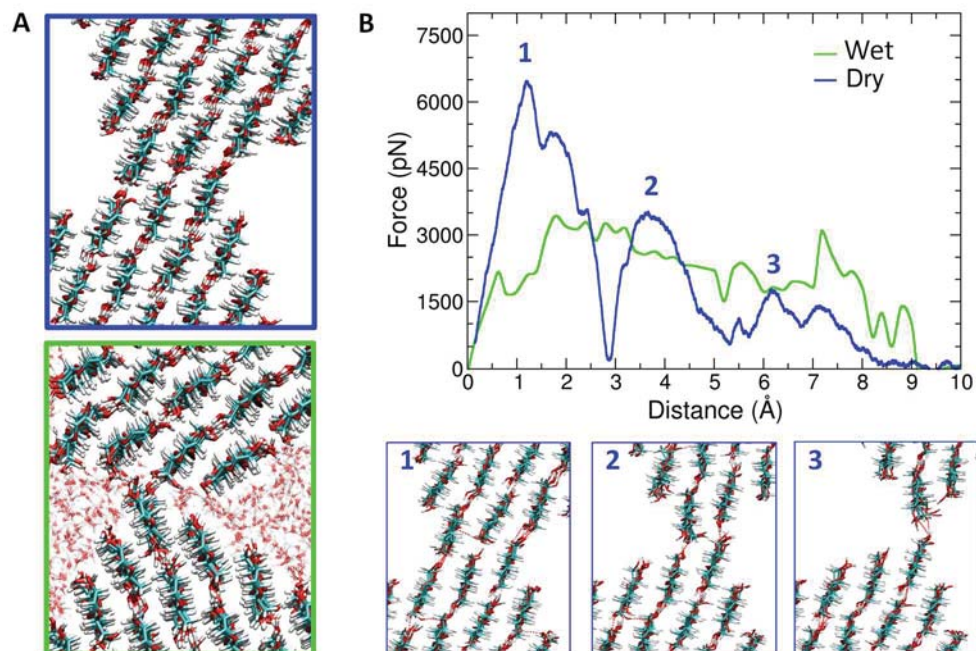
**Figure 10:** A) Peeling test sample preparation. B) DMA set-up. C) Sample arrangement: i) Glue the not-adherent ends of the BC bilayer strip in between pieces of paper. ii) Place each strip end on one clamp. iii) Clamp the end of the strip without applying tension to the strip. D) Force vs displacement curve, the area under the curve (brown) represents the interfacial energy needed to separate the films of a BC bilayer after drying.

By integrating and normalizing the area under the curve by the area of the sample ( $37.5 \text{ mm}^2$ ) from three independent experiments, interfacial energy mean value of  $46 \pm 20 \text{ J/m}^2$  was computed as the energy needed to separate the two films that integrate the BC bilayer. This value is higher than the value obtained from interaction simulations of microfibrillated plant cellulose with other fibers<sup>21,22</sup> and about twice the value previously reported for microfibrillated cellulose films from plants<sup>23</sup>, although the high error indicates that further replicas or bigger samples are needed.

---

Atomistic molecular dynamics (MD) simulations were performed in collaboration with the *Materials simulations and Theory* research group from ICMAB, led by Dr. Jordi Farauo, to gain insight into the nature of BC bilayer adhesion after drying. The detailed technical description regarding the simulation parameters applied is described in Annex I at the end of the thesis. The preferred configuration of two nanocellulose fibrils (4 nm diameter, 6 nm length) in contact in water (wet) and dry conditions at 25 °C were simulated and their interaction was quantified. However, it is necessary to highlight that the dry state simulations were an idealized case since water is always present in cellulose films absorbed or adsorbed. The obtained configurations are illustrated in Figure 11A, where O atoms are represented in red, C atoms in cyan and H atoms in white (CPK color scheme), and show substantial differences between the wet and dry scenarios. In dry conditions (blue highlighted), the two fibrils tend to form fibril-fibril hydrogen bonds in a large contact surface along the fibrils, aligning and extending the crystal structure, although other interactions might be present. Whereas, in wet conditions (green highlighted), the fibrils interact with the surrounding water molecules reducing the number of fibril-fibril hydrogen bonds and therefore, the two fibrils are nearby but separated by water molecules. Consequently, stronger adhesion forces were expected in dry conditions.

The next step was to simulate the force needed to detach the fibrils in both scenarios, starting from a contact position (configuration showed in Figure 11A) to full separation. The results are depicted in Figure 11B, where the x-axis refers to the distance between the mass center of each fibril. In wet conditions, ~1700 pN were required to separate the two fibrils. In contrast, in dry conditions the fibrils separate in three stages, corresponding to each peak observed in the force curve. At the first stage, a force of ~6500 pN was required as three alignments of hydrogen bonds between the fibrils were present (inset picture), the force decreased for the second step with two aligned hydrogen bonds left until an even smaller force of ~2000 pN needed in the last stage, with only one hydrogen bond to break. The enhanced adhesion energy appreciated during drying can be attributed to the increased contact between fibrils favored by the absence of water, while in wet conditions the number of hydrogen bonds between fibrils decreases and the force needed to separate the fibrils is reduced by 3 times.



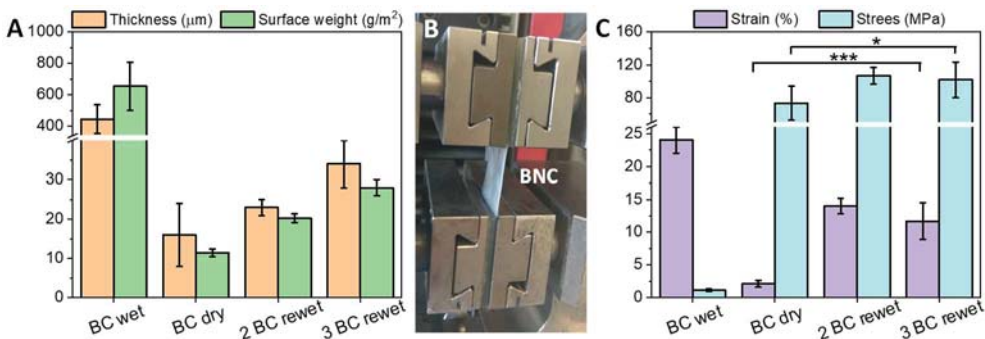
**Figure 11:** MD simulation at 25 °C with CPK color scheme. All snapshots were made using the visual molecular dynamics (VMD) program.<sup>24</sup> A) Cross-section view of the equilibrated configuration of the two fibrils in dry (blue frame) and wet (green frame) conditions. B) Adhesion force between the fibrils as a function of the separation distance between them in dry and wet conditions. Insets: snapshots of the fibril-fibril interface corresponding to the peaks indicated in the graph.

A way to extrapolate the simulation values to the experimental results was by the comparison of the maximum forces. The value of the maximum force observed in Figure 10 ( $\sim 0.10$  N) is comparable to have  $\sim 10^7$  aligned contacts fibril-fibril in dry conditions as the ones observed in Figure 11A. A more direct comparison of the results was challenging due to the complexity of the film surface. As I have mentioned before, roughness, fibril-fibril contacts in different orientations, entanglements, pore swelling/contraction upon drying or other secondary interactions would also provide important contributions to the adhesion forces obtained.

### 2.3.5 Tensile properties

The mechanical tensile performance of the films was evaluated in collaboration with *B. Braun Surgical*, a biomedical company located in Rubí, Spain. Five replicas of never-dried BC films (wet), dry BC and rewet BC multilayers (from 2 to 3 films) were analyzed expecting an increase of the mechanical resistance as more layers were

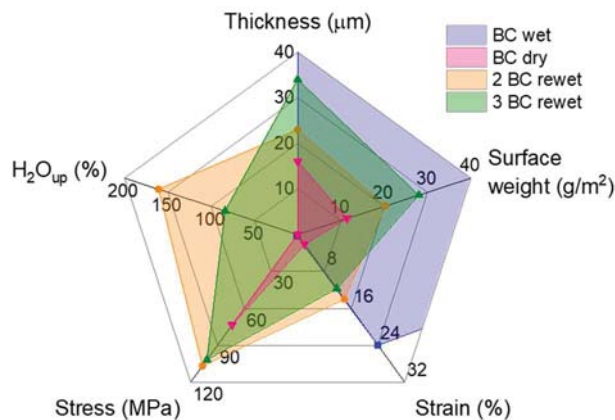
added. 20x50 mm BC pieces were cut from the original BC films of 12x12 cm (144 cm<sup>2</sup>) and their thickness and surface weight, calculated as the ratio between dry weight and area, were measured. Multilaminates were studied before rehydration. Quantitative data was analyzed using ordinary one-way ANOVA followed by Tukey's multiple comparison test accepting a statistical significance at 0.05. As shown in Figure 12A, the thickness experienced a decrease of more than 96% after drying (from 445 ± 91 μm for a wet film; to 16 ± 8 μm for a dry film) and the surface weight was approximately 60 times higher for wet films than for its dried counterparts (654 ± 153 g/m<sup>2</sup> wet film; 11 ± 1 g/m<sup>2</sup> dry film). These results are in accordance with the thickness measurement as, upon drying, the water is removed and 98% of the surface weight is lost, indicating that cellulose nanofibers account for only 2% of the mass. As expected, when compared to a monolayer, thickness and surface weight increased as more layers were added. More precisely, thickness raised to 23 ± 2 μm (2 layers) and 34 ± 6 μm (3 layers) and the surface weight to 20 ± 1 g/m<sup>2</sup> (2 layers) and 28 ± 2 g/m<sup>2</sup> (3 layers). Statistically significant differences between wet, dry and multilayers were found for both parameters except for the thickness between dry BC and the bilayer (P-values <0.01).



**Figure 12:** A) Thickness and surface weight of wet, dry and BC multilayers. (n=5) B) Tensile mechanical set-up. C) Mechanical study of BC films and multilayers in wet and dry conditions. (n=5)

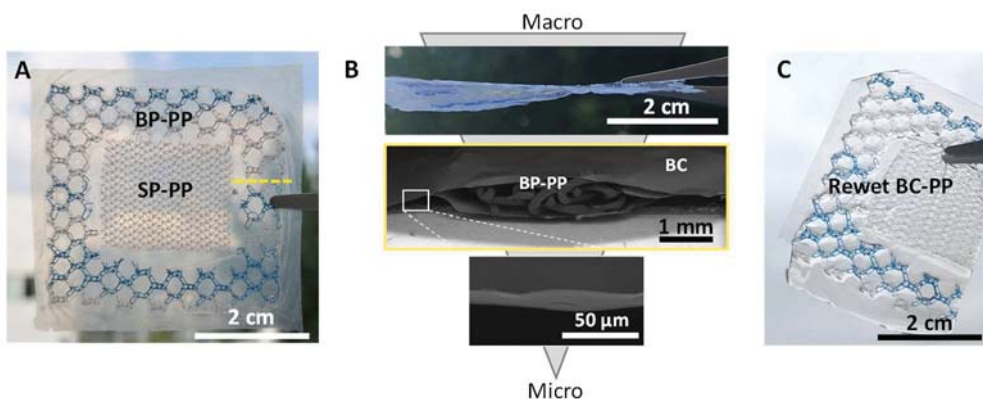
The samples were then clamped in a Zwick Z2.5 dynamometer with metallic clips containing a pneumatic flat rubber part to prevent their sliding (Figure 12B). Strain and stress values were acquired with a load cell of 2.5 kN and a test velocity of 100 mm/min and are presented in Figure 12C. Before the tensile study, the dried multilayered systems were immersed in a 0.9% NaCl solution for 5 min for rehydration to better simulate the physiological conditions for future possible biomedical

applications. Excess of liquid was removed as described before for wet films thickness and water uptake ( $H_2O_{up}$ ) percentage was calculated as  $(m_w - m_d)/m_d \cdot 100$ , where  $m_w$  is the weight of the wet sample after hydration and  $m_d$  is the weight of the dry sample before hydration. The stress to failure of wet BC was approximately 67% lower than that of dry BC ( $1.1 \pm 0.2$  MPa and  $74 \pm 21$  MPa respectively). On the contrary, the maximum strain increases 12-fold in wet conditions ( $24 \pm 2$  % in comparison to  $2.1 \pm 0.5$  % for dry BC). The different behavior could be explained through the microstructure observed in both scenarios. Wet BC presents a higher porosity with low fibril-fibril hydrogen bonding interactions where the nanofibers can reorganize upon an externally applied load, conferring to the film a higher strain. In contrast, the porosity of dry BC is substantially decreased and the fibril-fibril number of interactions is higher, as described by the simulations in the previous section, which confers to the film robustness towards applied loads. In addition, and as expected, multilayers constructs presented higher values; a maximum strain of  $14 \pm 1$  and  $12 \pm 3$  % and stress of  $107 \pm 10$  and  $102 \pm 22$  N/cm for 2 and 3 layers respectively. Double-layered BC maximum strain increased almost 7-fold compared to a single and dry BC layer and the stress increased 1.4-fold. Remarkably, during the tensile test, no peeling or separation of the rehydrated layers was observed. Statistically significant differences between wet, dry and rewet multilayers were found for both parameters except between laminated films ( $P$ -values  $< 0.05$ ). Figure 13 gathers the values obtained for all the studied systems for a clearer comparison. Lower water uptake was appreciated for the triple-layer possibly because the larger thickness impeded the complete diffusion of water in the given time.



**Figure 13:** Comparison of dry, wet and BC multilayers after rehydration.

The similar mechanical values obtained for the bi- and tri-layer constructs made us contemplate BC hybrid materials to further increase the mechanical resistance of BC films. For this purpose, we considered commercial polypropylene (PP) meshes as they are widely used for hernia treatment and present high mechanical strength properties.<sup>25,26</sup> The assembly of the hybrid material took place by a simple approach as placing a film of PP in between two BC layers and taking advantage of the self-adhesiveness. Figure 14A shows a frontal picture of a sandwich-like multilayer composite attained with PP meshes of two different pore sizes, as presented in Figure 14B. The BC-PP composite firmly integrates the synthetic meshes. The thickness of the dry composite varies depending on the incorporated PP material: for a PP mesh with small pores (named SP-PP) a thickness of  $332 \pm 8 \mu\text{m}$  was obtained, while when a PP mesh with bigger pores was employed (BP-PP) thickness increased up to  $589 \pm 23 \mu\text{m}$ . The SEM cross-section study (highlighted in yellow) showed the good integration of the BP-PP mesh in between the BC layers. Although the synthetic material did not adhere to the BC films, it was immobilized in an envelope-like structure due to the BC self-adhesion in the contact areas in between the pores of the PP mesh and at the composite perimeter (inset picture). In addition, the stability of the hybrid structure upon rehydration was tested. After 5 days in water, the construction was still flexible and easily handled without noticeable delamination (Figure 14C).

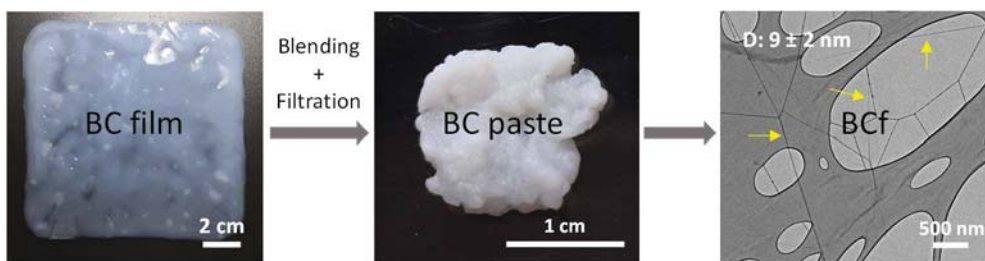


**Figure 14:** A) Frontal view of a BC bilayer combined with PP meshes with different pore sizes: big pores (BP) and small pores (SP). B) From up to bottom: lateral image of the BC-PP hybrid composite; SEM cross-section image of the BC-PP composite corresponding to the yellow line in A; higher magnification of the cross-section to appreciate the continuous adhesion between BC layers. C) BC-PP composite after 5 days rehydration.

## 2.4 Bacterial cellulose nanofibers

After harvesting and cleaning BC films, they can be post-processed to obtain other nanocellulose structures, for instance, fibers. BC nanofibers (BCf) are greatly interesting as allow the material to be dispersible in solution. This characteristic, along with the intrinsic properties of the material, has promoted its use as reinforcement or stabilizer.<sup>27,28</sup>

BCf were obtained after 10 min blending of 5 square films of 164 cm<sup>2</sup> in 1L of water using a commercial household blender. The solution was then vacuum filtered inside a biohood, avoiding Büchner cellulose-based filters, to prevent contamination from dust and other particles upon BCf collection. Finally, the nanofibers were collected as a whitish paste from the filter before being completely dried to circumvent hydrogen bond condensation of the hydroxyl groups (Figure 15). The water present in the paste was measured by weighing it before and after OD drying, obtaining a weight loss of  $90 \pm 3\%$  (n=9), similar to the values achieved for the BC films. BCf were diluted in 1 mL of EtOH, sonicated for better dispersion and analyzed by TEM with a grid with holes to enhance the contrast. As appreciated in the image, highlighted with yellow arrows, fibrils of  $9 \pm 2$  nm diameter (value calculated as the average of 24 measurements) were combined and connected shaping bigger fibers in a tangled net.

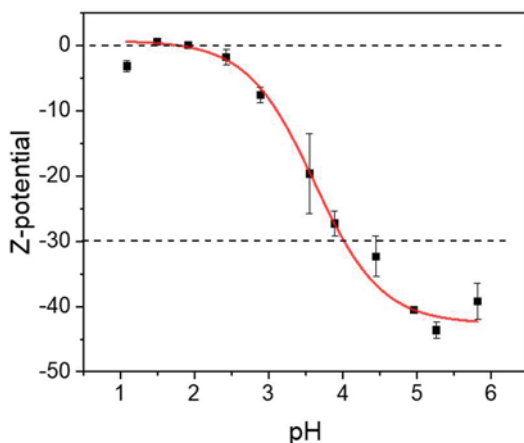


**Figure 15:** BCf production. BC films (164 cm<sup>2</sup>) are blended and filtrated to obtain a paste composed of cellulose nanofibers of 9 nm of diameter (yellow arrows on TEM image).

In addition, the stability of the nanofibers in suspension was studied. 2 mg of BCf were diluted in 1:10, 1:100 and 1:1000 solutions, left 24 h and analyzed by z-potential. A value of -30 mV or below indicates a stable solution and in all cases, those conditions were achieved. In addition, the isoelectric point of the fibers was studied by titration upon acid pH levels. The isoelectric point indicates the pH at



which the negative charges of the hydroxyl groups are compensated by the medium and the fibers possess no net electrical charge. In Figure 16 is represented the titration for the most diluted solution where it can be observed that at pH values lower than 4 the solution lost its stability (the z-potential is no longer below -30 mV) until finally reaching the isoelectric point at 2 pH. This value is lower than the one found for other cellulosic sources<sup>29</sup> and maintains when more concentrated solutions were analyzed.



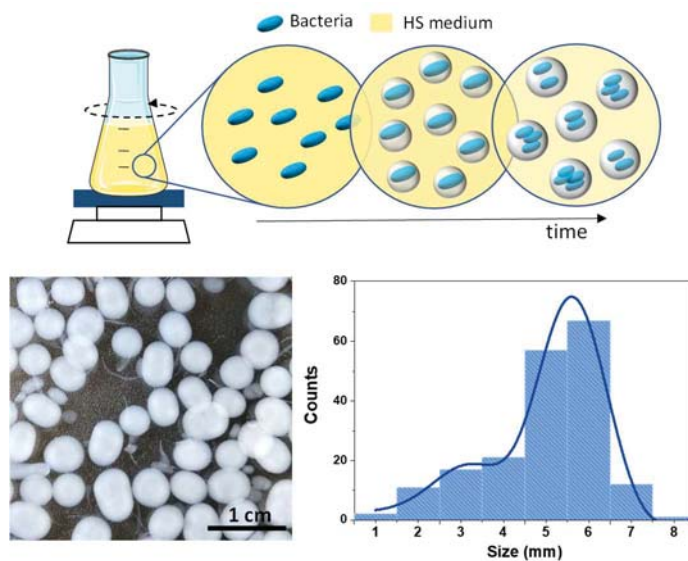
**Figure 16:** Titration of a 1:1000 BCF solution showing an isoelectric point at 2.

## 2.5 Bacterial cellulose spheres

Although the film BC production through the static culture is the most extended one, it does not allow the formation of intricate 3D shapes by simple approaches and the scalability is still challenging. Therefore, other cultivation techniques or variations of it are being investigated. In this scenario, our group had produced bacterial cellulose spheres (BCS) exploiting an accessible fabrication approach already published - biosynthesis under static conditions on hydrophobic surfaces<sup>30</sup> – that was expanded in this thesis and compared to other cultivation methods such as agitation.

The growing mechanism of the BC agitation approach was described by Hu *et al.*<sup>31</sup> and is depicted in Figure 17. 38 mL of culture medium were mixed with 2 mL of inoculum. During the culture time bacteria aggregate due to stirring and produce nanofibers creating skein-like structures trapping the bacteria inside, resulting in filled bacterial cellulose spheres (f-BCS). After 3 days at 30 °C in 150 rpm agitation, solid spheres of  $6 \pm 1$  mm diameter were obtained. The diameter was calculated by

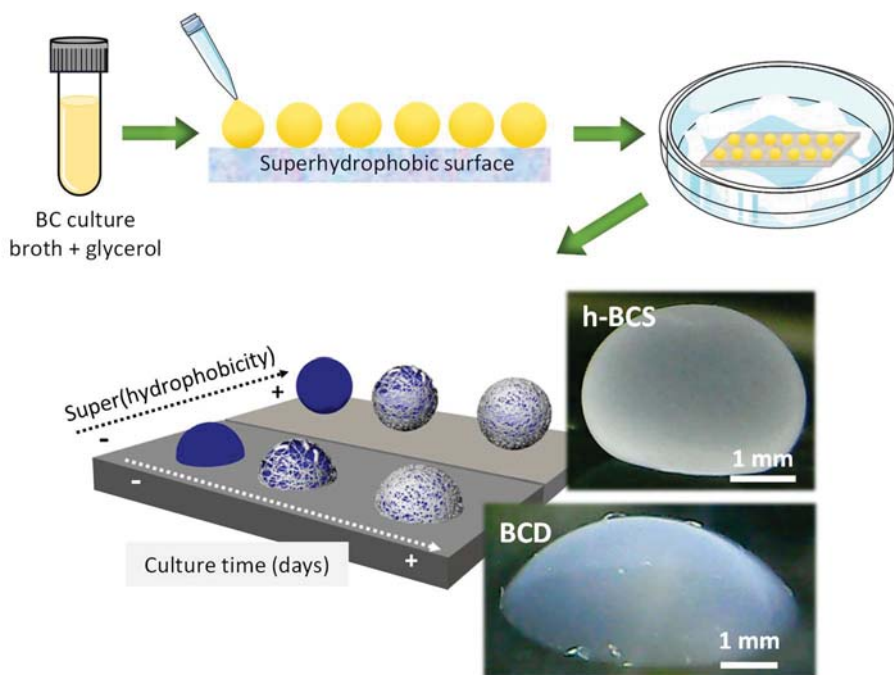
digital analysis with ImageJ software. By this approach, a good size and shape control of the spheres is complex to be attained as it depends on additional factors besides the bacteria concentration, temperature, carbon or nitrogen source such as the stirring speed or the available oxygen content.<sup>32,33</sup>



**Figure 17:** Scheme of the agitation biosynthesis method to produce filled bacterial cellulose spheres (f-BCS). Low panel: picture showing f-BCS and its size histogram with a maximum peak at  $6 \pm 1$  mm ( $n = 185$ ).

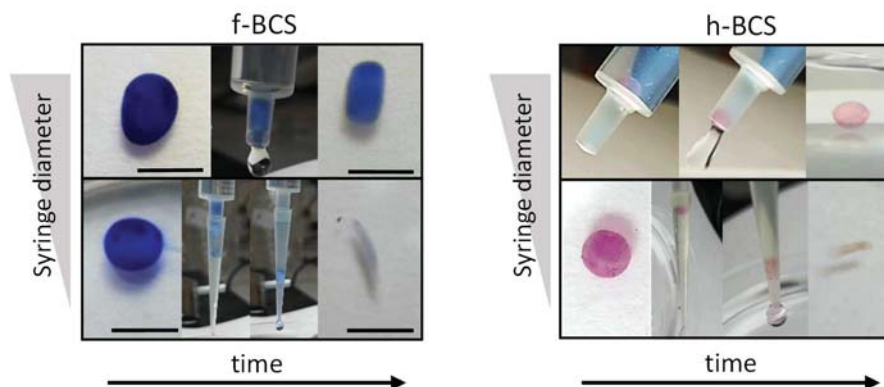
To afford a better size control, our group developed a static biosynthesis method using hydrophobic surfaces provided by the *Multifunctional Materials Systems research group* led by Pro. Pavel A. Levkin from KIT, Germany,<sup>30</sup> that resulted in hollow BC spheres, h-BCS. As shown in Figure 18, the bacterial culture broth was mixed at 10 %v/v with glycerol and 5  $\mu$ L drops of the mixture were deposited on a flat superhydrophobic surface (static water contact angle, WCA =  $150^\circ$ ), the surface was placed inside a close, but not sealed, Petri dish with a saturated humidity environment and the system was incubated for 3 days at  $30^\circ\text{C}$ . The humid environment provided by wet filter paper together with the glycerol avoids the premature drying of the drops. As cellulose grows at the air-liquid interface, it acquires the external shape of the drop and yields to hollow bacterial cellulose spheres (h-BCS). In addition, the drop shape can be modified by modulating the hydrophobic character of the surface, resulting in hollow dome-like shapes (BCD) for hydrophilic surfaces (WCA of  $86^\circ$ ). WCA analysis of the surfaces was performed by a drop shape analyzer (DSA 100) from

KRÜSS by depositing a 5  $\mu\text{L}$  drop of culture media on top of the surface and measuring the contact area between them with the system software. Three surfaces of each type were tested in three different areas obtaining a final value of  $150^\circ$  for superhydrophobic surfaces and  $86^\circ$  for petri dish (hydrophilic) surfaces.



**Figure 18:** Scheme of static culture bacterial cellulose spheres (BCS) production on hydrophobic surfaces. Lower panel: drop shape can be modified depending on the WCA of the surface, obtaining hollow BCD (h-BCD) for high WCA values and dome-like hollow structures (BCD) for lower WCA values.

The flexibility of both types of synthesized BCS (full and hollow) was qualitatively examined by squeezing them through syringes with different diameters (Figure 19). For clarity, BCS were colored with Thymol Blue and Safranin-O, which allowed confirming the conservation of the structural integrity of the spheres. Neither of the BCS could pass through a syringe of 0.4 mm without being completely squeezed and unable to recover its original structure (lower panel). However, while both structures were able to pass through a 2 mm syringe, only h-BCS recovered its original shape (upper panel). We believed this is mainly due to the flexibility conferred by the hollow internal structure.



**Figure 19:** Images showing the shape change of A) f-BCS and B) h-BCS, after being squeezed through a 2 mm syringe diameter (upper panel) and a 0.4 mm (bottom panel) syringe diameter. For better clarity, BCS were dyed with Thymol blue and Safranin-O respectively. Scale bar: 1 mm.

## 2.6 Conclusions

Several bacterial culture methods have been presented in this chapter. Depending on the employed system, a diversity of BC shapes and sizes were obtained showing the versatility of microbial cellulose production. The static, and most traditional culture technique, provides BC films where the size can be modulated by the container used. In this thesis, circular-shaped films of 1.5, 2.5 and 3.5 diameters and square films of 12 x 12 cm were obtained. Besides, a BC increased production at a laboratory scale up to 1 m<sup>2</sup> in just one culture batch has been demonstrated. In addition, how the drying route impacts the final properties of the film have been shown, obtaining low porosities, thin and highly transparent films when the BC is dried inside an oven at 60 °C (OD drying) and highly porous, thicker and less transparent films when drying by a supercritically (SCD) route. Characterization of OD films by UV-Vis and TGA has demonstrated that our films are highly transparent in the visible wavelength region and are thermally stable to an onset temperature of 280 °C, reaching full decomposition at 540 °C and with low residual mass (less than 2%). In addition, FTIR analysis proved that our films are mainly composed of cellulose I $\alpha$  as a shoulder was appreciated at 3240 cm<sup>-1</sup>.

OD allows the formation of multilayered films and by peel-off tests, we have determined the adhesion energy of the two self-adhered layers. The experimental results have been related to the values obtained from molecular dynamics (MD) simulations of the energy between two fibrils in dry and wet conditions. The MD

---

studies have demonstrated that the hydroxyl-rich fibrils promote strong molecular scale cellulose-cellulose adhesion between fibrils when they are in close proximity upon drying. Meanwhile, tensile mechanical tests have evidenced the high dependence of the BC microstructure on the stress and strain values. While wet BC presents high strain values, OD dried films present higher stress to failure values but are less deformable. Those values are increased for the rewet multilayers which did not present observable delamination. However, longer rehydration times would be needed to be tested. Finally, hybrid laminates consisting of BC and PP-meshes were produced as a proof-of-concept for materials with even higher enhanced mechanical properties as no significant difference was observed between bi- and tri-layered films. Those constructs can withstand a 5 days rehydration without appreciable delamination. In addition, in collaboration with *B. Braun Surgical*, the single-layered films were thoughtfully evaluated *in-vivo* for hernia repair treatment and good results in terms of suture and non-adherence appearance were found, which enables future studies with multilaminates and hybrid materials. The results are compiled in a publication entitled “In vivo soft tissue reinforcement with bacterial nanocellulose” (*Biomaterials Science*, 2021, 9, 3040).

Finally, other structures of BC have been produced and studied. Never-dried BC films were blended and filtered to obtain aqueous solutions of BC nanofibers (BCf) with high stability and a low isoelectric point that will be further used as reinforcement material for composites in Chapter 5. In addition, bacterial cellulose spheres (BSC) have been obtained by agitation and static culture, resulting in full or hollow spheres respectively. While agitation culture is highly dependent on the rotation speed and poorly size control of the spheres is attained, static culture on hydrophobic surfaces offers a higher size and shape control of the structures, as the final BC shape can be simply modulated by changing the hydrophobic character of the surface. Besides, the inner structure of the spheres has probed to define its flexibility, which could be of high interest for soft-actuators or drug delivery applications.

## 2.7 References

- (1) Ruka, D. R.; Simon, G. P.; Dean, K. M. Altering the Growth Conditions of *Gluconacetobacter Xylinus* to Maximize the Yield of Bacterial Cellulose. *Carbohydr. Polym.* **2012**, *89* (2), 613–622. <https://doi.org/10.1016/j.carbpol.2012.03.059>.
- (2) CECT. Handling instructions for CECT products <https://www.uv.es/uvweb/spanish-type-culture-collection/en/documentation/technical-instructions-procedures/handling-instructions-cect-products-1285953961369.html> (accessed May 25, 2021).
- (3) Shibazaki, H.; Kuga, S.; Okano, T. Mercerization and Acid Hydrolysis of Bacterial Cellulose. *Cellulose* **1997**, *4* (2), 75–87. <https://doi.org/10.1023/A:1024273218783>.
- (4) Faria-Tischer, P. C. S.; Tischer, C. A.; Heux, L.; Le Denmat, S.; Picart, C.; Sierakowski, M. R.; Putaux, J. L. Preparation of Cellulose II and III Films by Allomorphic Conversion of Bacterial Cellulose I Pellicles. *Mater. Sci. Eng. C* **2015**, *51*, 167–173. <https://doi.org/10.1016/j.msec.2015.02.025>.
- (5) Younesi, M.; Wu, X.; Akkus, O. Controlled Mercerization of Bacterial Cellulose Provides Tunability of Modulus and Ductility over Two Orders of Magnitude. *J. Mech. Behav. Biomed. Mater.* **2019**, *90*, 530–537. <https://doi.org/10.1016/j.jmbbm.2018.11.005>.
- (6) Gelin, K.; Bodin, A.; Gatenholm, P.; Mihranyan, A.; Edwards, K.; Strømme, M. Characterization of Water in Bacterial Cellulose Using Dielectric Spectroscopy and Electron Microscopy. *Polymer* **2007**, *48* (26), 7623–7631. <https://doi.org/10.1016/j.polymer.2007.10.039>.
- (7) Ul-Islam, M.; Khan, T.; Park, J. K. Water Holding and Release Properties of Bacterial Cellulose Obtained by In Situ and Ex Situ Modification. *Carbohydr. Polym.* **2012**, *88* (2), 596–603. <https://doi.org/10.1016/j.carbpol.2012.01.006>.
- (8) Illa, M. P.; Sharma, C. S.; Khandelwal, M. Tuning the Physiochemical Properties of Bacterial Cellulose: Effect of Drying Conditions. *J. Mater. Sci.* **2019**, *54* (18), 12024–12035. <https://doi.org/10.1007/s10853-019-03737-9>.
- (9) Zeng, M.; Laromaine, A.; Roig, A. Bacterial Cellulose Films: Influence of Bacterial Strain and Drying Route on Film Properties. *Cellulose* **2014**, *21* (6), 4455–4469. <https://doi.org/10.1007/s10570-014-0408-y>.
- (10) Ul-Islam, M.; Khattak, W. A.; Kang, M.; Kim, S. M.; Khan, T.; Park, J. K. Effect of Post-Synthetic Processing Conditions on Structural Variations and Applications of Bacterial Cellulose. *Cellulose* **2013**, *20* (1), 253–263. <https://doi.org/10.1007/s10570-012-9799-9>.
- (11) R. Rebelo, A.; Archer, A. J.; Chen, X.; Liu, C.; Yang, G.; Liu, Y. Dehydration of Bacterial Cellulose and the Water Content Effects on Its Viscoelastic and Electrochemical Properties. *Sci. Technol. Adv. Mater.* **2018**, *19* (1), 203–211. <https://doi.org/10.1080/14686996.2018.1430981>.
- (12) Szymańska-Chargot, M.; Cybulska, J.; Zdunek, A. Sensing the Structural Differences in Cellulose from Apple and Bacterial Cell Wall Materials by Raman and FT-IR Spectroscopy. *Sensors* **2011**, *11* (6), 5543–5560. <https://doi.org/10.3390/s110605543>.

- 
- (13) Gea, S.; Reynolds, C. T.; Roohpour, N.; Wirjosentono, B.; Soykeabkaew, N.; Bilotti, E.; Peijs, T. Investigation into the Structural, Morphological, Mechanical and Thermal Behaviour of Bacterial Cellulose after a Two-Step Purification Process. *Bioresour. Technol.* **2011**, *102* (19), 9105–9110. <https://doi.org/10.1016/j.biortech.2011.04.077>.
- (14) Wang, S. S.; Han, Y. H.; Ye, Y. X.; Shi, X. X.; Xiang, P.; Chen, D. L.; Li, M. Physicochemical Characterization of High-Quality Bacterial Cellulose Produced by *Komagataeibacter* Sp. Strain W1 and Identification of the Associated Genes in Bacterial Cellulose Production. *RSC Adv.* **2017**, *7* (71), 45145–45155. <https://doi.org/10.1039/c7ra08391b>.
- (15) Henrique, M. A.; Flauzino Neto, W. P.; Silvério, H. A.; Martins, D. F.; Gurgel, L. V. A.; Barud, H. D. S.; Morais, L. C. D.; Pasquini, D. Kinetic Study of the Thermal Decomposition of Cellulose Nanocrystals with Different Polymorphs, Cellulose I and II, Extracted from Different Sources and Using Different Types of Acids. *Ind. Crops Prod.* **2015**, *76*, 128–140. <https://doi.org/10.1016/j.indcrop.2015.06.048>.
- (16) Vasconcelos, N. F.; Feitosa, J. P. A.; Da Gama, F. M. P.; Morais, J. P. S.; Andrade, F. K.; De Souza Filho, M. D. S. M.; Rosa, M. D. F. Bacterial Cellulose Nanocrystals Produced under Different Hydrolysis Conditions: Properties and Morphological Features. *Carbohydr. Polym.* **2017**, *155*, 425–431. <https://doi.org/10.1016/j.carbpol.2016.08.090>.
- (17) Gardner, D. J.; Oporto, G. S.; Mills, R.; Samir, M. A. S. A. Adhesion and Surface Issues in Cellulose and Nanocellulose. *J. Adhes. Sci. Technol.* **2008**, *22*, 545–567. <https://doi.org/10.1163/156856108X295509>.
- (18) Pommet, M.; Juntaro, J.; Heng, J. Y. Y.; Mantalaris, A.; Lee, A. F.; Wilson, K.; Kalinka, G.; Shaffer, M. S. P.; Bismarck, A. Surface Modification of Natural Fibers Using Bacteria: Depositing Bacterial Cellulose onto Natural Fibers to Create Hierarchical Fiber Reinforced Nanocomposites. *Biomacromolecules* **2008**, *9* (6), 1643–1651. <https://doi.org/10.1021/bm800169g>.
- (19) Fornué, E. D.; Allan, G. G.; Quiñones, H. J. C.; González, G. T.; Saucedo, J. T. Fundamental Aspects of Adhesion between Cellulosic Surfaces in Contact – a Review. *O Pap.* **2011**, *72* (9), 85–90.
- (20) Persson, B. N. J.; Ganser, C.; Schmied, F.; Teichert, C.; Schennach, R.; Gilli, E.; Hirn, U. Adhesion of Cellulose Fibers in Paper. *J. Phys. Condens. Matter* **2013**, *25* (4), 045002. <https://doi.org/10.1088/0953-8984/25/4/045002>.
- (21) Youssefian, S.; Rahbar, N. Molecular Origin of Strength and Stiffness in Bamboo Fibrils. *Sci. Rep.* **2015**, *5*, 11116. <https://doi.org/10.1038/srep11116>.
- (22) Xia, W.; Qin, X.; Zhang, Y.; Sinko, R.; Keten, S. Achieving Enhanced Interfacial Adhesion and Dispersion in Cellulose Nanocomposites Via Amorphous Interfaces. *Macromolecules* **2018**, *51* (24), 10304–10311. <https://doi.org/10.1021/acs.macromol.8b02243>.
- (23) Lönnberg, H.; Fogelström, L.; Zhou, Q.; Hult, A.; Berglund, L.; Malmström, E. Investigation of the Graft Length Impact on the Interfacial Toughness in a Cellulose/Poly(e-Caprolactone) Bilayer Laminate. *Compos. Sci. Technol.* **2011**, *71*, 9–12. <https://doi.org/10.1016/j.compscitech.2010.09.007>.
- (24) Humphrey, W.; Dalke, A.; Schulten, K. VMD: Visual Molecular Dynamics. *J. Mol. Graph.* **1996**, *14*, 33–38. [https://doi.org/10.1016/0263-7855\(96\)00018-5](https://doi.org/10.1016/0263-7855(96)00018-5).

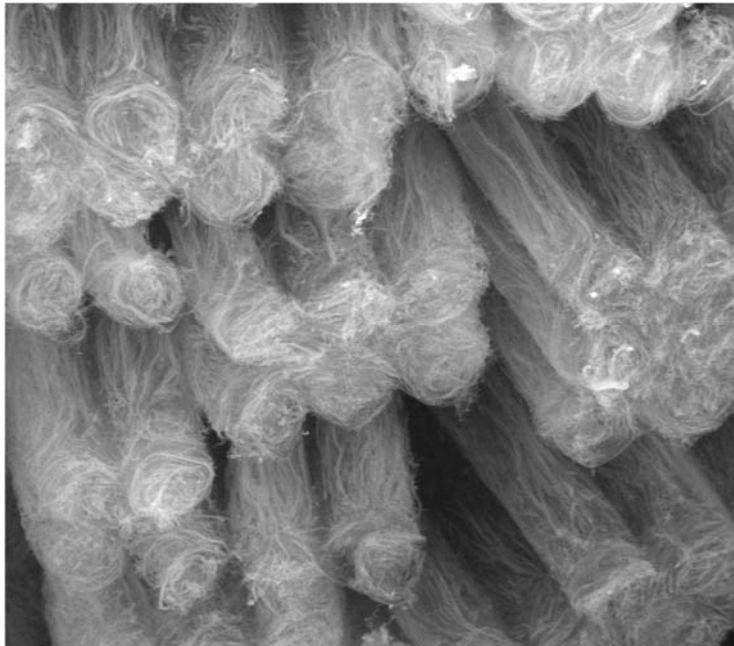
- (25) Klinge, U.; Klosterhalfen, B.; Conze, J.; Limberg, W.; Obolenski, B.; Öttinger, A. P.; Schumpelick, V. Modified Mesh for Hernia Repair That Is Adapted to the Physiology of the Abdominal Wall. *Eur. J. Surg.* **1998**, *164* (12), 951–960. <https://doi.org/10.1080/110241598750005138>.
- (26) Corduas, F.; Lamprou, D. A.; Mancuso, E. Next-Generation Surgical Meshes for Drug Delivery and Tissue Engineering Applications: Materials, Design and Emerging Manufacturing Technologies. *Bio-Design Manuf.* **2021**, *4* (2), 278–310. <https://doi.org/10.1007/s42242-020-00108-1>.
- (27) Paximada, P.; Tsouko, E.; Kopsahelis, N.; Koutinas, A. A.; Mandala, I. Bacterial Cellulose as Stabilizer of o/w Emulsions. *Food Hydrocoll.* **2016**, *53*, 225–232. <https://doi.org/10.1016/j.foodhyd.2014.12.003>.
- (28) Huang, J.; Zhao, M.; Cai, Y.; Zimmiewska, M.; Li, D.; Wei, Q. A Dual-Mode Wearable Sensor Based on Bacterial Cellulose Reinforced Hydrogels for Highly Sensitive Strain/Pressure Sensing. *Adv. Electron. Mater.* **2020**, *6* (1), 1900934. <https://doi.org/10.1002/aelm.201900934>.
- (29) Foster, E. J.; Moon, R. J.; Agarwal, U. P.; Bortner, M. J.; Bras, J.; Camarero-Espinosa, S.; Chan, K. J.; Clift, M. J. D.; Cranston, E. D.; Eichhorn, S. J.; et al. Current Characterization Methods for Cellulose Nanomaterials. *Chem. Soc. Rev.* **2018**, *47* (8), 2609–2679. <https://doi.org/10.1039/c6cs00895j>.
- (30) Laromaine, A.; Tronser, T.; Pini, I.; Parets, S.; Levkin, P. A.; Roig, A. Free-Standing Three-Dimensional Hollow Bacterial Cellulose Structures with Controlled Geometry via Patterned Superhydrophobic-Hydrophilic Surfaces. *Soft Matter* **2018**, *14*, 3955–3962. <https://doi.org/10.1039/c8sm00112j>.
- (31) Hu, Y.; Catchmark, J. M.; Vogler, E. A. Factors Impacting the Formation of Sphere-like Bacterial Cellulose Particles and Their Biocompatibility for Human Osteoblast Growth. *Biomacromolecules* **2013**, *14* (10), 3444–3452. <https://doi.org/10.1021/bm400744a>.
- (32) Meng, C.; Hu, J.; Gourlay, K.; Yu, C.; Saddler, J. N. Controllable Synthesis Uniform Spherical Bacterial Cellulose and Their Potential Applications. *Cellulose* **2019**, *26* (15), 8325–8336. <https://doi.org/10.1007/s10570-019-02446-5>.
- (33) Hu, Y.; Catchmark, J. M. Formation and Characterization of Spherelike Bacterial Cellulose Particles Produced by *Acetobacter Xylinum* JCM 9730 Strain. *Biomacromolecules* **2010**, *11* (7), 1727–1734. <https://doi.org/10.1021/bm100060v>.





# Chapter 3

## Surface patterning of bacterial cellulose films





## CHAPTER SUMMARY

Chapter 3 presents two methods to microstructure the surface of BC films using PDMS molds: i) during its biosynthesis by bio-lithography and ii) after the biosynthesis by soft-imprint lithography. Feature dimensions and fidelity upon different drying techniques will be contrasted and the structuration of large surfaces will be presented.

## CHAPTER INDEX

CHAPTER SUMMARY .....	- 61 -
3.1 Bacterial cellulose film lithography .....	- 63 -
3.1.1 Polydimethylsiloxane stamp fabrication .....	- 64 -
3.2 Bio-lithography .....	- 66 -
3.2.1 Well imprint .....	- 67 -
3.2.2 Pillar imprint .....	- 70 -
3.2.3 Combination of features and printing of large areas .....	- 72 -
3.3 Soft-imprint lithography .....	- 74 -
3.4 Conclusions .....	- 77 -
3.5 References .....	- 80 -



### 3.1 Bacterial cellulose film lithography

The increasing need for environment-friendly and biocompatible materials in high-tech products and devices can drive towards the adoption of approaches from the semiconductor and synthetic polymers technology (such as lithography<sup>1,2</sup> or 3D printing<sup>3</sup>) to process bio-based polymers such as bacterial cellulose, reaching materials with higher degrees of complexity and added value.<sup>4-6</sup> Besides all the characteristics of BC, one of its highly attractive features is the possibility of easily pattern the surface of the pellicle through lithography. It can be performed *in-situ* during the biosynthesis by taking advantage of the intrinsic growth of the material at the air-bacterial broth interface in static conditions and was first reported by Guang *et al.*<sup>7</sup> which coined it bio-lithography. The method consists of the placement of an elastomeric patterned stamp/mold on top of the bacterial culture media. The mold is usually made of polydimethylsiloxane (PDMS) as this material floats at the interface, presents high oxygen diffusion values<sup>8</sup> and can be easily patterned. With this approach, the bacteria produce a cellulose pellicle replicating the opposite (also called negative) topology of the stamp and the motifs (channels, grooves, wells or pillars) are created on the surface of the film.


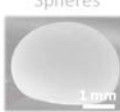
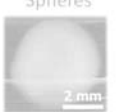


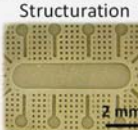


Such one-step and low-cost strategy has been already used by other groups<sup>9-12</sup> as BC patterned films have demonstrated improved properties in the medical sector. Recent studies showed the use of patterned BC as a substrate for expansion, proliferation and homogeneity of stem cell culture<sup>13</sup>, for cellular guided-growth,<sup>14</sup> as anti-fibrotic protection of implantable devices,<sup>15</sup> for scar-inhibition of wound dressings,<sup>16</sup> to accelerate wound healing<sup>17</sup> or to reduce biofilms fouling<sup>18</sup>. Due to the outstanding results, other more complex BC lithography approaches have also been studied. For example, the fabrication of BC implants mimicking vascular networks using PLA sacrificial templates<sup>19</sup> and silicone tubes<sup>20</sup>, the growth of complex BC films via controlled wetting of superhydrophobic molds<sup>21</sup> or photolithography over lyophilized BC films using CO<sub>2</sub> low-energy lasers.<sup>22</sup>

However, aspects such as the diversity and size of the features patterned - especially for pillars -, how those features withstand post-processing steps or if large areas can be patterned have not yet been thoughtfully addressed. Gathering knowledge on these characteristics could be beneficial for the already proposed healthcare applications.

In addition, it can extend the use of patterned nanocellulose-based materials in emerging fields such as transient batteries<sup>23</sup>, cellulose nanogenerators based on piezoelectric, triboelectric and thermoelectric effects<sup>24-26</sup> or single-use recyclable microfluidic platforms<sup>27</sup>.

In this chapter, bio-lithographed BC films with motifs such as wells, pillars, grooves and channels motifs of a wide range of sizes ranging from 200  $\mu\text{m}$  to the sub-micron scale will be presented and their fidelity will be analyzed in as-obtained conditions (wet) and after drying. Besides, soft-imprint lithography, a technique already used to structure vegetal nanocellulose,<sup>28,29</sup> will be also tested. Soft-imprint lithography consists of applying a load to a mold placed on top of a casting solution with an even surface. In this case, harvested and cleaned BC films would perform as the canvas platform and patterned PDMS as the mold, obtaining an *ex-situ* surface structuration (*i.e.*, after the BC biosynthesis). Both techniques, surface patterning of BC film *in-situ* and *ex-situ*, will be compared, as presented in Table 1. A reminder of the BC production and cleaning, as well as, technical details of the characterization, if needed, can be found on Annex I at the end of the thesis.

**Table 1:** Summary of the materials synthesized so far (in lighter shading) and the topics described in this chapter (highlighted).



		Static		Agitation	
Biosynthesis		Films 	Spheres 	Spheres 	
	Processing	Blending 	Structuration 	Structuration 	
		 <i>Ex-situ</i>		 <i>In-situ</i>	

### 3.1.1 Polydimethylsiloxane stamp fabrication


Polydimethylsiloxane (PDMS) stamps were used in both lithographic processes and their patterning was done in collaboration with the *Chemical Transducers research group* at the IMB-CSIC led by Dr. Cesar Fernández. The protocol, more detailed in

Annex I, consists of two main steps. First, masters were defined on 10 cm silicon wafers using a SU-8 negative photoresist at the IMB-CNM Clean Room facilities. A negative photoresist polymerizes under exposure to light. Second, the masters were replicated using PDMS as a mold. Special care was needed when curing the PDMS to avoid entrapped air bubbles into the PDMS solution and in the master surface. After curing (80 °C, 20 min), the PDMS mold was peeled off from the master. The stamps could be reused by cleaning them with ethanol between uses. An additional sterilization process (UV cycle of 15 min) was done for the molds used for biolithography. Feature dimensions of the molds were measured with SEM and optical microscopy and they are gathered in Table 2.

**Table 2:** Dimensions of the features of the PDMS molds used. (n = 15-50) The sample label corresponds to the theoretical dimensions of the feature.

 PDMS with square pillars					 PDMS with square wells				
Sample label	x (μm)	y (μm)	z (μm)	x/z	Sample label	x (μm)	y (μm)	z (μm)	x/z
200	200 ± 2	200 ± 2	142 ± 3	1.4	200	205 ± 1	204 ± 2	53 ± 1	3.9
50	50	50	50	1.0	50	60 ± 1	58 ± 1	53 ± 1	1.1
20	20	20	50	0.4	20	30 ± 1	30 ± 1	60.7 ± 0.3	0.5
5	6.9 ± 0.1	6.9 ± 0.1	17 ± 1	0.4					

 PDMS with circular pillars		
Diameter (μm)	z (μm)	x/z
0.6-0.7	1.05 - 1.10	0.8-1.0

The first observation was that for 20 μm square features and smaller, the sharp edges of the square motifs disappeared and depth was no longer stable at 50 μm, as presented in Table 3 where PDMS with square wells of different dimensions are depicted. To assure high depth values, possibly the photoresist was over-exposed and polymerized even in non-exposed areas close to the motifs, which lessened the 90° accentuated angles of the smaller squares. The PDMS mold fabrication technique needed further optimization to increase the sharp edge resolution at these sizes and should be addressed in future research as it limits the BC pattern replication. The



PDMS stamp with circular pillars at the sub-micron scale was kindly provided by Dr. Agustín Mihi from the *NANOPTO* group at the ICMAB.

**Table 3:** SEM images at different angles of PDMS molds with square wells of different dimensions. For 20  $\mu\text{m}$  features the features are no longer squares but circular shapes.

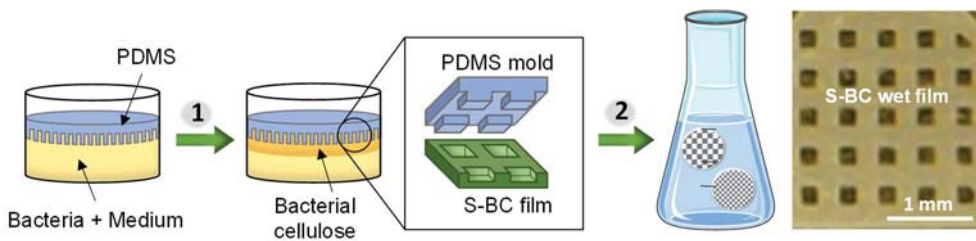


Sample label	Top view	Cross-section	Crosswise
200 $\mu\text{m}$			
50 $\mu\text{m}$			
20 $\mu\text{m}$			

### 3.2 Bio-lithography

To obtain structured BC films (S-BC) during the biosynthesis, 0.5 mL of bacteria broth was transferred to 4.5 mL of fresh medium and incubated for three days. Subsequently, a solution 1:14 inoculum:HS medium was prepared, 1.5 mL were transferred to 24-well plates and a PDMS mold was placed on top with the patterned side facing the liquid solution (step 1 of Figure 1). Since PDMS allows proper oxygen diffusion and has a lower density than water, it sits at the interface between air and bacteria broth and does not hinder the growth of the BC pellicle. Besides, the introduction of the mold forces the bacteria to produce a film that follows the

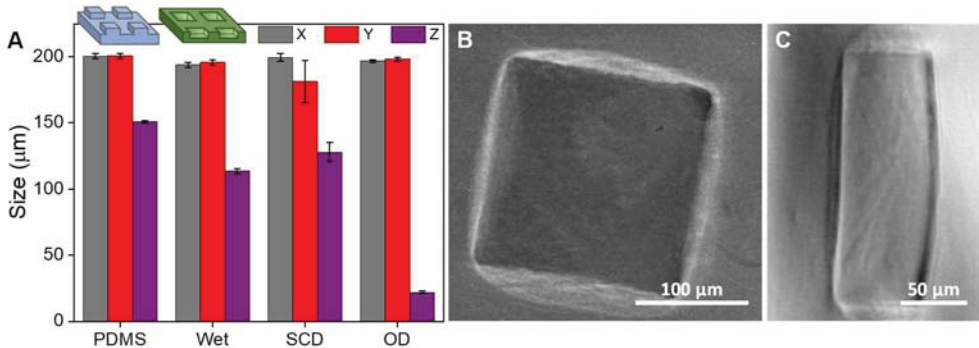
topology of the template, obtaining the counter pattern. After 3 days of incubation at 30 °C, the PDMS could be easily removed and the S-BC films were harvested and cleaned following the standard protocol. Finally, the films were rinsed with MQ water until neutralization of the pH and were stored in water at room temperature (step 2). By this method, wet and transparent S-BC films with wells, pillars, channels or the combination of them could be obtained simultaneously in a single and reproducible step. Motifs were stable over time after several days in water, however, to assess the fidelity of the patterns, the pellicles were dried by the different techniques already described in Chapter 2. The influence of supercritical drying (SCD), freeze-drying (FD) and oven drying (OD) at 60°C was studied.



**Figure 1:** Scheme of the production of structured BC films (S-BC) through bio-lithography. Step 1: incubation of the bacterial broth for 3 days at 30 °C with the patterned PDMS on top. Step 2: removal of the PDMS and cleaning of BC to obtain wet and transparent S-BC films (image).

### 3.2.1 Well imprint

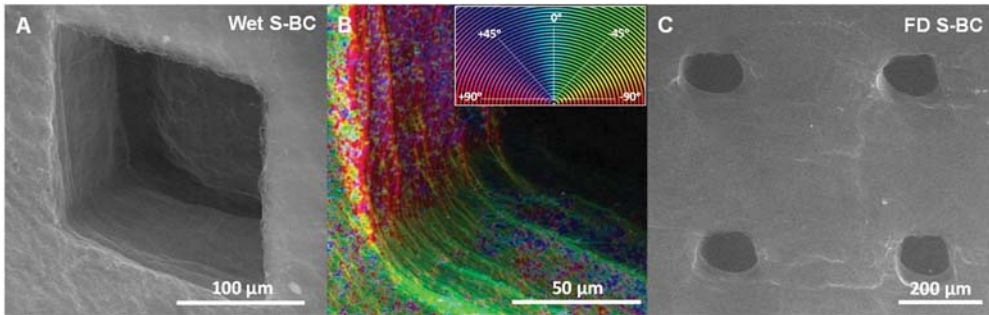
S-BC films with square wells of 200  $\mu\text{m}$  in the x and y-axis were evaluated first. The replication of the x,y, and z dimensions was studied in detail for wet, SCD and OD conditions with SEM and optical microscopy. Results are summarized in Figure 2A. The x and y dimensions were faithfully replicated in the wet and dried samples while size variations were computed in the z-dimension. Compared to the PDMS stamp, which presented a depth of 140  $\mu\text{m}$ , a decrease of  $\sim 15\%$  was measured for wet and SCD S-BC films, while an 85% reduction was found for the OD samples. This large reduction resulted in an increase of the cellulose fraction in the areas surrounding the features, visualized as brighter areas in SEM images (Figure 2B). Besides, a double edge at the borders of the wells was also observed, possibly caused by the volume compaction of the features (Figure 2C).



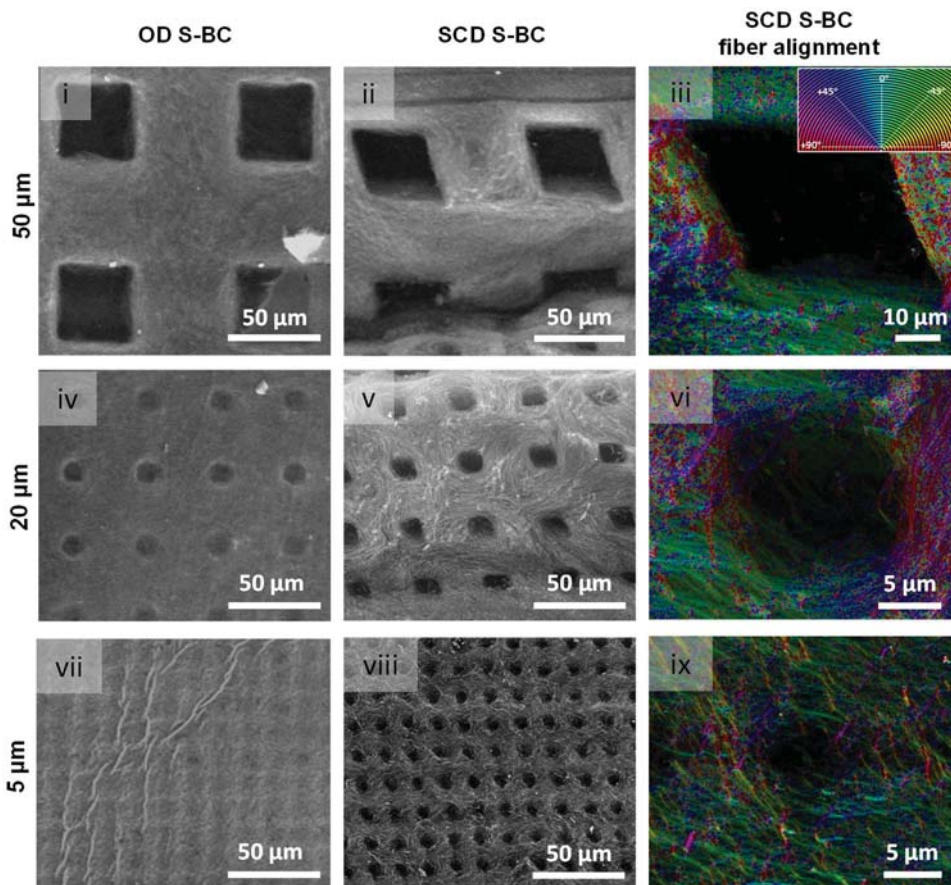
**Figure 2:** A) Dimension comparison of the replication of 200x200x140 μm PDMS square features under diverse conditions (n = 4-15). SEM images of OD S-BC showing B) brighter areas surrounding the features and C) double edge at the borders of the wells due to the compaction of the cellulose fibers.

As displayed in Figure 3A, wet S-BC presented an extremely good replication of the stamp with well-defined structures. A closer look at the fiber disposition revealed an alignment of the fibers at the wall of the well. Figure 3B shows a color map obtained with OrientationJ plugin from ImageJ software where hue indicates fiber orientation and color saturation is given by the alignment coherency. Two areas with different colors were noticeable, indicative of an ordered fiber arrangement at a 90° angle, corresponding to two orthogonal square well sides. This suggests that when bacteria encounter the PDMS mold, it surrounds the obstacle while producing the nanocellulose fibers, a behavior already reported for PDMS stamps with channels, where a fiber alignment is also observed.<sup>14</sup> In addition to OD and SCD, S-BC films were subjected to freeze-drying (FD), however, in this case, the wells did not maintain with enough fidelity the square shape as in the other drying techniques and rather circular configurations were observed (Figure 3C). A possible explanation could be that during freezing the water expanded, deforming the wells. Therefore, freeze-dried samples were not further studied.

Smaller wells with x, y-axis down to 5 μm (50, 20 and 5 μm) could also be replicated (Figure 4) and although OD compromised the depth of the wells (especially appreciated for the 5 μm features – vii image), good replication and fiber ordered arrangement surrounding the PDMS features can also be observed, particularly at high magnifications of samples subjected to SCD (third column – iii, vi, ix images). It is worth mentioning, however, that sharp edges of the square motifs disappeared for features smaller than 20 μm due to the PDMS mold employed.



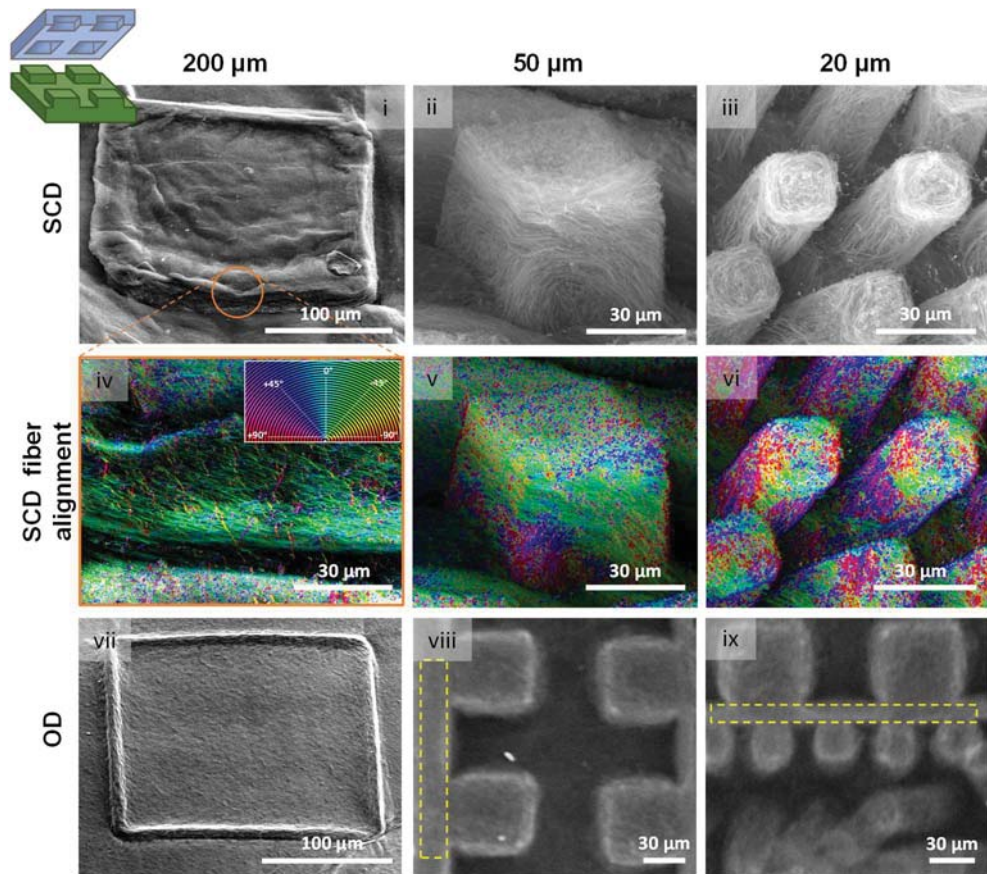
**Figure 3:** A) SEM image of a wet S-BC showing a well-defined square contour and the alignment of the fibers. B) High magnification image where the two directions of the aligned fibers are highlighted in a different color. Inset: legend with colors associated with a certain angle orientation. C) S-BC film with wells of 200  $\mu\text{m}$  after FD. The square wells acquired a circular shape.



**Figure 4:** SEM images of S-BC with wells of 50, 20 and 5  $\mu\text{m}$  in x, y-axis dimensions dried by OD and SCD (left and middle column respectively). The third column displays high magnification images of SCD structured samples where the ordered arrangement of the fibers surrounding the PDMS obstacles is clearly seen by differentiated color sections.

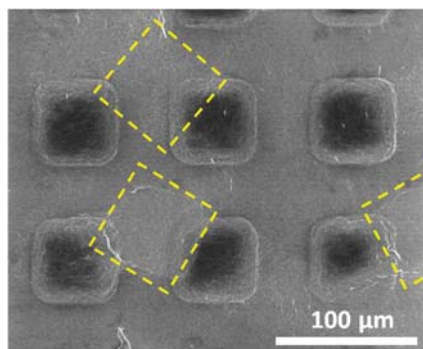
### 3.2.2 Pillar imprint

Next, the bio-lithography of stamps containing square pillars was studied. Figure 5 shows columns of different base dimensions (200, 50 and 20  $\mu\text{m}$ ) and z (height) of 50  $\mu\text{m}$ . Interestingly, by SCD was possible to obtain standing pillars for all the sizes investigated (images i, ii and iii) and an alignment or ordered growth of the fibers was appreciated (images iv, v and vi). While the x/z ratio decreases, those pillars became thinner, longer and wavier and the alignment of the fibers was more apparent.

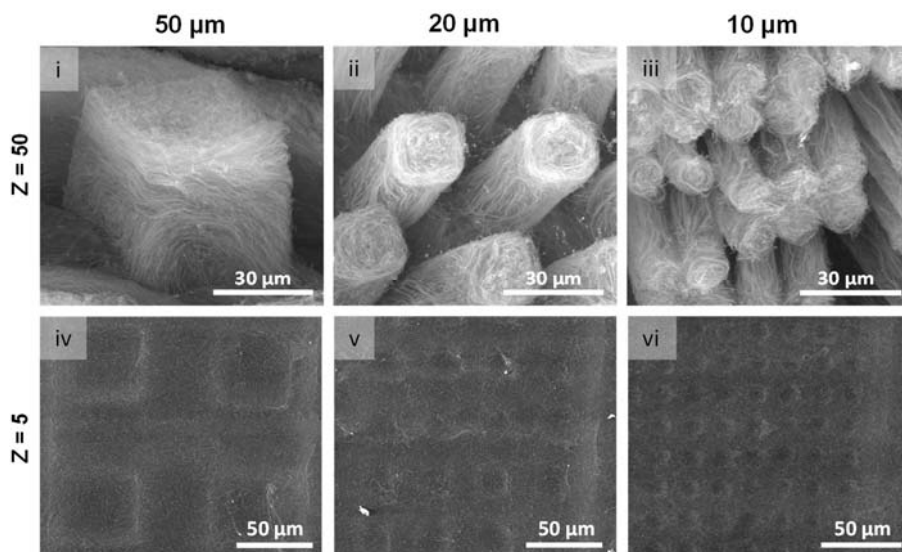


**Figure 5:** S-BC films with pillars of 50  $\mu\text{m}$  depth (z-value) and square base of 200, 50 and 20  $\mu\text{m}$  dried by SCD or OD (lines). The middle line displays the ordered distribution of fibers at the pillar walls after being subjected to SCD.

As previously observed in the case of wells, OD induced the feature collapse, as clearly appreciated in the 200  $\mu\text{m}$ -wide pillars (image vii) where the center section had a lower depth than the perimeter. OD also induced the bending of the pillars at lower  $x/z$  ratios (*aka* lower base dimensions) as depicted in Figure 6 where, while the pillar foot was noticeable in dark, other square sections appeared displaced. Those areas, delimited by a yellow dashed line for an easier appreciation, were assigned to the upper pillar section. However, when the pillar was in contact with another cellulosic structure supporting it (highlighted as a dashed yellow rectangle in Figure 5) well-defined standing pillars were obtained even by OD (images viii and ix).



**Figure 6:** SEM image of OD S-BC film with pillars of 50  $\mu\text{m}$  base ( $x, y$ -axis) and 50  $\mu\text{m}$  depth ( $z$ -axis). The yellow dashed lines delimitate the upper section of the pillars showing thereof bending upon drying.



**Figure 7:** SCD S-BC film with pillar features of 50 and 5  $\mu\text{m}$  depth (lines) and base dimensions of 50, 20 and 10  $\mu\text{m}$  (rows).

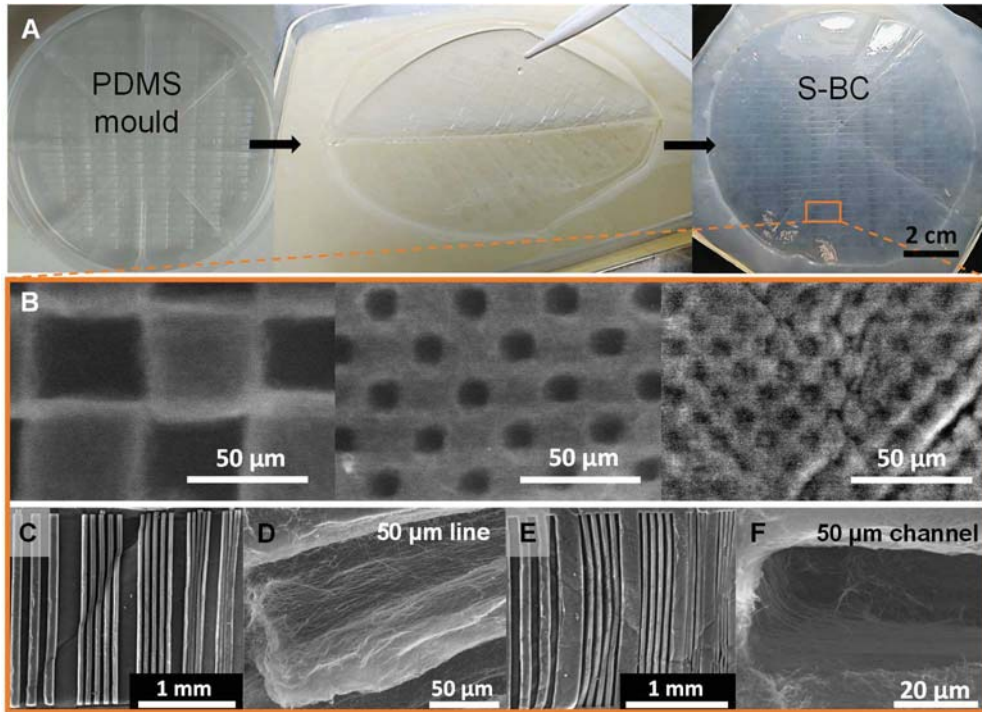
---

Exploring the limits of BC patterning replication and self-standing features, smaller features and PDMS stamps with lower depths were bio-lithographed. As shown in Figure 7, by decreasing the z dimension of the PDMS mold 10-fold, features were still patterned on BC and could be observed under the microscope although the appearance was more similar to a protuberance rather than a pillar and statistical mean values were tough to obtain (images iv, v and vi). Again, below 20  $\mu\text{m}$  in width, the square structure replicated as a circular one as the resolution limit of the PDMS mold was reached.

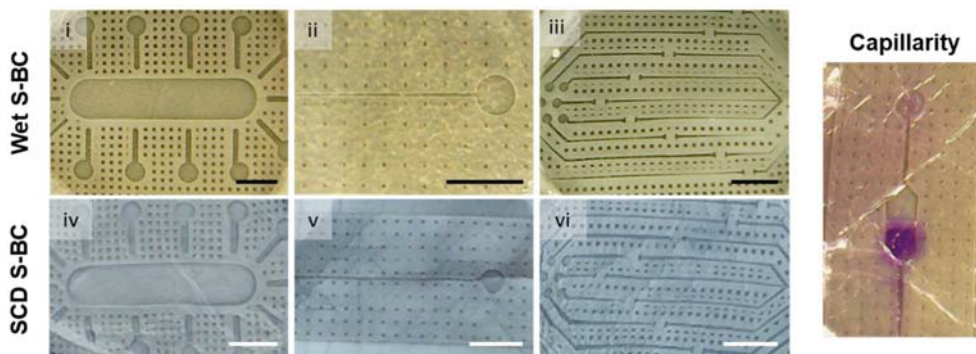
### **3.2.3 Combination of features and printing of large areas**

Finally, a large micropatterned PDMS mold of 70  $\text{cm}^2$  containing 567 replicas of a pattern that included grooves, lines, wells and pillars ranging from 100 to 1  $\mu\text{m}$  in size (x, y-axis) was used as a template (Figure 8A). In this particular case, a 12x12 cm plate was filled with 65mL of a 1:14 ratio bacteria:HS medium solution and the PDMS was placed on top. After an incubation period of 6 days, a S-BC film was obtained. Figure 8B depicts square zig-zag features with dimensions of 50, 20 and 10  $\mu\text{m}$  presented in the film. In addition, a good replication of channels and lines ranging from 100 to 30  $\mu\text{m}$  were obtained (Figure 4C and E). In both cases, the nanocellulose fiber alignment was observed (Figures 4D and F). From 30 to 1  $\mu\text{m}$  width, features could also be perceived although further study would be needed to obtain better resolution.

The same bio-lithographic process was used to obtain BC films with more intricate shapes as shown in Figure 9, which displays examples of wet S-BC films combining channels and wells simulating a chip. These films could withstand SCD drying and rehydration maintaining the structure and could be used to design paper microfluidic devices. For that, a preliminary test of their channel diffusion was attempted in wet S-BC. The excess of water of the wet film was removed by blotting the film with filter paper and a drop of crystal violet solution was deposited in the collection well. Capillarity was observed through the channel, though more optimization is needed to avoid diffusion through the porous nanocellulose matrix.



**Figure 8:** A) Bio-lithography process of a 9.5 cm diameter PDMS mold which contains 567 patterns with grooves, lines, wells and pillars ranging from 100 to 1 μm. One of those patterns is stressed in orange. B-F) SEM images of areas of the pattern contained in the 9.5 cm S-BC: B) Zig-zag display of well and pillars of 50, 20 and 10 μm respectively. C) Lines ranging from 100 to 30 μm. D) Line of 50 μm where the fiber alignment is seen. E) Grooves ranging from 100 to 30 μm. F) Groove of 50 μm where the fiber alignment is seen.



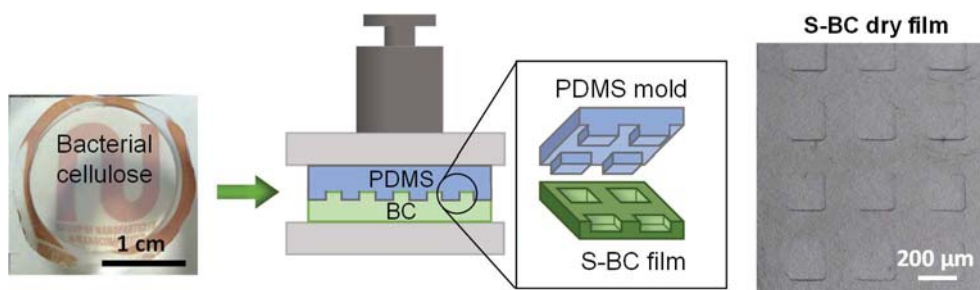
**Figure 9:** Wet and SCD S-BC films with combinations of channels and wells. Scale bar: 2 mm. Channel capillarity test on a wet S-BC film.



### 3.3 Soft-imprint lithography

The second patterning approach studied consisted of the printing of features on native and wet BC films by soft-imprint lithography. Imprinting is performed after the biosynthesis, harvesting and cleaning of the films, hence it is an *ex-situ* patterning process. In contrast, bio-lithography, which is performed during the biosynthesis of bacterial cellulose, is considered an *in-situ* patterning method.

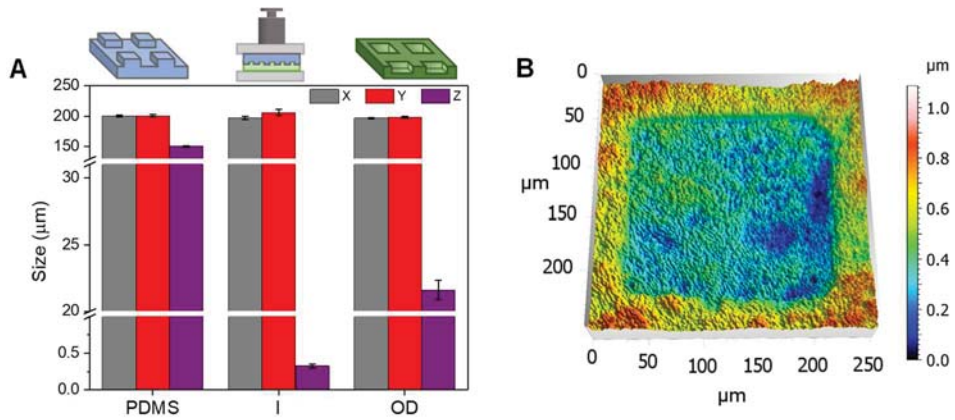
Figure 10 shows a schematic of the soft-imprint process. In brief, 2 mL of a solution 1:14 inoculum:HS medium was transferred to 24 well plates and after 3 days incubation at 30 °C, a flat BC pellicle (no patterned) was harvested and cleaned. Then, a PDMS stamp was placed above the wet bacterial cellulose with the patterned side facing the film and both layers were sandwiched between two Teflon plates for drying for 12 h at 60 °C under 1 kg weight pressure. By this strategy, the structuration is performed concomitantly with the drying of the film, always resulting in dried S-BC films.



**Figure 10:** Scheme of the process to produce structured BC films (S-BC) by soft-imprint lithography. The BC film was harvested from the culture media, cleaned and let dry in contact with a patterned PDMS mold for 12 h at 60 °C and applying pressure (1 kg weight). A dry S-BC film was obtained (image).

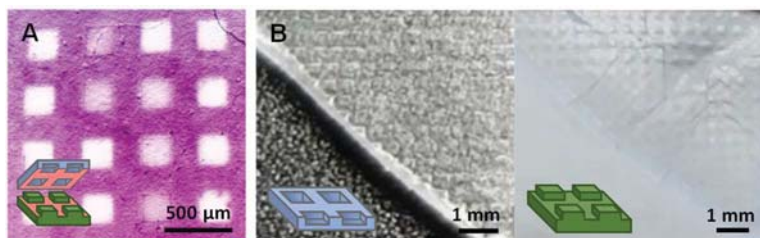
To start the study, a PDMS mold with square columns of 200  $\mu\text{m}$  base size and 140  $\mu\text{m}$  depth was employed to be able to establish a comparison between soft-imprint and bio-lithography after OD of BC. As shown in the graph of Figure 11A, while the x and y dimensions were maintained, the z was considerably reduced ( $\sim 99\%$ ) compared to the original PDMS depth size, which is a much larger reduction than for the OD S-BC counterpart film obtained by bio-lithography (85% reduction). Figure 11B displays a topographic image, obtained through a 3D confocal microscope, of one of those square features from a soft-imprinted S-BC film showing a well-defined

square shape with a depth of near  $0.33 \pm 0.03 \mu\text{m}$ , which is in agreement with the values calculated previously by electron and optical microscopy. Depth was calculated as the mean of three profiles.



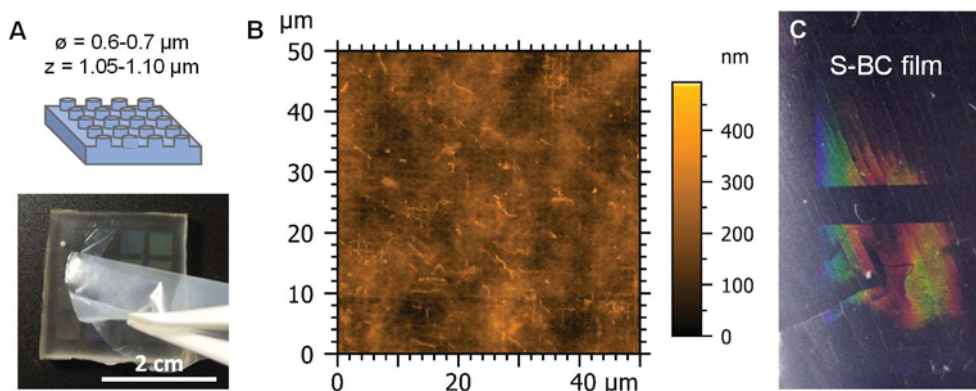
**Figure 11:** A) Dimensions of 200  $\mu\text{m}$  well-squares obtained from soft-imprint lithography vs bio-lithography ( $n = 4-20$ ). B) Topographic confocal image of S-BC with 200  $\mu\text{m}$  squares obtained from soft-imprint lithography.

This patterning approach also offered the opportunity to functionalize specific areas of the BC film just by a simple transfer from the PDMS mold to the BC. Figure 12A shows an S-BC film dyed with Safranin-O which was previously added to the PDMS mold. A differentiation between the areas in contact with the mold during the soft-imprint (dyed in pink) and the white spaces in between with well-defined edges, corresponding to the wells of the mold is appreciated. Besides, as this technique structured the BC during drying, we tried to soft-imprint under SCD conditions. For this, the OD set-up, *i.e.*, the BC film in contact with the patterned PDMS mold and sandwiched between Teflon plates, was fastened with two clamps and subjected to an ethanol solvent exchange and drying process as described in Chapter 2. Further details can be found in Annex I if needed. After drying, a good pattern transfer (Figure 12B) was appreciated, showing the versatility of this strategy.



**Figure 12:** A) Proof-of-concept of BC functionalization during soft-imprint. B) Image of an S-BC structured while performing an SCD process. Left: PDMS mold. Right: S-BC film.

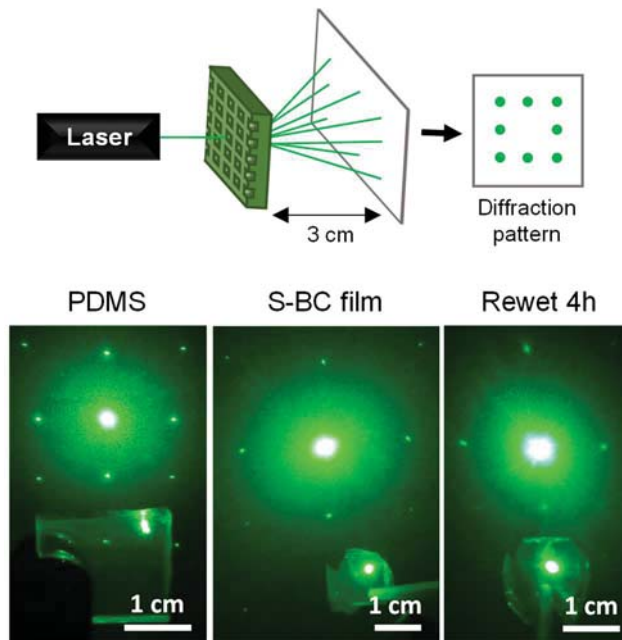
The soft-imprint lithography technique has been previously employed to structure films of drop-casted cellulose nanocrystals derived from wood pulp.<sup>28,30</sup> Recently, Espinha *et al.* applied soft lithography to hydroxypropyl cellulose (HPC) using PDMS stamps and reported cellulose-based photonic architectures.<sup>31</sup> Aiming to obtain photonic BC, a PDMS mold with circular pillars of 0.6-0.7  $\mu\text{m}$  of diameter and a pitch of 1.05-1.10  $\mu\text{m}$  grouped in square areas, as seen in Figure 13A, was soft-imprinted in a BC film. Due to the smaller feature sizes, AFM was needed to analyze the correct transfer of the patterning on BC. For that, the roughness of the BC film upon drying hindered a precise measurement of the pattern and, hence, the soft-imprint was performed above a cover glass slide to flatten the sample and restrict the intrinsic roughness of the film. After drying, AFM was employed on tapping mode to acquire the topographic images. Figure 13B shows that the structure was correctly transferred to the BC film reaching the point where cellulose fiber bundles became comparable to the feature sizes, making it difficult to visualize them. In addition, the dimensions of the patterned features and the distance between them were similar to the visible light wavelengths, providing the PDMS mold with birefringence. Characteristic also present in the S-BC films, as shown in Figure 13C, where colorful BC were produced.



**Figure 13:** A) PDMS mold scheme and image showing the peeling process of S-BC after the soft-imprint. B) AFM image showing the structuration of S-BC. C) S-BC presenting optical birefringence.

The grating of the S-BC films was also tested by passing a green laser through the pellicle and analyzing the diffraction pattern observed at 3 cm distance. Figure 14 shows the diffraction pattern obtained of the PDMS mold at the right corner and for the S-BC at the same spot. It can be observed that the diffraction pattern, although

less intense, corresponds to the square array configuration also found on the PDMS mold. In addition, the S-BC film was submerged in water for 4h and reanalyzed, obtaining the same pattern. Therefore, this technique offers the possibility to obtain BC films with optical properties that remains even if the sample is rehydrated.



**Figure 14:** Top: scheme of how the diffraction pattern was obtained and analyzed. Bottom: diffraction pattern images comparison of PDMS mold, S-BC and S-BC after being immersed in water for 4h.

### 3.4 Conclusions

In this chapter, structured bacterial cellulose (S-BC) films were obtained through two different micropatterning processes: bio-lithography (*in-situ* patterning of the film during the biosynthesis) and soft-imprint lithography (*ex-situ* patterning of the film after the biosynthesis). The lower limits and the quality of replication of both techniques to create S-BC films were evaluated and how the drying approach influences the S-BC films' integrity was investigated.

For the first method, patterns such as wells and pillars were attained with good quality in a wide size range (from 200 to 5  $\mu\text{m}$ ). The fidelity of the motifs was analyzed in wet conditions and after supercritical (SCD) or oven drying (OD). Based on our previous results (Chapter 2) we expected SCD pellicles to mimic more faithfully the

---

fibrillar arrangement of a wet S-BC film, while OD would reduce considerably the thickness and porosity of the film and, therefore, of the features.

As predicted, x and y dimensions were faithfully replicated in wet and dried samples but only wet and SCD films afforded mold accuracy in the z-direction. The features could withstand the different drying processes although the final feature height was dramatically reduced (85%) for OD. Between both drying techniques, SCD prevented the collapse of the z-dimension, maintained the porosity of the film and the features similar to the never-dried pellicles and allowed to visualize the fibers and fiber alignment. Freeze-drying (FD) was also tested but the shape of the features was compromised. In addition, x/z ratio should be taken into consideration for further studies as it behaves as a restriction parameter. When studied the same size features but reducing the z values by 10-fold (increasing the x/z ratio), no longer 3D self-standing features are observed. For smaller depth dimensions, the analysis became more challenging. In the future, efforts should be put on the optimization of the lithographic process to produce the silicon wafer master, used to produce patterned PDMS, with high-resolution motifs as it is a key factor to obtain well-defined features on BC films. In our case, squared structures showing widths below 20  $\mu\text{m}$  gradually change into circular-shaped features and the depths were no longer well controlled. Also, features could be larger separated between them to assure an easier size measurement. However, large replication areas up to 70  $\text{cm}^2$  with a mixture of different features (lines, grooves, wells and pillars) had been successfully bio-synthesized and films with intricate shapes have been obtained with potential applicability as bio-based platforms for microfluidics. In fact, those platforms have been preliminarily tested for cell seeding and proliferation by Dr. Irene Anton-Sales observing a higher cell population inside the wells.

On the other hand, soft-imprint lithography allowed us to easily and locally functionalize the BC films, a characteristic hard to achieve by bio-lithography. However, the depth of the features obtained is dramatically decreased and no alignment of the fibers is observed compared to bio-lithography. Even though, it allowed us to pattern submicron features stable even in rehydrated conditions and with sufficient depth to obtain S-BC films with optical properties. This characteristic was also tried by bio-lithography however, no successful results were obtained, possibly as a consequence of the bending and collapse of the features upon drying.

In conclusion, bio-lithography could be described as a one-step template-induced growth technique that allows the production of wet S-BC films with features that can withstand different drying methods, while soft-imprint lithography is a two-step technique that produces dried S-BC film and allows to more easily functionalize or obtain sub-micron patterned the films. The choice between both techniques would depend on the final application of the structured bacterial cellulose film. Despite their differences, both techniques can contribute to the expansion of the scope and versatility of BC in fields such as bioengineering, transient sensors, batteries, cellulosic nanogenerators or microfluidic devices by simple and scalable processes.

---

## 3.5 References

- (1) He, Q.; Ma, C.; Hu, X.; Chen, H. Method for Fabrication of Paper-Based Microfluidic Devices by Alkylsilane Self-Assembling and UV/O<sub>3</sub>-Patterning. *Anal. Chem.* **2013**, *85* (3), 1327–1331. <https://doi.org/10.1021/ac303138x>.
- (2) Kargl, R.; Mohan, T.; Köstler, S.; Spirk, S.; Doliška, A.; Stana-Kleinschek, K.; Ribitsch, V. Functional Patterning of Biopolymer Thin Films Using Enzymes and Lithographic Methods. *Adv. Funct. Mater.* **2013**, *23* (3), 308–315. <https://doi.org/10.1002/adfm.201200607>.
- (3) Palaganas, N. B.; Mangadlao, J. D.; De Leon, A. C. C.; Palaganas, J. O.; Pangilinan, K. D.; Lee, Y. J.; Advincula, R. C. 3D Printing of Photocurable Cellulose Nanocrystal Composite for Fabrication of Complex Architectures via Stereolithography. *ACS Appl. Mater. Interfaces* **2017**, *9* (39), 34314–34324. <https://doi.org/10.1021/acsami.7b09223>.
- (4) Barandun, G.; Soprani, M.; Naficy, S.; Grell, M.; Kasimatis, M.; Chiu, K. L.; Ponzoni, A.; Güder, F. Cellulose Fibers Enable Near-Zero-Cost Electrical Sensing of Water-Soluble Gases. *ACS Sensors* **2019**, *4* (6), 1662–1669. <https://doi.org/10.1021/acssensors.9b00555>.
- (5) Fan, J.; Zhang, S.; Li, F.; Shi, J. *Cellulose-Based Sensors for Metal Ions Detection*; Springer Netherlands, **2020**; Vol. 27. <https://doi.org/10.1007/s10570-020-03158-x>.
- (6) Fan, J.; Zhang, S.; Li, F.; Yang, Y.; Du, M. Recent Advances in Cellulose-Based Membranes for Their Sensing Applications. *Cellulose* **2020**, *27* (16), 9157–9179. <https://doi.org/10.1007/s10570-020-03445-7>.
- (7) Wang, G.; Chen, X. F.; Shi, X. D.; Yu, L. J.; Liu, B. F.; Yang, G. Bio-Fabrication of Patterned Cellulose Nano-Fibers. *Adv. Mater. Res.* **2008**, *47–50*, 1359–1362. <https://doi.org/10.4028/www.scientific.net/AMR.47-50.1359>.
- (8) Markov, D. A.; Lillie, E. M.; Garbett, S. P.; McCawley, L. J. Variation in Diffusion of Gases through PDMS Due to Plasma Surface Treatment and Storage Conditions. *Biomed. Microdevices* **2014**, *16* (1), 91–96. <https://doi.org/10.1007/s10544-013-9808-2>.
- (9) Uraki, Y.; Tamai, Y.; Hirai, T.; Koda, K.; Yabu, H.; Shimomura, M. Fabrication of Honeycomb-Patterned Cellulose Material That Mimics Wood Cell Wall Formation Processes. *Mater. Sci. Eng. C* **2011**, *31*, 1201–1208. <https://doi.org/10.1016/j.msec.2010.11.009>.
- (10) Bottan, S.; Robotti, F.; Jayathissa, P.; Hegglin, A.; Bahamonde, N.; Heredia-Guerrero, J. A.; Bayer, I. S.; Scarpellini, A.; Merker, H.; Lindenblatt, N.; et al. Surface-Structured Bacterial Cellulose with Guided Assembly-Based Biolithography (GAB). *ACS Nano* **2015**, *9* (1), 206–219. <https://doi.org/10.1021/nn5036125>.
- (11) Zang, S.; Zhang, R.; Chen, H.; Lu, Y.; Zhou, J.; Chang, X.; Qiu, G.; Wu, Z.; Yang, G. Investigation on Artificial Blood Vessels Prepared from Bacterial Cellulose. *Mater. Sci. Eng. C* **2015**, *46*, 111–117. <https://doi.org/10.1016/j.msec.2014.10.023>.
- (12) Prathapan, R.; Ghosh, A. K.; Knapp, A.; Vijayakumar, A.; Bogari, N. N. J.; Abraham, B. D.; Al-Ghabkari, A.; Fery, A.; Hu, J. In Situ Alignment of Bacterial Cellulose Using Wrinkling. *ACS Appl. Bio Mater.* **2020**, *3* (11), 7898–7907. <https://doi.org/10.1021/acsabm.0c01030>.
- (13) Kolind, K.; Leong, K. W.; Besenbacher, F.; Foss, M. Biomaterials Guidance of Stem Cell Fate on 2D Patterned Surfaces. *Biomaterials* **2012**, *33* (28), 6626–6633. <https://doi.org/10.1016/j.biomaterials.2012.05.070>.

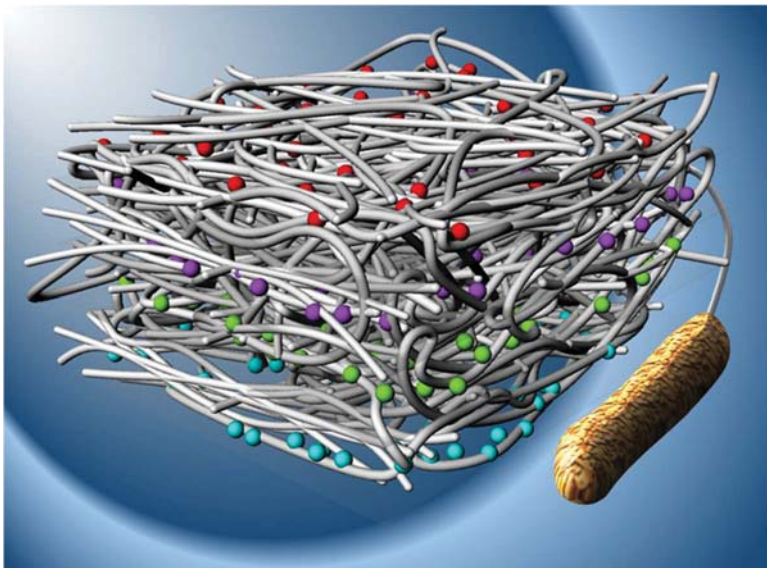
- (14) Geisel, N.; Clasohm, J.; Shi, X.; Lamboni, L.; Yang, J.; Mattern, K.; Yang, G.; Schäfer, K. H.; Saumer, M. Microstructured Multilevel Bacterial Cellulose Allows the Guided Growth of Neural Stem Cells. *Small* **2016**, *12* (39), 5407–5413. <https://doi.org/10.1002/sml.201601679>.
- (15) Robotti, F.; Sterner, I.; Bottan, S.; Monné Rodríguez, J. M.; Pellegrini, G.; Schmidt, T.; Falk, V.; Poulikakos, D.; Ferrari, A.; Starck, C. Microengineered Biosynthesized Cellulose as Anti-Fibrotic in Vivo Protection for Cardiac Implantable Electronic Devices. *Biomaterials* **2020**, 229, 119583. <https://doi.org/10.1016/j.biomaterials.2019.119583>.
- (16) Jin, M.; Chen, W.; Li, Z.; Zhang, Y.; Zhang, M.; Chen, S. Patterned Bacterial Cellulose Wound Dressing for Hypertrophic Scar Inhibition Behavior. *Cellulose* **2018**, *25* (11), 6705–6717. <https://doi.org/10.1007/s10570-018-2041-7>.
- (17) Cao, Y.; Liu, M.; Xue, Z.; Qiu, Y.; Li, J.; Wang, Y.; Wu, Q. Surface-Structured Bacterial Cellulose Loaded with HUSCs Accelerate Skin Wound Healing by Promoting Angiogenesis in Rats. *Biochem. Biophys. Res. Commun.* **2019**, *516* (4), 1167–1174. <https://doi.org/10.1016/j.bbrc.2019.06.161>.
- (18) Arias, S. L.; Cheng, M. K.; Civantos, A.; Devorkin, J.; Jaramillo, C.; Allain, J. P. Ion-Induced Nanopatterning of Bacterial Cellulose Hydrogels for Biosensing and Anti-Biofouling Interfaces. *ACS Appl. Nano Mater.* **2020**, *3* (7), 6719–6728. <https://doi.org/10.1021/acsnano.0c01151>.
- (19) Sämfors, S.; Karlsson, K.; Sundberg, J.; Markstedt, K.; Gatenholm, P. Biofabrication of Bacterial Nanocellulose Scaffolds with Complex Vascular Structure. *Biofabrication* **2019**, *11*, 045010. <https://doi.org/10.1088/1758-5090/ab2b4f>.
- (20) Bao, L.; Hong, F. F.; Li, G.; Hu, G.; Chen, L. Improved Performance of Bacterial Nanocellulose Conduits by the Introduction of Silk Fibroin Nanoparticles and Heparin for Small-Caliber Vascular Graft Applications. *Biomacromolecules* **2021**, *22*, 353–364. <https://doi.org/10.1021/acs.biomac.0c01211>.
- (21) Greca, L. G.; Rafiee, M.; Karakoç, A.; Lehtonen, J.; Mattos, B. D.; Tardy, B. L.; Rojas, O. J. Guiding Bacterial Activity for Biofabrication of Complex Materials via Controlled Wetting of Superhydrophobic Surfaces. *ACS Nano* **2020**, *14* (10), 12929–12937. <https://doi.org/10.1021/acsnano.0c03999>.
- (22) Hu, Y.; Liu, H.; Zhou, X.; Pan, H.; Wu, X.; Abidi, N.; Zhu, Y.; Wang, J. Surface Engineering of Spongy Bacterial Cellulose via Constructing Crossed Groove/Column Micropattern by Low-Energy CO<sub>2</sub> Laser Photolithography toward Scar-Free Wound Healing. *Mater. Sci. Eng. C* **2019**, *99*, 333–343. <https://doi.org/10.1016/j.msec.2019.01.116>.
- (23) Mittal, N.; Ojanguren, A.; Niederberger, M.; Lizundia, E. Degradation Behavior, Biocompatibility, Electrochemical Performance, and Circularity Potential of Transient Batteries. *Adv. Sci.* **2021**, *2004814*. <https://doi.org/10.1002/advs.202004814>.
- (24) Annamalai, P. K.; Nanjundan, A. K.; Dubal, D. P.; Baek, J. B. An Overview of Cellulose-Based Nanogenerators. *Adv. Mater. Technol.* **2021**, *6*, 2001164. <https://doi.org/10.1002/admt.202001164>.
- (25) Abol-Fotouh, D.; Dörling, B.; Zapata-Arteaga, O.; Rodríguez-Martínez, X.; Gómez, A.; Reparaz, J. S.; Laromaine, A.; Roig, A.; Campoy-Quiles, M. Farming Thermoelectric Paper. *Energy Environ. Sci.* **2019**, *12* (2), 716–726. <https://doi.org/10.1039/c8ee03112f>.



- 
- (26) Li, M.; Zong, L.; Yang, W.; Li, X.; You, J.; Wu, X.; Li, Z.; Li, C. Biological Nanofibrous Generator for Electricity Harvest from Moist Air Flow. *Adv. Funct. Mater.* **2019**, *29*, 1901798. <https://doi.org/10.1002/adfm.201901798>.
- (27) Akyazi, T.; Basabe-Desmonts, L.; Benito-Lopez, F. Review on Micro Fluidic Paper-Based Analytical Devices towards Commercialisation. *Anal. Chim. Acta* **2018**, *1001*, 1–17. <https://doi.org/10.1016/j.aca.2017.11.010>.
- (28) Zhou, Y.; Li, Y.; Dunder, F.; Carter, K. R.; Watkins, J. J. Fabrication of Patterned Cellulose Film via Solvent-Assisted Soft Nanoimprint Lithography at a Submicron Scale. *Cellulose* **2018**, *25* (9), 5185–5194. <https://doi.org/10.1007/s10570-018-1920-2>.
- (29) Khakalo, A.; Mäkelä, T.; Johansson, L. S.; Orelma, H.; Tammelin, T. High-Throughput Tailoring of Nanocellulose Films: From Complex Bio-Based Materials to Defined Multifunctional Architectures. *ACS Appl. Bio Mater.* **2020**, *3* (11), 7428–7438. <https://doi.org/10.1021/acsbm.0c00576>.
- (30) Zhao, T. H.; Parker, R. M.; Williams, C. A.; Lim, K. T. P.; Frka-Petesic, B.; Vignolini, S. Printing of Responsive Photonic Cellulose Nanocrystal Microfilm Arrays. *Adv. Funct. Mater.* **2018**, 1804531. <https://doi.org/10.1002/adfm.201804531>.
- (31) Espinha, A.; Dore, C.; Matricardi, C.; Alonso, M. I.; Goñi, A. R.; Mihi, A. Hydroxypropyl Cellulose Photonic Architectures by Soft Nanoimprinting Lithography. *Nat. Photonics* **2018**, *12*, 343–348. <https://doi.org/10.1038/s41566-018-0152-1>.

# Chapter 4

## Engineering bacterial cellulose nanocomposites





## CHAPTER SUMMARY

In this chapter, the potential of BC as a support for advanced multifunctional nanocellulose materials is described. Employing the BC structures detailed in Chapter 2, three approaches to incorporate inorganic nanoparticles into the nanocellulose network are described.

## CHAPTER INDEX

CHAPTER SUMMARY .....	85 -
4.1 Bacterial cellulose functionalization mechanisms .....	87 -
4.1.1 Nanoparticle microwave-assisted synthesis .....	90 -
4.2 Bacterial cellulose/nanoparticles films by microwave-assisted reaction .....	91 -
4.3 Characterization of bacterial cellulose/nanoparticles films .....	93 -
4.4 Multilayered bacterial cellulose nanocomposite .....	101 -
4.4.1 Multifunctional constructs and potential applications .....	104 -
4.5 Bacterial cellulose nanofibers decorated with magnetic nanoparticles .....	106 -
4.6 Functionalization of bacterial cellulose spheres .....	108 -
4.6.1 Magnetic bacterial cellulose spheres in an agitated culture system .....	109 -
4.6.2 Actuable bacterial cellulose spheres on hydrophobic surfaces .....	111 -
4.7 Conclusions .....	119 -
4.8 References .....	123 -



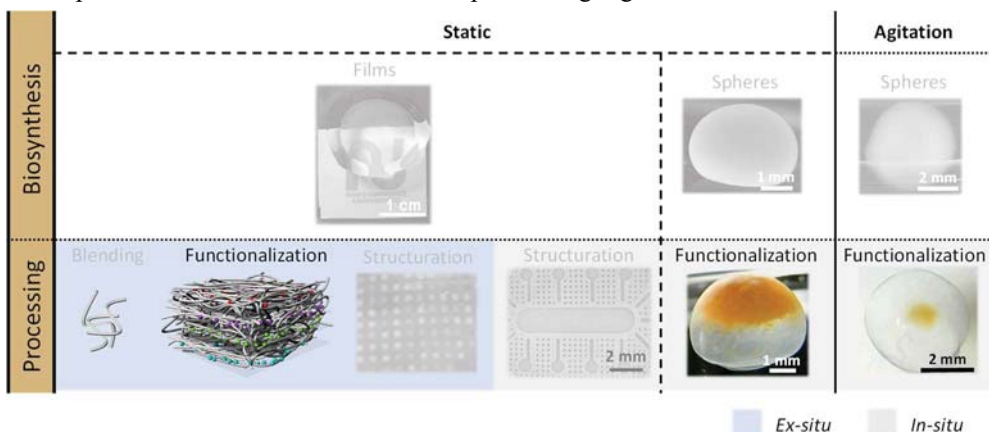
## 4.1 Bacterial cellulose functionalization mechanisms

So far, we have seen that BC presents transparency, modifiable porosity, thermal stability, self-adhesiveness upon drying, tunable mechanical properties and versatility to produce 3D structures and to be topographically shaped. Despite these properties, BC is not a functional material and the possibility to obtain composites with magnetic, conductive, plasmonic or biological activity greatly enlarge its applicability scope. Besides, the integration of advanced functional materials in consumer products and devices is increasingly demanding and the use of greener routes and sustainable resources, such as nanocellulose-based platforms, are gaining attention.

BC functionality can be achieved by the combination of the nanocellulose matrix with polymers, graphene derivatives, ceramics or metals.<sup>1,2</sup> These composites can synergistically exploit the characteristics of both constituents. The additive material provides electronic, optical, magnetic, catalytic or bioactivity properties. Meanwhile, the flexible and porous nanocellulose matrix provides easy mechanical handling, facilitates the interaction of the additive with the surrounding media and interestingly, allows the additive recovery by biodegrading the BC matrix. Recent research highlights the use of BC as versatile support of inorganic NPs and their application in catalysis, sensors, separation systems, functional food packaging and medical uses.<sup>3-6</sup> However, scarce information is provided about BC platforms with localized multifunctionalization.

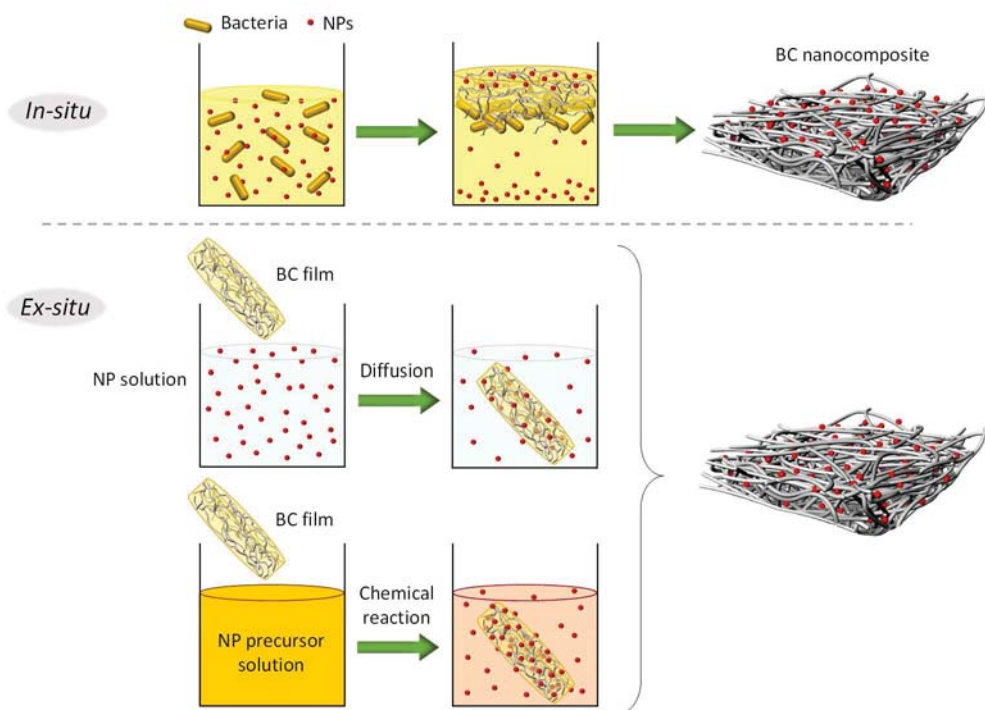
In this chapter, functional BC structures (films, fibers and spheres) using two different approaches are presented and summarized in Table 1. On one hand, an *ex-situ* route *via* a rapid synthesis technique adaptable to several NPs systems will be described. This strategy provides a high homogeneous nanoparticle distribution inside the BC film with nanoparticle size and loading control that can be also be applied to other BC shapes such as the nanofibers. Besides, taking advantage of the self-adhesiveness of BC, functional multilaminates with spatially confined properties will be created. Furthermore, two *in-situ* routes to obtain actuatable BC spheres with future applications as soft-actuators are described differing on the initial culturing process conditions (agitation or static) of the nanocellulose matrix, being able to obtain Janus structures in the second case.

**Table 1:** Scheme of the biosynthesis and processing routes treated so far in lighter shading. The topics that will be described in this chapter are highlighted.



In particular, this chapter focuses on the addition of four representative NPs systems: two metals (Au, Ag) and two metal oxides ( $\text{TiO}_2$ ,  $\text{Fe}_2\text{O}_3$ ). Au is known for its catalytic and photothermal properties affording BC nanocomposites with applications in catalysis or sensing.<sup>7-9</sup> Several applications of BC with silver NPs in food packaging and wound dressing have been reported due to the antibacterial properties of the silver.<sup>10-12</sup>  $\text{TiO}_2$  NPs are already used as a food additive (E171), in toothpaste, sunscreen, medicines or cosmetics due to their UV blocking characteristics, non-toxicity, antibacterial and photocatalytic properties.<sup>13</sup> Therefore, BC nanocomposites containing  $\text{TiO}_2$  have been reported for catalytic and sensing purposes, dye removal and antibacterial activity.<sup>14-16</sup> Finally, BC with magnetic  $\text{Fe}_2\text{O}_3$  nanoparticles have been proposed as radio-frequency shielding materials<sup>17</sup>, anti-counterfeiting papers<sup>18</sup>, ultra-thin loudspeakers<sup>19</sup> or for heavy metal and dye removal<sup>20,21</sup>.

The synthesis routes to afford functional BC nanocomposites can be grouped into three general approaches that differ at which stage the NPs are added (*in-situ* or *ex-situ*) and in the type of component added (ions or particles) as shown in Figure 1. For the *in-situ* approach, NPs are incorporated in the culture media prior to the biosynthesis of BC. For the *ex-situ* process, the NPs can be incorporated or directly synthesized into the BC film.



**Figure 1:** BC-nanocomposite synthesis processes. From up to down: *In-situ* incorporation of NPs in the BC network during the biosynthesis and *ex-situ* incorporation of NPs in the BC network by diffusion or by synthesis.

During the biosynthesis (*in-situ* approach), the interwoven network of nanofibers produced by the bacteria entraps the NPs dispersed in the culture media.<sup>22,23</sup> The main drawback of this method is the stability of the NPs in the bacterial media. The layer-by-layer BC growth mechanism and the precipitation of the NPs over time lead to films with high NPs load concentrations in the first BC layers produced with a decrease of them in the next layers as the culture time increases, producing inhomogeneous nanocomposite films in depth. An easier and more common approach is to immerse the already harvested and cleaned BC pellicle in a solution with dispersed nanoparticles. Functionalization then is conferred through the diffusion of the solution into the porous nanocellulosic structure and the interaction of the NPs with the fibers.<sup>25</sup> This approach, however, is limited to particles with a small enough size to penetrate the fibrous nanocellulosic network and could generate NPs leaching in wet conditions. Finally, the direct synthesis of NPs in the BC network consists of the immersion of a BC pellicle in a NP precursor solution. The ions and molecules can penetrate through the cellulose network and interact with the hydroxyl group of the nanofibers, that act as active sites to anchor them. Then, the system is subjected



---

to a chemical reaction (red-ox, sol-gel, hydrothermal,...) and nanoparticles are formed.<sup>25</sup> Although this method produces BC films with higher nanoparticle content, the reactions usually need long times and high temperatures. As a recapitulation, different drawbacks are present depending on the selected process and usually inhomogeneous particle disposition or weak nanoparticle attachment to the BC films is still observed.<sup>26,27</sup> Thus, it is challenging to develop BC nanocomposites controlling the nanoparticle properties, their volume fraction and their topographic distribution within the scaffold. Besides, how this incorporation affect the properties of the final material need to be systematically investigated.<sup>28,29</sup>

#### **4.1.1 Nanoparticle microwave-assisted synthesis**

Among the techniques to synthesize nanoparticles, microwave (MW) chemistry (*i.e.*, chemical reactions assisted by microwave radiation) is attracting considerable attention. The technique exploits the advantages of kinetically controlled synthesis and allows high-temperature reactions in short times, obtaining high yields and reducing energy and reagent costs.<sup>30-32</sup> It is based on the application of MW irradiation with a frequency ranging from 0.3-300 GHz which acts as an oscillating high-frequency electric field. When applied, the molecule-electrical dipoles of the solution try to align with the field. However, the continuous realignment of the dipoles due to the varying field originates a constant rotation of the molecules causing molecular friction and collisions, which release energy in the form of heat during the process.<sup>33</sup>

Microwave heating has several advantages compared to conventional heating, such as oil baths or hot plates, as summarized in Table 2. During conventional heating, the heat of the vessel surface is transferred to the solution by convection and conduction and a gradient of temperature and as a result, NP size polydispersity is often observed. In comparison, during MW irradiation, the radiation is directly coupled with the solution, reducing temperature gradients and producing efficient heating. The heating efficacy would, therefore, depend on the dielectric properties of the solvent, which needs to be polar. The fast heating promotes a synchronic NP nucleation and growth which results in a homogeneous nanocrystal distribution inside the reactor volume, accelerating the reaction by nearly 1000 times in some cases. Thus, MW chemistry appears as a versatile technique that affords a moderate control of NP sizes in a simple and energy-efficient way.<sup>35</sup>

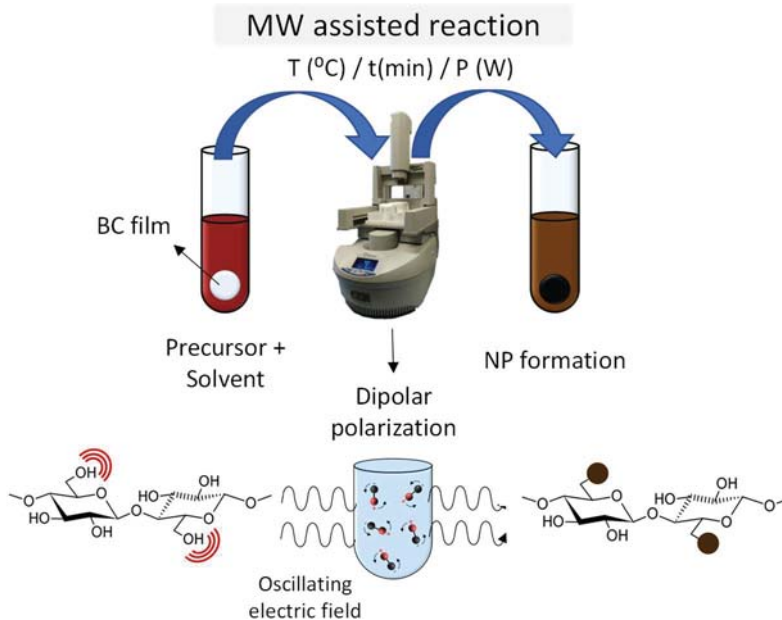
**Table 2:** Differences between microwave and conventional heating. Adapted from <sup>35</sup>.

MW heating	Conventional heating
Molecular dipole rotation	Conduction/convection
Volumetric heating of the solvent	Superficial heating of the vessel
Fast	Slow
Polar solvent	Independent of the solvent properties

#### 4.2 Bacterial cellulose/nanoparticles films by microwave-assisted reaction

The synthesis and production of NPs through MW irradiation have been extensively studied in our group.<sup>35-40</sup> More recently, we have reported that microwave-assisted thermal decomposition synthesis is an efficient and fast method to attain a uniform and controllable iron oxide nanoparticles load in BC films while preserving the intrinsic flexibility of the material. We hypothesize that the nucleation and growth of inorganic nanocrystals occur on the hydroxyl groups present on the cellulose nanofibrils that act as selective nucleation sites.<sup>41</sup> This approach has been expanded during this thesis to other inorganic phases; two metals (Au, Ag) and two semiconductors (TiO<sub>2</sub> and Fe<sub>2</sub>O<sub>3</sub>).

NPs were synthesized in never dried BC films using a microwave oven (CEM Discover Explorer-12 Hybrid reactor) with a controlled atmosphere operating at a frequency of 2.45 GHz and with a maximum power of 300 W. Before the syntheses, the cellulose films were immersed in benzyl alcohol (BA) twice for 3 h and a third time for 12 h to assure a complete solvent exchange, except for the silver nanoparticle reaction where this step was not needed as the reaction takes place in water. The films were then immersed in the precursor solution and temperature and time were set for each reaction. Power was automatically adjusted using a volume-independent infrared sensor that controls the temperature inside the reactor vessel. After the reaction, the samples were cooled down to 50 °C with compressed air and BC nanocomposites together with an excess of nanoparticles that remains in solution were obtained. The reactor set-up and synthesis scheme are represented in Figure 2.



**Figure 2:** MW reactor set-up and MW-assisted synthesis scheme.

Synthesis details for the four inorganic BC nanocomposites are described below. Technical details of the materials used and the characterization as well as a reminder of BC production and cleaning can be found in Annex I. In all cases, BC films were added to the solution just before heating:

- Silver NPs in bacterial cellulose (BC/Ag) were synthesized by adding 2 mL of 25 mM silver nitrate solution to a 2 mL 25 mM polyvinylpyrrolidone (PVP, molecular weight: 10 K) solution, sonicating 5 min and heating at 120 °C for 10 min. The excess of NPs in the suspension was collected by centrifugation at 6000 rpm for 15 min using acetone and 10  $\mu$ L PVP as electrostatic surfactant.
- BC/TiO<sub>2</sub> were obtained by mixing 0.04 mmol (14  $\mu$ L) of titanium (IV) butoxide (TBOT) in 4 mL BA, sonicating 1 min and heating first for 5 min at 50 °C and then 10 min at 190 °C. NPs excess was gathered by centrifugation at 6000 rpm for 20 min using acetone and 20  $\mu$ L TMAOH.

- BC/Fe<sub>2</sub>O<sub>3</sub> were fabricated by mixing 0.35 mmol (123.6 mg) iron(III) acetylacetonate (Fe(acac)<sub>3</sub>) in 4.5 mL BA, sonicating 1 min and heating also in two steps (5 min at 60 °C and 10 min at 210 °C).<sup>41</sup> Centrifugation at 6000 rpm for 30 min using acetone and 20 μL TMAOH was used to collect the NPs excess.
- BC/Au were obtained by mixing 26 μL of 250 mM gold(III) chloride hydrate (HAuCl<sub>4</sub>) solution in 1 mL of oleylamine (OA) and sonicating until complete dissolution. Then, the sample was heated at 120 °C for 5 min. The NPs were collected by 15 min centrifugation at 6000 rpm using ethanol. In this case, the reaction solvent (OA) also acts as an electrostatic surfactant and no additional surfactant was added.

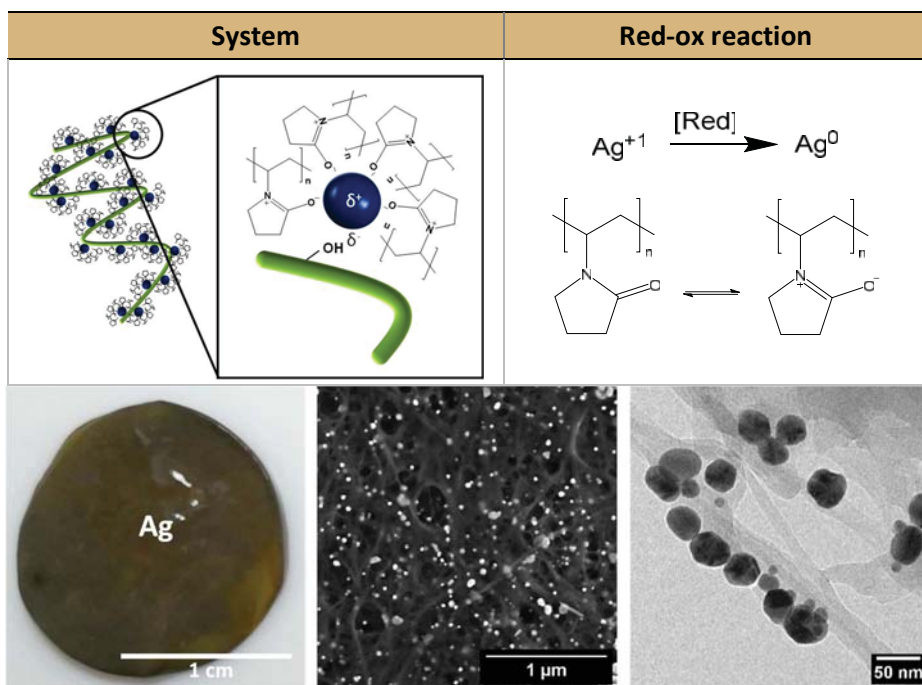
In all conditions, centrifugation was repeated twice by redispersing the precipitate and afterward, NPs were dried overnight in an oven at 60 °C and stored in Milli-Q (MQ) water with 10 μL of surfactant. On the other hand, BC nanocomposite films were harvested and cleaned twice for 10 min in acetone under gentle agitation. Ethanol was used in the case of BC/Au as ethanol dissolves better the excess of OA in cellulose. Finally, the films were cleaned with MQ water until a complete exchange of solvent and stored at room temperature.

### 4.3 Characterization of bacterial cellulose/nanoparticles films

First, the structural integrity of the nanocomposite films was investigated through electron microscopy and a possible synthesis mechanism was elucidated. A high-resolution SEM was used for seeing the NPs distribution on the cellulose nanofibers and TEM was employed to obtain images at higher magnifications.

#### **BC/Ag**

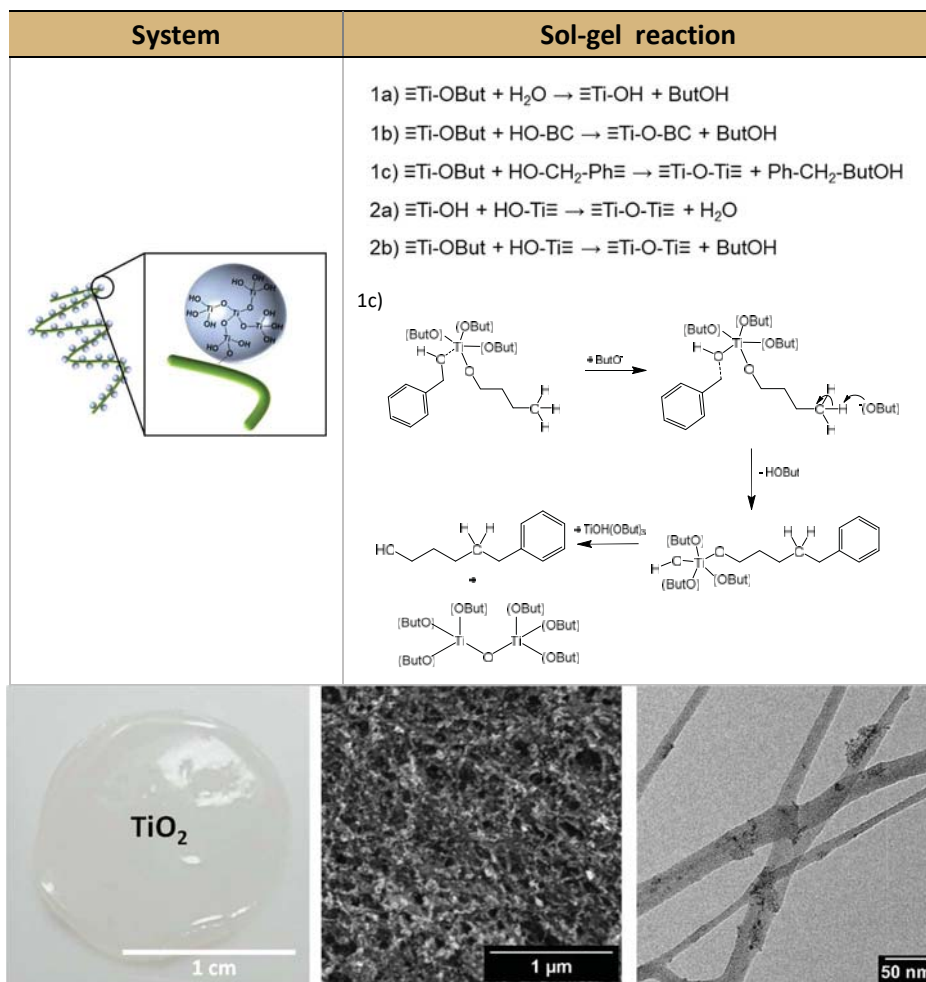
Ag NPs were formed by a redox reaction<sup>42,43</sup> where the PVP acted as a reducing and capping agent as shown in Figure 3. During the nanoparticle growth, the material was positively charged due to the cations in the surface, facilitating electrostatic interactions with the hydroxyl groups of the cellulose nanofibers. After the reaction, BC/Ag nanocomposite presented a brownish uniform color and SEM and TEM micrographs displayed a homogenous NPs coverage and attachment to the fibers.



**Figure 3:** Upper panel: scheme of the proposed synthesis mechanism of a BC/Ag film. Bottom panel: image of a BC/Ag film. SEM image showing the fibrils decorated with the nanoparticles. TEM image of the fibers at a higher magnification where the size and distribution of the nanoparticles are more apparent.

### BC/TiO<sub>2</sub>

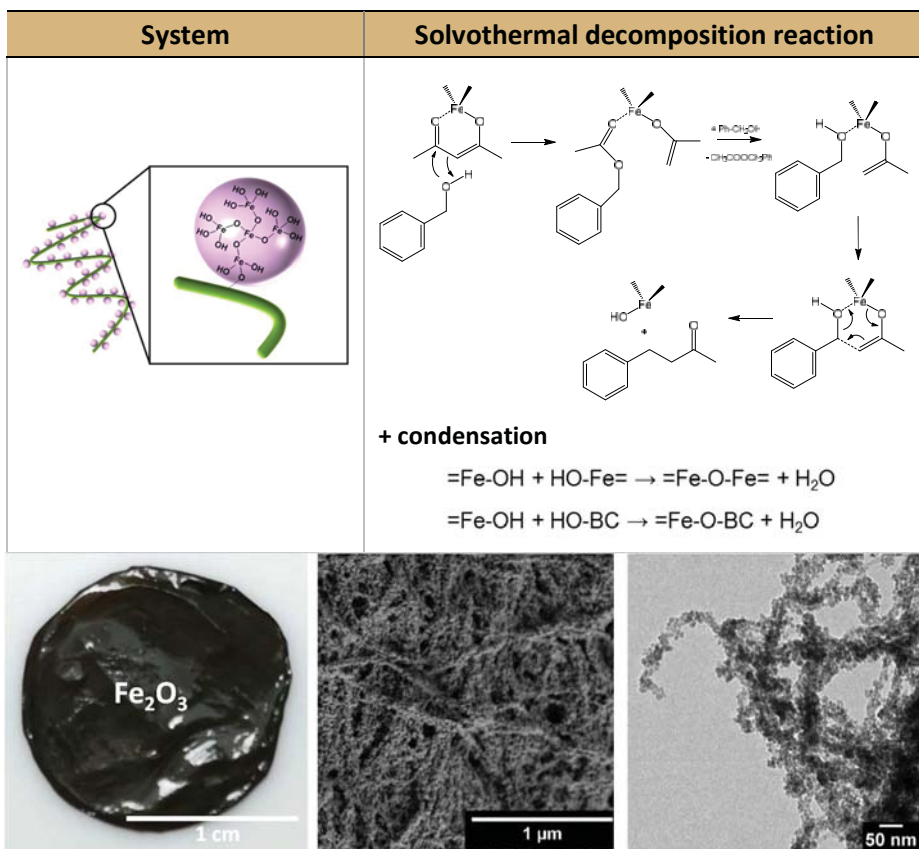
TiO<sub>2</sub> NPs were produced by a sol-gel reaction<sup>44</sup> on the hydroxyl groups of the nanofibers as displayed in Figure 4. First, TBOT molecules interacted with possible water still present in the solution, the hydroxyl groups of the cellulose nanofibers or the solvent (reactions 1a, 1b and 1c) and the intermediates generated originated a reaction cascade creating metal-oxo bonds. Reaction 1c has been more detailed described as it is more complex. Ti atoms are tetracoordinated, therefore, several reactions took place at the same time while the particle grew. Besides, as the hydroxyl groups of the cellulose are part of the reaction mechanism acting as anchoring points for the particle nucleation and growing, high coverage of the film was observed through SEM images. After the reaction, BC/TiO<sub>2</sub> presents a whitish color, not as transparent as the pristine BC films.



**Figure 4:** Upper panel: scheme of the proposed BC/TiO<sub>2</sub> synthesis mechanism. Bottom panel: image of a BC/TiO<sub>2</sub> after the synthesis. SEM image showing the fibers decorated with the NPs. TEM image of the fibers at higher magnification.

### BC/Fe<sub>2</sub>O<sub>3</sub>

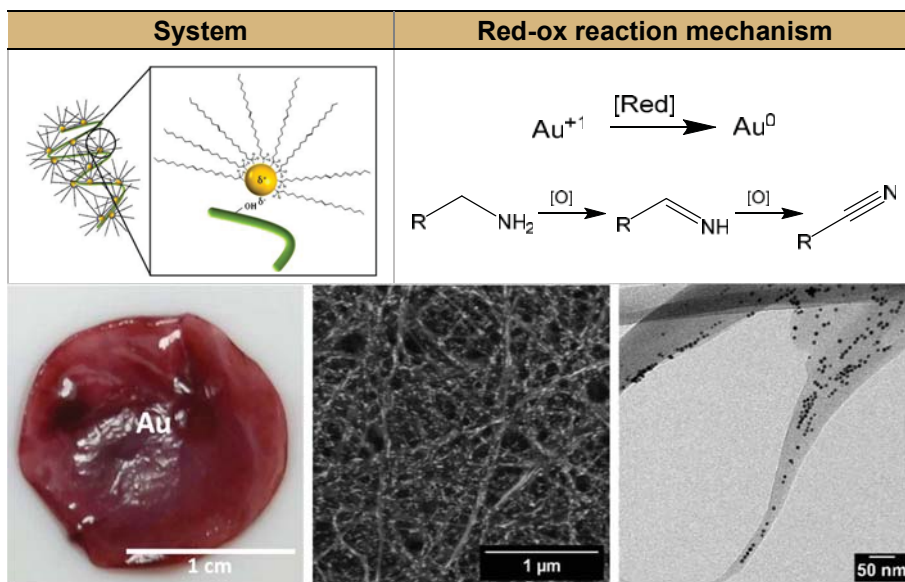
BC with Fe<sub>2</sub>O<sub>3</sub> presented a dark brownish color (almost black) with a high NPs coverage of the nanofibers as shown in the electron microscope images of Figure 5. The proposed mechanism for Fe<sub>2</sub>O<sub>3</sub> production is a solvothermal decomposition<sup>44</sup> followed by condensation. Again, the hydroxyl groups of the cellulose nanofibers are crucial, especially during the condensation reactions.



**Figure 5:** Upper panel: BC/Fe<sub>2</sub>O<sub>3</sub> proposed synthesis mechanism scheme. Bottom panel: image of a BC/ Fe<sub>2</sub>O<sub>3</sub> film after the synthesis. SEM image showing the fibers decorated with nanoparticles. TEM image at higher magnification exhibiting an elevated coverage.

### BC/Au

Similar to BC/Ag, the formation of Au nanoparticles occurred through a redox mechanism<sup>45</sup> where the solvent, in this case OA, acted as an all-in-one component (solvent, reduction and capping agent). Again, during nucleation and growth the nanoparticles were positively charged, interacting electrostatically with the hydroxyl groups of the cellulose nanofibers. BC/Au nanocomposite presented a homogenous red-wine color where the NPs coverage was homogeneous as SEM and TEM micrographs displayed in Figure 6.



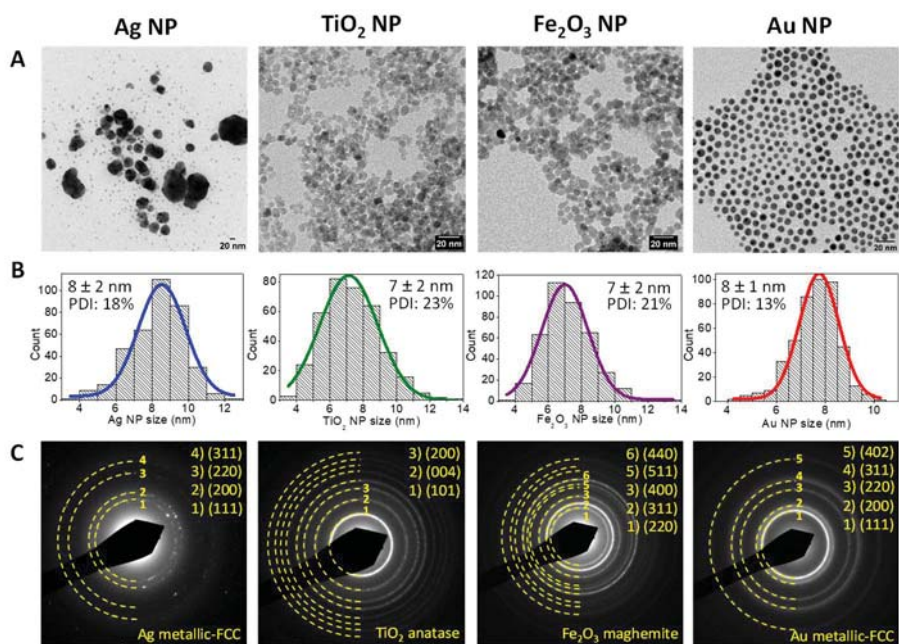
**Figure 6:** Upper panel: proposed BC/Au synthesis mechanism scheme. Bottom panel: BC/Au film image after the synthesis. SEM image showing the fibers decorated with the NPs. TEM image at higher magnification.

Each nanocomposite presented a uniform and characteristic color which corresponds to the particular NPs system. In addition, electronic microscope images evidence that the inorganic nanoparticles are homogeneously distributed along the fibrils, although differences in the coverage were observed depending on the system and the reaction mechanism for each material. For example, metal systems, that are hypothesized to be regulated by red-ox reactions, presented less coverage than metal oxides nanocomposites. This effect could also be associated with a sterical impediment offered by the surfactant, only used in those systems. Besides, although not described in the proposed mechanisms, the surfactant could also interact with the cellulose nanofibers making them less accessible for nanoparticle anchoring and formation.

The study of the NPs' size and crystal phase was performed by collecting and analyzing the reaction supernatants by TEM (Figure 7). In each case, 300-400 NPs size histogram was fitted to a Gaussian function and the mean size values were obtained. Polydispersity (PDI) estimates the size heterogeneity of the NPs population considering values  $\leq 20\%$  an acceptable monodisperse size distribution and 100% a polydisperse size distribution and was computed as the percentage of the standard deviation divided by the mean value. Particle size histograms resulted in mean



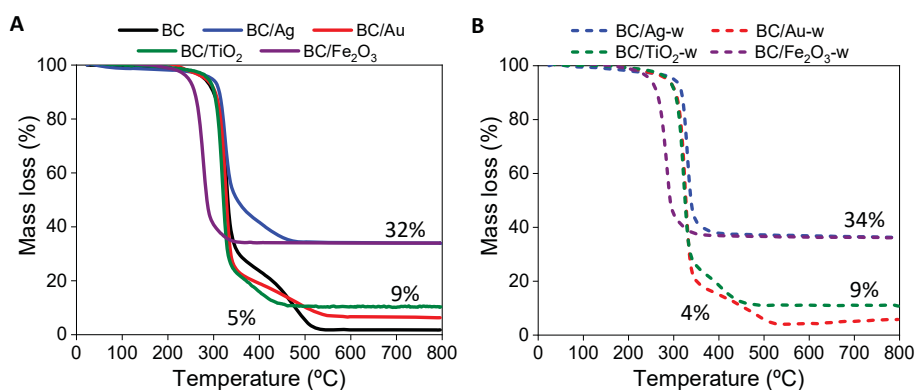
particle sizes of  $7 \pm 2$ ,  $7 \pm 2$  and  $8 \pm 1$  nm for  $\text{TiO}_2$ ,  $\text{Fe}_2\text{O}_3$  and Au respectively with a maximum polydispersity index of 23%, indicating a homogenous NPs size distribution. In the case of Ag, a bimodal distribution was obtained as seen in TEM image of Figure 7A. While the main NPs size corresponds to  $8 \pm 2$  nm (PDI 18%), a second lesser population of  $40 \pm 19$  nm (PDI 47%), which corresponds to sporadic larger shapes was also appreciated. In addition, selected area electron diffraction (SAED) analyses were performed. As shown in Figure 7C, each ring corresponds to a diffraction plane of the NP crystalline structure. Analyzing the most representative planes (*i.e.*, the most intense), we could confirm the face-centered cubic crystal structure of metallic gold and silver, the anatase phase for titania and maghemite for iron oxide.



**Figure 7:** A) TEM images of the synthesized NPs collected from the supernatant. B) Particle size distribution computed from TEM images. C) SAED images of the different nanoparticles. Each characteristic crystallographic plane is highlighted.

Next, we evaluated the inorganic NP mass, volume fraction and adhesion to the nanofibers in each nanocomposite film. Pellicles were cut in half and one part was immersed in 8 mL MQ water for 30 days under gentle horizontal agitation. Then, both sections were analyzed by TGA-DSC/DTA, measuring from room temperature to  $800\text{ }^\circ\text{C}$  in air with a heating rate of  $10\text{ }^\circ\text{C min}^{-1}$ . Figure 8 contains the nanoparticle

content quantified before and after immersion and compared to pristine BC. Percentages show the final NP content after subtracting the BC residual mass. In view of the results, only  $\text{Fe}_2\text{O}_3$  acted as a catalyst in the pyrolysis of bacterial cellulose, decreasing its degradation temperature by about  $50\text{ }^\circ\text{C}$  (from  $320$  to  $275\text{ }^\circ\text{C}$ ). Besides, we could confirm that no leaching of the NPs occurred as the loading fraction (32, 9, 32, 5 wt% or 3, 1, 5, 0.2 vol% for Ag,  $\text{TiO}_2$ ,  $\text{Fe}_2\text{O}_3$  and Au respectively) is maintained, which reinforces the strong chemical bonding formation hypothesis between the NPs and the cellulose fibrils. Additionally, an ICP analysis of the remanent water was performed from one of the systems ( $\text{BC}/\text{TiO}_2$ ) obtaining a percentage of Ti lower than the detection limit of the technique.



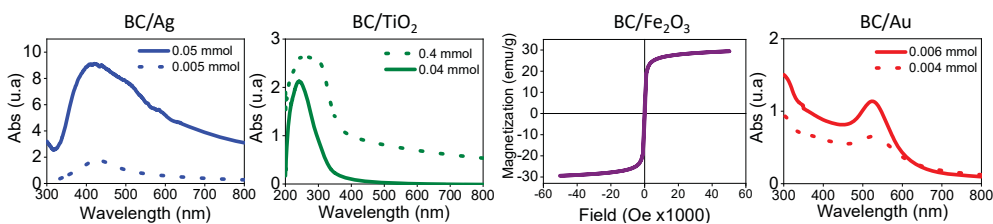
**Figure 8:** A) TGA of pristine BC (black line) and nanocomposite BC films. B) TGA analysis of the BC/nanoparticles films after they have been immersed in water under gentle agitation for 30 days. No leaching of the nanoparticles is observed.

**Table 3:** Strategies to vary the inorganic loading fraction in the BC films.

System	[NP precursor] (mmol)	NP loading (%)
BC/Ag	0.05 $\text{AgNO}_3$	$32 \pm 2$
	0.005 $\text{AgNO}_3$	$4 \pm 2$
BC/ $\text{TiO}_2$	0.4 TBOT	$13 \pm 2$
	0.04 TBOT	$9 \pm 3$
BC/ $\text{Fe}_2\text{O}_3$	0.35 $\text{Fe}(\text{acac})_3$	$32 \pm 2$
BC/Au	0.006 $\text{HAuCl}_4$	$5 \pm 1$
	0.004 $\text{HAuCl}_4$	$4 \pm 1$

Along with the results already mentioned, the MW-assisted reaction allowed controlling the nanoparticle content by modifying the initial precursor concentration. Table 3 exhibits the nanocomposite NP loading at different precursor solution concentrations.

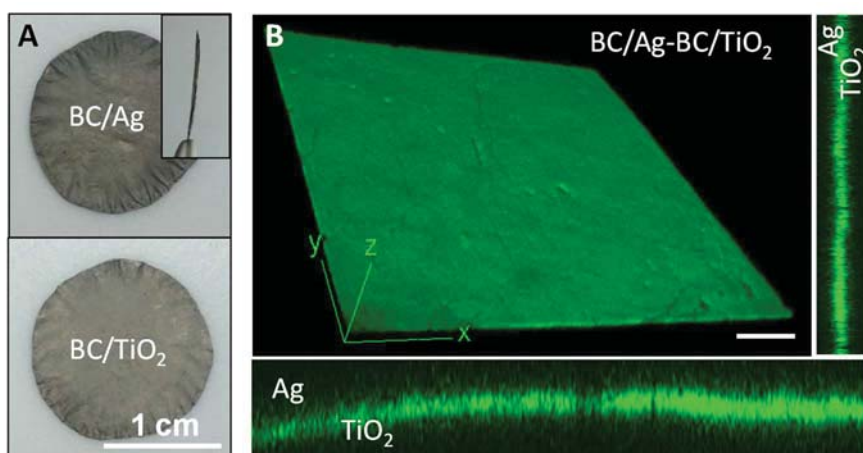
After drying the films, their optical transmittance was measured as shown in Figure 9, illustrating a functional characteristic for each film. Surface plasmon resonance (SPR) absorption bands were measured for BC/Au and BC/Ag films. A broad SPR band for BC/silver, with maximum absorption at 420 nm and a smaller shoulder at 520 nm, indicated the presence of a larger NP size distribution, with some anisotropically shaped particles such as triangles, hexagons or rods as observed in TEM images.<sup>46,47</sup> The BC/Au SPR depicted a maximum absorption peak at 525 nm as expected for ~8 nm gold NPs.<sup>48,49</sup> Besides, UV absorption with a maximum at 242 nm is characteristic of the BC/TiO<sub>2</sub> composite.<sup>50,51</sup> On top of that, UV-Vis spectroscopy allowed to monitor the final nanoparticle content inside the films when the precursor concentration of the reaction was changed. Finally, bacterial cellulose with iron oxide nanoparticles was characterized by measuring its magnetization *versus* an applied magnetic field at 300K as the optical signal was extremely saturated. BC/Fe<sub>2</sub>O<sub>3</sub> film showed superparamagnetic behavior due to the superparamagnetic character of the small iron oxide nanoparticles (SPIONs) that are decorating the cellulose nanofibrils. A saturation magnetization of 30 emu/g was measured for the nanocomposite film, which is a rather high value for a nanocomposite with a non-magnetic matrix.



**Figure 9:** UV-VIS absorption spectra for each nanocomposite. For BC/Fe<sub>2</sub>O<sub>3</sub>, the magnetization curve is shown. Solid line: main concentration studied in this chapter. Dashed line: alternatives concentrations.

#### 4.4 Multilayered bacterial cellulose nanocomposite

As seen in Chapter 2, bilayers and multilayers constructs of pristine BC could be obtained due to the self-adhesion through hydrogen bonding formation between films upon drying, creating millefeuille-like structures. Our interest, therefore, resided in the possibility to obtain laminates with the nanocomposite BC films, which owned less available hydroxyl groups. Multilayers were obtained by piling the wet nanocomposite films one above another in the desired order between two Teflon plates and drying them at 60 °C with 1 kg weight (OD) to avoid entrapped air bubbles. After drying, those laminates performed as a single integrated and thicker film.



**Figure 10:** A) Upper panel: BC/Ag side of a bilayer BC/Ag-BC/TiO<sub>2</sub>. Inset: cross-view of the thickness of the material. Low panel: BC/TiO<sub>2</sub> side of the same bilayer. B) Confocal microscope image of the bilayer with the Ag layer on top. The rectangle images show the z-axis along x and y. Scale bar: 200µm.

Figure 10A shows a bilayer example of BC/Ag with BC/TiO<sub>2</sub> where a different color is noticeable depending on the face-up film (grey for BC/Ag and a more whitish appearance for BC/TiO<sub>2</sub>). The bilayer exhibited a thickness of  $34 \pm 3 \mu\text{m}$  (inset picture) which corresponds to the double of the thickness reported in Chapter 2 for a single and pristine BC film ( $15 \pm 2 \mu\text{m}$ ). The sample was then stained with 1 mL of 1% Safranin-O solution for 12 hours and a confocal study was performed to analyze the bilayer intersection. Figure 10B displays the bilayer with the Ag layer on top where the small rectangular images show the z-axis along x and y. Interestingly, after

---

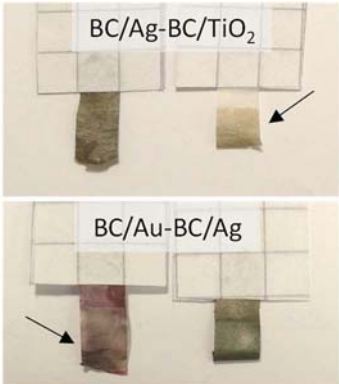
rewetting the sample, the bilayer showed an integrated interface that could not be distinguished although the thickness increased more than 2-fold, up to 84  $\mu\text{m}$ .

NPs were expected to reduce the number of available hydroxyl groups and block the cellulosic nanofibril surface contact, which would impede a high adhesion between films. However, the inclusion of nanoparticles in the BC nanofibrils was found to increase the roughness of the film, as estimated from tapping mode AFM data acquired in the case of BC/TiO<sub>2</sub> (root mean square (rms) roughness values:  $\sim 0.20$   $\mu\text{m}$  for BC/TiO<sub>2</sub> and  $\sim 0.08$   $\mu\text{m}$  for pristine BC).<sup>52</sup> To elucidate if BC multilayers containing nanoparticles also displayed such strong self-adhesive behavior as observed for pristine BC laminates, bilayers combining the different systems were fabricated and mechanically analyzed by peeling tests at *Prof. Lars Berghund research group* facilities at KTH, Sweden, as described in Chapter 2 (Table 4). The study was undertaken for bilayers either combining the same metal, two different metals or a semiconductor and a metal. As a short reminder, a spacing of an anti-adherent material was placed in between the bilayer before drying, covering half of the surface. After drying, the samples were cut using a blade and the two not-adhered ends of the strip were glued between papers and placed between clamps. The force needed as a function of the displacement was recorded and the area below the curve normalized by the peel-off area of the sample (37.5 mm<sup>2</sup>) was calculated as the peeling energy needed to separate the two BC nanocomposite pieces. The BC/Ag-BC/TiO<sub>2</sub> bilayer resulted in adhesion energy equal to the pristine BC bilayer (46 J/m<sup>2</sup>) which made us thought that the expected possible blocking effects from NPs coverage are compensated by the increased film roughness. Slightly smaller values than pristine BC were found for the Au bilayer (33 N/m) and the BC/Au-BC/Ag bilayer (34 J/m<sup>2</sup>). The results suggested that the polymeric surfactants used in the metal nanoparticle synthesis (PVP for silver and OA for gold) might intercede during the drying and influence the adhesion strength. A significantly reduced value (10 J/m<sup>2</sup>) was found for the silver bilayer. This could be a consequence of three combined conditions: the use of a surfactant, the larger Ag NPs size population found and the high nanoparticle content (3 vol%), which could block the intimate contact of the bacterial cellulose nanofibrils upon drying obtaining such low adhesion energy values. In addition, after the peel-off an as a consequence of the color provided by the NPs it was possible to observe that the separation often occurred between the layers of one of the films and not at the interface of the nanocomposite pellicles (right panel images, where a layer transference is marked with arrows). Finally, the

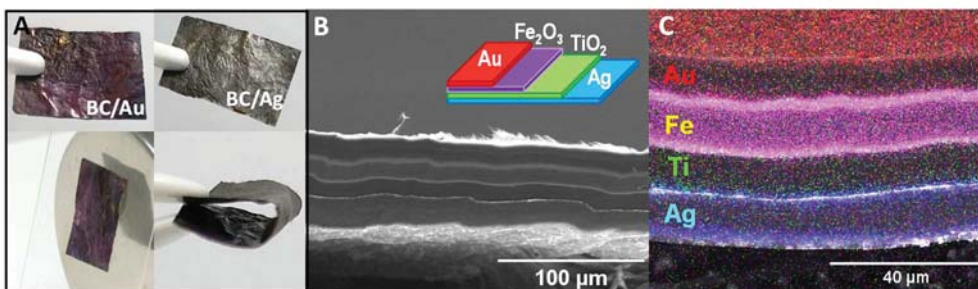
flexibility during manual bending of all BC/nanoparticles dried films and the bilayers was comparable to that of pristine BC, except for BC/Fe<sub>2</sub>O<sub>3</sub>, which showed a more brittle behavior, and therefore no peeling test could be performed. This was attributed to the higher particle content (5 vol%), twice the content than other BC/NPs samples.

**Table 4:** Peeling energy values for various bilayer combinations. (n=3) Right panel: Examples of bilayers after the peel-off test where the transference between films is clearly seen.

Sample	Peeling Energy (J/m <sup>2</sup> ) (±40%)
BC-BC	46
BC/Ag-BC/TiO <sub>2</sub>	46
BC/Au-BC/Au	33
BC/Au-BC/Ag	34
BC/Ag-BC/Ag	10

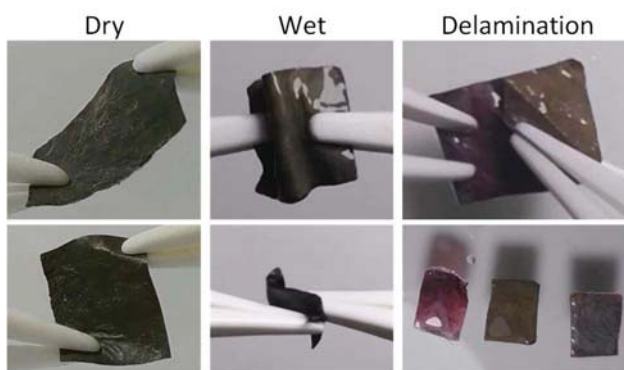


The next step was to extend the bilayer approach to a millefeuille construct comprising four BC layers, each containing a different type of inorganic nanoparticles (that corresponds to the four systems described in this chapter). The resulting multifunctional material behaved as one film of ~ 50 μm thickness with the different nanoparticles confined in each layer. Figure 11A shows a BC/Ag-BC/TiO<sub>2</sub>-BC/Fe<sub>2</sub>O<sub>3</sub>-BC/Au millefeuille construction (1 cm x 1.5 cm) where the two sides are distinguished. BC/Au with the characteristic red/violet coloration of small gold NPs on one side and the reverse with the grey color given by the silver NPs. Besides, the film could be bent without any apparent signs of mechanical failure and responded to a FeNdB permanent magnet (3 cm of diameter x 8 mm width) even when the BC/Fe<sub>2</sub>O<sub>3</sub> film was not placed on the outside. The cross-section was analyzed by electron microscopy. Figure 11B displays an SEM image of the millefeuille cross-section where the layers were differentiated due to electron density variations. Still, they presented a similar thickness and the interface did not exhibit spaces or holes, denoting a proper adhesion between them. Additionally, an electron dispersive X-ray (EDX) mapping analysis, where red corresponds to Au atoms, pink to Fe, green to Ti and blue to Ag, confirmed the distinctive and spatially confined nanomaterial distribution without appreciable diffusion between layers (Figure 11C).



**Figure 11:** A) Upper panels: millefeuille construct showing the two exterior, Au and Ag, layers. Lower panel: the millefeuille responding to a permanent magnet and the folded film without any apparent signs of mechanical failure. B) Millefeuille configuration scheme and SEM image of the cross-section with the four layers visible due to the different contrast of the NPs. C) EDX scan confirming the confined location of the NPs.

To test the flexibility of the laminate construct and the adhesion between the layers, the material was subjected to stringent manipulation (*i.e.*, continuous pulling and bending). As presented in Figure 12, the construct presented an absence of delamination in the dry form and even after several days in water. Interestingly after one week rehydration and harsh handling, a corner of the two metal layers was delaminated and by pulling carefully, the BC/Ag and BC/Au films could be recovered intact.

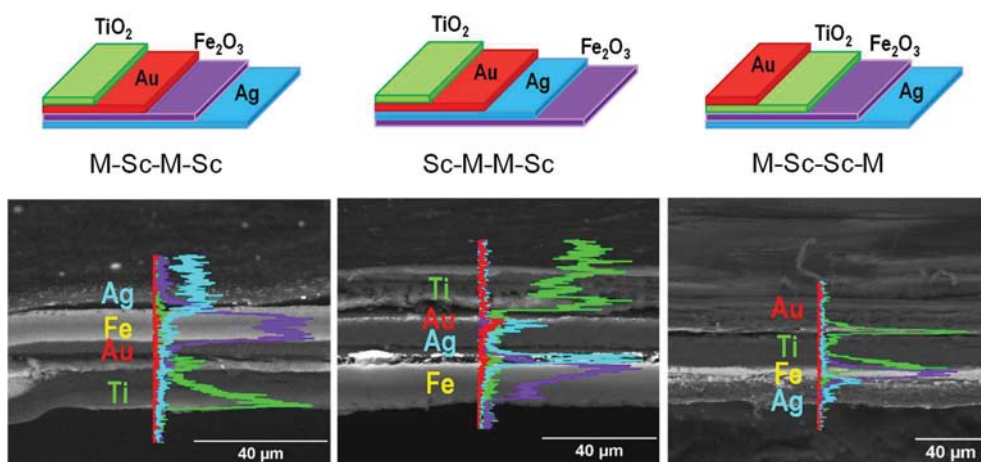


**Figure 12:** Snapshots showing the mechanical properties of a BC millefeuille: left) after drying, middle) after rewetting, right) delamination after one week of harsh manipulation.

#### 4.4.1 Multifunctional constructs and potential applications

The millefeuille strategy facilitates the production of other laminated configurations *ad libitum* just by simply changing the stacking order of the wet BC nanocomposites films before drying. As presented in Figure 13, three different configurations were

obtained playing with the positions of the metals (M) and the semiconductors (Sc). SEM cross-section images and the corresponding EDX line scan showed a confined space distribution of the nanoparticles in all the cases although it is worth mentioning that the Au contribution was smaller, as the precursor concentration was ten times lower than the other systems. The effortless configuration production could enable laminated materials which order would be determined by their final application. For example, if antibacterial properties are important then the BC/Ag layer would be positioned outside, while if the relevant property is the plasmonic characteristic of the nanosilver, then the BC/Ag layer could be hidden in the inner area. For catalytic applications, BC/TiO<sub>2</sub> could be placed on the surface while in the inner structure the layer would provide UV absorption properties. Moreover, for some purposes, the dielectric materials might be placed in between the metal layers (as the configuration showed above) as it would simulate a condenser set-up, while for other applications alternating the metals with the semiconductors might be the preferred sequence.

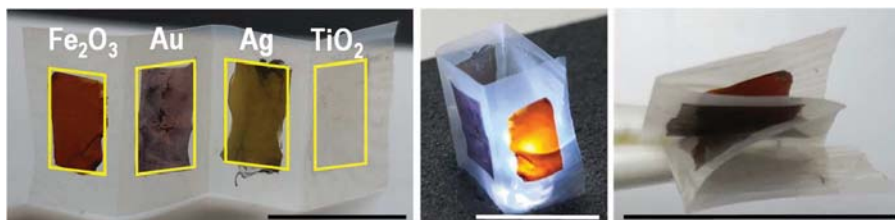


**Figure 13:** Scheme and cross-section SEM image of different conformations of a laminated millefeuille construction with its particular EDX line scan confirming the confined space distribution of the NPs. M: metal, Sc: semiconductor.

Along with the multilayer assembly, other configurations are displayed in Figures 14 and 15 to demonstrate the versatility of the approach. In Figure 14, a brochure-like bilayer construct is presented. It was made by drying strips of BC/NP over a rectangular-shaped pristine BC film, creating a material with linearly arranged functionalities where each pamphlet page had a specific BC/nanocomposite. The configuration could stand as a 3D structure and allowed contacting two NPs systems

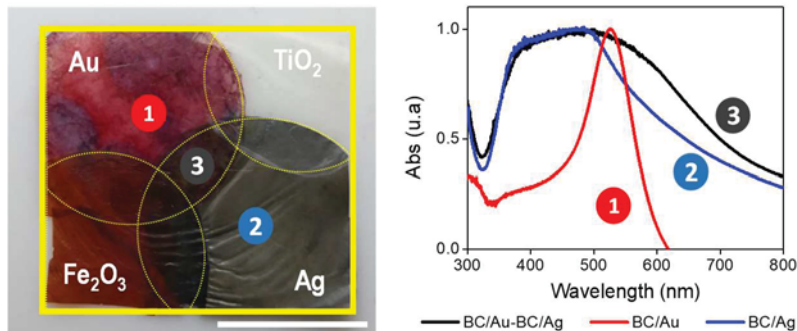


at a particular moment and shift towards other configurations on demand just by folding.



**Figure 14:** Pamphlet BC nanocomposite bilayer where BC/NP films with metal and metal oxide are adhered to a pristine BC film and adaptability of the configuration creating 3D structures and upon folding. Scale bar: 1 cm.

Figure 15 shows a film with a multilayer arrangement of nanocomposite BC where single, double or triple functionalities coexisted (the last two are delimited by the intersections of the yellow dot lines). This type of configuration provided the opportunity to obtain, for instance, different plasmon resonances spatially distributed (marked points 1 and 2) or superimposed (marked point number 3) based on the functionality and number of layers of the spot analyzed.

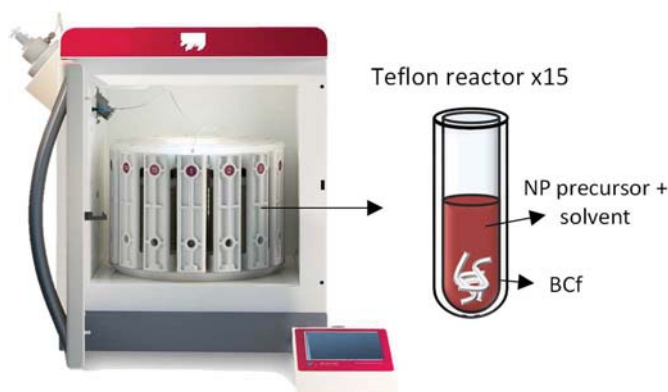


**Figure 15:** Configuration where single, double and triple multifunctionalities can be achieved on demand. The marked points show different or superimposed plasmon resonance depending on the functionality and number of layers of the material. Scale bar: 1 cm.

#### 4.5 Bacterial cellulose nanofibers decorated with magnetic nanoparticles

In addition to films, the MW-assisted reaction process was used with other nanocellulose forms. That is the case of the BC nanofibers (BCf) described in Chapter 2. In this section, magnetic nanofibers were produced, confirming the suitability of this synthesis method over a variety of cellulose structures. Additionally, scale-up modifications of the process towards higher production yields were performed.

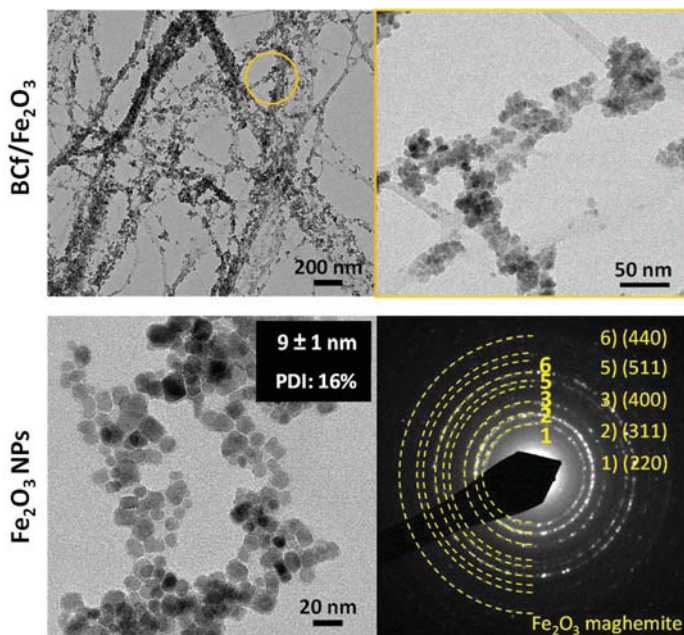
For that, a large capacity MW oven (Advanced flexible microwave synthesis platform from Milestone) was used as shown in Figure 16. This equipment possesses a carousel that allows parallel synthesis with larger reactor vessels (100 mL in volume), increasing the NPs production and, therefore, the amount of BC covered with them. For security reasons, the working operation took place with the reactor half-filled and in one vessel, 3.11 mmol (1100 mg) of  $\text{Fe}(\text{acac})_3$  were mixed with 40 mL BA and 10 mg of BCf were added. Then the mixture was heated in two steps (5 min at 60 °C and 10 min at 210 °C) and BCf/ $\text{Fe}_2\text{O}_3$  were obtained. The large volume reactor enabled a 5-fold production increase of functionalized BC. Although for our studies no more than three reactions were performed at the same time, the oven could perform 15 reactions in a row.



**Figure 16:** MW oven with the set-up to perform 15 reactions in parallel and scheme of BCf magnetic functionalization through the MW-assisted reaction mechanism.

After the synthesis, the cleaning of the BCf with SPIONs and the collection of nanoparticles were done as described for the BC/ $\text{Fe}_2\text{O}_3$  films. However, in this particular case, the fibers were filtered with a cell strainer (40  $\mu\text{m}$  Nylon mesh, Fisherbrand) between cleaning steps. The filter employed during BCf production (Stericup Quick Release Filter Millipore with a PES membrane of 0.22 $\mu\text{m}$ ) could not be used as the BA degrades the membrane. After cleaning, the nanofibers and the supernatant were analyzed by TEM. A homogeneous coating of NPs covering the BCf with nanoparticles of 9 nm (PDI: 16%) is shown in the images of the upper panel of Figure 17 at different magnifications. The nanoparticle's mean size was calculated from the supernatant over a population of 400 NPs and the polydispersity (PDI) value, obtained as the percentage of standard deviation/mean value, indicates that a good

NPs size homogeneity was obtained during the synthesis. In addition, SAED data confirmed the presence of maghemite crystal structures.



**Figure 17:** Upper panel: TEM images at different magnifications of BCF coated with SPIONs NPs. Bottom panel: TEM images of the NPs extracted from the supernatant and thereof diffraction pattern, which corresponds to a maghemite crystalline phase.

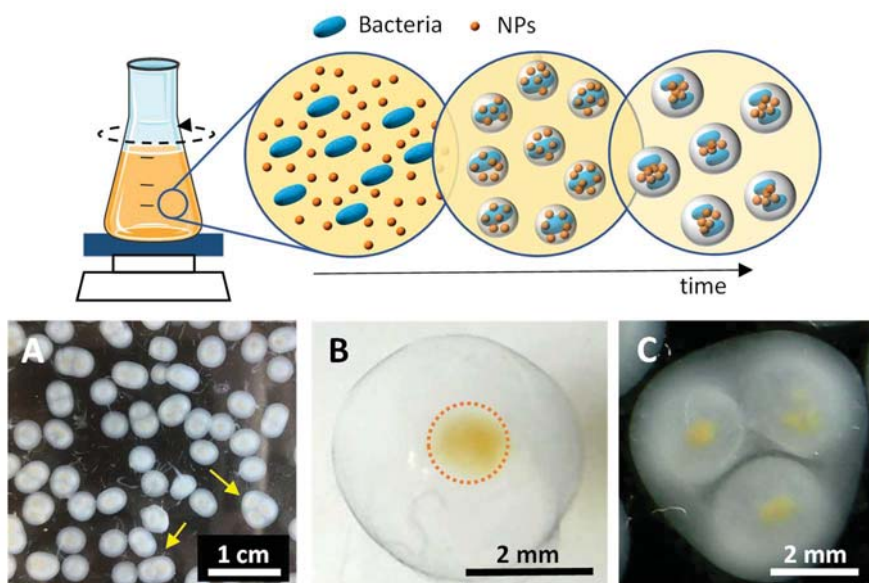
#### 4.6 Functionalization of bacterial cellulose spheres

Several strategies have been reported to produce bacterial cellulose spheres (BCS) such as 3D printing<sup>53</sup>, microfluidics affording hollow BC microspheres<sup>54</sup> or spray-drying yielding BC microparticles<sup>55</sup>, however, specialized equipment is required in all cases. Besides, although these approaches facilitate intricate BC structures, adding localized functionalization is not simple and more research efforts are still needed. To afford functional filled and hollow BCS, as the ones described in Chapter 2, *in-situ* incorporation of pre-synthesized NPs during the BC biosynthesis was employed. As described at the beginning of this chapter, the method consists of dispersing NPs in the culture medium so the bacteria can entrap them inside the interwoven nanocellulose network upon growing. This strategy is mainly used in agitation culture conditions to avoid NPs precipitation and the formation of an inhomogeneous material. However, we took advantage of the precipitation to afford multifunctional

BC spheres in static conditions. The studies were fundamentally done using the iron oxide NPs (SPIONs) obtained from the MW-assisted reaction and in collaboration with Oriol Torrecilla, a laboratory fellow from the NN research group.

#### 4.6.1 Magnetic bacterial cellulose spheres in an agitated culture system

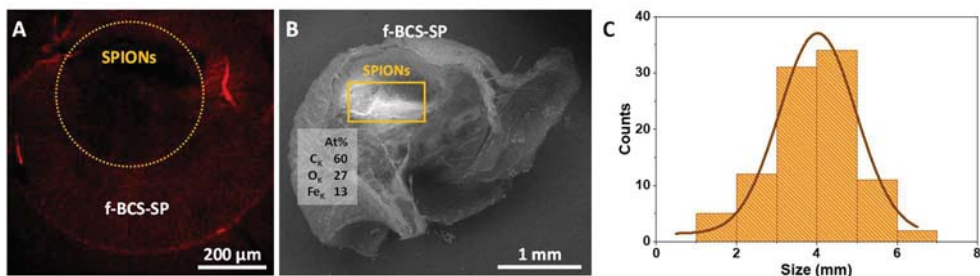
To produce magnetic-filled BC spheres (f-BCS-SP), *K. xylinus* was inoculated on 6 mL of HS culture medium and incubated statically for 7 days at 30 °C. Then, 2 mL were transferred to a 100 mL conical flask with 38 mL of fresh HS medium and 200  $\mu$ L SPIONs solution (10 mg/mL in HS medium) and the system was placed in an orbital shaker inside the incubator. As described in Chapter 2 and represented in Figure 18, upon stirring bacteria aggregate and create skein-like shapes of nanofibers trapping themselves and the nanoparticles inside. After 3 days at 30 °C in 150 rpm agitation, f-BCS-SP composites were collected by filtration and cleaned as usual. Finally, they were washed until pH neutralization and kept in MQ water until further use.



**Figure 18:** Scheme of the agitation biosynthesis approach to produce filled bacterial cellulose spheres with magnetic NPs in their center (f-BCS-SP). A) f-BCS-SP image after 3 days culture. Yellow arrows indicate the presence of multispheres. B) Single f-BCS-SP core-shell structure. The magnetic core is delineated by an orange circle. C) Multisphere f-BCS-SP core-shell structure.

The brown spot in the center of the f-BCS-SP indicates the presence of the SPIONs and the formation of core-shell structures. However, secondary structures, *i.e.*, spheres embedded within the same structure, were also observed (arrows in Figure 18A and Figure 18C). This organization confirmed that during cell growth, bacteria produced cellulose nanofibers around themselves, embedding the SPIONs during the process. At some point, no more NPs were available and bacteria continue producing cellulose, generating skein-like structures with a core-shell organization. In addition, the continuous agitation favored the spheres to physically interact and, in some cases, to coalesce in complex geometries with several spheres embedded. Therefore, the precise NP loading and size control of the spheres is challenging with this methodology.

f-BCS-SP were immersed for 12 h with 1 mL Safranin-O solution (0.5 mM) to stain the nanocellulose and were subjected to a confocal study which confirmed the filled core-shell morphology (Figure 19A) as cellulose can be observed in all the structure except for a black region in the center which we assigned to the SPIONs blocking the fluorescence signal. In addition, the spheres were cut in half with a blade and lyophilized to maintain the structure upon drying. After drying, the samples were placed on a SEM holder and analyzed. SEM images are depicted in Figure 19B and also confirmed on one hand, the filled nanocellulose structure and, on the other hand, the presence of a high electron-density material in the center of the sphere (brighter area) identified with EDX analysis as SPIONs as iron presence was locally detected (13% At). Finally, without taking into consideration the multispheres, digital image analysis of 100 spheres determined a mean diameter size of  $4 \pm 1$  mm (Figure 19C), smaller than the one obtained for pristine f-BCS ( $6 \pm 1$  mm).

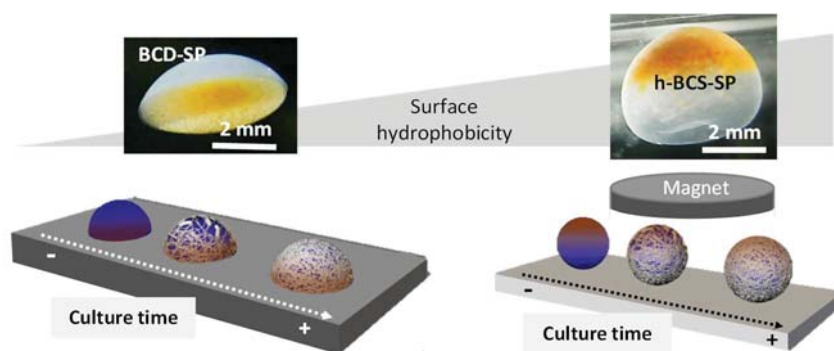


**Figure 19:** A) Confocal image showing the no-fluorescence of the core of the f-BCS-SP due to the presence of SPIONs. B) SEM picture of a lyophilized half f-BCS-SP. The bright area indicates the location of SPIONs. C) Size histogram with a maximum peak centered at  $4 \pm 1$  mm ( $n = 100$ ).

#### 4.6.2 Actuable bacterial cellulose spheres on hydrophobic surfaces

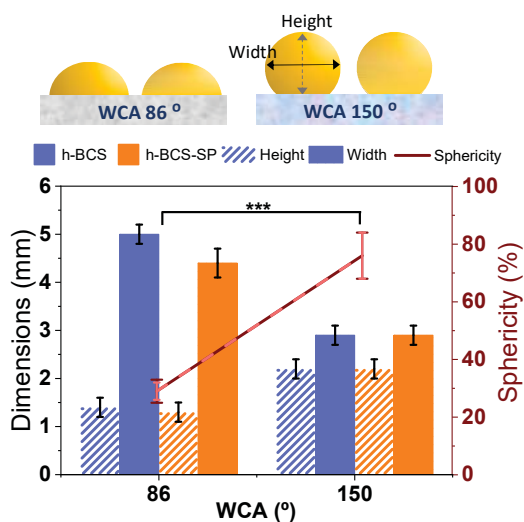
To achieve better control on the size and shape of the functional BCS than in agitation culture and to better regulate the SPIONs location and concentration within them, the static biosynthesis approach over superhydrophobic surfaces presented in Chapter 2 was expanded, obtaining magnetic hollow BCS (h-BCS-SP). h-BCS-SP were prepared by mixing an initial bacterial culture volume with 10 %v/v of glycerol to increase the viscosity and avoid deformation due to evaporation during the incubation period. Then, a SPIONs solution (in HS medium) was added in a 1:1 ratio to the solution and drops of 5  $\mu$ L were deposited on superhydrophobic (SH) slides (WCA of 150°) and hydrophilic surfaces (Petri dishes with WCA of 86°). The spheres were incubated for 3 days at 30 °C in a saturated humidity environment and static conditions. Afterward, they were gently removed from the surface with water and cleaned and stored using the standard protocol.

As bacterial cellulose grows at the air-liquid interface, the final material would acquire the external shape of the drop, which would depend on the hydrophobic character of the surface: hollow spherical structures for superhydrophobic surfaces or hollow dome-like shaped structures for hydrophilic surfaces. In addition, as presented in Figure 20, by the application of a magnetic field the location of SPIONs on the bacterial broth and within the BCS could be controlled.



**Figure 20:** Scheme of the static biosynthesis of magnetic hollow structures with different shapes and SPIONs location, depending on the surface hydrophobicity and the application of a magnetic field. Left: hollow dome-shaped structure with magnetic NPs at the bottom (BCD-SP). Right: hollow bacterial cellulose sphere with NPs on top (h-BCS-SP).

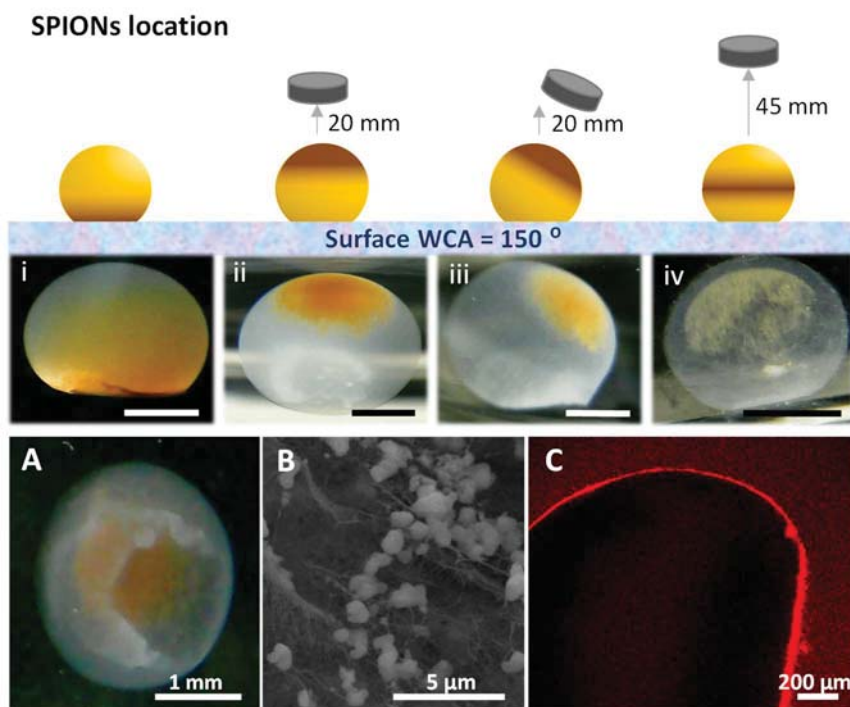
As has been mentioned in Chapter 2 and we previously reported,<sup>56</sup> the sphericity of the h-BCS structures improved as the hydrophobicity of the surface increased and h-BCS-SP maintained this behavior. Sphericity was calculated as the mean value of the structure height/width ratio percentage from 6 to 21 spheres, considering 100% a perfect sphere. In addition, one-way ANOVA followed by Tukey's multiple comparison test was used for statistical analysis with an accepted significance of 0.05. The results presented in Figure 21 showed a sphericity of 30% on surfaces with a WCA of 86°, where dome-shaped structures were obtained. Whereas spheres with ~80% sphericity can be attained using surfaces with a WCA of 150°. Increasing the WCA produced and sphericity increase of the hollow structure of almost 3-fold not affected by the addition of NPs.



**Figure 21:** Scheme and study of surface hydrophobicity effect on the morphology of h-BCS with (orange columns) and without (blue columns) SPIONS (P-values < 0.001).

Taking advantage of the magnetization property of SPIONs, an external NdFeB magnet was employed to immobilize the NPs at different heights (y-axis) inside the drop by placing the magnet over the surface as presented in Figure 22(i-iv). Without a magnetic field, SPIONs precipitated at the bottom spherical cap of the h-BCS-SP. However, with a magnet at 20 mm from the surface, SPIONs were located on the top spherical cap of the sphere. Additionally, if the magnet was shifted in the x-axis at the start of the biosynthesis, it was also possible to displace the final NPs position in

that direction. Interestingly, by modifying the distance of the magnet from the surface to 45 mm, the NPs were maintained at the equatorial area of the structure.



**Figure 22:** i-iv) h-BCS-SP under different magnetic field conditions on a superhydrophobic surface (WCA = 150°). Scale bar: 1 mm. A) Broken h-BCS-SP where the hollow structure and the localized SPIONs loading are clearly seen. B) SEM picture of the cellulose wall of a lyophilized h-BCS-SP with SPIONs aggregates on the nanofibers. C) Confocal image of h-BCS-SP biosynthesized with a magnetic field at 45 mm. At the middle of the sphere, fluorescence is observed due to nanocellulose growth.

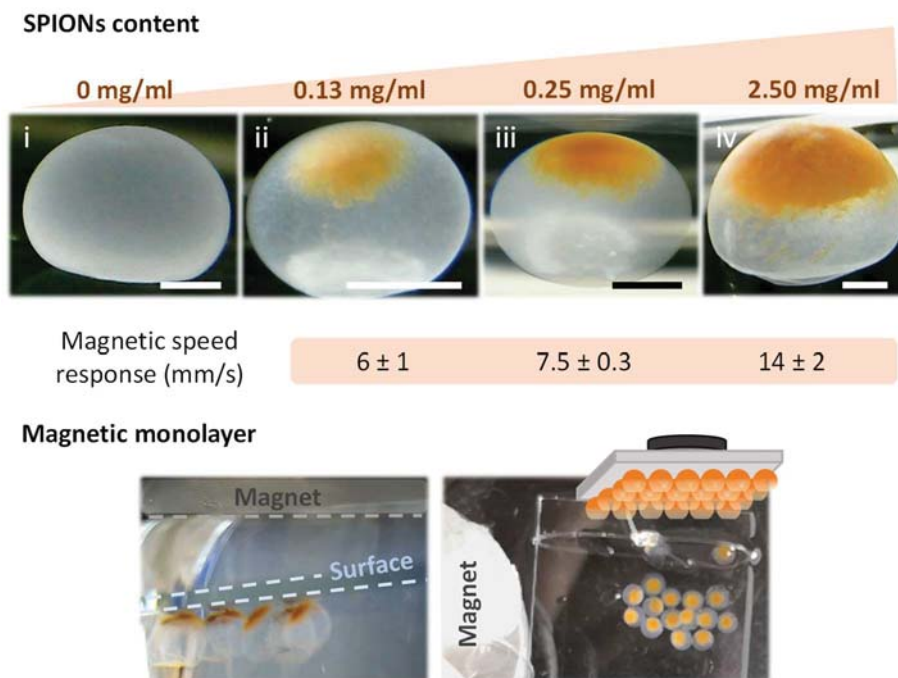
In all cases, the nanoparticles entangled within the nanocellulose fibers during the biosynthesis and remained in the same position after the magnet removal and the cleaning process. Figure 22A shows an open h-BCS-SP exhibiting the hollow structure and the SPIONs trapped in a localized area of the sphere wall. SEM analysis (Figure 22B) of lyophilized h-BCS-SP also corroborated the entrapment of the SPIONs, since aggregates bonded to the fibrous cellulosic structure were seen. This feature was especially remarkable in the drops where SPIONs were stably located in the middle of the drop, suggesting that some cellulose was produced also in the center, fastening the NPs. To visualize the internal configuration and corroborate the hypothesis, spheres were analyzed by confocal microscopy. Figure 22C shows a h-BCS-SP (at 45 mm magnetic field) where the hollow structure is clearly seen since



---

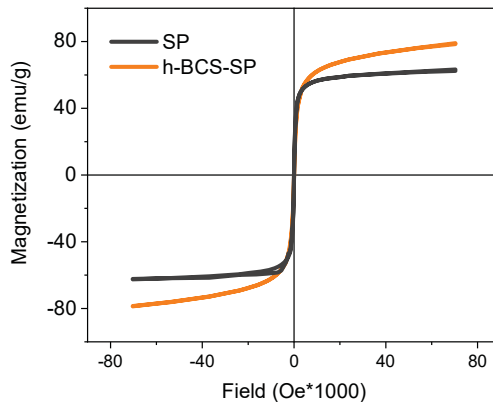
the fluorescence signal, which corresponds to cellulose, is delimiting the sphere diameter. Remarkably, for this particular sample, fluorescence was also found in the middle of the structure, which indicated the presence of nanocellulose where SPIONs were located. We hypothesize that some bacteria attached to the SPIONs and migrate with them when the magnetic field was applied, producing nanocellulose from that location towards the sphere interface, where the oxygen availability is higher, and entrapping the nanoparticles during the process.

The magnetic loading of the h-BCS-SP could also be easily controlled by varying the initial SPIONs concentration into the bacterial culture medium, obtaining spheres with 0.13, 0.25 and 2.50 mg SPIONs/mL, as presented in Figure 23(i-iv). The increase of SPIONs concentration was directly correlated with a higher surface covered by nanoparticles, being  $26 \pm 6$  % coverage for a SPIONs concentration of 0.13 mg/mL,  $33 \pm 7$  % for 0.25 mg/mL and  $51 \pm 6$  %, for 2.50 mg/mL. Additionally, the h-BCS-SP speed response towards a magnetic field was measured and also exhibited a straightforward proportion to the amount of SPIONs presented within the structure. To calculate the speed response, a sphere was placed 10 mm apart from a vessel wall where the magnet was allocated. The time needed by the sphere to cover the distance was computed considering  $t=0$  the moment the drop orientates towards the magnet and the final time when it reached the glass wall in contact with the magnet. A 2.50 mg/mL load showed a faster reaction (speed of 14 mm/s) towards the magnet than 0.25 mg/mL (speed of 6 mm/s). Remarkably, h-BCS-SP did not change shape after actuation. Besides, as depicted in Figure 23 (lower panel), the magnetical control of the spheres allowed to assemble them into a single monolayer on a surface. This magnetic actuation could facilitate the recovery of the spheres in a solution where they may act as catalysts or switching layers.<sup>57,58</sup>



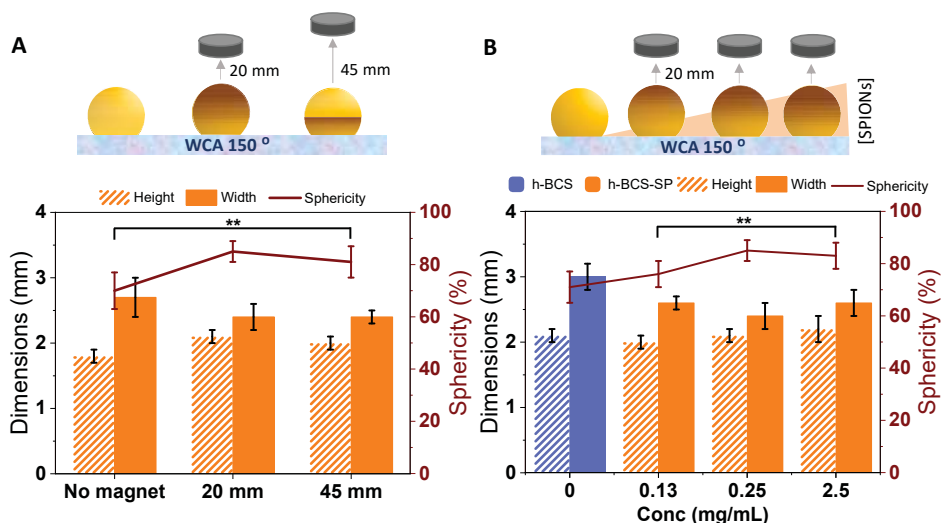
**Figure 23:** i-iv) h-BCS-SP with different SPIONs concentration under the same magnetic field (at 20 mm) on a superhydrophobic surface and their magnetic response ( $n=3$ ) towards a magnetic field. Scale bar: 1 mm. Lower panel: example of an h-BCS-SP monolayer ordered arrangement on a crystal surface.

Furthermore, the magnetization of h-BCS-SP was studied. A sphere with 2.50 mg/mL SPIONs concentration was dried in the middle of a paper strip at room temperature. The strip was then placed inside a plastic tube of similar diameter and sealed with cotton. A h-BCS of the same size was dried at room temperature in another strip and a drop of the h-BCS-SP precursor solution was deposited above. This was done to avoid the spreading of the drop through the strip and to have a similar cellulose volume. To maintain the same SPIONs concentration as the h-BCS-SP, the drop had a volume of  $5\mu\text{L}$ . Magnetization vs. applied magnetic field was measured from 0 to 70 kOe at 300 K and the magnetic response of the SPIONs trapped in the cellulose sphere and the free SPIONs were compared. Given the results depicted in Figure 24, NPs did not degrade during the sphere biosynthesis process as a superparamagnetic behavior similar to the native NPs was observed. In addition, after one year in solution, h-BCS-SP appearance did not change which led us to confirm the strong entrapment of the nanoparticles into the nanocellulosic matrix with almost negligible leaching of SPIONs.



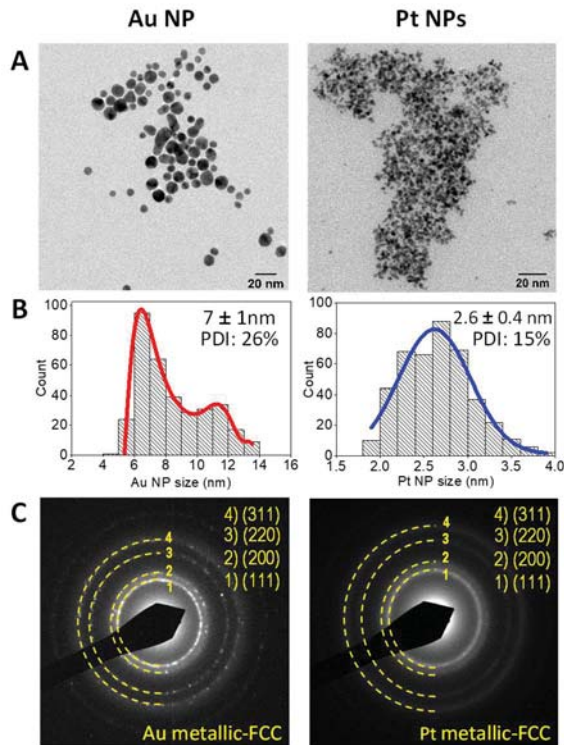
**Figure 24:** Magnetization per gram of SPIONs vs. applied magnetic field at 300K comparison of native 2.50 mg/mL SPIONs solution (black line) and a h-BCS-SP with the same concentration (orange line).

Finally, the influence of the magnetic field and the SPIONs concentration on the morphology of the BCS was studied. When h-BCS-SP biosynthesized with 0.25 mg/mL SPIONs solution were examined (Figure 25A), a 10-15% increased sphericity was observed for the spheres cultivated under a magnetic field compared to h-BCS-SP cultivated without the magnetic field. However, no statistical difference in sphericity was detected when the magnet distance was changed. On the other hand, risen SPIONs concentration increased sphericity (Figure 25B), being able to observe a maximum sphericity value for a concentration of 0.25 mg/mL, which increases the sphericity 14% in comparison to the control (*i.e.*, without NPs). At higher concentrations such as 2.50 mg/mL, the sphericity was maintained without statistically significant differences. Therefore, SPIONs addition did not affect the bacterial growth either the sphericity of the final structure. We hypothesize that, as the SPIONs were attracted towards the magnet, the magnetic force applied prevented the drop to flatter and maintained the spherical shape while, at the same time, the presence of nanoparticles could increase the oxygen availability in the drop.



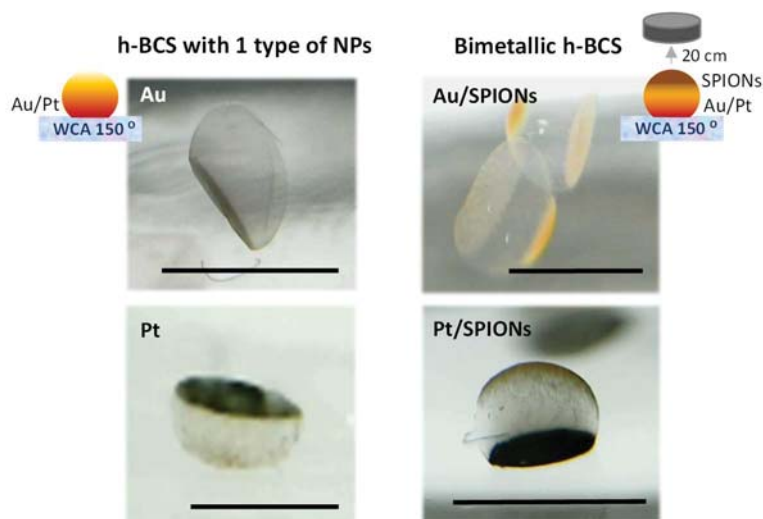
**Figure 25:** A) Magnetic field distance effect on the morphology of h-BCS-SP with 0.25 mg/mL SPIONs. B) SPIONs concentration morphological effect on h-BCS-SP production under a magnetic field. h-BCS without SPIONs are represented in blue and h-BCS-SP are represented in orange.

Going one step further and by applying the same biosynthesis procedure, different functionalities had been added to the h-BCS. Gold nanoparticles (Au NPs, 2.5 mg/mL HS medium), platinum nanoparticles (Pt NPs, 10 mg/mL HS medium) or a mixture of them with SPIONs in equal proportions were added in a 1:1 ratio to the bacterial broth solution containing glycerol and were cultivated as described previously. Au NPs were obtained through the Turkevich method<sup>59</sup> while Pt NPs were commercially available. The study of the NPs' size and crystal phase was performed by TEM (Figure 26). In each case, 300-400 NPs size histogram was fitted to a Gaussian function and the mean size values were obtained. Polydispersity (PDI) was computed as the percentage of the standard deviation divided by the mean value. Particle size histograms resulted in mean particle sizes of  $7 \pm 1$  and  $2.6 \pm 0.4$  nm for Au and Pt respectively with a polydispersity index of 26 and 15%. In the case of Au, a second lesser population of  $11 \pm 1$  nm was observed. In addition, SAED analyses confirm the face-centered cubic crystal structure of metallic gold and platinum.



**Figure 26:** A) TEM images of the NPs used to functionalize the h-BCS. B) Particle size distribution computed from TEM images. C) SAED images of the nanoparticles. Each characteristic crystallographic plane is highlighted.

As shown in Figure 27, the addition of Au or Pt NPs on the media allowed to create h-BCS-Au and h-BCS-Pt respectively. Besides, due to the magnetic properties of SPIONs, several nanoparticles could be added at once and locate in specific areas inside the h-BCS just by using a magnet, obtaining Janus actuable structures. While SPIONs were situated on the top of the structure, Au NPs or Pt NPs were embedded on the lowermost part of the spherical structure due to gravity-based deposition. The simplicity of the approach allows to modify the type of nanoparticles, concentrations and parameters of the static culture protocol to create multifunctional structures on-demand and settles this strategy as a new path to create complex and multifunctional bacterial cellulose spheres.



**Figure 27:** Left) h-BCS structures synthesized with other nanoparticles. Scale bar: 2mm. Right) Janus magnetic h-BCS showing diverse functionality. Scale bar: 2 mm.

#### 4.7 Conclusions

Two main strategies to produce functionalized BC nanocomposites have been described in this chapter: 1) synthesis of NPs in the BC network through MW-assisted reaction and 2) incorporation of NPs inside the BC network during the biosynthesis by the addition of pre-formed NPs in the bacterial broth.

The energy-efficient MW-assisted reaction synthesis allowed the fabrication of several inorganic nanoparticles/BC nanocomposites. This technique, previously reported by our group for iron oxide, was extended to titania, gold and silver NPs and enabled the volume fraction control of particles within the nanocellulosic porous scaffold. Besides, nanocomposites with homogeneous size particles and with a homogenous coverage were obtained, exhibiting a strong bond between the nanofibers and the NPs where no leaching was detected.

In addition, a concept of laminated multifunctional nanocellulose films was developed. The millefeuille construction contained between two to four layers of BC strongly attached and with the nanofibrils in each layer decorated by specific inorganic nanoparticles (Au, Ag, Fe<sub>2</sub>O<sub>3</sub> and TiO<sub>2</sub>), presenting complementary functional properties but also spatial confinement distribution along the cross-section.

---

The proposed laminate could be *ad libitum* assembled through molecular scale fibril-fibril hydrogen bond formation during BC film drying, as discussed in Chapter 2. The 3D network nature of high-strength BC ribbons provides excellent mechanical integrity to the layers and to the final multifunctional laminate. However, film roughness or the surfactant used to cover the NPs systems could also be relevant. Further studies on these topics could clarify the adhesion mechanism between nanocomposite BC films.

The viability of the methodology was shown by presenting data for various  $\sim 50 \mu\text{m}$  thick and flexible film constructions even combining functional layers with pristine BC films. This millefeuille concept greatly enlarges the materials design possibilities of multifunctional nanocellulose as several nanotechnologies could be integrated into one material. Therefore, although the concept presented is generic and preliminary, the potential for laminated structures in multifunctional sensors may be particularly interesting. For example, preliminary tests were done with multilaminates composed by several layers of BC/Fe<sub>2</sub>O<sub>3</sub> and BC/TiO<sub>2</sub> as those NPs systems are known as good absorbers of MW radiation. The MW absorption capacity of those multilayers was studied in collaboration with *Prof. Zhiming research group* from the Ocean University of China, obtaining encouraging first results for 8-films laminates, however, further optimization is needed. The UV absorption property of BC/TiO<sub>2</sub> was studied as a platform for cell proliferation and the results are compiled in the publication entitled “Bacterial nanocellulose and titania hybrids: cytocompatible and cryopreservable cell carriers” (*ACS Biomaterials Science & Engineering*, 2020, 6 (8), 4893-4902). Besides, preliminary assays were performed on BC/Au films for surface-enhanced Raman spectroscopy (SERS).

Additionally, trying to close a little the gap between research and industry and to prove the versatility of the MW-assisted reaction strategy, higher production of functional BC was tested doing several syntheses in parallel in larger reaction vessels with other nanocellulose forms. Fe<sub>2</sub>O<sub>3</sub> synthesis on BCf was tested for that purpose, obtaining an increased reactor production of 5-fold with nanofibers homogeneously covered by NPs of similar size than using lab-scale instruments with lower capacity. Those results would allow to easily and fast scale functional BC in the future, although still at a laboratory level.

The second strategy used to functionalize BC structures was the *in-situ* incorporation of pre-formed NPs inside the BC network during biosynthesis. This approach was performed in two culture conditions (agitation and static over hydrophobic surfaces) and was mainly studied for magnetic BC structures although it could be extrapolated to other NP, changing the functionality of the material.

The agitated bacterial culture produced filled BCS structures with a core-shell organization and with the magnetic nanoparticles located at the center. However, multispheres (spheres embedded in a bigger one) were also obtained, being challenging to control the size of those structures and the NP load of the spheres. On the contrary, the static approach based on hydrophobic surfaces allowed the production of hollow structures with high control on the sphere size and the location and concentration of the functional loading within the structure. By controlling the surface hydrophobicity, different functional 3D structures such as spheres or dome-like shapes were achieved. Besides, the application of a magnetic field demonstrated a highly specific control of the NPs, being able to even fasten them in the middle of the structure and to maintain the spherical shape while the bacteria is growing. In addition, h-BCS-SP supported nanoparticle loadings of approximately half of its volume and integrated them inside the nanocellulose network as no leaching was observed after one year in solution. Those NPs did not present a magnetization degradation when subjected to the biosynthesis and their increased concentration did not report an effect on the bacterial growth. Note that, SPIONs were used as a model system in this study but other systems could be employed to produce BCS with functionality on demand. However, only h-BCS offered the possibility to produce spheres with located multifunctionality, such as the synthesized Au-SPIONs or Pt-SPIONs hybrids, obtaining Janus bacterial cellulose spheres. The novel biosynthetic procedure described opens the avenue to unique nanocellulose-based structures otherwise complicated to obtain.

Both strategies launched cost-effective and renewable approaches for advanced application nanocellulose-based materials. A few examples were outlined here, however, higher research efforts regarding applications where specific functions are confined to spatially well-defined locations, such as multifunctional sensors or nanostructured devices and reactors for multiple catalytic effects, would be of great interest in the future. In the case of the spheres, we hypothesize that those structures



---

would be applied in fields where currently silica or collagen spheres are used for cargo delivery systems, theragnostic, tissue engineering or programmable and self-organizing systems.

## 4.8 References

- (1) Torres, F. G.; Arroyo, J. J.; Troncoso, O. P. Bacterial Cellulose Nanocomposites: An All-Nano Type of Material. *Mater. Sci. Eng. C* **2019**, *98*, 1277–1293. <https://doi.org/10.1016/j.msec.2019.01.064>.
- (2) Liu, W.; Du, H.; Zhang, M.; Liu, K.; Liu, H.; Xie, H.; Zhang, X.; Si, C. Bacterial Cellulose-Based Composite Scaffolds for Biomedical Applications: A Review. *ACS Sustain. Chem. Eng.* **2020**, *8* (20), 7536–7562. <https://doi.org/10.1021/acssuschemeng.0c00125>.
- (3) Hu, W.; Chen, S.; Yang, J.; Li, Z.; Wang, H. Functionalized Bacterial Cellulose Derivatives and Nanocomposites. *Carbohydr. Polym.* **2014**, *101*, 1043–1060. <https://doi.org/10.1016/j.carbpol.2013.09.102>.
- (4) Farooq, A.; Patoary, M. K.; Zhang, M.; Mussana, H.; Li, M.; Naeem, M. A.; Mushtaq, M.; Farooq, A.; Liu, L. Cellulose from Sources to Nanocellulose and an Overview of Synthesis and Properties of Nanocellulose/Zinc Oxide Nanocomposite Materials. *Int. J. Biol. Macromol.* **2020**, *154*, 1050–1073. <https://doi.org/10.1016/j.ijbiomac.2020.03.163>.
- (5) Ahankari, S. S.; Subhedar, A. R.; Bhadauria, S. S.; Dufresne, A. Nanocellulose in Food Packaging: A Review. *Carbohydr. Polym.* **2021**, *255*, 117479. <https://doi.org/10.1016/j.carbpol.2020.117479>.
- (6) Sriplai, N.; Pinitsoontorn, S. Bacterial Cellulose-Based Magnetic Nanocomposites: A Review. *Carbohydr. Polym.* **2021**, *254*, 117228. <https://doi.org/10.1016/j.carbpol.2020.117228>.
- (7) Zang, S.; Zhang, R.; Chen, H.; Lu, Y.; Zhou, J.; Chang, X.; Qiu, G.; Wu, Z.; Yang, G. Investigation on Artificial Blood Vessels Prepared from Bacterial Cellulose. *Mater. Sci. Eng. C* **2015**, *46*, 111–117. <https://doi.org/10.1016/j.msec.2014.10.023>.
- (8) Smith, C. J.; Wagle, D. V.; O'Neill, H. M.; Evans, B. R.; Baker, S. N.; Baker, G. A. Bacterial Cellulose Ionogels as Chemosensory Supports. *ACS Appl. Mater. Interfaces* **2017**, *9*, 38042–38051. <https://doi.org/10.1021/acsami.7b12543>.
- (9) Lv, P.; Zhou, H.; Mensah, A.; Feng, Q.; Wang, D.; Hu, X.; Cai, Y.; Amerigo Lucia, L.; Li, D.; Wei, Q. A Highly Flexible Self-Powered Biosensor for Glucose Detection by Epitaxial Deposition of Gold Nanoparticles on Conductive Bacterial Cellulose. *Chem. Eng. J.* **2018**, *351*, 177–188. <https://doi.org/10.1016/j.cej.2018.06.098>.
- (10) Pal, S.; Nisi, R.; Stoppa, M.; Licciulli, A. Silver-Functionalized Bacterial Cellulose as Antibacterial Membrane for Wound-Healing Applications. *ACS Omega* **2017**, *2* (7), 3632–3639. <https://doi.org/10.1021/acsomega.7b00442>.
- (11) Liu, L. P.; Yang, X. N.; Ye, L.; Xue, D. D.; Liu, M.; Jia, S. R.; Hou, Y.; Chu, L. Q.; Zhong, C. Preparation and Characterization of a Photocatalytic Antibacterial Material: Graphene Oxide/TiO<sub>2</sub>/Bacterial Cellulose Nanocomposite. *Carbohydr. Polym.* **2017**, *174*, 1078–1086. <https://doi.org/10.1016/j.carbpol.2017.07.042>.
- (12) Alonso-Díaz, A.; Floriach-Clark, J.; Fuentes, J.; Capellades, M.; Coll, N. S.; Laromaine, A. Enhancing Localized Pesticide Action through Plant Foliage by Silver-Cellulose Hybrid Patches. *ACS Biomater. Sci. Eng.* **2019**, *5* (2), 413–419. <https://doi.org/10.1021/acsbmaterials.8b01171>.
- (13) Waghmode, M. S.; Gunjal, A. B.; Mulla, J. A.; Patil, N. N.; Nawani, N. N. Studies on the Titanium Dioxide Nanoparticles: Biosynthesis, Applications and Remediation. *SN Appl. Sci.* **2019**, *1*, 310. <https://doi.org/10.1007/s42452-019-0337-3>.

- 
- (14) Dal'acqua, N.; De Mattos, A. B.; Krindges, I.; Pereira, M. B.; Da Silva Barud, H.; Ribeiro, S. J. L.; Duarte, G. C. S.; Radtke, C.; Almeida, L. C.; Giovanela, M.; et al. Characterization and Application of Nanostructured Films Containing Au and TiO<sub>2</sub> Nanoparticles Supported in Bacterial Cellulose. *J. Phys. Chem. C* **2015**, *119* (1), 340–349. <https://doi.org/10.1021/jp509359b>.
- (15) Khan, S.; Ul-Islam, M.; Khattak, W. A.; Ullah, M. W.; Park, J. K. Bacterial Cellulose-Titanium Dioxide Nanocomposites: Nanostructural Characteristics, Antibacterial Mechanism, and Biocompatibility. *Cellulose* **2015**, *22*, 565–579. <https://doi.org/10.1007/s10570-014-0528-4>.
- (16) Hu, J.; Wu, D.; Feng, Q.; Wei, A.; Song, B. Soft High-Loading TiO<sub>2</sub> Composite Biomaterial Film as an Efficient and Recyclable Catalyst for Removing Methylene Blue. *Fibers Polym.* **2020**, *21* (8), 1760–1766. <https://doi.org/10.1007/s12221-020-9543-2>.
- (17) Vural, M.; Crowgey, B.; Kempel, L. C.; Kofinas, P. Nanostructured Flexible Magneto-Dielectrics for Radio Frequency Applications. *J. Mater. Chem. C* **2014**, *2*, 756–763. <https://doi.org/10.1039/C3TC32113D>.
- (18) Hendrick, E.; Frey, M.; Herz, E.; Wiesner, U. Cellulose Acetate Fibers with Fluorescing Nanoparticles for Anti-Counterfeiting and pH-Sensing Applications. *J. Eng. Fiber. Fabr.* **2010**, *5* (1), 21–30.
- (19) Galland, S.; Andersson, R. L.; Salajková, M.; Ström, V.; Olsson, R. T.; Berglund, L. A. Cellulose Nanofibers Decorated with Magnetic Nanoparticles – Synthesis, Structure and Use in Magnetized High Toughness Membranes for a Prototype Loudspeaker. *J. Mater. Chem. C* **2013**, *1*, 7963. <https://doi.org/10.1039/c3tc31748j>.
- (20) Zhu, H.; Jia, S.; Wan, T.; Jia, Y.; Yang, H.; Li, J.; Yan, L.; Zhong, C. Biosynthesis of Spherical Fe<sub>3</sub>O<sub>4</sub>/Bacterial Cellulose Nanocomposites as Adsorbents for Heavy Metal Ions. *Carbohydr. Polym.* **2011**, *86*, 1558–1564. <https://doi.org/10.1016/j.carbpol.2011.06.061>.
- (21) Zhu, Z.-S.; Qu, J.; Hao, S.-M.; Han, S.; Jia, K.-L.; Yu, Z.-Z.  $\alpha$ -Fe<sub>2</sub>O<sub>3</sub> Nanodisk/Bacterial Cellulose Hybrid Membranes as High-Performance Sulfate-Radical-Based Visible Light Photocatalysts under Stirring/Flowing States. *ACS Appl. Mater. Interfaces* **2018**, *10* (36), 30670–30679. <https://doi.org/10.1021/acsami.8b10128>.
- (22) Luo, H.; Xiong, G.; Yang, Z.; Raman, S. R.; Si, H.; Wan, Y. A Novel Three-Dimensional Graphene/Bacterial Cellulose Nanocomposite Prepared by In Situ Biosynthesis. *RSC Adv.* **2014**, *4* (28), 14369–14372. <https://doi.org/10.1039/c4ra00318g>.
- (23) Abol-Fotouh, D.; Dörling, B.; Zapata-Arteaga, O.; Rodríguez-Martínez, X.; Gómez, A.; Reparaz, J. S.; Laromaine, A.; Roig, A.; Campoy-Quiles, M. Farming Thermoelectric Paper. *Energy Environ. Sci.* **2019**, *12*, 716–726. <https://doi.org/10.1039/c8ee03112f>.
- (24) Zmejkoski, D. Z.; Marković, Z. M.; Budimir, M. D.; Zdravković, N. M.; Trišić, D. D.; Bugárová, N.; Danko, M.; KozYROVSKA, N. O.; Špitalský, Z.; Kleinová, A.; et al. Photoactive and Antioxidant Nanochitosan Dots/Biocellulose Hydrogels for Wound Healing Treatment. *Mater. Sci. Eng. C* **2021**, *122*, 111925. <https://doi.org/10.1016/j.msec.2021.111925>.
- (25) Mashkour, M.; Moradabadi, Z.; Khazaeian, A. Physical and Tensile Properties of Epoxy Laminated Magnetic Bacterial Cellulose Nanocomposite Films. *J. Appl. Polym. Sci.* **2017**, *134*, 45118. <https://doi.org/10.1002/app.45118>.
- (26) Wei, H.; Rodriguez, K.; Renneckar, S.; Vikesland, P. J. Environmental Science and Engineering Applications of Nanocellulose-Based Nanocomposites. *Environ. Sci. Nano* **2014**, *1*, 302–316. <https://doi.org/10.1039/C4EN00059E>.

- (27) Hu, W.; Chen, S.; Yang, J.; Li, Z.; Wang, H. Functionalized Bacterial Cellulose Derivatives and Nanocomposites. *Carbohydr. Polym.* **2014**, *101* (1), 1043–1060. <https://doi.org/10.1016/j.carbpol.2013.09.102>.
- (28) Foresti, M. L.; Vázquez, A.; Boury, B. Applications of Bacterial Cellulose as Precursor of Carbon and Composites with Metal Oxide, Metal Sulfide and Metal Nanoparticles: A Review of Recent Advances. *Carbohydr. Polym.* **2017**, *157*, 447–467. <https://doi.org/10.1016/j.carbpol.2016.09.008>.
- (29) Thomas, B.; Raj, M. C.; Athira, B. K.; Rubiyah, H. M.; Joy, J.; Moores, A.; Drisko, G. L.; Sanchez, C. Nanocellulose, a Versatile Green Platform: From Biosources to Materials and Their Applications. *Chem. Rev.* **2018**, *118* (24), 11575–11625. <https://doi.org/10.1021/acs.chemrev.7b00627>.
- (30) Baghbzadeh, M.; Carbone, L.; Cozzoli, P. D.; Kappe, C. O. Microwave-Assisted Synthesis of Colloidal Inorganic Nanocrystals. *Angew. Chemie - Int. Ed.* **2011**, *50* (48), 11312–11359. <https://doi.org/10.1002/anie.201101274>.
- (31) Bilecka, I.; Elser, P.; Niederberger, M. Kinetic and Thermodynamic Aspects in the Microwave-Assisted Synthesis of ZnO Nanoparticles in Benzyl Alcohol. *ACS Nano* **2009**, *3* (2), 467–477. <https://doi.org/10.1021/nn800842b>.
- (32) Pascu, O.; Carenza, E.; Gich, M.; Estradé, S.; Peiró, F.; Herranz, G.; Roig, A. Surface Reactivity of Iron Oxide Nanoparticles by Microwave-Assisted Synthesis; Comparison with the Thermal Decomposition Route. *J. Phys. Chem. C* **2012**, *116* (28), 15108–15116. <https://doi.org/10.1021/jp303204d>.
- (33) Schütz, M. B.; Xiao, L.; Lehnen, T.; Fischer, T.; Mathur, S. Microwave-Assisted Synthesis of Nanocrystalline Binary and Ternary Metal Oxides. *Int. Mater. Rev.* **2018**, *63* (6), 341–374. <https://doi.org/10.1080/09506608.2017.1402158>.
- (34) De La Hoz, A.; Díaz-Ortiz, A.; Prieto, P. *Alternative Energy Sources for Green Chemistry - Chapter 1: Microwave-Assisted Green Organic Synthesis*; Stefanidis, G., Stankiewicz, A., Eds.; The Royal Society of Chemistry, **2016**. <https://doi.org/10.1039/9781782623632-00001>.
- (35) Pascu, O.; Carenza, E.; Gich, M.; Estradé, S.; Peiró, F.; Herranz, G.; Roig, A. Surface Reactivity of Iron Oxide Nanoparticles by Microwave-Assisted Synthesis; Comparison with the Thermal Decomposition Route. *J. Phys. Chem. C* **2012**, *116* (28), 15108–15116. <https://doi.org/10.1021/jp303204d>.
- (36) Carenza, E.; Barceló, V.; Moráncho, A.; Montaner, J.; Rosell, A.; Roig, A. Rapid Synthesis of Water-Dispersible Superparamagnetic Iron Oxide Nanoparticles by a Microwave-Assisted Route for Safe Labeling of Endothelial Progenitor Cells. *Acta Biomater.* **2014**, *10* (8), 3775–3785. <https://doi.org/10.1016/j.actbio.2014.04.010>.
- (37) Hachtel, J. A.; Yu, S.; Lupini, A. R.; Pantelides, S. T.; Gich, M.; Laromaine, A.; Roig, A. Gold Nanotriangles Decorated with Superparamagnetic Iron Oxide Nanoparticles: A Compositional and Microstructural Study. *Faraday Discuss.* **2016**, *191*, 215–227. <https://doi.org/10.1039/c6fd00028b>.
- (38) Gonzalez-Moragas, L.; Yu, S.-M.; Murillo-Cremaes, N.; Laromaine, A.; Roig, A. Scale-up Synthesis of Iron Oxide Nanoparticles by Microwave-Assisted Thermal Decomposition. *Chem. Eng. J.* **2015**, *281*, 87–95. <https://doi.org/10.1016/j.cej.2015.06.066>.
- (39) May-Masnou, A.; Soler, L.; Torras, M.; Salles, P.; Llorca, J.; Roig, A. Fast and Simple Microwave Synthesis of TiO<sub>2</sub>/Au Nanoparticles for Gas-Phase Photocatalytic Hydrogen Generation. *Front. Chem.* **2018**, *6* (110), 1–13. <https://doi.org/10.3389/fchem.2018.00110>.

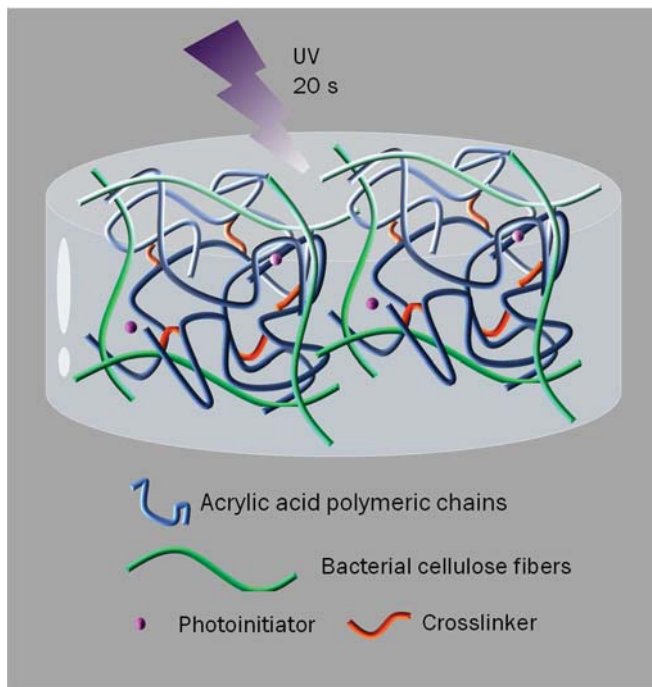
- 
- (40) Torras, M.; Roig, A. From Silver Plates to Spherical Nanoparticles: Snapshots of Microwave-Assisted Polyol Synthesis. *ACS Omega* **2020**, *5* (11), 5731–5738. <https://doi.org/10.1021/acsomega.9b03748>.
- (41) Zeng, M.; Laromaine, A.; Feng, W.; Levkin, P. A.; Roig, A. Origami Magnetic Cellulose: Controlled Magnetic Fraction and Patterning of Flexible Bacterial Cellulose. *J. Mater. Chem. C* **2014**, *2* (31), 6312–6318. <https://doi.org/10.1039/C4TC00787E>.
- (42) Hoppe, C. E.; Lazzari, M.; Pardiñas-Blanco, I.; López-Quintela, M. A. One-Step Synthesis of Gold and Silver Hydrosols Using Poly(N-Vinyl-2-Pyrrolidone) as a Reducing Agent. *Langmuir* **2006**, *22* (16), 7027–7034. <https://doi.org/10.1021/la060885d>.
- (43) Jeon, S.-H.; Xu, P.; Mack, N. H.; Chiang, L. Y.; Brown, L.; Wang, H.-L. Understanding and Controlled Growth of Silver Nanoparticles Using Oxidized N-Methyl-Pyrrolidone as a Reducing Agent. *J. Phys. Chem. C* **2010**, *114* (1), 36–40. <https://doi.org/10.1021/jp907757u>.
- (44) Niederberger, M.; Garnweitner, G. Organic Reaction Pathways in the Nonaqueous Synthesis of Metal Oxide Nanoparticles. *Chem.-A Eur. J.* **2006**, *12*, 7282–7302. <https://doi.org/10.1002/chem.200600313>.
- (45) Sashuk, V.; Rogaczewski, K. A Halogen-Free Synthesis of Gold Nanoparticles Using Gold(III) Oxide. *J. Nanoparticle Res.* **2016**, *18*, 261. <https://doi.org/10.1007/s11051-016-3576-x>.
- (46) Maneerung, T.; Tokura, S.; Rujiravanit, R. Impregnation of Silver Nanoparticles into Bacterial Cellulose for Antimicrobial Wound Dressing. *Carbohydr. Polym.* **2008**, *72* (1), 43–51. <https://doi.org/10.1016/j.carbpol.2007.07.025>.
- (47) Venkatesham, M.; Ayodhya, D.; Madhusudhan, A.; Veera Babu, N.; Veerabhadram, G. A Novel Green One-Step Synthesis of Silver Nanoparticles Using Chitosan: Catalytic Activity and Antimicrobial Studies. *Appl. Nanosci.* **2014**, *4*, 113–119. <https://doi.org/10.1007/s13204-012-0180-y>.
- (48) He, Y. Q.; Liu, S. P.; Kong, L.; Liu, Z. F. A Study on the Sizes and Concentrations of Gold Nanoparticles by Spectra of Absorption, Resonance Rayleigh Scattering and Resonance Non-Linear Scattering. *Spectrochim. Acta - Part A* **2005**, *61*, 2861–2866. <https://doi.org/10.1016/j.saa.2004.10.035>.
- (49) Jain, P. K.; Lee, K. S.; El-Sayed, I. H.; El-Sayed, M. A. Calculated Absorption and Scattering Properties of Gold Nanoparticles of Different Size, Shape, and Composition: Applications in Biological Imaging and Biomedicine. *J. Phys. Chem. B* **2006**, *110* (14), 7238–7248. <https://doi.org/10.1021/jp057170o>.
- (50) Dvoranová, D.; Brezová, V.; Mazúr, M.; Malati, M. A. Investigations of Metal-Doped Titanium Dioxide Photocatalysts. *Appl. Catal. B Environ.* **2002**, *37* (2), 91–105. [https://doi.org/10.1016/S0926-3373\(01\)00335-6](https://doi.org/10.1016/S0926-3373(01)00335-6).
- (51) Luo, Y.; Huang, J. Hierarchical-Structured Anatase-Titania/Cellulose Composite Sheet with High Photocatalytic Performance and Antibacterial Activity. *Chem. - A Eur. J.* **2015**, *21* (6), 2568–2575. <https://doi.org/10.1002/chem.201405066>.
- (52) Anton-Sales, I.; Roig-Sanchez, S.; Sánchez-Guisado, M. J.; Laromaine, A.; Roig, A. Bacterial Nanocellulose and Titania Hybrids: Cytocompatible and Cryopreservable Cell Carriers. *ACS Biomater. Sci. Eng.* **2020**, *6*, 4893–4902. <https://doi.org/10.1021/acsbiomaterials.0c00492>.
- (53) Schaffner, M.; Rühs, P. A.; Coulter, F.; Kilcher, S.; Studart, A. R. 3D Printing of Bacteria into Functional Complex Materials. *Sci. Adv.* **2017**, *3* (12). <https://doi.org/10.1126/sciadv.aao6804>.
- (54) Yu, J.; Huang, T. R.; Lim, Z. H.; Luo, R.; Pasula, R. R.; Liao, L. De; Lim, S.; Chen, C. H. Production of Hollow Bacterial Cellulose Microspheres Using Microfluidics to Form an

- Injectable Porous Scaffold for Wound Healing. *Adv. Healthc. Mater.* **2016**, *5* (23), 2983–2992. <https://doi.org/10.1002/adhm.201600898>.
- (55) Amin, M. C. I. M.; Abadi, A. G.; Katas, H. Purification, Characterization and Comparative Studies of Spray-Dried Bacterial Cellulose Microparticles. *Carbohydr. Polym.* **2014**, *99*, 180–189. <https://doi.org/10.1016/j.carbpol.2013.08.041>.
- (56) Laromaine, A.; Tronser, T.; Pini, I.; Parets, S.; Levkin, P. A.; Roig, A. Free-Standing Three-Dimensional Hollow Bacterial Cellulose Structures with Controlled Geometry via Patterned Superhydrophobic-Hydrophilic Surfaces. *Soft Matter* **2018**, *14*, 3955–3962. <https://doi.org/10.1039/c8sm00112j>.
- (57) Chen, M.; Kang, H.; Gong, Y.; Guo, J.; Zhang, H.; Liu, R. Bacterial Cellulose Supported Gold Nanoparticles with Excellent Catalytic Properties. *ACS Appl. Mater. Interfaces* **2015**, *7*, 21717–21726. <https://doi.org/10.1021/acsami.5b07150>.
- (58) Wang, Q.; Tian, D.; Hu, J.; Huang, M.; Shen, F.; Zeng, Y.; Yang, G.; Zhang, Y.; He, J. Harvesting Bacterial Cellulose from Kitchen Waste to Prepare Superhydrophobic Aerogel for Recovering Waste Cooking Oil toward a Closed-Loop Biorefinery. *ACS Sustain. Chem. Eng.* **2020**, *8* (35), 13400–13407. <https://doi.org/10.1021/acssuschemeng.0c04212>.
- (59) Zhao, L.; Jiang, D.; Cai, Y.; Ji, X.; Xie, R.; Yang, W. Tuning the Size of Gold Nanoparticles in the Citrate Reduction by Chloride Ions. *Nanoscale* **2012**, *4* (16), 5071–5076. <https://doi.org/10.1039/c2nr30957b>.



# Chapter 5

## Bacterial cellulose nanofibers to reinforce photocurable polyacrylic acid hydrogels







## CHAPTER SUMMARY

Chapter 5 reports on the combination of BC nanofibers with a synthetic polymer such as polyacrylic acid to create double network hydrogels by UV-photopolymerization with enhanced mechanical properties and lower swellability upon pH changes with potential use in tissue engineering applications.

## CHAPTER INDEX

CHAPTER SUMMARY .....	129 -
5.1 Hydrogels for tissue engineering .....	131 -
5.1.1 Bacterial cellulose double network hydrogels .....	135 -
5.2 Bacterial cellulose nanofibers/polyacrylic acid hydrogel synthesis.....	137 -
5.3 Bacterial cellulose nanofibers/polyacrylic acid double network hydrogel characterization .....	139 -
5.3.1 Unconfined mechanical compression characterization.....	140 -
5.3.2 Scanning electron microscopy analysis .....	145 -
5.3.3 Water absorption capacity.....	147 -
5.3.4 Freeze-thawing robustness.....	149 -
5.4 Functionalized bacterial cellulose nanofibers/polyacrylic acid hydrogel ....	149 -
5.5 Conclusions.....	150 -
5.6 References.....	152 -



## 5.1 Hydrogels for tissue engineering

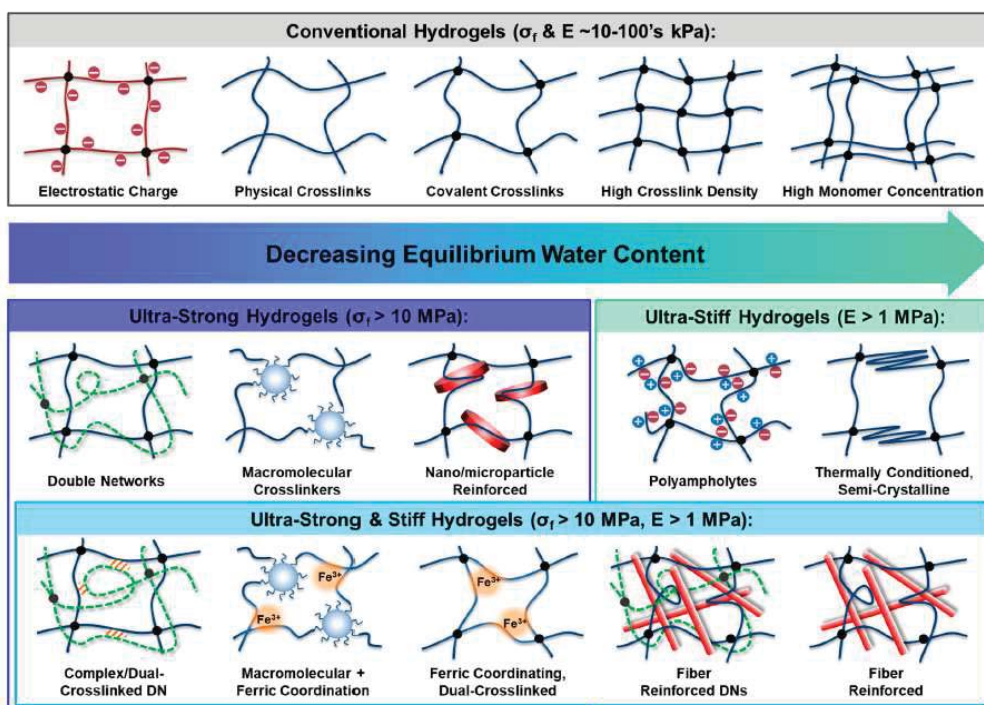
Tissue engineering seeks new materials that can replace or restore damaged tissue, usually caused by aging, chronic diseases or acute trauma. In particular, bioengineering soft tissue replacements (such as skin, tendons, ligaments, cartilages or blood vessels) is extremely challenging owing to the high demanding characteristics of the materials which encompass biocompatibility - as they should behave as an extracellular matrix (ECM) helping the cells and nutrients to penetrate and grow -, durability, high wear resistance, low friction or precise tuning of the water to mimic the tissue water content. In addition, they should present tunable mechanical performance differentiated for each specific type of implant.<sup>1-3</sup> A table with general values for selected soft tissues is depicted in Table 1. As an example, blood vessel mechanical properties differ depending on their direction (arteries or veins), presenting elastic modulus values (E) ranging from 0.1-10 MPa and failure stress values ( $\sigma_f$ ) from 0.3-5 MPa.<sup>4</sup> On the other hand, articular cartilage is an anisotropic and highly heterogeneous tissue with limited self-repair properties. It is defined by the joint (location, age and thereof fatigue) and presents mechanical properties ranging from 1-170 MPa for elastic modulus and from 4-50 MPa for failure stress.<sup>5,6</sup>

**Table 1:** Soft tissue general mechanical properties range values comparison.<sup>7</sup>

Soft tissue	E	$\sigma_f$
Vascular tissue	100 kPa	1 MPa
Skin	100 kPa	10 MPa
Cartilage	1 MPa	10 MPa
Ligament	100 MPa	10 MPa

Among the tissue replacement materials reported, hydrogels are gathering attention as between 50 - 98% of their weight corresponds to trapped water within a porous polymeric 3D network, they can be cytocompatible and their physical properties are adjustable. Indeed, hydrogels have been suggested for vitreous humor, ligament,

adipose tissue, liver, muscle or blood vessel regeneration and replacement.<sup>8–12</sup> However, hydrogels often do not exhibit sufficient strength and stiffness. Thus, although different scaffolds for soft tissue replacements are already approved for medical use<sup>13</sup>, they are not fully optimized and huge efforts are still needed to properly accomplish the sought-after requirements.



**Figure 1:** Hydrogels classified by their polymerization mechanism, failure stress ( $\sigma_f$ ), elastic modulus (E) and equilibrium water content. Extracted from <sup>7</sup>.

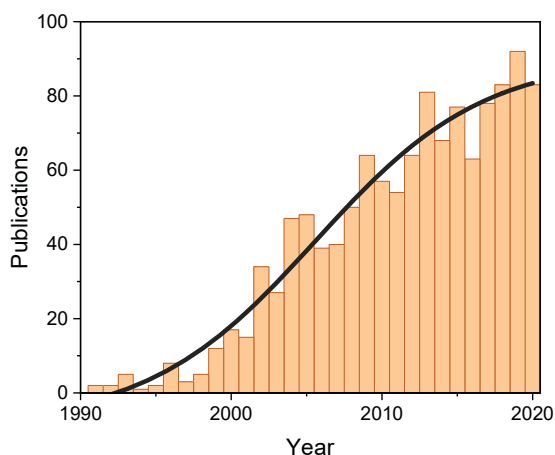
Hydrogels can be classified according to their polymerization mechanism or their properties. Conventional hydrogels are single network hydrogels obtained by physically or chemically cross-linking without fillers, presenting low elastic modulus and failure stress values. In general, the stiffness can be increased by increasing the cross-linking density at the expense of decreasing the water content. To enhance the mechanical properties of a hydrogel without compromising the water content capacity, different strategies such as nanoparticle and fiber reinforcements, interpenetrating networks, macromolecular cross-linkers or chemically graft of

molecules have been explored.<sup>14-19</sup> Figure 1 classifies several approaches to obtain hydrogels regarding stress failure, elastic modulus and water content. Within the family of multicomponent hydrogels, double network (DN) hydrogels which consist of two interpenetrating polymer networks are the best positioned to create strong scaffolds with high water content and modulable stiffness. For this DN approach, synthetic polymers are generally used as they allow better control of the chemical and physical properties of the final material; however, biocompatibility can be compromised. One strategy to surpass such difficulty is the addition of natural polymers such as alginate, chitosan or cellulose.

As mentioned before, hydrogels undergo a gelation process by cross-linking. This step can be triggered by a physical, ionic, enzymatic or chemical stimulus.<sup>20</sup> For example, physical cross-linking can be initiated by pH or temperature changes while ionic cross-linking is produced through electrostatic interactions when a charged polymer is mixed with a di- or tri-valent ion of opposite charge. On the other hand, chemical cross-linked hydrogels are more resistant to mechanical loads due to the covalent bond formation between the polymer chains. Photo-crosslinked hydrogels are included in this category. Photopolymerization is produced by the radical decomposition of a photoinitiator under exposure to visible or UV light and the interaction of the free radicals with the hydrogel precursor, forming the final material. As UV/visible light irradiation is a non-invasive technique that can be applied *in vivo*, photocurable hydrogels have been increasingly studied during the past few years as Figure 2 reflects. Among the possible polymers to be photosynthesized, the more commonly used are the acrylates family, *i.e.*, polyacrylic acid (PAA) and polyacrylamides (PAAm).

Acrylate systems are biocompatible pH-responsive polymers worth considering for soft tissue bioengineering as they are already being exploited in sensors and actuators,<sup>14,21</sup> separation systems,<sup>16,22,23</sup> adhesives<sup>24,25</sup>, wound dressings<sup>26,27</sup> or drug delivery systems<sup>18,28-30</sup>. By applying UV-light, acrylic monomers can be fast photopolymerized at room temperature while a crosslinking agent is usually added to

control the mechanical properties of the hydrogel.<sup>31,32</sup> The possibility to easily obtain UV-photocurable acrylate hydrogels increases their potential to customize their shapes and be used in 3D bioprinting inks.<sup>33</sup> Unfortunately, similar to other single network polyelectrolytes, acrylic acid hydrogels present weak mechanical properties and large dimensional changes when immersed in solutions with varying pH. Acrylic acid is a weak anionic polyelectrolyte and swells fast in basic solutions as a result of the electrostatic repulsions of the negatively charged polymer chains. This large swelling results in hydrogels with mechanical fragility and low tolerance to compression loads, compromising their use in patient-tailored printable implants. To control and enhance those properties, the field has witnessed an increasing number of PAA reinforced hydrogels<sup>34,35</sup> displaying interesting properties such as phase transition from rubbery to glassy in PAA/Ca-acetate hydrogels<sup>36</sup> or 3D printable PAA-graphene oxide-Ca<sup>2+</sup> biosensors<sup>37</sup>.



**Figure 2:** Published documents searching “photopolymerization hydrogel” keywords. Source: Scopus, March 2021.

Due to the compelling properties of BC (mechanical strength, biocompatibility, high water capacity and stability in water – some of them already seen in the previous chapters), and the appealing characteristics of the fast production of photocurable PAA hydrogels, seemed interesting to fabricate double network hydrogels comprising PAA and BC, which would be translated in hydrogels with enhanced

mechanical properties while keeping a high water content, enthralling for soft tissue implant.

### 5.1.1 Bacterial cellulose double network hydrogels

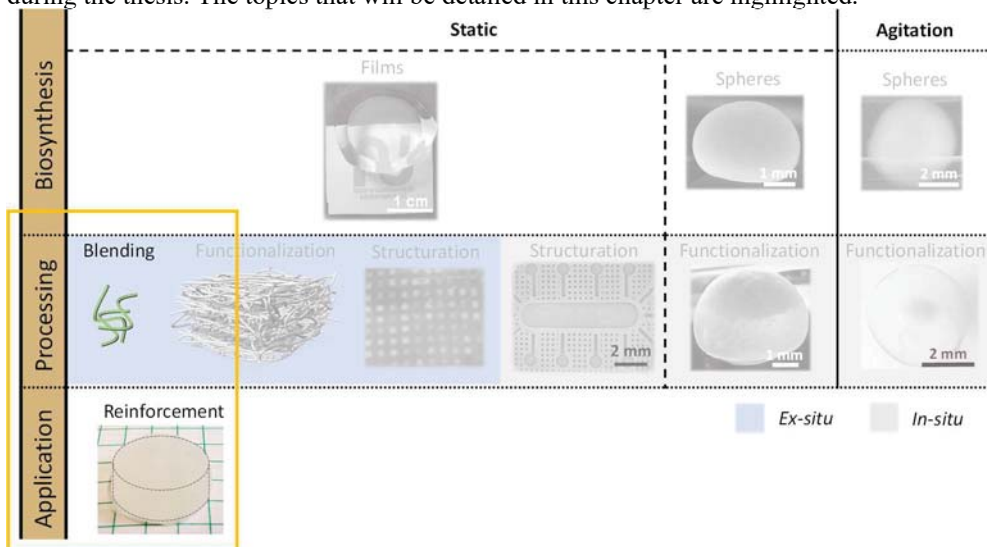
Double network (DN) hydrogels consist of two interpenetrating polymer networks with contrasting mechanical properties and different polymerization mechanisms. The first network is commonly charged, highly stretched and densely crosslinked, making the hydrogel stiff and brittle. The second network is neutral, flexible and sparsely cross-linked, making it soft and stretchable.<sup>38</sup> DN hydrogels are characterized by their high compressive failure stress, high strain and high water content with a low elastic modulus and they are commonly produced sequentially. First, a single network hydrogel is polymerized, then it is soaked in a solution that contains the precursor of the second network and a curing process forms the secondary network inside the pre-existing first network.

Gong *et al.* have pioneered the field of DN hydrogels<sup>39</sup> and also investigated DN systems using two bio-based polymers such as cellulose and gelatin, as well as mixtures of a bio-based polymer with a synthetic one.<sup>40-43</sup> Whereas in the first case deterioration of the properties was identified after body implantation, when bacterial cellulose (BC) was combined with polyacrylamides (PAAm) excellent mechanical properties in terms of tensile strength and good integration in the body were reported, which in this particular case was proposed as a ligament substitute.<sup>40,41</sup> BC/PAAm DN hydrogels were obtained by the interpenetrated polymerization of a PAAm network on a pristine BC film. The interwoven fibrous architecture of the BC film, besides the high-water uptake capability (approx. 90%w/w)<sup>44</sup>, provided flexibility and improved the mechanical properties of the hydrogel. However, the main drawback of this approach resided in the unfeasibility to produce 3D printable hydrogels, as the BC matrix was a continuous pellicle, and on the lengthy (*circa* ten days) synthetic steps needed for the hydrogel's processing. Other strategies using BC



fibers or powder have been reported, although specific and expensive equipment or long synthesis times were also needed.<sup>45–48</sup>

**Table 1:** Scheme of the biosynthesis, processing routes and BC materials described so far during the thesis. The topics that will be detailed in this chapter are highlighted.



Until now through the thesis, different shapes and sizes of BC were obtained. Those forms were functionalized and structured *in-situ* and *ex-situ* (*i.e.*, before and after the biosynthesis), giving special attention to self-standing films and spheres and their potential applications. In this chapter, the focus will be given to the BC nanofibers (BCf) resulting from the mechanical blending of BC films (Table 1). BCf can expand the applications of BC as they can be integrated into other materials as a reinforcement to enhance or modify the final attributes. In particular, the fabrication and characterization of a photocurable DN hydrogel composed of PAA and bacterial cellulose nanofibers (BCf) as the secondary network will be presented. This work was performed during my stay at the Hebrew University of Jerusalem (HUJI), under the guidance of *Prof. Shlomo Magdassi and in collaboration with his research group.* The use of fibers instead of the native pellicle allowed to create in just one synthetic step hydrogels with the desired shape, avoiding extra sequential polymerization steps. Besides, the photopolymerization of PAA by UV-light enabled the obtention of hydrogels in few seconds with economical affordable techniques and evading long-

time synthesis. In addition, the change of properties when BCf are added towards potential applications as implants for tissue replacement would be described.

## **5.2 Bacterial cellulose nanofibers/polyacrylic acid hydrogel synthesis**

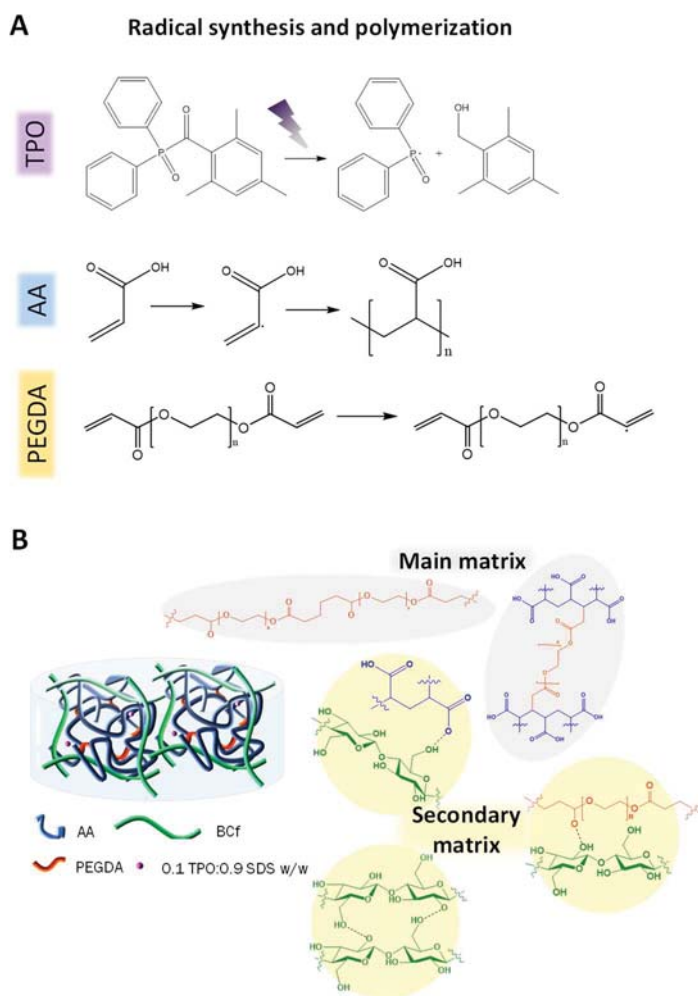
To prepare the hydrogels a photoinitiator sensitive to UV light was needed. Therefore, the preparation of the precursor hydrogel solution was performed in vials covered with aluminum foil. BCf were dispersed in water, then acrylic acid monomers (AA), poly(ethylene glycol) diacrylate (PEGDA) as crosslinker and diphenyl(2,4,6-trimethylbenzoyl) phosphine oxide (TPO) particles as photoinitiator were added in that order with stirring between additions. Before utilization, TPO was coated with sodium dodecyl sulfate (SDS) surfactant in a proportion 1:9 w/w TPO:SDS to increase TPO solubility in water.

Photocurable hydrogels require all the constituents to be water-compatible.<sup>49</sup> However, photoinitiator compounds are usually low water-soluble, leading to high concentrations inside the hydrogel and low polymerization rates. TPO was chosen in this study as it is highly efficient, commercially available and our collaborators had previous experience in successfully coating it with a biocompatible surfactant (SDS) to increase its solubility and to facilitate the fabrication of PAA hydrogels with high water content (60 wt%) without affecting the polymerization efficiency.<sup>50</sup> In addition, although potential cytotoxicity from the use of photoinitiators in biomaterials production is still under discussion,<sup>51,52</sup> a cell viability above 93% was computed for hydrogels with the SDS coated TPO photoinitiator at concentrations up to 0.1 wt%.<sup>32</sup> For this study, a lower amount of photoinitiator was used (0.03 wt%) and demonstrated to be sufficient to fully polymerized the hydrogel. A UV LED source ( $\lambda=395\text{nm}$ , Integration Technology Limited) with a time of exposure of 20 s was employed for polymerization. BCf/PAA cylindrical hydrogels of 20 mm diameter and 5 mm height, and with varying BCf content, were made in just one step at room temperature by pouring 2 mL of the precursor solution into a silicon mold and applying the UV radiation. Table 3 shows the weight proportions of the systems

studied, where BCf percentage is given for dry weight. For a proper comparison, the solid content was maintained in all systems.

**Table 3:** Weight percentages of the systems studied.

System (%wt)	AA	PEGDA	0.1 TPO:0.9 SDS	BCf	Water
x% BCf/PAA	41.20-41.70	2.20	0.03	0.00-0.50	56.00



**Figure 3:** A) Initial polymerization reactions of the synthetic polymers for the production of BCf/PAA DN hydrogel. B) Schematic illustration of photo-curable BCf/PAA hydrogel and its molecular interactions. The main synthetic matrix (PAA) is cross-linked with PEGDA chains and interpenetrated with BCf. The chain-chain and chain-matrix interactions (grey highlighted), hydrogen bonding (yellow highlighted) and BCf network entanglement contribute to improving the toughness of the hydrogel.

Figures 3 schematize our hypothesis of the polymerization mechanism upon UV radiation. The radicals from the water-compatible TPO<sup>53</sup> opened the double bonds of the acrylic acid monomers and PEGDA molecules, starting the polymerization. While polymerizing, the synthetic polymeric chains would covalently bond through matrix-chain (PAA-PEGDA) and chain-chain (PEGDA-PEGDA) interactions (highlighted in grey in Figure 3B) creating a permanently crosslinked main network.<sup>54,55</sup> Simultaneously, the long BCf would form an interpenetrated secondary crosslinked network entrapping the synthetic polymeric chains and interacting with them and with the other BCf through hydrogen bonds (interactions highlighted in yellow in Figure 3B) forming a DN hydrogel with tougher properties than the single network counterpart.

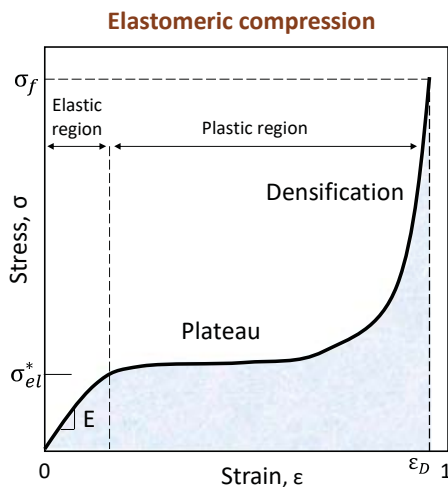
### **5.3 Bacterial cellulose nanofibers/polyacrylic acid double network hydrogel characterization**

To prove our hypothesis, BCf/PAA hydrogels with different BCf concentrations were mechanically evaluated and their swelling capacity was tested. Besides, a comparison with hydrogels containing PAA only, or PAA with another cellulose source as cellulose nanocrystals (CNC) was performed. If needed, additional material description and technical details can be found in Annex I at the end of the thesis.

The first step was to qualitative study the maximum load of BCf to the precursor solution which enabled an ink rheologically compatible with printing techniques as it would open new processing opportunities for the BCF/PAA hydrogels in 3D printing. Up to a 0.5 wt% BCf content, the solution was homogeneous, easy to manipulate and not too viscous. For 0.75 wt% addition, the fibers started to aggregate and the solution was no longer homogeneous, it was more viscous and harder to be extruded. When 1 wt% BCf was used, the solution became a paste unable to be extruded through a pipette. From this, we concluded that BCf concentrations higher than 0.5 wt% would not be suitable for future 3D printing applications and therefore were not further addressed in the study.

### 5.3.1 Unconfined mechanical compression characterization

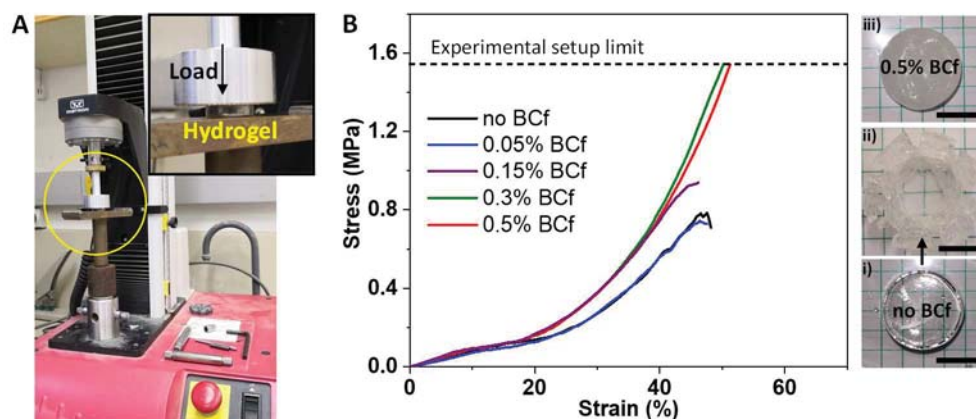
To study the mechanical properties of a hydrogel, different mechanical tests can be performed such as tensile, compression or torsion. In this chapter, unconfined compression was measured. This mechanical test gives the maximum axial compressive stress that a hydrogel can withstand under zero confining stress, which can be considered the worst compression scenario a hydrogel can be subjected to. When plotting stress-strain curves, the mechanical behavior of a hydrogel can be classified as elastomeric, plastic or brittle.<sup>56</sup> Figure 4 shows a representative elastomeric strain-stress curve like the one expected for soft tissues under compression. Two regimes can be distinguished: the elastic and plastic regions. The elastic region is described as the regime where the material can return to its original shape after the load is applied and is delimited by the yield point ( $\sigma_{el}^*$ ). The Young modulus (E) can be calculated by the slope of this region. Above this point, the hydrogel starts to deform (plastic region). This region can be split into: i) the plateau area where large deformation occurs at constant stress and ii) the densification area where further deformation compresses the hydrogel steeply rising the stress until the failure point ( $\sigma_f$ ). The area below the curve (in blue) is the toughness and represents how a hydrogel can absorb energy and deform before cracks appear.



**Figure 4:** Elastomeric compression curve adapted from <sup>56</sup>.

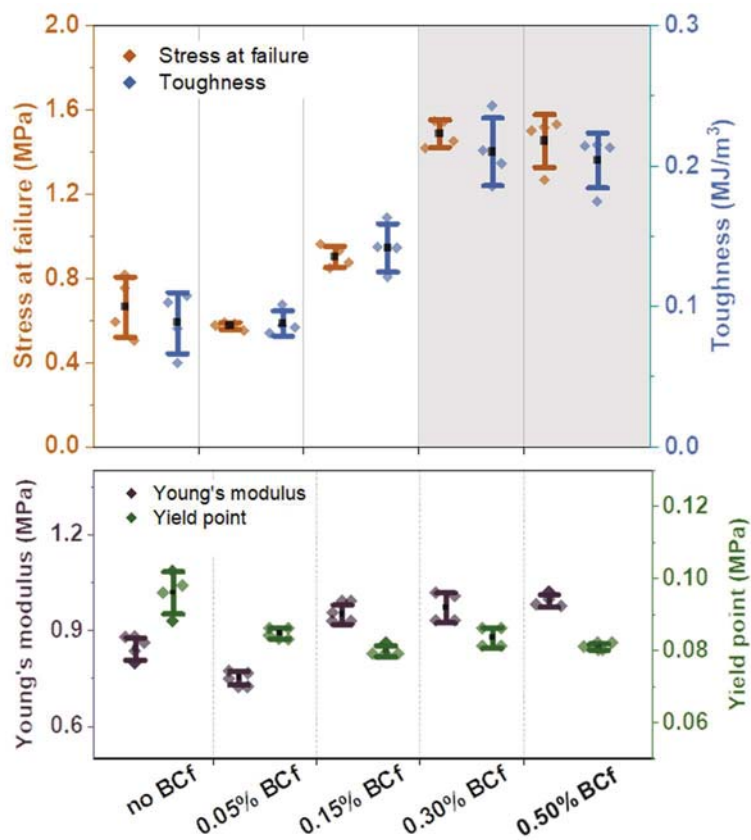
Hydrogels with concentrations of BCf ranging from 0.05 to 0.5 wt% were mechanically evaluated. For each system, 4 samples were measured under unconfined compression parameters right after the polymerization to avoid water evaporation. The test was performed with an Instron 3345 press equipped with a 500 N load cell and at a speed of 1 mm/min. As displayed in Figure 5A, the hydrogels were placed in a metal base and load was applied until fracture or until the load limit was reached, then strain-stress curves were obtained. Young's modulus was calculated in the strain range from 0 – 10 %.

All samples studied underwent an elastomeric compression. Figure 5B depicts the representative strain-stress curves obtained where a linear elastic region till approx. 10% of strain is appreciated. The elastic region was followed by a plastic deformation till break or till reaching the maximum limit of the experimental load-cell. Hydrogels without BCf or with a BCf load  $\leq 0.15$  wt% presented low compressive stress at failure values (0.6-0.9 MPa) and strain values ranging between 41-44%, characteristics of fragile materials. Additional evidence of the brittleness was seen in the discontinuity of the stress-strain curves, which could be attributable to small fractures development during the measurement before the final failure of the sample. On the other hand, continuous smooth curves were obtained for samples over 0.15 wt% BCf, where the final fracture point was not observed as the experimental stress setup limit was reached. Thus, BCf/PAA hydrogels with BCf  $\geq 0.3$  wt% withstood higher compressive stresses before failure than PAA hydrogels, which indicates the stiffening of the material as the BCf load increases, behaving as a DN. Another validation that the BCf/PAA hydrogels with 0.5 wt% BCf were less fragile is illustrated in the image panels. PAA hydrogel shattered during the compression loading cycle (sample before loading cycle is depicted in panel i while the same sample after the loading cycle is depicted in panel ii) whereas BCf/PAA hydrogel with 0.5 wt% BCf endures the applied load (panel iii). Note also that the addition of BCf produced a reduction of the hydrogel transparency towards a more whitish and translucent appearance.



**Figure 7:** A) Unconfined compression set-up. B) Representative compression strain-stress curves of the different DN hydrogels with increasing BCf content (n=4). Right panels: Transparent pristine PAA hydrogel i) before and ii) after the compression load. iii) Translucent BCF/PAA DN hydrogel with 0.5 wt% BCf. Scale bar: 1 cm.

A detailed comparison of the mechanical characteristics of the various systems is depicted in Figure 8. Higher values of stress and toughness were observed as the concentration of BCf increases. Values of BCf 0.3 wt% and 0.5 wt% systems are depicted with darker backgrounds indicating that they were obtained when the test finished and not at the hydrogel failure. In comparison, Young's modulus and yield point values were maintained constant. Results indicated that the addition of bacterial cellulose hardened the material without affecting the elasticity of the hydrogel which could be explained if a double network system was created. While the main PAA network, higher crosslinker, dissipated the stress through fractures, the ductile BCf second network remained intact keeping the elastic moduli in the sub-MPa range. Moreover, the values obtained for  $\geq 0.3\%$  BCf/PAA hydrogels were adequate for the mechanical requirements needed for vascular (elastic modulus: 0.1-10 MPa and failure stress: 0.3-5 MPa) and cartilage (elastic modulus: 1-170 MPa and failure stress: 4-50 MPa) replacements. However, further studies reducing the size sample or increasing the load cell would be necessary to fully acquire the strain-stress curves of the systems with higher BCf loadings.



**Figure 8:** Stress, toughness, Young's modulus and yield point comparative study vs. BCf content for the casted hydrogels. Grey background values represent that the measurement finished at the experimental set-up limit.

To continue our validation of the DN polymer formation hypothesis, BCf was replaced with the same concentration, 0.5 %wt, of cellulose nanocrystals (CNC, Celluforce) and their mechanical performance was compared. Detailed weight percentages are presented in Table 4. Both materials were cellulose-based, highly crystalline and presented comparable nanometre cross-sections (BCf with a diameter of  $9 \pm 2$  nm and CNC with  $\sim 4$  nm<sup>57</sup>). However, while CNC was approximately 200 nm in length, BCf length was around several hundred microns, a difference of three orders of magnitude.

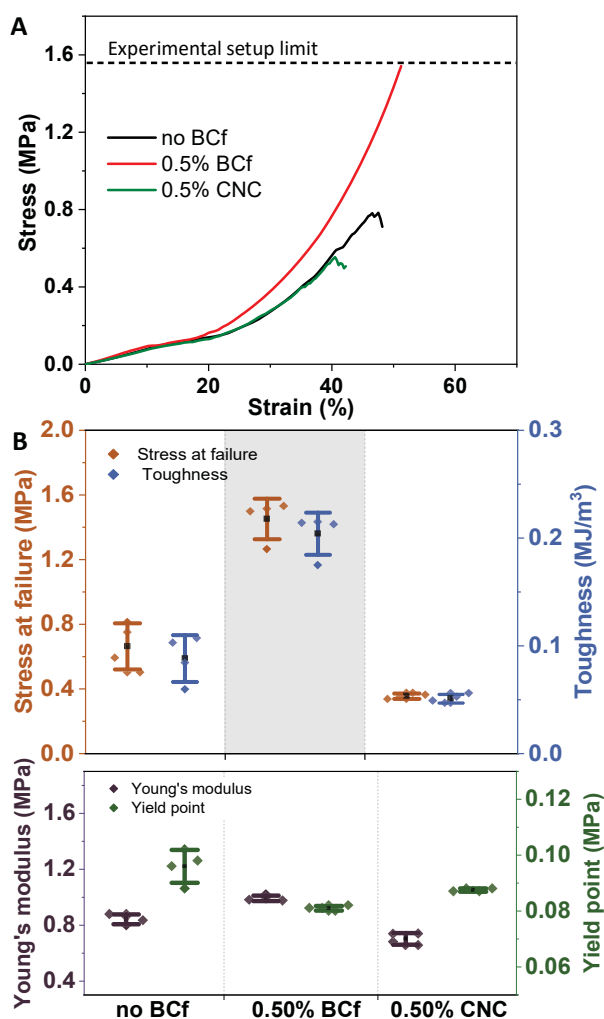


**Table 4:** Weight percentages of the systems used for this section of the study.

System (% wt)	AA	PEGDA	0.1 TPO:0.9 SDS	BCf	CNC	Water
0.5% BCf/PAA	41.20	2.20	0.03	0.50	0.00	56.00
0.5% CNC/PAA	41.20	2.20	0.03	0.00	0.50	56.00

A similar trend, depicted in Figure 9, between 0.5 wt% CNC/PAA hydrogel and without cellulose filler addition was observed. This similarity could be seen in both elastic and plastic regions on the stress-strain curves, indicating similar Young's modulus, yield point and even similar failure properties. Even so, it is important to emphasize that CNC samples failed at lower stresses and presented lower toughness values, indicating an even more fragile nature of those hydrogels. In comparison, 0.5 %wt BCf/PAA stress and toughness values were four-fold higher: from  $0.35 \pm 0.02$  MPa for CNC/PAA to  $1.5 \pm 0.1$  MPa for BCf/PAA in stress and from  $0.051 \pm 0.004$  MJ/m<sup>3</sup> for CNC/PAA to  $0.20 \pm 0.02$  MJ/m<sup>3</sup> for BCf/PAA in toughness. Besides, this ratio would be even higher since the BCf hydrogel test did not finish at failure. In both systems, the linear elastic region was preserved, with an almost constant Young's modulus and yield point values.

Thus, the addition of CNC did not change the elasticity of the PAA system although fragilizes the hydrogel. The obtained results pointed out that the stiffening of the material when BCf was added was related to the morphology of the fibers, whose length made it possible to create a secondary network inside the synthetic polymer. Similar behavior was already observed by Xu *et al.* when plant-derived CNC and cellulose nanofibrils (CNF) properties were compared.<sup>58</sup> This conduct was also coherent with the gelling and stabilizer properties observed for bacterial cellulose<sup>59,60</sup> while CNC is usually applied as a dispersant.<sup>61</sup> It could be assumed then, that the DN consisted of PAA as the dominant mechanism for the linear region, while BCf governs the plastic region.

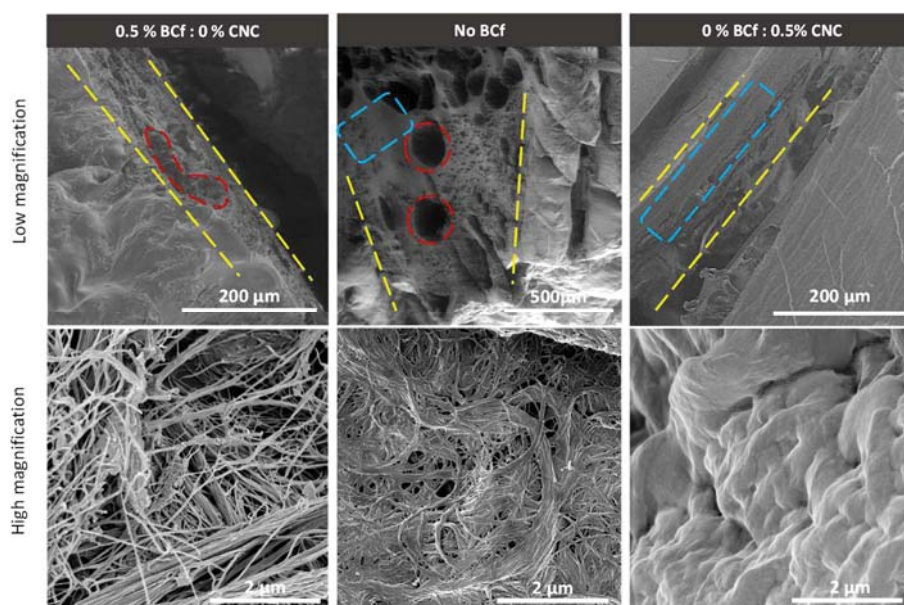


**Figure 9:** A) Representative strain-stress curves from compression tests of systems with different nanocellulose derivatives (n=4). B) Stress, toughness, Young's modulus and yield point comparative study vs. nanocellulose source. Grey background values represent the values obtained at the experimental set-up limit.

### 5.3.2 Scanning electron microscopy analysis

To analyze the morphologic differences of the hydrogels with different nanocellulose sources, an SEM study on supercritically dried (SCD) hydrogels was performed. After polymerization, samples were transformed into alcogels through a gradual water-to-ethanol solvent exchange, then they were placed inside a 300 mL autoclave filled with ethanol and the supercritical drying took place. As the samples were

thicker than the BC films we worked with in previous chapters, longer times were applied to assure complete drying. The autoclave was pressurized at 100 bars at room temperature and liquid CO<sub>2</sub> was dispensed for 2 h with a flow of 1 kg/h. The reactor was then heated to 45 °C to reach supercritical conditions and supercritical CO<sub>2</sub> was pumped for another 2 h at the same flow rate. SC dried hydrogels were cut with a PTFE coated blade and the cross-sections were analyzed. Low magnification hydrogel images were acquired under low vacuum conditions while a 5 nm Pt coating and high vacuum were used to obtain high magnification images.



**Figure 10:** SEM cross-section and close-up images where the fibrous structures are clearly seen. From left to right: 0.5 wt% BCF/PAA hydrogel, pristine PAA hydrogel (no BCF) and 0.5 wt% CNC/PAA. Yellow dashed lines delimited the hydrogel cross-section, red dashed lines remark big pores location and blue dashed lines highlight smooth areas.

Figure 10 depicts the cross-section of the hydrogels which is delimited by yellow dotted lines in the low magnification images. The PAA system (no BCF) showed a hierarchical porous structure with some large pores (highlighted in red) and smoother areas (highlighted in blue) in which pores were hardly seen. This initial structure became spongier, more homogeneous and without observable smooth areas when BCF was added (left panel), although some big pores were still appreciable. In contrast, the porosity was dramatically decreased with the addition of CNC (right

panel), where larger smooth areas were observed. For higher magnification images was noticeable that BCf/PAA showed less fiber densification than PAA hydrogel whereas CNC/PAA presented a bumpy smooth surface where the fibers were not visible. It could be concluded that the addition of BCf conferred to the PAA hydrogel a higher entangled nanofiber network avoiding fiber compaction, which is translated into a toughness improvement, and that the appearance of smoother areas, like the one observed for CNC/PAA, fragilized the hydrogel.

### 5.3.3 Water absorption capacity

As already mentioned, one of the main drawbacks of the implantation of PAA hydrogels as soft tissue replacements is the large dimensional expansion they suffer when immersed in basic pH solutions, with the corresponding deterioration of the mechanical performance. Therefore, the swelling capacity of 0.5%BCf/PAA was analyzed and compared with 0.5%CNC/PAA hydrogels. In addition, ring-shaped gels were cast for this study as a first step towards more intricate shapes needed as implants. Interestingly, PAA hydrogel samples were very fragile and broke under manipulation and therefore, was not possible to perform the swelling test on those systems. To study the swelling response of the systems at different pH conditions, the water absorption capacity (WAC) was measured. The hydrogels were immersed in distilled water at pH values ranging from 4 to 10 for 24 h at room temperature and WAC was calculated as follows:

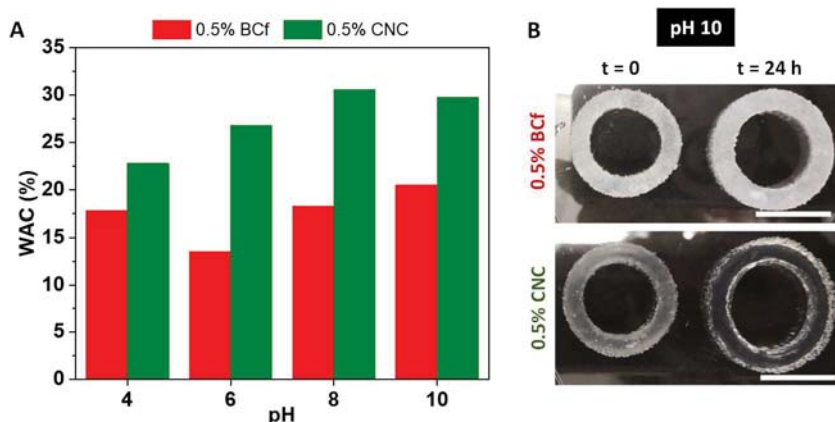
$$\text{WAC (\%)} = \frac{(W_s - W_0)}{W_0} \cdot 100$$

Where  $W_0$  is the mass of the hydrogel right after the polymerization and  $W_s$  is the mass of the hydrogel after 24 h in solution.

The obtained values are depicted in Figure 11A. The behavior for CNC/PAA was similar to the one expected for PAA hydrogels<sup>62</sup> (*i.e.*, the size increased when basic

solutions were used) since, at basic pHs, the carboxylic groups of the polymeric matrix deprotonate and repulsive electrostatic interactions force the hydrogel to swell. In contrast, BCf/PAA WAC values remained almost constant at all the pH studied, indicating that BCf inhibited the expected increase of WAC. The swelling dimensional change could be also macroscopically appreciated, as depicted in Figure 11B, where images of the 0.5%BCf/PAA and 0.5%CNC/PAA hydrogels as-prepared ( $t = 0$ ) and after being immersed in water for 24 h at pH 10 are shown. 0.5%BCf/PAA hydrogel presented a smaller dimensional change (less swelling) with a WAC value of  $\leq 20\%$  for all the conditions tested, while when CNC was added the swelling capacity increases 1.5-fold at basic pH values.

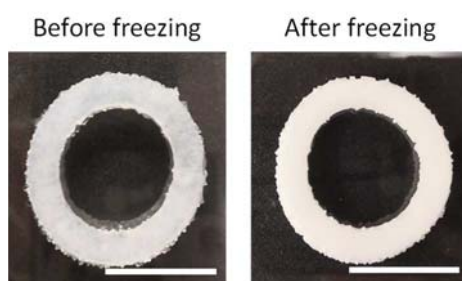
The lower swelling capacity of the 0.5%BCf/PAA system is compatible with a DN hydrogel configuration, where the presence of a secondary network reduces the expansion of the PAA chains. In addition, the pH non-response of BCf/PAA hydrogels would restrict the possible mechanical variations derived from swelling which often are seen in acrylate systems and, therefore, would allow their implementation as biocompatible implants with a more robust mechanical performance.



**Figure 11:** Left: WAC values of 0.5%BCf/PAA and 0.5%CNC/PAA hydrogels at different pH solution conditions. Right: 0.5%BCf/PAA and 0.5%CNC/PAA ring-shaped hydrogel images before and after undergoing the swelling test at pH 10. Scale bars: 2 cm.

### 5.3.4 Freeze-thawing robustness

Finally, the hydrogels were frozen in liquid nitrogen and thaw at room temperature for two cycles to study the sturdiness of the materials. Figure 12 depicts a 0.5%BCF/PAA hydrogel before and after a cycle respectively. All hydrogels could stand the two defrosting cycles without macroscopic structural changes, showing their robustness and making them suitable for storage in cryogenic conditions which would be a valuable advantage when combining them with cells.



**Figure 12:** System with 0.5 wt% BCf before freezing and after freezing. Scale bar: 2 cm.

### 5.4 Functionalized bacterial cellulose nanofibers/polyacrylic acid hydrogel

To further expand the applications of BCf/PAA hydrogels, systems with nanocomposites BCf were prepared. Being able to functionalize biocompatible hydrogels with nanoparticles is compelling as it can broaden the application of these materials in the biomedical field. However, the degradation of the hydrogel and the corresponding leaching of the NPs to the biological system is still under concern as they can accumulate inside the body producing local toxicity. By MW-assisted synthesis, we demonstrated in Chapter 4 that BCf with magnetic NPs firmly anchored can be obtained. Therefore, functionalized BCf/PAA hydrogels were fabricated using them. The synthesis was maintained, still, as SPIONs absorb radiation, higher irradiation exposure and lower BCf concentrations were needed to obtain a hydrogel as the one presented in Figure 13. However, the hydrogel presented was a first attempt and further investigation would be needed regarding their mechanical properties,

---

biocompatibility and synthesis optimization. Nevertheless, the method described here paves the way to achieve functionalized photocurable PAA with BCf.



**Figure 13:** Photocurable BCf/PAA hydrogel with BCf decorated with SPIONs obtained after 2 min of UV irradiation.

## 5.5 Conclusions

In this chapter, the fabrication of BCf/PAA hydrogels was presented. The approach described a single-step synthesis based on the photopolymerization of acrylic acid monomers while BCf is added as a secondary network. The addition of BCf demonstrated to expand the stiffness and control the swellability of the fragile polyelectrolyte matrix. The double network hypothesis considered that the high surface area of the nanofibers, their micrometric length and their high content of hydroxyl groups are the characteristics that promote BCf as a secondary hydrogel network interacting with the polymeric PAA main matrix through hydrogen bonding and entrapping the synthetic polymer chains during the process.

This hypothesis was validated as BCf/PAA hydrogels with BCf loads of 0.3 and 0.5 %wt were found to be more resistant to cracks, show an increased stiffness and a low ( $\leq 20\%$ ) water absorption capacity compared to single PAA network hydrogels while keeping similar elastic properties (Young's modulus  $\sim 1$  MPa). Those characteristics corresponded to the formation of a DN; the addition of a secondary network (BCf) stiffens the hydrogel while maintaining the water holding capacity and its elastic moduli. Interestingly, the effects described were not observed when hydrogels with the same cellulose load fraction (0.5 wt%) but different cellulose sources (CNC vs

BCf) were compared, implying that in that case a DN was not formed. On the contrary, CNC/PAA hydrogels were fragile and pH-dependent when considering their swelling capacity. Finally, the BCf/PAA DN hydrogels stood several thaw cycles without structural macroscopic damage, which made them suitable for cryogenic storage conditions often used in biomedical settings.

However, stress and Young modulus obtained for BCf/PAA hydrogels with BCf load  $\geq 0.3$  %wt were not representative of the system failure and further studies would be needed with smaller samples or higher loads to properly analyze those systems. Despite that fact, the tendency of the value (stress at failure:  $1.5 \pm 0.1$  MPa, Young's modulus:  $0.99 \pm 0.02$  MPa), the robustness and non-pH-response with low WAC endorse them as good candidates for printable soft-tissue bioactive vascular or cartilage implants. Therefore, cell seeding tests should be undertaken in the future to assure their biocompatibility.

Finally, although very preliminary, the easy fabrication of NPs covalently attached to BCf through MW-assisted reaction used during this thesis demonstrated to be suitable for the production of functionalized PAA hydrogels in the future, as toxicity problems derived from the leaching of NPs to the biological system could be avoided.



---

## 5.6 References

- (1) Zhao, H.; Liu, M.; Zhang, Y.; Yin, J.; Pei, R. Nanocomposite Hydrogels for Tissue Engineering Applications. *Nanoscale* **2020**, *12* (28), 14976–14995. <https://doi.org/10.1039/d0nr03785k>.
- (2) Wei, W.; Dai, H. Articular Cartilage and Osteochondral Tissue Engineering Techniques: Recent Advances and Challenges. *Bioact. Mater.* **2021**, *6* (12), 4830–4855. <https://doi.org/10.1016/j.bioactmat.2021.05.011>.
- (3) Zheng, X.; Zhang, P.; Fu, Z.; Meng, S.; Dai, L.; Yang, H. Applications of Nanomaterials in Tissue Engineering. *RSC Adv.* **2021**, *11* (31), 19041. <https://doi.org/10.1039/d1ra01849c>.
- (4) Miramini, S.; Fegan, K. L.; Green, N. C.; Espino, D. M.; Zhang, L.; Thomas-Seale, L. E. J. The Status and Challenges of Replicating the Mechanical Properties of Connective Tissues Using Additive Manufacturing. *J. Mech. Behav. Biomed. Mater.* **2020**, *103*, 103544. <https://doi.org/10.1016/j.jmbbm.2019.103544>.
- (5) Wasyleczko, M.; Sikorska, W.; Chwojnowski, A. Review of Synthetic and Hybrid Scaffolds in Cartilage Tissue Engineering. *Membranes.* **2020**, *10* (11), 348. <https://doi.org/10.3390/membranes10110348>.
- (6) Riemenschneider, P. E.; Rose, M. D.; Giordani, M.; McNary, S. M. Compressive Fatigue and Endurance of Juvenile Bovine Articular Cartilage Explants. *J. Biomech.* **2019**, *95*, 109304. <https://doi.org/10.1016/j.jbiomech.2019.07.048>.
- (7) Means, A. K.; Grunlan, M. A. Modern Strategies to Achieve Tissue-Mimetic, Mechanically Robust Hydrogels. *ACS Macro Lett.* **2019**, *8* (6), 705–713. <https://doi.org/10.1021/acsmacrolett.9b00276>.
- (8) Fan, M.; Ma, Y.; Zhang, Z.; Mao, J.; Tan, H.; Hu, X. Biodegradable Hyaluronic Acid Hydrogels to Control Release of Dexamethasone through Aqueous Diels-Alder Chemistry for Adipose Tissue Engineering. *Mater. Sci. Eng. C* **2015**, *56*, 311–317. <https://doi.org/10.1016/j.msec.2015.04.004>.
- (9) Ye, S.; Boeter, J. W. B.; Penning, L. C.; Spee, B.; Schneeberger, K. Hydrogels for Liver Tissue Engineering. *Bioengineering* **2019**, *6* (3), 59. <https://doi.org/10.3390/bioengineering6030059>.
- (10) Boso, D.; Maghin, E.; Carraro, E.; Giagante, M.; Pavan, P.; Piccoli, M. Extracellular Matrix-Derived Hydrogels as Biomaterial for Different Skeletal Muscle Tissue Replacements. *Materials (Basel)*. **2020**, *13* (11), 2483. <https://doi.org/10.3390/ma13112483>.
- (11) Zhang, F.; King, M. W. Biodegradable Polymers as the Pivotal Player in the Design of Tissue Engineering Scaffolds. *Adv. Healthc. Mater.* **2020**, *9*, 1902358. <https://doi.org/10.1002/adhm.201901358>.
- (12) Lin, Q.; Lim, J. Y. C.; Xue, K.; Su, X.; Loh, X. J. Polymeric Hydrogels as a Vitreous Replacement Strategy in the Eye. *Biomaterials* **2021**, *268*, 120547. <https://doi.org/10.1016/j.biomaterials.2020.120547>.
- (13) Aswathy, S. H.; Narendrakumar, U.; Manjubala, I. Commercial Hydrogels for Biomedical Applications. *Heliyon* **2020**, *6* (4), e03719. <https://doi.org/10.1016/j.heliyon.2020.e03719>.

- (14) Lu, F.; Wang, Y.; Wang, C.; Kuga, S.; Huang, Y.; Wu, M. Two-Dimensional Nanocellulose-Enhanced High-Strength, Self-Adhesive, and Strain-Sensitive Poly(Acrylic Acid) Hydrogels Fabricated by a Radical-Induced Strategy for a Skin Sensor. *ACS Sustain. Chem. Eng.* **2020**, *8* (8), 3427–3436. <https://doi.org/10.1021/acssuschemeng.9b07467>.
- (15) Fan, X.; Liu, H.; Wang, J.; Tang, K. Investigation of Double Network Hydrogel with Controllable Swelling Behavior by Response Surface Methodology. *J. Appl. Polym. Sci.* **2020**, *137* (24), 48805. <https://doi.org/10.1002/app.48805>.
- (16) Safavi-Mirmahalleh, S.-A.; Salami-Kalajahi, M.; Roghani-Mamaqani, H. Effect of Surface Chemistry and Content of Nanocrystalline Cellulose on Removal of Methylene Blue from Wastewater by Poly(Acrylic Acid)/Nanocrystalline Cellulose Nanocomposite Hydrogels. *Cellulose* **2019**, *26* (9), 5603–5619. <https://doi.org/10.1007/s10570-019-02490-1>.
- (17) Myung, D.; Waters, D.; Wiseman, M.; Duhamel, P.-E.; Noolandi, J.; Ta, C. N.; Frank, C. W. Progress in the Development of Interpenetrating Polymer Network Hydrogels. *Polym. Adv. Technol.* **2008**, *19*, 647–657. <https://doi.org/10.1002/pat>.
- (18) Follmann, H. D. M.; Oliveira, O. N.; Lazarin-Bidóia, D.; Nakamura, C. V.; Huang, X.; Asefa, T.; Silva, R. Multifunctional Hybrid Aerogels: Hyperbranched Polymer-Trapped Mesoporous Silica Nanoparticles for Sustained and Prolonged Drug Release. *Nanoscale* **2018**, *10* (4), 1704–1715. <https://doi.org/10.1039/c7nr08464a>.
- (19) Yang, W.; Shao, B.; Liu, T.; Zhang, Y.; Huang, R.; Chen, F.; Fu, Q. Robust and Mechanically and Electrically Self-Healing Hydrogel for Efficient Electromagnetic Interference Shielding. *ACS Appl. Mater. Interfaces* **2018**, *10* (9), 8245–8257. <https://doi.org/10.1021/acsami.7b18700>.
- (20) Hunt, J. A.; Chen, R.; Van Veen, T.; Bryan, N. Hydrogels for Tissue Engineering and Regenerative Medicine. *J. Mater. Chem. B* **2014**, *2* (33), 5319–5338. <https://doi.org/10.1039/c4tb00775a>.
- (21) Breger, J. C.; Yoon, C.; Xiao, R.; Kwag, H. R.; Wang, M. O.; Fisher, J. P.; Nguyen, T. D.; Gracias, D. H. Self-Folding Thermo-Magnetically Responsive Soft Microgrippers. *ACS Appl. Mater. Interfaces* **2015**, *7* (5), 3398–3405. <https://doi.org/10.1021/am508621s>.
- (22) Mathew, M. L.; Gopalakrishnan, A.; Aravindakumar, C. T.; Aravind, U. K. Low-Cost Multilayered Green Fiber for the Treatment of Textile Industry Waste Water. *J. Hazard. Mater.* **2019**, *365*, 297–305. <https://doi.org/10.1016/j.jhazmat.2018.11.014>.
- (23) Takemori, A.; Butcher, D. S.; Harman, V. M.; Brownridge, P.; Shima, K.; Higo, D.; Ishizaki, J.; Hasegawa, H.; Suzuki, J.; Yamashita, M.; et al. PEPPI-MS: Polyacrylamide-Gel-Based Prefractionation for Analysis of Intact Proteoforms and Protein Complexes by Mass Spectrometry. *J. Proteome Res.* **2020**, *19* (9), 3779–3791. <https://doi.org/10.1021/acs.jproteome.0c00303>.
- (24) Li, A.; Jia, Y.; Sun, S.; Xu, Y.; Minsky, B. B.; Stuart, M. A. C.; Cölfen, H.; Von Klitzing, R.; Guo, X. Mineral-Enhanced Polyacrylic Acid Hydrogel as an Oyster-Inspired Organic-Inorganic Hybrid Adhesive. *ACS Appl. Mater. Interfaces* **2018**, *10* (12), 10471–10479. <https://doi.org/10.1021/acsami.8b01082>.
- (25) Su, X.; Wang, H.; Tian, Z.; Duan, X.; Chai, Z.; Feng, Y.; Wang, Y.; Fan, Y.; Huang, J. A Solvent Co-Cross-Linked Organogel with Fast Self-Healing Capability and Reversible Adhesiveness at Extreme Temperatures. *ACS Appl. Mater. Interfaces* **2020**, *12*, 29757–29766. <https://doi.org/10.1021/acsami.0c04933>.

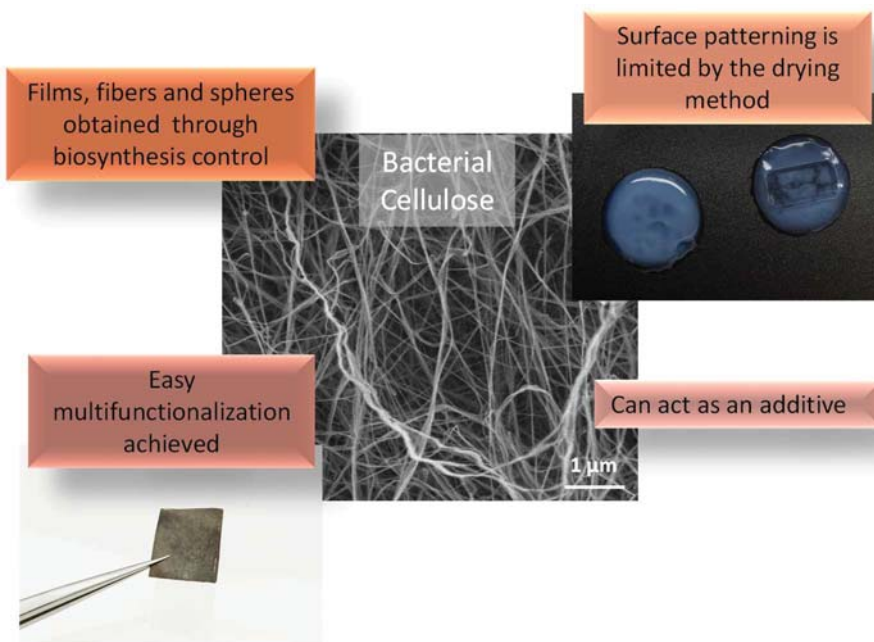
- 
- (26) Agarwal, A.; Nelson, T. B.; Kierski, P. R.; Schurr, M. J.; Murphy, C. J.; Czuprynski, C. J.; McAnulty, J. F.; Abbott, N. L. Polymeric Multilayers That Localize the Release of Chlorhexidine from Biologic Wound Dressings. *Biomaterials* **2012**, *33* (28), 6783–6792. <https://doi.org/10.1016/j.biomaterials.2012.05.068>.
- (27) Champeau, M.; Póvoa, V.; Militão, L.; Cabrini, F. M.; Picheth, G. F.; Meneau, F.; Jara, C. P.; de Araujo, E. P.; de Oliveira, M. G. Supramolecular Poly(Acrylic Acid)/F127 Hydrogel with Hydration-Controlled Nitric Oxide Release for Enhancing Wound Healing. *Acta Biomater.* **2018**, *74*, 312–325. <https://doi.org/10.1016/j.actbio.2018.05.025>.
- (28) Zhang, W.; Zhu, Y.; Liu, X.; Wang, D.; Li, J.; Jiang, L.; Jin, J. Salt-Induced Fabrication of Superhydrophilic and Underwater Superoleophobic PAA-g-PVDF Membranes for Effective Separation of Oil-in-Water Emulsions. *Angew. Chemie - Int. Ed.* **2014**, *53*, 856–860. <https://doi.org/10.1002/anie.201308183>.
- (29) Tian, B.; Liu, S.; Wu, S.; Lu, W.; Wang, D.; Jin, L.; Hu, B.; Li, K.; Wang, Z.; Quan, Z. pH-Responsive Poly (Acrylic Acid)-Gated Mesoporous Silica and its Application in Oral Colon Targeted Drug Delivery for Doxorubicin. *Colloids Surfaces B Biointerfaces* **2017**, *154*, 287–296. <https://doi.org/10.1016/j.colsurfb.2017.03.024>.
- (30) Kim, B.-S.; Park, S. W.; Hammond, P. T. Hydrogen-Bonding Layer-by-Layer-Assembled Biodegradable Polymeric Micelles as Drug Delivery Vehicles from Surfaces. *ACS Nano* **2008**, *2* (2), 386–392. <https://doi.org/10.1021/nn700408z>.
- (31) Ma, T.; Sheng, S.; Dong, X.; Zhang, Y.; Li, X.; Zhu, D.; Lv, F. A Photo-Triggered Hydrogel for Bidirectional Regulation with Imaging Visualization. *Soft Matter* **2020**, *16* (32), 7598–7605. <https://doi.org/10.1039/d0sm01156h>.
- (32) Zhang, B.; Li, S.; Hingorani, H.; Serjouei, A.; Larush, L.; Pawar, A. A.; Goh, W. H.; Sakhaei, A. H.; Hashimoto, M.; Kowsari, K.; et al. Highly Stretchable Hydrogels for UV Curing Based High-Resolution Multimaterial 3D Printing. *J. Mater. Chem. B* **2018**, *6* (20), 3246–3253. <https://doi.org/10.1039/c8tb00673c>.
- (33) Choi, G.; Cha, H. J. Recent Advances in the Development of Nature-Derived Photocrosslinkable Biomaterials for 3D Printing in Tissue Engineering. *Biomater. Res.* **2019**, *23* (18), 1–7. <https://doi.org/10.1186/s40824-019-0168-8>.
- (34) Chen, Q.; Chen, H.; Zhu, L.; Zheng, J. Fundamentals of Double Network Hydrogels. *J. Mater. Chem. B* **2015**, *3* (18), 3654–3676. <https://doi.org/10.1039/c5tb00123d>.
- (35) Fuchs, S.; Shariati, K.; Ma, M. Specialty Tough Hydrogels and Their Biomedical Applications. *Adv. Healthc. Mater.* **2020**, *9* (2), 1901396. <https://doi.org/10.1002/adhm.201901396>.
- (36) Nonoyama, T.; Lee, Y. W.; Ota, K.; Fujioka, K.; Hong, W.; Gong, J. P. Instant Thermal Switching from Soft Hydrogel to Rigid Plastics Inspired by Thermophile Proteins. *Adv. Mater.* **2020**, *32* (4), 1905878. <https://doi.org/10.1002/adma.201905878>.
- (37) Wang, Y.; Chang, Q.; Zhan, R.; Xu, K.; Wang, Y.; Zhang, X.; Li, B.; Luo, G.; Xing, M.; Zhong, W. Tough but Self-Healing and 3D Printable Hydrogels for E-Skin, E-Noses and Laser Controlled Actuators. *J. Mater. Chem. A* **2019**, *7* (43), 24814–24829. <https://doi.org/10.1039/c9ta04248b>.
- (38) Ducrot, E.; Chen, Y.; Bulters, M.; Sijbesma, R. P.; Creton, C. Toughening Elastomers with Sacrificial Bonds and Watching Them Break. *Science*. **2014**, *344* (6180), 186–189. <https://doi.org/10.1126/science.1248494>.

- (39) Gong, J. P. Why Are Double Network Hydrogels so Tough? *Soft Matter* **2010**, *6* (12), 2583–2590. <https://doi.org/10.1039/b924290b>.
- (40) Azuma, C.; Yasuda, K.; Tanabe, Y.; Taniguro, H.; Kanaya, F.; Nakayama, A.; Chen, Y. M.; Gong, J. P.; Osada, Y. Biodegradation of High-Toughness Double Network Hydrogels as Potential Materials for Artificial Cartilage. *J. Biomed. Mater. Res. Part A* **2007**, *81* (2), 373–380. <https://doi.org/10.1002/jbm.a.31043>.
- (41) Hagiwara, Y.; Putra, A.; Kakugo, A.; Furukawa, H.; Gong, J. P. Ligament-like Tough Double-Network Hydrogel Based on Bacterial Cellulose. *Cellulose* **2010**, *17* (1), 93–101. <https://doi.org/10.1007/s10570-009-9357-2>.
- (42) Nakayama, A.; Kakugo, A.; Gong, J. P.; Osada, Y.; Takai, M.; Erata, T.; Kawano, S. High Mechanical Strength Double-Network Hydrogel with Bacterial Cellulose. *Adv. Funct. Mater.* **2004**, *14* (11), 1124–1128. <https://doi.org/10.1002/adfm.200305197>.
- (43) Yasuda, K.; Gong, J. P.; Katsuyama, Y.; Nakayama, A.; Tanabe, Y.; Kondo, E.; Ueno, M.; Osada, Y. Biomechanical Properties of High-Toughness Double Network Hydrogels. *Biomaterials* **2005**, *26* (21), 4468–4475. <https://doi.org/10.1016/j.biomaterials.2004.11.021>.
- (44) Zeng, M.; Laromaine, A.; Roig, A. Bacterial Cellulose Films: Influence of Bacterial Strain and Drying Route on Film Properties. *Cellulose* **2014**, *21* (6), 4455–4469. <https://doi.org/10.1007/s10570-014-0408-y>.
- (45) Trovatti, E.; Oliveira, L.; Freire, C. S. R.; Silvestre, A. J. D.; Pascoal Neto, C.; Cruz Pinto, J. J. C.; Gandini, A. Novel Bacterial Cellulose-Acrylic Resin Nanocomposites. *Compos. Sci. Technol.* **2010**, *70* (7), 1148–1153. <https://doi.org/10.1016/j.compscitech.2010.02.031>.
- (46) Halib, N.; Mohd Amin, M. C. I.; Ahmad, I.; Abrami, M.; Fiorentino, S.; Farra, R.; Grassi, G.; Musiani, F.; Lapsin, R.; Grassi, M. Topological Characterization of a Bacterial Cellulose-Acrylic Acid Polymeric Matrix. *Eur. J. Pharm. Sci.* **2014**, *62*, 326–333. <https://doi.org/10.1016/j.ejps.2014.06.004>.
- (47) Ahmad, N.; Amin, M. C. I. M.; Mahali, S. M.; Ismail, I.; Chuang, V. T. G. Biocompatible and Mucoadhesive Bacterial Cellulose-g-Poly(Acrylic Acid) Hydrogels for Oral Protein Delivery. *Mol. Pharm.* **2014**, *11* (11), 4130–4142. <https://doi.org/10.1021/mp5003015>.
- (48) Hua, J.; Liu, C.; Ng, P. F.; Fei, B. Bacterial Cellulose Reinforced Double-Network Hydrogels for Shape Memory Strand. *Carbohydr. Polym.* **2021**, *259*, 117737. <https://doi.org/10.1016/j.carbpol.2021.117737>.
- (49) Matusiak, M.; Kadlubowski, S.; Rosiak, J. M. Nanogels Synthesized by Radiation-Induced Intramolecular Crosslinking of Water-Soluble Polymers. *Radiat. Phys. Chem.* **2020**, *169*, 108099. <https://doi.org/10.1016/j.radphyschem.2018.12.019>.
- (50) Pawar, A. A.; Saada, G.; Cooperstein, I.; Larush, L.; Jackman, J. A.; Tabaei, S. R.; Cho, N.-J.; Magdassi, S. High-Performance 3D Printing of Hydrogels by Water-Dispersible Photoinitiator Nanoparticles. *Sci. Adv.* **2016**, *2* (4), e1501381. <https://doi.org/10.1126/sciadv.1501381>.
- (51) Williams, C. G.; Malik, A. N.; Kim, T. K.; Manson, P. N.; Elisseff, J. H. Variable Cytocompatibility of Six Cell Lines with Photoinitiators Used for Polymerizing Hydrogels and Cell Encapsulation. *Biomaterials* **2005**, *26* (11), 1211–1218. <https://doi.org/10.1016/j.biomaterials.2004.04.024>.

- 
- (52) Bryant, S. J.; Nuttelman, C. R.; Anseth, K. S. Cytocompatibility of UV and Visible Light Photoinitiating Systems on Cultured NIH / 3T3 Fibroblasts In Vitro. *J. Biomater. Sci. Polym. Ed.* **2000**, *11* (5), 439–457. <https://doi.org/10.1163/156856200743805>.
- (53) Kolczak, U.; Rist, G.; Dietliker, K.; Wirz, J. Reaction Mechanism of Monoacyl- and Bisacylphosphine Oxide Photoinitiators Studied by <sup>31</sup>P-, <sup>13</sup>C-, and <sup>1</sup>H-CIDNP and ESR. *J. Am. Chem. Soc.* **1996**, *118* (27), 6477–6489. <https://doi.org/10.1021/ja9534213>.
- (54) Ulanski, P.; Bothe, E.; Hildenbrand, K.; Rosiak, J. M.; Von Sonntag, C. Hydroxyl-Radical-Induced Reactions of Poly(Acrylic Acid); a Pulse Radiolysis, EPR and Product Study. Part I. Deoxygenated Aqueous Solutions. *J. Chem. Soc., Perkin Trans. 2* **1996**, 13–22.
- (55) Ulanski, P.; Bothe, E.; Hildenbrand, K.; Rosiak, J. M.; Von Sonntag, C. Hydroxyl-Radical-Induced Reactions of Poly(Acrylic Acid); a Pulse Radiolysis, EPR and Product Study. Part II. Oxygenated Aqueous Solutions. *J. Chem. Soc. Perkin Trans. 2* **1996**, *1*, 23–28. <https://doi.org/10.1039/p29960000013>.
- (56) Gibson, L. J.; Ashby, M. F. *Cellular Solids: Structure and Properties*, Second Edition; Cambridge University Press, **1999**.
- (57) Beck-Candanedo, S.; Roman, M.; Gray, D. G. Effect of Reaction Conditions on the Properties and Behavior of Wood Cellulose Nanocrystal Suspensions. *Biomacromolecules* **2005**, *6* (2), 1048–1054. <https://doi.org/10.1021/bm049300p>.
- (58) Xu, X.; Liu, F.; Jiang, L.; Zhu, J. Y.; Haagensohn, D.; Wiesenborn, D. P. Cellulose Nanocrystals vs. Cellulose Nanofibrils: A Comparative Study on Their Microstructures and Effects as Polymer Reinforcing Agents. *ACS Appl. Mater. Interfaces* **2013**, *5* (8), 2999–3009. <https://doi.org/10.1021/am302624t>.
- (59) Okiyama, A.; Motoki, M.; Yamanaka, S. Bacterial Cellulose II. Processing of the Gelatinous Cellulose for Food Materials. *Food Hydrocoll.* **1992**, *6* (5), 479–487. [https://doi.org/10.1016/S0268-005X\(09\)80033-7](https://doi.org/10.1016/S0268-005X(09)80033-7).
- (60) Zhai, X.; Lin, D.; Liu, D.; Yang, X. Emulsions Stabilized by Nanofibers from Bacterial Cellulose: New Potential Food-Grade Pickering Emulsions. *Food Res. Int.* **2018**, *103*, 12–20. <https://doi.org/10.1016/j.foodres.2017.10.030>.
- (61) Hosseinpour Feizi, Z.; Fatehi, P. Carboxymethylated Cellulose Nanocrystals as Clay Suspension Dispersants: Effect of Size and Surface Functional Groups. *Cellulose* **2020**, *27* (7), 3759–3772. <https://doi.org/10.1007/s10570-020-03024-w>.
- (62) Naficy, S.; Razal, J. M.; Whitten, P. G.; Wallace, G. G.; Spinks, G. M. A pH-Sensitive, Strong Double-Network Hydrogel: Poly(Ethylene Glycol) Methyl Ether Methacrylates-Poly(Acrylic Acid). *J. Polym. Sci. Part B Polym. Phys.* **2012**, *50* (6), 423–430. <https://doi.org/10.1002/polb.23016>.

# Chapter 6

## Summary and prospects



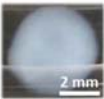



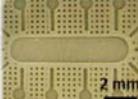

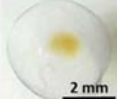






## Summary

This thesis has demonstrated the versatility of bacterial cellulose beyond the current state-of-the-art paving the way to future applications of nanocellulosic materials from non-plant-derived cellulose. The materials developed and the main processes performed during this thesis are summarized in Table 1.

**Table 1:** Research lines introduced during the thesis.

	Static				Agitation			
Biosynthesis	Films 				Spheres 		Spheres 	
Processing	Blending 	Functionalization 	Structuration 	Structuration 	Functionalization 	Functionalization 		
Application	Reinforcement 							

Based on the compiled results several conclusions can be drawn:

- 1) Bacterial cellulose films, multilaminates, fibers and spheres with different morphology (filled or hollow) can be easily obtained by changing the bacterial cell culture method.**

The first part of the thesis includes from one side, the replication of previous results from the group and the literature and secondly, the scaling up production of BC in our laboratory and the processing of BC in form of fibers, spheres and multilaminates. From this section, I would like to emphasize:



- 
- Through static culture, up to 1 m<sup>2</sup> of BC films have been produced on plates in one batch. Their morphology, porosity and mechanical properties can be modulated by the drying process selected, obtaining more porous material when supercritical drying (SDC) is applied and more compacted and translucent films when oven drying (OD) is employed.
  - As expected, the characterization of OD films shown the elevated light transmittance of those pellicles, a moderate-high decomposition temperature (280 °C) and a crystalline structure mainly composed of cellulose I<sub>α</sub>, as previously reported by us and in the literature.
  - By OD stacks of wet films, they self-adhere creating multilaminates with increased mechanical performance. Upon drying, the hydroxyl groups of the fibers of different films condensate creating a robust thicker film that does not delaminate even after rehydration.
  - Mechanical blending of the film produces stable solutions of BC nanofibers (BCf) with an isoelectric point of 2. Those solutions were used as a reinforcement filler of UV-polymerized hydrogels in chapter 5.
  - Filled self-standing BC spheres (BCS) are produced in a large quantity using agitation culture at the expense of sub-optimal size control. Hollow self-standing BC spheres can be obtained by a static culture on superhydrophobic surfaces with a better size and shape control but with a lower production yield. The shape can be modulated by adjusting the hydrophobic character of the culture surface and the hollow core confers them enough flexibility to be extruded through a 2 mm syringe and recover their original appearance.

In the following sections, I summarize the most original findings reported in this thesis.

## **2) Surface patterning of microfeatures on bacterial cellulose films can be achieved through two approaches and the structural preservation is governed by the drying process used.**

Surface patterning of BC films has been attained by using PDMS molds through two lithography approaches: during the BC biosynthesis through bio-lithography (*in-situ*) and after the biosynthesis through soft-imprint lithography (*ex-situ*). From this part, the most remarkable aspects are:

- Pillar motifs from 200  $\mu\text{m}$  to 10  $\mu\text{m}$  have been obtained through bio-lithography. The study confirmed that x and y-axis dimensions of the motifs are maintained on wet samples and those subjected to OD and SCD, as previously reported in the bibliography for groove features. Samples dried using SCD keep with greater accuracy the original depth (z-axis) while an alignment of the nanocellulose fibers is observed.
- The x/z motif ratio is critical to obtain self-standing pillars under SCD conditions. An acceptable range has been observed for values between 0.2 to 1, obtaining wavier and thinner pillars for lower values.
- Large areas with a combination of features have been attained through bio-lithography in a single step. Those materials can withstand rehydration and their capillarity and diffusion have been preliminarily tested.
- Soft-imprint lithography produces dried patterned BC films (under OD and SCD) with low z-axis dimensions (nanometric range) that also support rehydration. Sub-micro motifs were successfully transferred into the BC films conferring them optical properties. In addition, this method facilitates a selectively patterned functionalization of BC during the process.

## **3) Multifunctionalization of bacterial cellulose with spatial confinement of the functional nanoparticles can be achieved**

Functionalization of BC has been obtained through two main strategies: *ex-situ* by the synthesis of NPs in the BC network through MW-assisted reaction and *in-situ* by the incorporation of preformed NPs in the bacterial broth.

- 
- *Ex-situ* functionalization through MW-assisted reaction was performed with four inorganic systems (Au, Ag, Fe<sub>2</sub>O<sub>3</sub> and TiO<sub>2</sub> NPs) and afforded BC-hybrid films with homogeneous particle size and homogenous film coverage.
  - MW-assisted synthesis technique allowed some control of the volume fraction of nanoparticles within the cellulosic porous scaffold and negligible leaching was observed. In addition, parallel syntheses in larger reaction vessels were afforded, increasing the yield production.
  - Functionalized BC films along with the self-adhesive characteristic of the nanocellulose enable the creation of *ad libitum* assembled millefeuille constructions integrating several properties into one film.
  - *In-situ* functionalization during agitation culture produced magnetic core-shell full spheres with unknown NPs load. By profiting superhydrophobic surfaces in static culture, hollow spheres and dome-like shaped structures of BC were loaded with inorganic NPs controlling the load and location of them by an external magnet. The hollow magnetic spheres presented a negligible magnetization degradation and no leaching was observed after one year in solution. In addition, the method was easily adapted to other inorganic systems (Pt, and Au NPs) and Janus sphere-like structures were obtained by the simultaneous addition of them.

#### **4) Bacterial cellulose fibers can act as an additive to enhance the performance of photocurable polyacrylic acid hydrogels.**

One-pot synthesis of a double network photocurable polyacrylic acid (PAA) hydrogel was produced where BCf act as a secondary network.

- Hydrogels with BCf presented higher resistance to cracks, increased stiffness and lower water absorption capacity compared to pristine PAA hydrogels while keeping similar elastic properties. Those properties were not achieved when other cellulosic sources such as cellulose nanocrystals were employed.
- In addition, the hydrogels containing BCf could stand freeze-thawing cycles without structural macroscopic damage, which is of high interest for biomedical cryogenic storage.

- In the light of the results, we have proposed a configuration of a double network hydrogel where the BCf interact mainly through hydrogen bonding and entrapping the synthetic polymer chains during the process.
- A preliminary assay proved the feasibility to incorporate magnetic functionalized BCf into the PAA hydrogels, which would widen the properties of the material.

In summary, this thesis has contributed to: i) Determine the relevance of the drying method on the properties (not only porosity and transmittance but self-adhesiveness) and morphology of the BC, being a limitation when structuring the surface of films or to create multilaminates. ii) Pave the way to produce multifunctional BC-based materials without appreciable leaching of nanoparticles, a worrisome aspect especially for biomedical applications. iii) Introduce BC as a reinforcement in other synthetic materials which would increase the scope of application of the material in other sectors.

### **Next challenges and prospects**

To understand better the mechanisms that govern the BC and the limitations of the materials, several aspects could be more thoughtfully addressed:

- 1) Self-adherence has been one of the pillars of the thesis as it is the main reason for the production of multifunctional laminates. The collaboration with the group of Dr. Jordi Faraudo simulated the adherence of two crystals of bacterial cellulose and showed the importance of the hydroxyl condensation during the process, whereas the peeling experiments demonstrated that the adherence between films, even coated with NPs, is tough. However, the impact of the nanoparticles coating with further mechanical testing, such as tensile tests or peeling of bigger samples, would provide a better understanding of the self-adhesion mechanism of the composites. In addition, more complex and realistic environments simulation studies (bigger samples or humid scenarios) would also be interesting to be tested.

- 
- 2) Two critical points were found for the structuration of BC film surfaces: i) The resolution of the PDMS mold. ii) The drying process. Better control of the silicon wafer lithography process is needed to achieve well-defined features on the PDMS and thereof on the BC motives. Besides, larger separation between the motifs would allow a better study of their dimensional changes under different drying conditions. In addition, the contribution of the fiber alignment observed to the mechanical properties of the structured films would be also interesting to investigate deeply in the future as the literature has demonstrated that an ordered arrangement of the nanofibers enhances the properties of the material. Other interesting lines where the research could focus would be the study of ways to control the diffusion of the lab-on-a-chip BC films, such as the addition of a hydrophobic coating or decreasing the film porosity. In addition, the effect of the pillar structure and the fiber alignment on cell growth and differentiation should also be interesting to be studied as some compelling results have been found in grooves and wells. Besides, this characteristic is especially relevant as the material can be applied as a cell scaffold mimicking an intestine 3D environment.
  - 3) The self-adhesion property afforded a collection of BC multilaminar structures and hybrid materials which applicability can be studied. Indeed, a publication in collaboration with B.Braun regarding the suitability of native laminated materials as soft-tissue reinforcement to treat abdominal hernias was published during the thesis. By the addition of nanoparticles, several examples of possible uses have been mentioned and, in the future, should be properly studied and corroborated. In the case of the films, preliminary tests for surface-enhanced Raman spectroscopy (SERS) and MW radiation absorbance have been performed showing promising results, although further optimization is needed. The BCf coated with magnetic NPs have been tested as ink for cellulose-based magnetic resonance image (MRI) contrast agents.
  - 4) Finally, the robustness and non-pH-response with low water absorption capacity endorse BCf/PAA as good candidates for soft-tissue bioactive vascular or cartilage implant replacement. In addition, the facility to construct personalized hydrogel shapes is a favorable aspect that could be considered in future 3D approaches. However, additional work is required on those systems: i) strain-stress curves for hydrogels with high BCf loads should be optimized to represent

the system failure using smaller samples or higher loads. ii) biocompatible studies would be beneficial for the final bioimplant application.

In a more general view, bacterial cellulose, along with the nanocellulose materials, present high standing properties which makes the material unique and adaptable to a large number of sectors and applications. Advanced materials are slowly been commercially available, especially in the biomedical sector, however, the traditional plant-based working industry is well established and higher efforts are still needed to be able to implant the BC-based products into the market and the society.



# Annex I

## Technical details







## Materials

The bacteria strain *Komagataeibacter xylinus* (*K. xylinus*) (NCIMB 5346) was provided by the Spanish Type Culture Collection (CECT, Spain). Hestrin-Schramm (HS) culture media was prepared using glucose, peptone, yeast extract and agar (Conda Lab), disodium hydrogen phosphate dodecahydrate and citrate acid monohydrate (Sigma-Aldrich). NaOH (Sigma-Aldrich) and EtOH (Panreac) were used for the cleaning process. Cellulose nanocrystals, CNC, were kindly provided by Cellulforce (75nm Z-average by DLS). PP meshes (Optilene® Mesh Elastic and Optilene® Mesh LP) were provided by B. Braun Surgical, S.A.U., Spain. Superhydrophobic surfaces were produced at Karlsruhe Institute of Technology (KIT, Germany) by *Prof. Pavel A. Levkin research group* using a polymer-based method already published.<sup>1,2</sup>

To prepare the polydimethylsiloxane (PDMS) stamps, a soda-lime anti-reflective chrome mask was purchased from DELTA MASK B.V. SU-8 (2005 and 2050) negative epoxy photoresists and the developer were purchased from Micro Resist Technology GmbH (Berlin, Germany). PDMS Sylgard 184 elastomer kit was purchased from Dow Corning (Midland, MI, USA).

For the BC nanocomposites: iron(III) acetylacetonate ( $\text{Fe}(\text{acac})_3$ , 97%), titanium(IV) butoxide (TBOT, 97%), oleyamine (OA, 70%), polyvinylpyrrolidone (PVP, molecular weight 10k) and gold(III) chloride hydrate ( $\text{HAuCl}_4$ ) were purchased from Sigma-Aldrich. Silver nitrate ( $\text{AgNO}_3$ ) was purchased from Panreac and benzyl alcohol (BA, 99%) from Scharlau.

When BC spheres (BCS) were produced, gold nanoparticles (AuNPs) were synthesized as previously reported through the Turkevich method.<sup>3</sup> Platinum nanoparticles (1mg/mL, 3nm) and glycerol ( $\geq 99.5\%$ ) were purchased from Sigma-Aldrich. SPIONs solution (10 mg/mL in HS medium) was prepared through the dispersion of our MW-assisted reaction synthesized NPs in the bacterial medium. Neodymium iron boron (NdFeB) magnetic disk (60x5 mm) was purchased from Ingeniería Magnética Aplicada, S.L. (IMA), Spain.

---

For hydrogel production, acrylic acid (AA) was acquired from Sigma-Aldrich, polyethylene glycol diacrylate (PEGDA, SR-610) from Sartomer and diphenyl (2,4,6-trimethylbenzoyl) phosphine oxide (TPO) from IGM Resins. Water compatible TPO photoinitiator was prepared in powder formulations containing sodium dodecyl sulfate (SDS) as described in previous works by *Prof. Shlomo Magdassi research group* in the Hebrew University of Jerusalem (HUJI).<sup>4</sup>

## **BC production**

Work was performed under sterile conditions inside an ESCO laminar flow cabin. The material was subjected to a 15 min UV light cycle inside the cabin before manipulation. Incubator (OPAC C-Refrig from OVAN) was used at 30 °C under a saturated humidity environment. In addition, it incorporates an orbital shaker (orbital maxi MD, OVAN) used for BC spheres production. Autoclave (Presoclave-8, P-Selecta), when needed, was applied for 20 min at 120 °C.

*K. xylinus* bacteria were grown in HS solid medium. Then, an aggregate of bacterial cells was expanded in 6 mL of the same liquid medium (*i.e.*, without agar) for 7 days at 30 °C. 0.5 mL were inoculated into 4.5 mL of fresh medium and incubated for another three days. Finally, a dilution of the bacterial solution with fresh medium was done in a 1:14 ratio and transferred into 24 well-plates for 3 days. BC pellicles were harvested and cleaned with a 50% ethanol solution for 10 min, twice with boiling water and then other two times with a 0.1M sodium hydroxide solution for 20 min at 90 °C to lyse the bacterial cells. Then, the pellicles were washed with Milli-Q (MQ) water until neutral pH and were stored in water at room temperature until further use.

BC nanofibers (BCf) were obtained after 10 min blending of 5 films of 164 cm<sup>2</sup> in 1 L of water using a commercial household blender (Jata electro Mod. BT1200). The solution was vacuum filtered with Stericup Quick Release Filter Millipore with a PES membrane of 0.22µm.

For BCS production the static water contact angle (WCA) of the surfaces employed was calculated by a DSA 100 from KRÜSS by depositing a 5 µL drop of culture media on top of the surface and analyzing the contact area with the system software.

Three surfaces of each type were tested in three different areas obtaining a final value of 150° for superhydrophobic surfaces and 86° for petri dish surfaces.

Full BC spheres (f-BCS) were prepared by mixing 2 mL of the bacterial broth with 38 mL of fresh HS medium in a 100 mL conical flask and culturing the system in an orbital shaker (OVAN, orbital maxi MD) inside the incubator for 3 days at 30 °C and 150 rpm. Whereas, hollow BC spheres (h-BCS) were prepared by mixing an initial bacterial culture volume with 10 %v/v of glycerol. Then, drops of 5 µL were deposited on superhydrophobic and hydrophilic surfaces and were incubated for 3 days at 30 °C in a saturated humidity environment and static conditions. Afterward, the spheres were gently removed from the surface with water and cleaned and stored as described before.

## **BC drying**

### *- Oven drying (OD):*

Bacterial cellulose films were dried between two PTFE (polytetrafluoroethylene, Teflon) plates at 60 °C with a 1 kg weight placed on top. For soft imprint, a PDMS stamp was placed above the wet bacterial cellulose with the patterned side facing the film and the set-up was sandwiched between two Teflon plates for drying. For the bilayers and millefeuille constructs, cellulose nanocomposites films were placed one above another using the same set-up.

### *- Freeze drying (FD):*

BC samples were immersed in the smallest amount of MQ water needed (~2 ml) to fully cover the sample in the vial. Then, the vial was sealed with pierced aluminum paper and placed inside the lyophilizer (LYOQUEST-85 from Telstar) at 0.05 mbar and -80 °C for 48 h until complete ice water sublimation.

### *- Supercritical drying (SCD):*

Samples were distributed on a paper accordion, each fold containing one sample. The accordion was then soaked twice in ethanol for 30 min and left overnight (12 h) in fresh ethanol for complete solvent exchange. Samples were then placed on a 300 mL autoclave vessel filled with the solvent (SCF 300 mL plant). The system was pressurized to 100 bars and the drying process took place in two steps. First, ethanol

---

was exchanged with liquid CO<sub>2</sub> at a flow rate of 1500 mL/h for 1.5 h. Then, the reactor was heated at 45 °C with a CO<sub>2</sub> flow of 1500 mL/h for 1h. Finally, the vessel was slowly depressurized to avoid pore collapse and BC aerogels were obtained. For soft-imprint, PDMS stamp was placed above the wet bacterial cellulose with the patterned side facing the film, the set-up was fastened with two clamps between Teflon plates and the sample was subjected to the solvent exchange and drying process as described above.

### **Production of polydimethylsiloxane stamps**

The fabrication of the patterned polydimethylsiloxane (PDMS) stamps consists of two main steps: first, the definition of a master using SU-8 negative photoresist and second, the mold replication of the master using PDMS.

Masters were fabricated on 10 cm silicon wafers at the IMB-CNM clean room facilities in two stages. First, a 5- $\mu$ m thick seed layer of SU-8 2005 was spun coated, pre-baked at 95 °C for 2 min, exposed to UV and post-baked at 120 °C for 90 min. Then a layer of SU-8 2050 was spun coated, pre-baked at 95 °C for 120 min, exposed to UV through a mask containing the desired patterns for 26 s, post-baked at 95 °C for 16 min, developed by immersion in the developer solution for 2.5 min, rinsed with isopropanol and eventually hard-baked at 120 °C for 160 min. The mask was designed using Klayout software.

PDMS stamps were obtained by vigorously mixing Sylgard 184 resin and curing agent at a 10:1 ratio. The mixture was then poured into the master and vacuum was applied (Vacuo-Temp from P-Selecta) to remove air bubbles entrapped into the PDMS solution and in the master surface. After curing (80 °C, 20 min), the PDMS stamp was peeled off the master. The master was then cleaned with EtOH and the process was repeated if needed. The PDMS stamp with the smallest features used for soft-imprinting was kindly provided by the *NANOPTO* group led by Dr. Agustín Mihi from ICMAB.

## BC nanocomposite synthesis

Before the syntheses, the nanocellulose films were subjected to a solvent exchange from water to benzyl alcohol. This step was not necessary for the silver nanoparticles (NPs) reaction, which takes place in water.

NPs were *in situ* synthesized in never dried BC films using a microwave oven with controlled atmosphere (CEM Discover Explorer-12 Hybrid reactor operating at a frequency of 2.45 GHz and with a maximum power of 300 W). Temperature and time were specifically set for each reaction while the power was automatically adjusted to heat the sample using a volume-independent infrared sensor that controls the temperature inside the reaction vessel. After the reaction, the samples were cooled down to 50 °C with compressed air.

## Hydrogel synthesis

As the photoinitiator is sensitive to light, the preparation of the precursor hydrogel solution was performed in vials covered with aluminum foil. First, the nanocellulose derivatives (BCf or CNC) were dispersed in water, then acrylic acid monomers, PEGDA and TPO were added in that order with stirring between additions. Ultrasonication was needed before the addition of extra compounds when CNC was used. Before utilization, TPO was coated with a surfactant (SDS) in a proportion of 1:9 w/w TPO:SDS to increase TPO solubility in water<sup>4</sup>. 2 mL of the precursor solution were poured in silicon containers and exposed to 20 s of UV LED light ( $\lambda=395\text{nm}$ , Integration Technology Limited) for polymerization.

- SCD:

Hydrogels were subjected to a gradual water-to-ethanol solvent exchange. Then, they were placed inside a 300 mL autoclave filled with ethanol and supercritical drying took place. The autoclave was pressurized at 100 bars at room temperature and liquid CO<sub>2</sub> was dispensed for 2 h with a flow of 1 kg/h. The reactor was then heated to 45 °C to reach supercritical conditions. Supercritical CO<sub>2</sub> was pumped for another 2 h at the same flow rate and, finally, the vessel was slowly depressurized.

---

## Characterization (alphabetically ordered)

### *Atomic force microscopy (AFM)*

Dried films were fixed with tape to a holder and a Keysight 5100 atomic force microscope was employed on tapping mode to acquire topographic images, which were analyzed with MountainsMap 8.2 software. Prior to performing the soft-imprint, BC films were placed over a cover glass to reduce the intrinsic roughness of the BC films upon drying.

### *Confocal Microscope*

Topographic studies of S-BC were done by a LEICA DCM 3D dual-core 3D measuring microscope. Samples were placed on a microscope glass slide and images were obtained with 10x and 50x magnifications. Stacks of images covering the z deviation of the surface were acquired and 3D reconstructions and 2D profiles were analyzed with MountainsMap 8.2 software by analyzing 3 patterns.

To analyze BC nanocomposite structures, the samples were first stained overnight in a 24-well plate with Safranin-O (1% aqueous solution) and rinsed with Milli-Q water several times. After removing the excess water, the wet bilayer BC/Ag-BC/TiO<sub>2</sub> was placed on an IBIDI glass-bottom dish and multiple stack images were taken with a Leica SP5 confocal microscope from the microscope services from UAB. Safranin-O was excited with an argon laser at  $\lambda=488$  nm at 10X magnification and 3D reconstructions and image processing was performed with ImageJ-Fiji software.

BCS internal structure was also evaluated. After the staining, the sphere was placed in a hand-made holder that consist of a glass cover with a glued plastic washer and the extra water was removed. A laser of HeNe ( $\lambda = 570$  nm) was used to excite Safranin-O and multistack images were obtained with a Leica SP5 at the Centre for Research in Agricultural Genomics (CRAG, Spain) under the following conditions: 1.55 x 1.55 format, pinhole 1, zoom 1 bidirectional, 10X magnification, step size of 0.8  $\mu$ m, a maximum size of 1.5 mm and a speed of 600 Hz. ImageJ-Fiji software was used for image processing.

*Dynamic mechanical analysis (DMA) – Peel-off and tensile tests*

For the peeling test of BC and BC nanocomposite films, two BC films were dried one above the other at 60 °C with a spacing material, to which the cellulose does not adhere, in between covering half of the surface. After drying, the samples were cut using a blade, obtaining a final dimension of the stuck area of 5 x 7.5 mm. The two not-adherent ends of the strip were glued in between pieces of paper of 1.5 x 1.5 cm and placed between clamps. The tests were conducted using a linear variable differential transformer, an ADMET load cell of 100 N and a displacement sensor to move both ends at a constant speed of 0.69 mm/s under controlled temperature and humidity conditions (23±1 °C and 25±1 % humidity). The force needed to separate both layers as a function of the displacement was recorded and the interfacial energy needed to separate the two BC pieces was calculated as the area below the curve normalized by the peel-off area of the sample (37.5 mm<sup>2</sup>). The tests were recorded by a Leica M205FA microscope.

Zwick Z2.5 dynamometer with a load cell of 2.5 kN was used for tensile experiments of BC films and multilayer constructs. The clamps were metallic with a pneumatic flat rubber part in contact with the sample. The test velocity was 100 mm/min, the pressure of the clamps was 6 bars, the distance between them was 20 mm and the preload applied was 0.05 N. Strain and stress values were acquired for 5 replicas. Multilayered systems were immersed for 5 min in a 0.9% NaCl solution for rehydration before the tensile study. Excess of liquid was removed by placing the samples on a filter paper to blot them. All the samples were weighted and sized with an Acculab Atilon ATL-244-1 analytical balance, Stanley Millesimal rule and Mitutoyo 543-250B micrometer respectively previous to the analysis.

*Freeze-thawing test*

Ring-shaped hydrogels were frozen in liquid nitrogen and thaw at room temperature two times to study the robustness of the materials.

*Fourier transform infrared spectroscopy (FTIR)*

FTIR spectra were acquired by folding 4 times the BC film and placing it on a Jasco 4700 FTIR-ATR spectrometer. Three sample replicates were measured averaging 32 scans in a range between 400 and 4000 cm<sup>-1</sup> with a resolution of 4.0 cm<sup>-1</sup>. Table 1 depicts a detailed assignment of the peaks observed.



**Table 1:** Detailed vibration assignment to each peak observed on the FTIR spectrometry.<sup>5,6</sup>

Peak wavenumber (cm <sup>-1</sup> )	Assignment
~3330	O-H stretching (hydrogen bonding and cellulose I)
2895	C-H stretching (CH <sub>2</sub> and CH <sub>3</sub> groups)
2360	Amino stretching
1645	H-O-H bending of absorbed water
1540	Protein amine II absorption
1426	CH <sub>2</sub> symmetric bending or O-H in-plane bending
1360	C-H bending
1335	C-H deformation or O-H in-plane bending
1316	Out of plane wagging of the CH <sub>2</sub> groups
1281	C-H bending
1162	C-O-C antisymmetric stretching (1,4-β-glucoside)
1111	C-O or C-C bending (cellulose ring)
899	Antisymmetric out-of-phase ring stretching
668	O-H out of phase bending

*Inductively coupled plasma – optical emission spectroscopy (ICP-OES)*

After the leaching test, Ti content in water samples that contained BC/TiO<sub>2</sub> was analyzed by an ICP-OES Optima 4300DV Perkin-Elmer.

*(All atomic) Molecular dynamics (MD) simulations*

The MD simulations were performed by Dr. Carlos Malaspina and Dr. Jordi Faraudo from the *Materials simulations and Theory research group* from ICMAB using the NAMD 2.12 software<sup>7</sup> with a Langevin thermostat at 298 K. In the simulations with water solvent, a barostat (Langevin piston) at 1 bar was also employed. Cellulose fibrils were build using the cellulose builder toolkit<sup>8</sup> and described using the carbohydrate section of the CHARMM force field.<sup>9</sup> MD simulations have been performed in dry (no water) and wet conditions (full hydration). In wet conditions, water was described employing the TIP4P/2005 model,<sup>10,11</sup> which best capture hydrogen-bonding features of liquid water at all pressures.<sup>12</sup> Minimization,

equilibration and production runs (20 ns) of two cellulose fibrils interacting in vacuum and water were performed. Simulations were periodic in all directions, obtaining results similar to infinite long fibrils in the y-direction.

The force analysis was performed with biased molecular dynamics simulations, using two different methods (due to the different strength of the interactions in the dry and wet scenarios). For fibrils in vacuum, the Steered Molecular Dynamics (SMD) method was applied to measure the adhesion force, while for the fibrils in water the Adaptive Biasing Force (ABF) method was used.<sup>13</sup>

#### *Morphology and statistical analysis*

The thickness of 1.5 cm diameter pellicles was calculated with a Mitutoyo QuantuMike series 293 micrometer by placing them between two cover glass and measuring in five points of the film. Three replicates were measured. In the case of never-dried (as-obtained) BC, samples were deposited first on a filter paper to blot excess of water and, when measuring, the plunger of the micrometer was lifted and lowered three times and the thickness value was recorded when it was stable for more than 2 s during the third time.

12x12 cm BC sheets and multilayers were cut in 20x50 mm pieces and the weight, size and thickness were measured with an Acculab Atilon ATL-244-1 analytical balance, Stanley Millesimal rule and Mitutoyo 543-250B micrometer respectively. Results were computed from five replicas. Surface weight was calculated as the ratio between weight and area. Water uptake ( $H_2O_{up}$ ) percentage was calculated as  $(m_w - m_d)/m_d \cdot 100$ , where  $m_w$  is the weight of the wet sample after hydration and  $m_d$  is the weight of the dry sample before hydration.

Morphology of the BCS was determined by analysis of digital images with ImageJ software. The size of the f-BCS was computed from populations of 100 to 200 spheres. h-BCS height and width average values were obtained for sample populations of 6 to 21 spheres and the spherical ratio (sphericity) was calculated as the height/width ratio. One-way ANOVA followed by Tukey's multiple comparison test was used for statistical analysis,  $p > 0.05$ .

---

### *Optical Microscope*

S-BC films were placed on a microscope glass slide and observed through 5x, 20x, 50x and 100x magnifications (Olympus BX51 and Nikon SMZ2800N with a XM Full HD camera, MicroscopiaDigital). Size values of the patterns were calculated by analyzing from 4 to 15 features using ImageJ software.

### *Scanning Electron Microscopy (SEM)*

To image BC film microstructure and nanofiber distribution, the films were fixed with adhesive carbon tape on top of aluminum SEM holders. A high-resolution scanning electron microscope (FEI Magellan 400L XHR SEM, ICN2) was used under high vacuum with an acceleration voltage of 2 kV, a current of 0.10 nA, a working distance of 5 mm and a vCD detector. OV and FD films were sputtered with 5 nm of Pt for correct imaging. Same SEM working conditions were used to analyze the nanoparticle distribution and coverage of the BC nanofibers.

For the cross-section images of the multilayer construction and the electron-dispersive x-ray (EDX), the film was cut with a blade (Personna GEM single edge, 3-facet stainless steel, PTFE coated blade, 0.23mm) to obtain a clean cut and was placed in a holder with an 80-90° tilt. FEI Quanta 650FEG ESEM (from ICN2) was used under low vacuum conditions, with an acceleration voltage of 20 kV, an electron beam spot of 3-4 mm and a working distance of 10 mm.

BCS were cut with the PTFE coated blade and lyophilized to maintain the structure upon drying. After drying, images and EDX were taken from 4 to 15 patterns with a QUANTA FEI 200 FEG-ESEM under low vacuum conditions, an acceleration voltage of 10–15 kV, an electron beam spot of 3.5 mm and a working distance of 10 mm. The same conditions were used to study BCf microstructure and nanoparticle coating and the replica molding on S-BC films. In this particular case, the samples were also tilted to study the z dimensions and fiber orientation was analyzed by the OrientationJ package from ImageJ software.

SCD hydrogels were cut with the PTFE coated blade and fixed on an aluminum SEM holder with adhesive carbon tape. They were analyzed by QUANTA FEI 200 FEG-ESEM under low vacuum conditions, an acceleration voltage of 5 kV and a working distance of 10 mm for low magnification images and, after a 5 nm Pt coating, by FEI

Magellan 400L XHR SEM under high vacuum, an acceleration voltage of 1 kV, current of 0.10 nA and a working distance of 4 mm for high magnification images.

#### *Response towards a magnetic field*

The movement velocity for magnetic h-BCS (h-BCS-SP) under a magnetic field application was calculated as follows: a sphere was placed in the middle of a vessel with water and with a magnet allocated in the wall. The distance covered by the sphere (10 mm) was computed considering  $t = 0$  the moment the drop orientates towards the magnet and the final time when it reached the glass wall in contact with the magnet. Three replicas were performed for each SPIONs concentration.

#### *Superconducting quantum interference device (SQUID)*

BC/SPIONs were characterized by measuring their magnetization *versus* an applied magnetic field from 0 to 70 kO at 300 K in a Quantum Design MPMS-XL equipment.

The magnetic response of the SPIONs trapped in an h-BCS-SP was also measured and compared to free SPIONs in solution. In brief, a sphere with 2.50 mg/mL SPIONs concentration was dried in the middle of a paper strip at room temperature. At the same time, a h-BCS was dried at room temperature in another strip and a drop of a SPIONs solution with the same concentration and volume (5  $\mu$ L, 2.50 mg/mL) was deposited above. This was done to avoid the spreading of the drop through the strip and to have a similar cellulose volume. The strips were then placed inside plastic tubes with similar diameters and sealed with cotton. Magnetization *vs.* applied magnetic field was measured from 0 to 70 kOe at 300 K.

#### *Swelling test*

To study the swelling response of the PAA/BCf hydrogels at different pH conditions, ring-shaped hydrogels were immersed for 24 h at room temperature in distilled water with a pH value ranging from 4 to 10. The water absorption capacity (WAC) was calculated as follows:

$$\text{WAC (\%)} = \frac{(W_s - W_0)}{W_0} \cdot 100$$

Where  $W_0$  is the mass of the hydrogel right after the polymerization and  $W_s$  is the mass of the hydrogel after 24 h in solution.

---

### *Thermogravimetric Analysis (TGA)*

A TGA-DSC/DTA analyzer (NETZSCH STA 449 F1 Jupiter) with a heating rate of 10 °C min<sup>-1</sup> from room temperature to 800 °C in air was used to evaluate the residual mass of BC films and the inorganic NP mass and volume fraction in each nanocomposite. For the leaching evaluation, half of the same film was immersed in 8 mL MQ water for 30 days under gentle horizontal agitation conditions and another TGA was run.

### *Transmission electron microscopy (TEM)*

JEOL JEM-1210 electron microscope operating at 120 kV with an ORIUS 831 SC 600, Gatan camera was used to obtain TEM images and diffraction patterns of the nanoparticles by the selected area electron diffraction (SAED) mode. A histogram of 300-400 nanoparticles diameter measurements was fitted to a Gaussian function to calculate the mean size of the population. Polydispersity (PDI) value was calculated as the percentage of standard deviation/mean value.

BCf images were obtained by diluting them in 1 mL of EtOH and sonicated for good dispersion. BC fiber mean diameter was calculated as the average value of 24 measures obtained by ImageJ software.

### *Unconfined compression*

PAA/BCf hydrogels were subjected to an unconfined mechanical compression test. For each system, 4 replicas were measured right after the polymerization to avoid water evaporation. The test was performed with an Instron 3345 press equipped with a 500 N load cell and at a speed of 1 mm/min and strain-stress curves were obtained. The maximum limit of the load cell was reached for some samples. Young's modulus was calculated in the strain range from 0 – 10 % and the toughness values correspond to the area below the strain-stress curve.

### *UV-VIS spectroscopy*

After drying the films, their optical transmittance was measured by a Varian Cary 5000 spectrophotometer in the range between 200 and 800 nm. The samples were placed between an opaque holder with an aperture in the middle and a cover glass, which was fixed with tape to the holder to assure the complete immobilization of the sample. Three replicates were measured for each sample.

## References

- (1) Feng, W.; Li, L.; Ueda, E.; Li, J.; Heißler, S.; Welle, A.; Trapp, O.; Levkin, P. A. Surface Patterning via Thiol-Yne Click Chemistry: An Extremely Fast and Versatile Approach to Superhydrophilic-Superhydrophobic Micropatterns. *Adv. Mater. Interfaces* **2014**, *1* (7), 1–6. <https://doi.org/10.1002/admi.201400269>.
- (2) Popova, A. A.; Demir, K.; Hartanto, T. G.; Schmitt, E.; Levkin, P. A. Droplet-Microarray on Superhydrophobic-Superhydrophilic Patterns for High-Throughput Live Cell Screenings. *RSC Adv.* **2016**, *6* (44), 38263–38276. <https://doi.org/10.1039/c6ra06011k>.
- (3) Zhao, L.; Jiang, D.; Cai, Y.; Ji, X.; Xie, R.; Yang, W. Tuning the Size of Gold Nanoparticles in the Citrate Reduction by Chloride Ions. *Nanoscale* **2012**, *4* (16), 5071–5076. <https://doi.org/10.1039/c2nr30957b>.
- (4) Pawar, A. A.; Saada, G.; Cooperstein, I.; Larush, L.; Jackman, J. A.; Tabaei, S. R.; Cho, N.-J.; Magdassi, S. High-Performance 3D Printing of Hydrogels by Water-Dispersible Photoinitiator Nanoparticles. *Sci. Adv.* **2016**, *2* (4), e1501381. <https://doi.org/10.1126/sciadv.1501381>.
- (5) Wang, S. S.; Han, Y. H.; Ye, Y. X.; Shi, X. X.; Xiang, P.; Chen, D. L.; Li, M. Physicochemical Characterization of High-Quality Bacterial Cellulose Produced by *Komagataeibacter* Sp. Strain W1 and Identification of the Associated Genes in Bacterial Cellulose Production. *RSC Adv.* **2017**, *7* (71), 45145–45155. <https://doi.org/10.1039/c7ra08391b>.
- (6) Gea, S.; Reynolds, C. T.; Roohpour, N.; Wirjosentono, B.; Soykeabkaew, N.; Bilotti, E.; Peijs, T. Investigation into the Structural, Morphological, Mechanical and Thermal Behaviour of Bacterial Cellulose after a Two-Step Purification Process. *Bioresour. Technol.* **2011**, *102* (19), 9105–9110. <https://doi.org/10.1016/j.biortech.2011.04.077>.
- (7) Phillips, J. C.; Braun, R.; Wang, W.; Gumbart, J.; Tajkhorshid, E.; Villa, E.; Chipot, C.; Skeel, R. D.; Kalé, L.; Schulten, K. Scalable Molecular Dynamics with NAMD. *J. Comput. Chem.* **2005**, *26* (16), 1781–1802. <https://doi.org/10.1002/jcc.20289>.
- (8) Gomes, T. C. F.; Skaf, M. S. Cellulose-Builder: A Toolkit for Building Crystalline Structures of Cellulose. *J. Comput. Chem.* **2012**, *33*, 1338–1346. <https://doi.org/10.1002/jcc.22959>.
- (9) Guvench, O.; Mallajosyula, S. S.; Raman, E. P.; Hatcher, E.; Vanommeslaeghe, K.; Foster, T. J.; Jamison, F. W.; MacKerell, A. D. CHARMM Additive All-Atom Force Field for Carbohydrate Derivatives and Its Utility in Polysaccharide and Carbohydrate-Protein Modeling. *J. Chem. Theory Comput.* **2011**, *7* (10), 3162–3180. <https://doi.org/10.1021/ct200328p>.
- (10) Abascal, J. L. F.; Vega, C. A General Purpose Model for the Condensed Phases of Water: TIP4P/2005. *J. Chem. Phys.* **2005**, *123*, 234505. <https://doi.org/10.1063/1.2121687>.
- (11) Vega, C.; Abascal, J. L. F. Simulating Water with Rigid Non-Polarizable Models: A General Perspective. *Phys. Chem. Chem. Phys.* **2011**, *13* (44), 19663–19688. <https://doi.org/10.1039/c1cp22168j>.
- (12) Calero, C.; Martí, J.; Guàrdia, E. 1 H Nuclear Spin Relaxation of Liquid Water from Molecular Dynamics Simulations. *J. Phys. Chem. B* **2015**, *119* (5), 1966–1973. <https://doi.org/10.1021/jp510013q>.
- (13) Hénin, J.; Fiorin, G.; Chipot, C.; Klein, M. L. Exploring Multidimensional Free Energy Landscapes Using Time-Dependent Biases on Collective Variables. *J. Chem. Theory Comput.* **2010**, *6* (1), 35–47. <https://doi.org/10.1021/ct9004432>.



# Annex II

*Curriculum vitae* and publications







# SOLEDAD ROIG-SANCHEZ

✉ solroigsan@gmail.com

☎ +36 65566073

📍 Barcelona, Spain

Soon-to-be Ph.D. in Material Science with a thesis entitled "Novel bacterial cellulose materials: Structuration, functional nanocomposites and photocurable hydrogels" dedicated to the research of advanced materials based on bacterial cellulose, under the supervision of Dr. Anna Roig and Dr. Anna Laromaine from the NN Group at the Institute of Materials Science of Barcelona (ICMAB-CSIC). (2016-2021)

 0000-0002-7474-3769

## PERSONAL SKILLS

- Organizational capacity
- Results-oriented
- Commitment
- Innovative
- Ability to motivate coworkers and maintain good relations
- Resilient

## LANGUAGES

Spanish - native  
Catalan - native (C2)  
English - C1  
French - A2

## AWARDS

- Polymar2018 - Severo Ochoa travel grant and oral presentation price.
- FPI Spanish government fellowship - (2016-2021).
- Travel grant to pursue the master thesis at USA.
- Honorary mention to the best academic results (Years 2010-2011 and 2013-2014).
- "Congreso de estudiantes de Química de la Universidad de Alicante" (2010) - oral prize.

## EXPERIENCE

- |           |  |
|-----------|--|
| 2015-2016 | Researcher at ICMUV (Institute of Materials Science of the University of Valencia)<br><br>Study hollow mesostructured silica spheres for theragnostic uses at the Nanostructured Material research group under the supervision of Pedro Amorós del Toro. |
| 2014      | Technician at AIDIMA (Furniture, Wood and Packaging Technological Institute), Valencia - Spain.<br><br>3-months internship characterizing varnishes and surfaces applicable to the furniture industry according to ISO standards.                        |
| 2013      | Computational chemistry research<br><br>Summer internship at the Medium Effects research group at the University of Valencia.  |

## TECHNICAL SKILLS

- Experience in clean rooms, sterile environments and culturing bacteria.
- Particle synthesis: lyophilization, microwave-assisted reaction, supercritical drying
- Ultra-high vacuum: XPS, RHEED, MBE
- Characterization: AFM, ellipsometry, LALLS, DLS, TEM, SEM, BET, spectroscopy techniques and mechanical testing
- ISO standards
- IT: Microsoft Office, Origin, GIMP, Photoshop, Linux (basic)

## EDUCATION

- |           |   |
|-----------|---|
| 2014-2015 | MASTER IN NANOTECHNOLOGY- Rovira i Virgili University<br>8.95/10 or 2.62/4<br><br>MSC thesis: "MgO thin film deposition on Si(100) by MBE". Supervisor: Katherine S. Ziemer, Northeastern University, USA.  |
| 2010-2014 | BACHELOR OF SCIENCE: CHEMISTRY - University of Valencia<br>8.44/10 or 2.49/4<br><br>Final year thesis: "Gd <sub>2</sub> Zr <sub>2</sub> O <sub>7</sub> nanometric synthesis and preparation of thereof stable suspensions in aqueous media". Supervisor: Eduardo Martinez Tamayo. |

## TEACHING

---

- TA at Thermodynamics, Kinetics and Phase transformations Lab, UAB (2018-2019). 18 hours.

## OUTREACH

---

- Finalist of the contest "Defense your thesis in 4 minutes" (2018).
- MATBIO2017 - In charge of the activity "Synthesis of Au-NPs" (2017).
- Expociencia 2014 and 2016 at University of Valencia.
- Member of the theater association "Teatro Químico" (2010-2016).

## OTHER ACTIVITIES

---

- Organizer of the JPHD2019 meeting (4th Scientific Meeting of BNC-b Students).
- Organizer of "Congreso de Estudiantes de Química de Comunidad Valenciana" (2013).
- Lab manager coordinator (2017).
- Mentor and guide for Erasmus students, freshmen and prospective students at university (2012-2014).
- Student representative in the academic board at high school and university.

## PUBLICATIONS

---

Roig-Sanchez, S.\*, Torrecilla, O.\*, Floriach-Clark, J, Parets, S, Levkin, P.A, Roig, A., Laromaine, A. Soft and actuable bacterial cellulose spheres with controlled localization of functional nanoparticles. - under submission. (\* Equal contribution.)

Mira-Cuenca, C., Meslier, T., Roig-Sanchez, S., Laromaine, A., Roig, A. Patterning bacterial cellulose films with iron oxide nanoparticles and MRI monitoring. ACS Applied Polymer Materials, 2021 - accepted

Roig-Sanchez, S., Fernández-Sanchez, C., Laromaine, A, Roig, A. Bio and soft-imprinting lithography on bacterial cellulose films. Materials Today Chemistry, 2021 - accepted.

Wang, W., Khabazian, S., Roig-Sanchez, S., Laromaine, A., Roig, A., Tonti, D. Carbons derived from alcohol-treated bacterial cellulose with optimal porosity for Li-O2 batteries, Renewable Energy, 2021, 177, 209-215

Anton-Sales, I.\*, Roig-Sanchez, S.\*, Traeger, K., Weis, C., Laromaine, A., Turon. P., Roig, A. In vivo soft tissue reinforcement with bacterial nanocellulose. Biomaterials Science, 2021, 9, 3040 (\*Equal contribution)

Herburger, K., Franková, L., Sanhueza, D., Roig-Sanchez, S., Meulewaeter, F., Hudson, A., Thomson, A., Laromaine, A., Butdova, T., Fry S.C. Enzymatically attaching oligosaccharides-linked "cargoes" to cellulose and other commercial polysaccharides via stable covalent bonds International Journal of Biological Macromolecules, 2020, 164, 4359-4369.

Anton-Sales, I., Roig-Sanchez, S., Sánchez-Guisado, M., Laromaine, A., Roig, A. Bacterial nanocellulose and titania hybrids: cytocompatible and cryopreservable cell carriers. ACS Biomaterials Science & Engineering, 2020, 6, 4893-4902

Roig-Sanchez, S., Jungstedt, E., Anton-Sales, I., Malaspina, D. C., Farauo, J., Berglund, L. A., Laromaine, A., Roig, A. Nanocellulose Films with Multiple Functional Nanoparticles in Confined Spatial Distribution. Nanoscale Horizons, 2019, 4, 634-341.

Garcia-Barbera, A., Culebras, M., Roig-Sanchez, S., Gomez, C.M., Cantarero, A. Three-dimensional PEDOT nanowires network, Synthetic Metals, 2016, 220, p. 208-212.

## ATTENDANCE to CONFERENCES

---

4th International EPNOE Junior Scientist Meeting- February. 2021 - Oral communication. "Photocurable double network polyacrylic acid (PAA) hydrogels with bacterial cellulose nanofibers (BCf)"

ICNF2019 (4th International conference of natural fibers) - July, 2019. Oral communication. "Multilayer bacterial cellulose with confined nanoparticle distribution."

Polymar2018 (2nd Conference for early-stage researchers in polymer science through the Aegean) - October, 2018. Oral communication. "Microstructuration and functionalization of bacterial cellulose."

EMN2018 (Energy Materials and Nanotechnology) - Sept, 2018. Oral communication. "Confined nanoparticle multilayer bacterial cellulose composite."

JPHD2017 (3rd Scientific Meeting of BNC-b Students) - Nov, 2017. Poster contribution. "Engineering bacterial cellulose during the biosynthesis."

XXXVI Reunión Bial de la RSEQ - June, 2017. Oral communication. "Engineering bacterial cellulose."

NANOTEC2016 (International Conference on Nanotechnology Applications) - Sept, 2016. Poster contribution. "Mesoporous silica nanoparticles as drug delivery systems: influence of the particle topology"

"Congreso de Estudiantes de Química de la Universidad de Alicante" - Nov, 2010. Oral communication. "A year of chemistry".



## Nanocellulose films with multiple functional nanoparticles in confined spatial distribution†

Cite this: *Nanoscale Horiz.*, 2019, 4, 634

Received 17th September 2018,  
Accepted 9th January 2019

DOI: 10.1039/c8nh00310f

rsc.li/nanoscale-horizons

Soledad Roig-Sanchez, <sup>a</sup> Erik Jungstedt, <sup>b</sup> Irene Anton-Sales, <sup>a</sup>  
David C. Malaspina, <sup>a</sup> Jordi Faraudó, <sup>a</sup> Lars A. Berglund, <sup>b</sup>  
Anna Laromaine <sup>a</sup> and Anna Roig <sup>\*a</sup>

Industries, governments and consumers increasingly request sustainable resources and greener routes for the integration of advanced functional nanocomposites in products and devices. Among renewable biopolymers, cellulose deserves special consideration since it is the most abundant one. While inorganic nanoparticles add functional properties to a nanocomposite, a flexible and porous cellulosic support will facilitate the interaction of the nanoparticles with the surroundings, their handling and recycling. A significant challenge is to develop high strength, flexible nanobiocomposites controlling the nanoparticle properties, their volume fraction and their topographic distribution within the scaffold. A new concept is presented here for multifunctional laminates where layers consist of bacterial cellulose fibrils decorated by inorganic nanoparticles. Each layer can provide a specific function using a different nanoparticle. As model systems, we have selected two metals (Au, Ag) and two semiconductors (TiO<sub>2</sub> and Fe<sub>2</sub>O<sub>3</sub>). Energy-efficient microwave-assisted synthetic routes have been used to *in situ* nucleate and grow the inorganic nanocrystals on the cellulose fibrils. Then, functionalized bacterial cellulose films can be arranged as laminates in a millefeuille construct simply by layering and drying the wet films at 60 °C. After drying, they perform as a single integrated and thicker film. Structural, functional and mechanical integrity of the laminates have been investigated. Molecular dynamics simulations were used to compute the surface adhesion energy between two cellulose fibrils and the results are discussed in light of the experimental peel-off data for the separation of the layers in the laminate.

### Conceptual insights

Unique properties of bacterial cellulose, specifically the nanometric dimensions of the chemically modifiable hydrophilic fibrils and the 3D interwoven nature of the pellicle network, have inspired a facile concept of creating multifunctional nanocellulose laminates. These constructs are based on layers of bacterial cellulose strongly bonded and with the cellulose fibrils in each layer decorated by specific inorganic nanoparticles, thus providing a topographic order of the particles resembling a flexible millefeuille. The approach enlarges the materials design scope for functional nanocelluloses so that several nanotechnologies could be integrated in one material. The proposed modular laminates can be *ad libitum* assembled by means of molecular scale cellulose–cellulose adhesion during film drying. Forces involved in the self-adhesive behavior of two layers have been experimentally computed using peel off tests and compared with values resulting from molecular dynamics simulation.

combine cellulose's properties with the high surface area of nanomaterials. Increasing demand for cost-effective renewable high-performance materials makes nanocelluloses attractive for advanced applications in many sectors ranging from photonics,<sup>1</sup> to food packaging,<sup>2</sup> flexible electronics<sup>3</sup> or health.<sup>4</sup> Cellulose nanocrystals and individual nanofibrils derived from plants are obtained after processing, which may require high energy and chemicals that are not eco-friendly. Another class of nanocellulose is bacterial cellulose (BC) that is readily produced in pure form by microorganisms. In BC, the elementary fibrils have a diameter between 1.5 and 3.5 nm, the microfibrils between 10 and 30 nm and the microfibrillar bands have a width of ~100 nm and many micrometres in length. In the present text, the term “fibril” is used for these fibrous entities. BC also presents higher crystallinity than cellulose fibrils from wood fibres or parenchyma cells (*i.e.*, 65–80% for BC compared to 40–55% for dissolved pulp).<sup>5</sup> Among the many organisms extracellularly producing cellulose, the bacteria *Komagataeibacter xylinus* (*K. xylinus*) is an extremely efficient one.<sup>6,7</sup>

During BC's biosynthesis in static conditions, high aspect ratio bacterial cellulose's fibrils are interwoven to form a stable and non-soluble 3D-porous network that grows as a flat film at the liquid-air interface also known as fleece or pellicle.

## 1. Introduction

Cellulose is an almost inexhaustible biopolymer of widespread use since prehistoric times. Interestingly, nanocelluloses

<sup>a</sup> Institut de Ciència de Materials de Barcelona (ICMAB), Campus UAB, Bellaterra, Catalonia, E-08193, Spain. E-mail: roig@icmab.es

<sup>b</sup> Department of Fiber and Polymer Technology, Wallenberg Wood Science Center, Royal Institute of Technology (KTH), SE-100 44 Stockholm, Sweden

† Electronic supplementary information (ESI) available: Experimental section, supplementary figures and videos. See DOI: 10.1039/c8nh00310f



Moreover, nanocomposites,<sup>8</sup> film microstructure<sup>9</sup> and non-flat 3D geometries<sup>10,11</sup> can also be attained during the biosynthetic process. Bacterial cellulose films are characterized by their light weight, transparency, thermal stability up to  $\sim 280$  °C, high mechanical flexibility and remarkably high tensile strength together with an exceptional liquid absorption capacity (up to 100 times its own weight in water), biocompatibility and non-immunogenicity.<sup>12</sup> Inorganic nanoparticles can be combined with the chemically modifiable cellulose nanofibrils to constitute new products and devices. Recent reviews have highlighted the preparation and applications of nanocelluloses (including bacterial cellulose) as versatile supports for nanoparticles to be applied in catalysis,<sup>13</sup> sensors,<sup>14</sup> functional food packaging,<sup>15</sup> or medical uses.<sup>16</sup> However, inhomogeneous particle disposition or weak nanoparticle attachment are major reported drawbacks.<sup>17,18</sup>

In this work, we increased the material design scope for multifunctional nanocellulose using a laminate concept that takes advantage of the self-adhesive behaviour of wet BC films upon drying. The laminate is formed by BC layers, which have different functions endowed by the specific inorganic nanoparticles decorating the cellulose fibres. Each layer spatially confines the nanoparticles across the whole cross-section of the film. Thus, the nanoparticle-decorated bacterial cellulose layers could be *ad libitum* arranged as a millefeuille laminate simply by drying the films in the desired order. Next, we assessed the functional and mechanical integrity of the millefeuille laminate. Specifically, we used confocal and electron microscopy to investigate the layer interfaces and a peel off test to evaluate surface adhesion energy between the different functional layers during delamination process. In addition, surface adhesion energy of two crystalline cellulose fibrils has been studied by molecular dynamic simulations and the results are discussed in light of the experimental peel off data.

## 2. Results and discussion

Functional cellulose nanocomposites are particularly attractive since the resulting nanomaterial can synergistically exploit the characteristics of both components; the electronic, optical, magnetic, catalytic or bioactivity properties provided by the nanoparticles and the outstanding structural characteristics of the bacterial cellulose (fibrous and mesoporous microstructure, flexibility and high fibre tensile strength, ...). The laminate created here contain different nanoparticles with complementary properties but also spatial confinement thus enlarging the materials design space for multifunctional nanocelluloses. Two metals (Au, Ag) and two semiconductors ( $\text{TiO}_2$  and  $\text{Fe}_2\text{O}_3$ ) were selected as model systems. Bacterial cellulose-based nanocomposites with Ag and  $\text{TiO}_2$  have been reported for antibacterial applications.<sup>19,20</sup>  $\text{TiO}_2$  and Au nanocomposites were applied in catalysis<sup>21–23</sup> while sensing applications were also reported for BC–Au.<sup>24</sup> BC with  $\text{Fe}_2\text{O}_3$  nanoparticles<sup>25,26</sup> was proposed as radio-frequency shielding materials,<sup>27</sup> anti-counterfeiting papers,<sup>28</sup> ultra-thin loudspeakers<sup>29</sup> or for heavy metal removal.<sup>30</sup>

In our approach, metal and metal oxide nanoparticles decorate the bacterial cellulose fibrils. This is accomplished by *in situ* preparation through energy efficient microwave-assisted syntheses. Microwave heating represents an attractive synthetic route for colloidal chemistry in terms of energy and reagents costs, due to the favourable kinetics and high yield resulting from the chemical reactions.<sup>31–33</sup> Compared to other heating methods, microwave radiation avoids temperature gradients within the vessel and promotes synchronic nucleation and growth. Moreover, the hydroxyl groups of the cellulose fibrils may act as selective nucleation sites providing homogeneous nanocrystal distribution in the material volume. We have previously shown that microwave-assisted thermal decomposition is an efficient and fast method to attain uniform and controllable iron oxide nanoparticles content in BC films while preserving the flexibility of the cellulose and avoiding leaching of the inorganic phase during the *in operando* conditions in liquids.<sup>25</sup> In this study, we have extended the approach to other nanoparticle (NP) systems (Au, Ag and  $\text{TiO}_2$ ) and developed a lamination strategy for multifunctional nanomaterials.

A detailed description on the bacterial cellulose harvesting, the microwave synthetic routes employed to functionalize the BC layers and their characterization are provided in the Experimental section of the ESI† Fig. 1A includes images of wet BC films composed with Ag,  $\text{TiO}_2$ ,  $\text{Fe}_2\text{O}_3$  and Au NPs. Films show a uniform characteristic colour from each nanoparticle. Scanning and transmission electron microscopy (SEM and TEM) micrographs show the cellulose ribbons decorated with the respective nanoparticles, Fig. 1B and C. Images evidence that the inorganic nanoparticles are homogeneously distributed along the fibrils. Differences in nanoparticle content are observed depending on the nanoparticle system and the reaction mechanism for each material (Table S1 contains the proposed reaction mechanism, ESI†). Moreover, by increasing the initial precursor concentration is possible to increase the final nanoparticle content in the films as shown in Table S1 (ESI†). Thermal gravimetric analysis (TGA) (Fig. S1, ESI†) quantifies the nanoparticle content of the nanocomposites (5, 33, 32, 3 wt% or 0.2, 2.7, 4.7, 0.6 vol% for Au, Ag,  $\text{Fe}_2\text{O}_3$  and  $\text{TiO}_2$  respectively). Fig. S1 (ESI†) also contains the TGA data for the same films after they were immersed in water for 30 days under gentle agitation. We can confirm that no leaching of the NP occurred, supporting their chemical bonding to the cellulose fibrils. From the TGA analysis it can also be noted that only  $\text{Fe}_2\text{O}_3$  acts as a catalyst in the pyrolysis reaction of the cellulose decreasing its degradation temperature by about 50 °C.

Fig. S2 (ESI†) depicts TEM images of the nanoparticles collected from the supernatant of the reaction. Selected area electron diffraction (SAED) data is provided, confirming the crystal structure of metallic gold and silver, the anatase phase for the titania and maghemite for the iron oxide. Particle size histograms computed from TEM images resulted in mean particle sizes of 7.5, 7.1 and 7.1 nm for Au,  $\text{TiO}_2$  and  $\text{Fe}_2\text{O}_3$  respectively with a maximum polydispersity index of 23%. A bimodal distribution was observed in the case of Ag nanoparticles with mean sizes of 8.2 and 40 nm, whilst sporadic dendritic larger sizes were also observed.



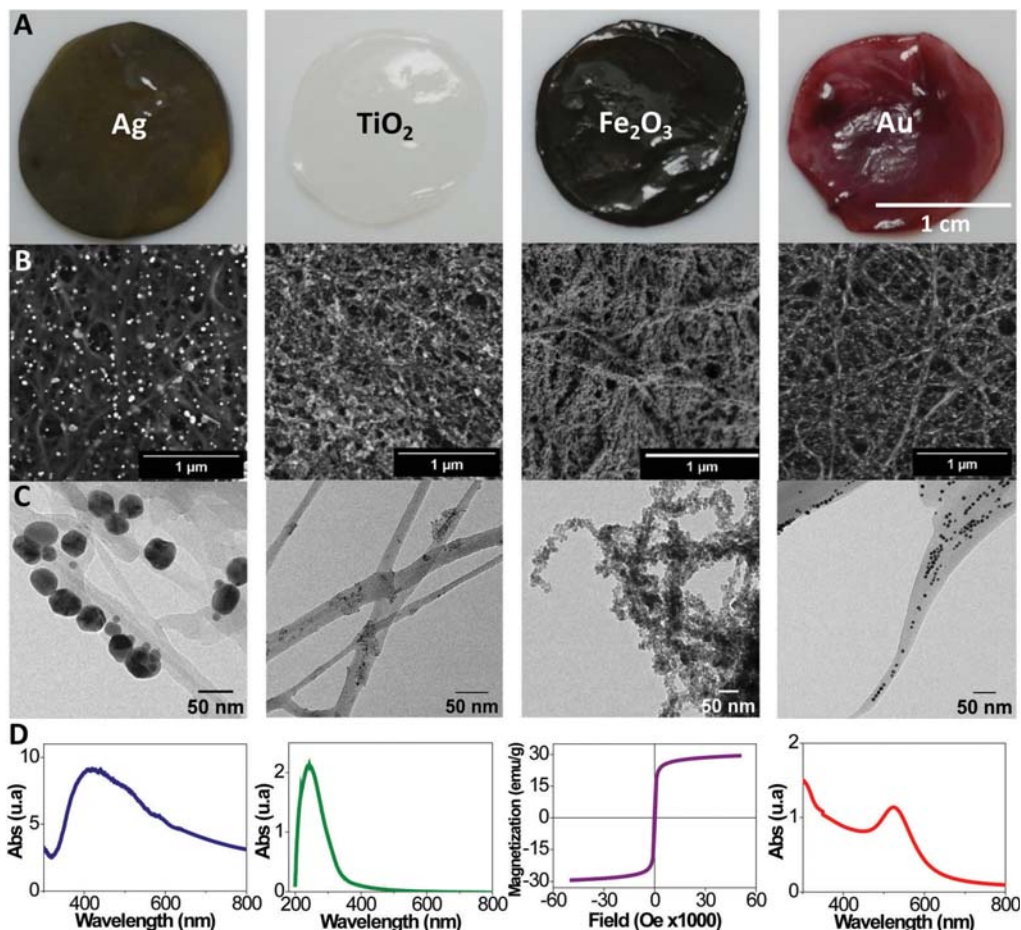


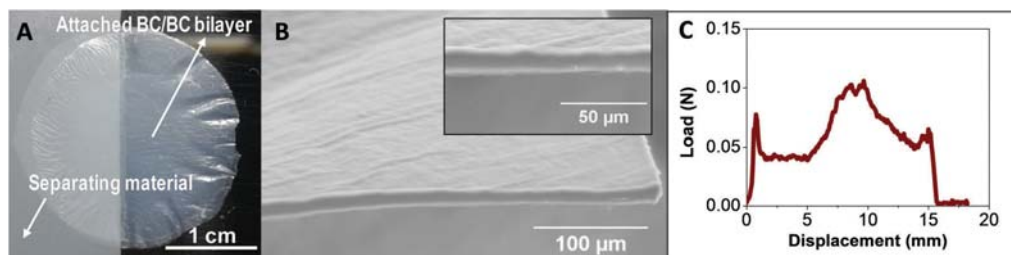
Fig. 1 (A) Bacterial cellulose films with different nanoparticles. (B) SEM images of the fibrils decorated with the nanoparticles where the size and distribution of the nanoparticles is more clearly apparent. (C) TEM images of the fibrils where the size and distribution of the nanoparticles is more clearly apparent. (D) UV-VIS absorption spectra of each nanocomposite. In the case of the BC/Fe<sub>2</sub>O<sub>3</sub>, the magnetization curve is shown instead.

Fig. 1D illustrates a functional characteristic of each film. Plasmon absorption bands are observed for BC/gold and BC/silver films respectively. The BC/Au shows a maximum at 525 nm as expected for ~10 nm gold particles.<sup>34</sup> A broad band for the BC/Ag, with a maximum at 420 nm and a smaller shoulder at 520 nm, indicates a larger particle size distribution for this material, and the presence of some anisotropic shaped particles such as triangles, hexagons and rods. Interestingly, by combining several plasmonic nanoparticles in one film or layering films of different metals, a multiplasmon film could be assembled. UV-absorption with a maximum at 242 nm is characteristic for the BC/TiO<sub>2</sub> composite. In turn, the BC/Fe<sub>2</sub>O<sub>3</sub> film displays superparamagnetic behaviour due to the superparamagnetic character of the small iron oxide nanoparticles decorating the cellulose fibrils. A saturation magnetization of 30 emu g<sup>-1</sup> is measured for the nanocomposite film, which is a rather high value for a nanocomposite with a non-magnetic matrix.

Next, we investigate the interfacial adhesion of two wet and native BC films dried on top of each other at 60 °C between two polytetrafluoroethylene (PTFE) plates using a Dynamic Mechanical Analysis (DMA) instrument. Fig. 2A shows a photograph of the resulting bilayer. Note that in order to perform the measurements half of the film is dried using a non-sticky paper between the two layers to prevent self-adhesion in this region. A SEM image of the bilayer cross section shows a smooth and continuous surface (Fig. 2B). The interface boundary between the two layers is not visible even in an enlargement of the cross section (inset of Fig. 2B). Thus, after drying, the two films look as a single thicker one.

Fig. 2C shows the peeling force as a function of the displacement. The curve depicts the behaviour of an increased load to achieve the initial displacement and more constant load with increasing displacement as the layers are peeled apart. We hypothesize that the drying facilitates a better adhesion towards the edges of the films so that the peeling crack is





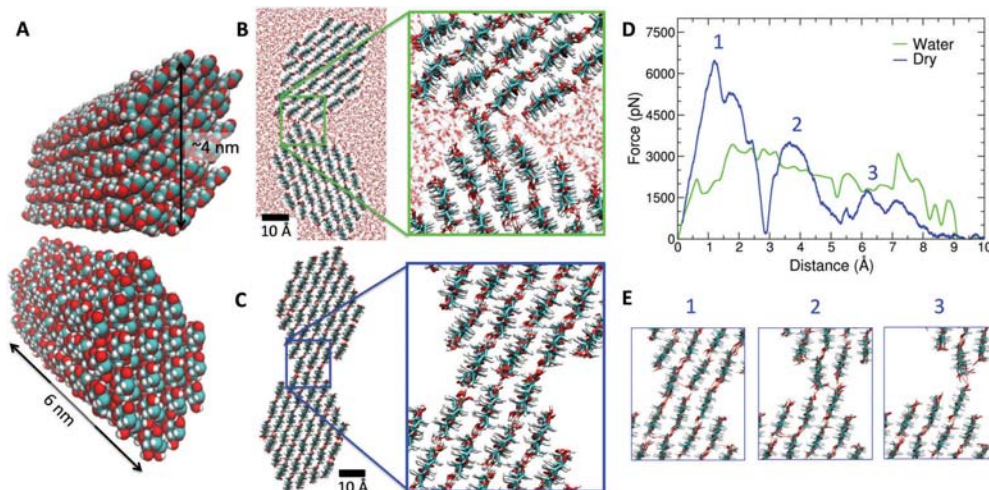
**Fig. 2** (A) Set-up for a peeling test sample. The BC films were dried at 60 °C one above the other and between PTFE plates. Half of the sample was well attached and half was dried with a non-sticking paper in between to be able to attach the two ends of the layers to the test machine. (B) SEM image of the cross section of the bilayer. Inset is a magnification of the cross section. The interface of the two films is not visible. (C) Force vs. displacement curve, the area under the curve represents the interfacial energy needed to separate the BC films after drying.

arrested and propagation continues inside one of the layers rather than at the interface between them. That is the reason we are able to observe increased forces at the second middle of the sample *i.e.*, at displacements of 10 and 15 mm (Fig. S3 (ESI<sup>†</sup>) contains a video of the peeling test experiment represented in Fig. 2C). A mean value for interfacial energy of 46 J m<sup>-2</sup> was computed by integrating the area under the curve averaged from three independent experiments. This value is about twice the value previously reported for microfibrillated cellulose films from plants.<sup>35</sup>

To gain insight into the microscopic nature of cellulose–cellulose adhesion, we performed a series of molecular dynamics simulations (see ESI<sup>†</sup> for technical details). In our simulations, we consider in full atomistic detail the adhesion of two elementary crystalline cellulose fibrils of 6 nm length (18 144 atoms), as shown in Fig. 3A. We then studied two situations, namely, the case of two fibrils in water (full hydration with ~16 000 water molecules) and

the case of dry conditions (no water). First, we determined their preferred configuration at 25 °C after adhesion (*i.e.* with the two fibrils in contact). The obtained equilibrium configuration shows substantial differences between the wet and dry scenarios (Fig. 3B and C). In the fully hydrated case, the two fibrils are in close proximity along a narrow strip but separated by water molecules, whereas in dry conditions the two fibrils adhere having a large contact surface along the fibrils. In dry conditions, the two fibrils tend to form aligned fibril–fibril hydrogen bonds, extending along the crystal structure. On the contrary, in the fully hydrated case, the two fibrils interact forming hydrogen bonds with water molecules at the cost of reducing the number of fibril–fibril hydrogen bonds.

Once the equilibrium configurations were determined, we performed pulling simulations in which the two fibrils were separated, allowing the calculation of the adhesion force as the



**Fig. 3** MD simulation results at 25 °C. (A) Image of the atomic model for two bacterial cellulose fibrils with atoms shown in van der Waals size. The colour scheme is CPK (O in red, C in cyan and H in white). (B) Cross section view of the equilibrated configuration of the two fibrils in water at 25 °C. (C) Same as (B) but in dry conditions (no water). The inset denoted the increased contact surface, as compared with (B). (D) Adhesion force between the fibrils (in picoNewton, pN) as a function of the separation between the fibrils obtained in biased MD simulations in dry (blue line) and wet (green line) conditions. In dry conditions, three different particular events are indicated with numbers in the force curve. (E) Snapshots of the fibril–fibril interface corresponding to the events indicated by numbers in the force curve in (D). All snapshots were made using the VMD program.<sup>36</sup>



force required to detach completely the fibrils. In Fig. 3D, we show the force needed to detach the fibrils in both cases (full hydration and dry fibrils), from contact as starting position (configurations shown in Fig. 3B and C) to full separation. In dry conditions, simulations indicate that a force of  $\sim 6500$  pN is required to separate the fibrils (first peak highlighted in Fig. 3D). Interestingly, the dry fibrils separate in three stages (see the three peaks indicated in Fig. 3D), corresponding to the three alignments of hydrogen bonds between the fibrils shown in Fig. 3E. Each stage or event indicated in Fig. 3E corresponds to a peak in the force curve (Fig. 3D). In the first stage, a force of  $\sim 6500$  pN is required, whereas a smaller force of  $\sim 2000$  pN is needed in the third (and last) stage with only one hydrogen bond per contact to break (see Fig. 3E). In the simulations with fully hydrated cellulose fibrils, one third of the force ( $\sim 2000$  pN) is required to separate the two fibrils and the three stages or events observed in the pulling of dried fibrils (Fig. 3E) do not appear. As discussed above, the number of hydrogen bonds between hydrated fibrils is smaller than in the case of dry conditions due to the competition between fibril–fibril and water–fibril hydrogen bonds. Thus, our atomistic simulations of crystalline cellulose fibrils provide a physical, microscopic mechanism for the increase of adhesion energy due to drying. According to our simulations, it is due to a stronger contact and a larger number of hydrogen bonds between fibrils favoured by the absence of water. The value of the maximum force observed in Fig. 2C ( $\sim 0.10$  N) is comparable with having  $\sim 10^7$  aligned fibril–fibril contacts in dry conditions as the ones observed in Fig. 3C. Other complex factors not considered in the model (contacts in different orientations, entanglements, pore swelling/contraction) might also modulate the value of adhesion forces, but their consideration in the simulations is beyond the capabilities of atomistic models.

To elucidate if BC films containing nanoparticles also display such strong self-adhesive behaviour, two BC films with inorganic nanoparticles were dried together (Fig. 4A). Peel off tests were undertaken for bilayers either combining the same

metal (BC/Au–BC/Au, BC/Ag–BC/Ag), two different metals (BC/Au–BC/Ag) or a semiconductor and a metal (BC/TiO<sub>2</sub>–BC/Ag). From one side, the inclusion of nanoparticles in the BC fibrils increases the roughness of the film as estimated from AFM data in the case of BC/TiO<sub>2</sub> (rms roughness values:  $\sim 0.20$   $\mu\text{m}$  for BC/TiO<sub>2</sub> and  $\sim 0.08$   $\mu\text{m}$  for BC). On the other hand, nanoparticles might obstruct hydrogen–hydrogen interaction by either spacing the fibrils or decreasing the amount of hydroxyls on the cellulose fibril surface. The BC/Ag–BC/TiO<sub>2</sub> bilayer resulted in an adhesion energy equal to the neat BC bilayer ( $46$   $\text{J m}^{-2}$ ). This indicates that the hindering effects from the NPs decoration are compensated by the increase in roughness. Slightly smaller values are found by the BC/Au–BC/Au ( $33$   $\text{N m}^{-1}$ ) and the BC/Au–BC/Ag bilayers ( $34$   $\text{J m}^{-2}$ ) suggesting that the polymeric surfactants used in the metal nanoparticles synthesis (polyvinylpyrrolidone for silver, oleylamine for gold) may influence the strength of adhesion between two layers. A significantly smaller value ( $10$   $\text{J m}^{-2}$ ) was found for the silver bilayer. We believe that the larger size of the silver nanoparticles inhibits a more intimate contact of the bacterial cellulose nanofibrils upon drying. Interestingly, confocal microscopy of the bilayer BC/Ag with BC/TiO<sub>2</sub> shows an integrated interface between the two films where the interface cannot be distinguished even though the image is obtained with the film submerged in water (rewetted). Fig. 4 collects the information regarding the bilayered materials. The flexibility during manual bending of all BC/nanoparticle dried films and of the bilayers was comparable to that of pristine BC, except for BC/Fe<sub>2</sub>O<sub>3</sub>, which showed a more brittle behaviour. This is attributed to the higher particle content (4.7 vol%), which is more than twice the content in other BC/NP samples).

Finally, we extended the bilayer approach to a millefeuille construct comprising four BC layers, each containing a different type of inorganic nanoparticle. The resulting multifunctional material behave as one film ( $\sim 50$   $\mu\text{m}$ ) with the different nanoparticles geometrically confined in each layer. Fig. 5 shows a BC/Ag–BC/TiO<sub>2</sub>–BC/Fe<sub>2</sub>O<sub>3</sub>–BC/Au film, and Fig. S4 (ESI†) depicts other layering types confirming that the layers can be

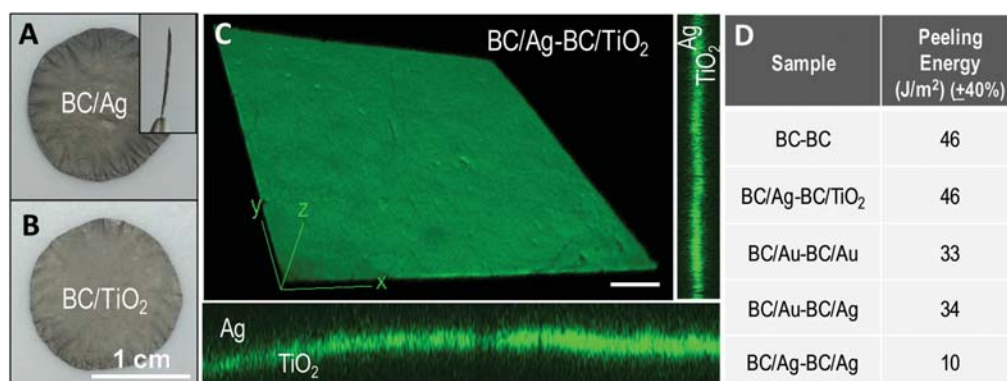


Fig. 4 (A) BC/Ag side of a bilayer BC/Ag–BC/TiO<sub>2</sub>. Inset: Cross view of the thickness of the material ( $34 \pm 3$   $\mu\text{m}$ ). (B) BC/TiO<sub>2</sub> side of the same bilayer. (C) Confocal microscope image of the bilayer with the Ag layer on top. Thickness is  $84$   $\mu\text{m}$  for the rewetted bilayer. The small images show the z-axis along x and y. Scale bar:  $200$   $\mu\text{m}$ . (D) Peeling energy values for various bilayer combinations.





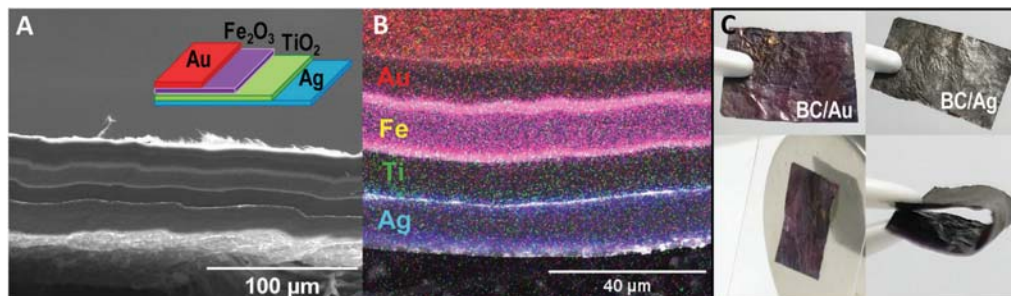


Fig. 5 (A) Milleduille scheme of one of the possible configurations and SEM image of the cross section with the four layers of similar thicknesses visible due to the different contrasts of the nanoparticles. (B) EDX scan confirming the confined location of the different nanoparticles. (C) Upper panels: Milleduille construct (1 cm × 1.5 cm) showing the two exterior, Au and Ag, layers. Lower panel: The milleduille responding to a FeNdB permanent magnet (3 cm of diameter × 8 mm width) and the folded film without any apparent signs of mechanical failure.

laminated *ad libitum*. The layer stacking order would be determined by the final application envisioned for the material, *i.e.*, if antibacterial properties are important, then the BC/Ag layer will be placed outside, but if the relevant property is the plasmonic characteristic of the nanosilver then the BC/Ag layer can be a hidden one. Moreover, for some applications, the dielectric materials may be placed in between the metal layers (configuration shown in Fig. 5A) as it would be in a condenser set-up while for other applications, alternating the metals with the semiconductors might be the preferred sequence. Note that although the present concept is generic, the potential for laminated structures in multifunctional sensors may be particularly interesting. A SEM image of the milleduille cross section with an electron dispersive X-ray (EDX) mapping analysis is depicted in Fig. 5B. The distribution of nanomaterials is

apparent. Fig. 5C shows the two sides of the milleduille, BC/Au with the characteristic red/violet coloration of small gold particles and the reverse side with the grey colour given by the silver particles. Fig. 5C also shows the response of the material to a permanent magnet even when the BC/Fe<sub>2</sub>O<sub>3</sub> is not in the outside part, as in this particular stacking order. The bending performance of the film is also illustrated.

Fig. S5 (ESI<sup>†</sup>) contains three videos showing the flexibility of the laminate construct and the good adhesion between the layers demonstrated by the absence of delamination during stringent manipulation (continuous pulling and bending) in the dry form and even after rewetting the construct for up to one week. Interestingly after one week in water and the harsh handling, a corner of the two metal layers was delaminated and by pulling it carefully, the films could be recovered intact (results not shown).

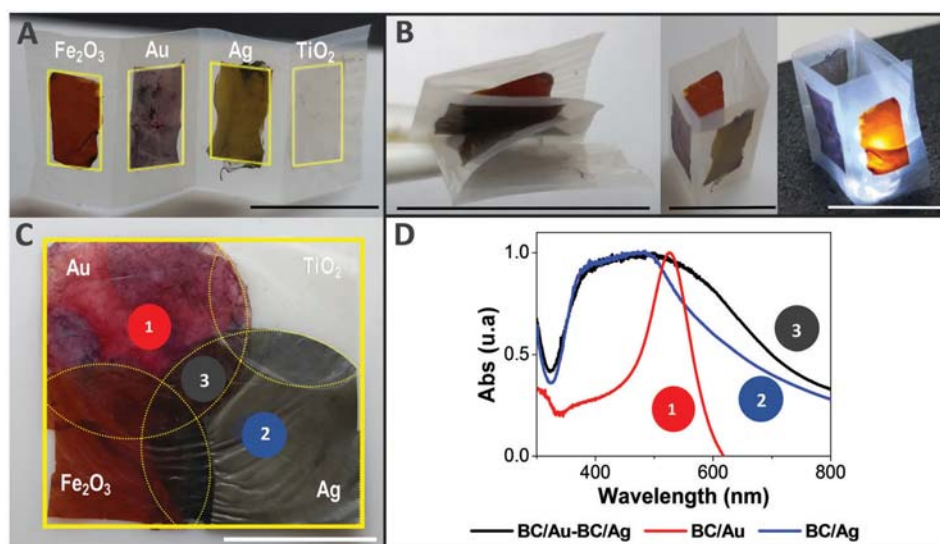


Fig. 6 (A) Planar configuration where BC films nanocomposited with metal and metal oxide nanoparticles are attached to a pristine BC film. (B) Versatility of the configuration made upon flexibility or creating 3D structures. (C) Configuration where single, double and triple multifunctionalities can be achieved on demand. (D) UV-VIS of the configuration shown in the scheme on (C). Scale bar = 1 cm.



Other interesting configurations are displayed in Fig. 6 to demonstrate the versatility of the approach. In the upper panel, Fig. 6A and B, a bilayer construct is displayed. It was made by drying layers of BC/NP over a pristine BC film, forming a strip of linearly arranged functionalities supporting the folding, or standing up as a 3D structure. The lower panel (Fig. 6C) shows another arrangement where single, double or triple functionalities coexist. Fig. 6D depicts the plasmon absorption spectra at the three points marked in Fig. 6C. Interestingly, in a single film one can measure different plasmon resonances spatially distributed or superimposed.

### 3. Conclusions

A concept of laminated multifunctional nanocellulose films has been developed, which is based on layers of bacterial cellulose strongly attached and with the fibrils in each layer decorated by specific inorganic nanoparticles. This millefeuille concept greatly enlarges the design space for multifunctional nanocellulose materials so that several nanotechnologies could be integrated in one material. The inorganic nanoparticles are strongly bonded to the fibrils by energy-efficient microwave-assisted synthesis routes. This method was previously reported for iron oxide, but was here extended to titania, gold and silver nanoparticles.

The proposed modular laminate could be *ad libitum* assembled by means of molecular scale cellulose–cellulose bond formation during cellulose film drying. This is possible because the unique properties of bacterial cellulose, namely, the nanometric dimensions of the fibrils allowing strong fibril–fibril interaction after drying. In addition, the 3D network nature of high-strength BC ribbons obtained from biosynthesis provides excellent mechanical integrity of the layers and of the final multifunctional laminate. The adhesion energy involved in the self-adhesive behaviour of two layers has been experimentally determined using peel off tests and related to values resulting from molecular dynamics simulations of different cases.

In this study, we have shown the viability of the methodology by presenting data for various  $\sim 50 \mu\text{m}$  thick films constituted by up to four types of particles spatially confined in orderly manner across the film cross section. Thus, flexible nanocomposites from renewable sources with controlled nanoparticle properties were obtained. The topographic distribution of nanoparticles was controlled, as well as the volume fraction of particles within the porous scaffold, using simple approaches. The presented route paves the way to combining multiple functionalities and geometrical shapes in flexible cellulose-based substrates. Only a few examples of the concept have been outlined here, but multifunctional sensors, nanostructured devices and reactors for multiple catalytic effects are of interest, where specific functions are confined to spatially well-defined locations.

### Conflicts of interest

There are no conflicts to declare.

### Acknowledgements

Authors acknowledge the financial support from the Spanish Ministry of Science, Innovation and Universities through the MAT2015-64442-R project, the ‘Severo Ochoa’ Programme for Centers of Excellence in R&D (SEV-2015-0496) and the PhD scholarships of S. R. (BES-2016-077533) and I. A. (BE-2016-076734) and the Generalitat de Catalunya for the 2017SGR765 project. D. C. M. is supported by the European Union’s horizon 2020 research and innovation programme under Marie Skłodowska-Curie grant agreement No. 6655919. We thank CESGA Supercomputing center for technical support and computer time at the supercomputer Finisterrae II. The Wallenberg Wood Science Center is acknowledged for funding of KTH activities.

### References

- 1 A. Espinha, C. Dore, C. Matricardi, M. I. Alonso, A. R. Goñi and A. Mihi, *Nat. Photonics*, 2018, **12**, 343–348.
- 2 F. Li, E. Mascheroni and L. Piergiovanni, *Packag. Technol. Sci.*, 2015, **28**, 475–508.
- 3 Y. H. Jung, T.-H. Chang, H. Zhang, C. Yao, Q. Zheng, V. W. Yang, H. Mi, M. Kim, S. J. Cho, D.-W. Park, H. Jiang, J. Lee, Y. Qiu, W. Zhou, Z. Cai, S. Gong and Z. Ma, *Nat. Commun.*, 2015, **6**, 7170.
- 4 T. Tronser, A. Laromaine, A. Roig and P. A. Levkin, *ACS Appl. Mater. Interfaces*, 2018, **10**, 16260–16269.
- 5 D. Klemm, B. Heublein, H.-P. Fink and A. Bohn, *Angew. Chem., Int. Ed.*, 2005, **44**, 3358–3393.
- 6 D. Klemm, E. D. Cranston, D. Fischer, M. Gama, S. A. Kedzior, D. Kralisch, F. Kramer, T. Kondo, T. Lindström, S. Nietzsche, K. Petzold-Welcke and F. Rauchfuß, *Mater. Today*, 2018, **21**, 720–748.
- 7 T. Abitbol, A. Rivkin, Y. Cao, Y. Nevo, E. Abraham, T. Ben-Shalom, S. Lapidot and O. Shoseyov, *Curr. Opin. Biotechnol.*, 2016, **39**, 76–88.
- 8 D. Abol-Fotouh, B. Dörling, O. Zapata-Arteaga, X. Rodríguez-Martínez, A. Gómez, J. S. Reparaz, A. Laromaine, A. Roig and M. Campoy-Quiles, *Energy Environ. Sci.*, 2019, DOI: 10.1039/c8ee03112f.
- 9 Y. Guo, K. Zheng and P. Wan, *Small*, 2018, **14**, 1704497.
- 10 A. Laromaine, T. Tronser, I. Pini, S. Parets, P. A. Levkin and A. Roig, *Soft Matter*, 2018, **14**, 3955–3962.
- 11 L. G. Greca, J. Lehtonen, B. L. Tardy, J. Guo and O. J. Rojas, *Mater. Horiz.*, 2018, **5**, 408–415.
- 12 M. Zeng, A. Laromaine and A. Roig, *Cellulose*, 2014, **21**, 4455–4469.
- 13 M. Kaushik and A. Moores, *Green Chem.*, 2016, **18**, 622–637.
- 14 H. Golmohammadi, E. Morales-Narváez, T. Naghdi and A. Merkoçi, *Chem. Mater.*, 2017, **29**, 5426–5446.
- 15 H. M. C. Azeredo, M. F. Rosa and L. H. C. Mattoso, *Ind. Crops Prod.*, 2017, **97**, 664–671.
- 16 N. Lin and A. Dufresne, *Eur. Polym. J.*, 2014, **59**, 302–325.
- 17 H. Wei, K. Rodriguez, S. Renneckar and P. J. Vikesland, *Environ. Sci.: Nano*, 2014, **1**, 302–316.
- 18 W. Hu, S. Chen, J. Yang, Z. Li and H. Wang, *Carbohydr. Polym.*, 2014, **101**, 1043–1060.



- 19 S. Pal, R. Nisi, M. Stoppa and A. Licciulli, *ACS Omega*, 2017, **2**, 3632–3639.
- 20 A. Alonso-Diaz, J. Floriach-Clark, J. Fuentes, M. Capellades, N. S. Coll and A. Laromaine, *ACS Biomater. Sci. Eng.*, 2019, DOI: 10.1021/acsbomaterials.8b01171.
- 21 N. Dal'acqua, A. B. De Mattos, I. Krindges, M. B. Pereira, H. Da Silva Barud, S. J. L. Ribeiro, G. C. S. Duarte, C. Radtke, L. C. Almeida, M. Giovanela, J. Da Silva Crespo and G. Machado, *J. Phys. Chem. C*, 2015, **119**, 340–349.
- 22 M. Chen, H. Kang, Y. Gong, J. Guo, H. Zhang and R. Liu, *ACS Appl. Mater. Interfaces*, 2015, **7**, 21717–21726.
- 23 S. Khan, M. Ul-Islam, W. A. Khattak, M. W. Ullah and J. K. Park, *Cellulose*, 2015, **22**, 565–579.
- 24 C. J. Smith, D. V. Wagle, H. M. O'Neill, B. R. Evans, S. N. Baker and G. A. Baker, *ACS Appl. Mater. Interfaces*, 2017, **9**, 38042–38051.
- 25 M. Zeng, A. Laromaine, W. Feng, P. A. Levkin and A. Roig, *J. Mater. Chem. C*, 2014, **2**, 6312–6318.
- 26 R. T. Olsson, M. A. S. A. Samir, G. Salazar-Alvarez, L. Belova, V. Ström, L. A. Berglund, O. Ikkala, J. Nogués and U. W. Gedde, *Nat. Nanotechnol.*, 2010, **5**, 584–588.
- 27 M. Vural, B. Crowgey, L. C. Kempel and P. Kofinas, *J. Mater. Chem. C*, 2014, **2**, 756–763.
- 28 E. Hendrick, M. Frey, E. Herz and U. Wiesner, *J. Eng. Fibers Fabr.*, 2010, **5**, 21–30.
- 29 S. Galland, R. L. Andersson, M. Salajková, V. Ström, R. T. Olsson and L. A. Berglund, *J. Mater. Chem. C*, 2013, **1**, 7963.
- 30 H. Zhu, S. Jia, T. Wan, Y. Jia, H. Yang, J. Li, L. Yan and C. Zhong, *Carbohydr. Polym.*, 2011, **86**, 1558–1564.
- 31 M. Baghbanzadeh, L. Carbone, P. D. Cozzoli and C. O. Kappe, *Angew. Chem., Int. Ed.*, 2011, **50**, 11312–11359.
- 32 I. Bilecka, P. Elser and M. Niederberger, *ACS Nano*, 2009, **3**, 467–477.
- 33 O. Pascu, E. Carenza, M. Gich, S. Estradé, F. Peiró, G. Herranz and A. Roig, *J. Phys. Chem. C*, 2012, **116**, 15108–15116.
- 34 W. Haiss, N. T. K. Thanh, J. Aveyard and D. G. Fernig, *Anal. Chem.*, 2007, **79**, 4215–4221.
- 35 H. Lönnberg, L. Fogelström, Q. Zhou, A. Hult, L. Berglund and E. Malmström, *Compos. Sci. Technol.*, 2011, **71**, 9–12.
- 36 W. Humphrey, A. Dalke and K. Schulten, *J. Mol. Graphics*, 1996, **14**, 33–38.





Cite this: *Biomater. Sci.*, 2021, **9**, 3040

## *In vivo* soft tissue reinforcement with bacterial nanocellulose†

Irene Anton-Sales,  ‡<sup>a</sup> Soledad Roig-Sanchez,  ‡<sup>a</sup> Kamelia Traeger,  <sup>b</sup> Christine Weis,  \*<sup>b</sup> Anna Laromaine,  <sup>a</sup> Pau Turon  <sup>b</sup> and Anna Roig  \*<sup>a</sup>

The use of surgical meshes to reinforce damaged internal soft tissues has been instrumental for successful hernia surgery; a highly prevalent condition affecting yearly more than 20 million patients worldwide. Intraoperative adhesions between meshes and viscera are one of the most threatening complications, often implying reoperation or side effects such as chronic pain and bowel perforation. Despite recent advances in the optimization of mesh porous structure, incorporation of anti-adherent coatings or new approaches in the mesh fixation systems, clinicians and manufacturers are still pursuing an optimal material to improve the clinical outcomes at a cost-effective ratio. Here, bacterial nanocellulose (BNC), a bio-based polymer, is evaluated as a soft tissue reinforcement material regarding mechanical properties and *in vivo* anti-adhesive performance. A double-layer BNC laminate proved sufficient to meet the standards of mechanical resistance for abdominal hernia reinforcement meshes. BNC-polypropylene (BNC-PP) composites incorporating a commercial mesh have also been prepared. The *in vivo* study of implanted BNC patches in a rabbit model demonstrated excellent anti-adherent characteristics of this natural nanofibrous polymer 21-days after implantation and the animals were asymptomatic after the surgery. BNC emerges as a novel and versatile hernioplasty biomaterial with outstanding mechanical and anti-adherent characteristics.

Received 7th January 2021,  
Accepted 23rd February 2021

DOI: 10.1039/d1bm00025j

rsc.li/biomaterials-science

## 1. Introduction

Abdominal hernias occur when internal organs protrude through weakened zones of the abdominal cavity. To date, surgical intervention is the only effective approach to repair such a highly prevalent condition that yearly affects more than 20 million patients worldwide.<sup>1</sup> Instrumental for successful hernia surgery has been the use of surgical meshes (*i.e.* hernioplasty) to reinforce the damaged region. Those implants are predominantly manufactured from synthetic polymers, mainly polypropylene (PP), and aim at providing mechanical support to the herniated area. Implantation of a non-resorbable PP-mesh has become the standard procedure for hernia repair, however, complications related to mesh implantation such as seroma, adhesions, chronic severe pain and infections are driving constant innovation in the field.<sup>2,3</sup>

Adhesions developed between PP-mesh and viscera, as a result of tissue reaction due to foreign body implant, are particularly threatening since they often cause complicated re-operations in the previously implanted area, increasing the surgical risk and the chances of suffering side effects such as chronic pain and bowel perforation.<sup>4</sup> High rates of adhesion are reported in approx. 15% of the cases one year after surgery, resulting in a high burden to healthcare systems.<sup>5</sup> Aiming to reduce the complications caused by those intraoperative adhesions, research efforts have been focused on improving the characteristics of PP meshes. Strategies include the optimization of mesh porous structure,<sup>6</sup> incorporation of anti-adherent coatings and improvements of mesh fixation systems (*i.e.* glueing).<sup>7,8</sup> Besides, multi-component grafts have been advocated as a well-suited strategy to isolate the PP mesh from the viscera by adding an additional layer of a synthetic<sup>9,10</sup> or natural biomaterial<sup>11,12</sup> that acts as an anti-adherent barrier. Despite recent advances, clinicians and manufacturers are still pursuing an optimal mesh to improve the clinical outcome and the cost-effectiveness ratio of hernioplasty procedures by leveraging the selection of materials, porous structure, mechanical resistance, anti-adhesive properties, biocompatibility, long term mechanical stability, tissue integration and conformability.<sup>13</sup>

Considering the requirements of hernia repair implants, the bio-based polymer bacterial nanocellulose (BNC) could be

<sup>a</sup>Institute of Materials Science of Barcelona (ICMAB-CSIC), Campus UAB, 08193 Bellaterra, Catalonia, Spain. E-mail: anna.roig@csic.es

<sup>b</sup>Department of Research and Development, B. Braun Surgical, S.A.U., Carretera de Terrassa 121, Rubí, 08191 Barcelona, Spain. E-mail: christine.weis@bbraun.com

†Electronic supplementary information (ESI) available. See DOI: 10.1039/d1bm00025j

‡Authors with equal contribution



deemed as a strong candidate for the above-mentioned tissue reinforcement application.<sup>14</sup> BNC is biotechnologically produced as a highly pure, non-soluble nanocellulose fibrillary network entrapping a large amount of liquid and exhibiting excellent mechanical properties.<sup>15–17</sup> These attributes have enabled an ever-increasing number of bio-applications in wound dressing and drug delivery.<sup>18–20</sup> Moreover, BNC is emerging as a high-performing alternative to repair other defects where non-biodegradable implants are desirable, such as damage of the dura mater,<sup>21</sup> the eardrum<sup>22</sup> or as an anti-fibrotic agent for cardiac implants.<sup>23</sup> As for soft tissue reinforcement, a hybrid biomaterial combining BNC with PP-meshes and its *in vitro* low adhesion properties has recently been described.<sup>24</sup> Besides, Zharikov and co-workers compared the anti-adhesive behaviour of BNC with PP meshes revealing a lower occurrence of adhesion in BNC-implanted dogs together with the absence of infections.<sup>25</sup> For that study, wet native BNC pellicles were employed and no mechanical tests were carried out. In more recent work, Rauchfuß *et al.* tested two surgical methods to implant wet BNC into the abdominal wall of rats.<sup>26</sup> These authors observed adhesion formation when using BNC as an abdominal wall replacement together with a tissue reaction assessed to be of low clinical significance. Interestingly, this work provides mechanical testing of BNC after explantation showing variable values and calling for future work on the suitability of BNC for hernia repair in terms of mechanical properties. These studies, although preliminary, concur with the absence of major postoperative complications and emphasize the underexploited potential of BNC in herniology.

Our work aims at providing further insight into the prospects of BNC for hernia repair surgery. To expand on the mechanical suitability of BNC for soft tissue reinforcement, the mechanical performance of several types of BNC implants –dry and wet forms as well as single to triple-layered BNC constructs– are evaluated. Furthermore, an *in vivo* study based on a novel animal model (rabbit) and the implantation of dry BNC is presented to demonstrate the anti-adherent properties of BNC.

## 2. Materials and methods

### 2.1 Bacterial nanocellulose (BNC) production

BNC films were obtained as previously described in Roig-Sanchez S. *et al.*<sup>27</sup> In brief, *Komagataeibacter xylinus* (*K. xylinus*) strain (NCIMB 5346, from CECT, Spain) was inoculated on 6 mL of Hestrin-Schramm (HS) fresh medium and expanded for 7 days at 30 °C. HS medium was prepared as follows: 5 g peptone, 5 g yeast, 20 g dextrose (Conda Lab), 1.15 g citric acid and 6.8 g Na<sub>2</sub>HPO<sub>4</sub>·12H<sub>2</sub>O (Sigma-Aldrich) per 1 L of Milli-Q (MQ) water. Then, 0.5 mL of the mixture was transferred to 4.5 mL of fresh HS medium and let to proliferate for another three days. Finally, bacteria were diluted to a proportion 1:14 inoculum:HS medium and 65 mL were cultivated for 6 days in 12 × 12 cm plates (Labbox polystyrene Petri

dishes) at 30 °C. The square BNC pellicles formed at the liquid-air interface of the wells were harvested and cleaned 10 minutes in a 50% ethanol-water solution, twice with boiling water for 20 min and twice with 0.1 M NaOH (Sigma-Aldrich) at 90 °C for 20 min. Lastly, the films were washed with MQ water until neutralization and sterilized by autoclave (121 °C, 20 min). To obtain the dry and flat BNC films used in the mechanical and *in vivo* tests, BNC hydrogels were placed between two Teflon papers at 60 °C and with a 2 kg weight on top for 12 h as previously described.<sup>27</sup> Systems with two and three BNC layers were prepared by drying size-matched BNC pellicles in close contact following the same procedure. To achieve a smooth interface between the BNC films, the superficial water was removed by blotting BNC with filter paper and air bubble formation was avoided by applying manual pressure. BNC-PP composites were prepared similarly by placing fragments of PP meshes (Optilene® Mesh Elastic and Optilene® Mesh LP both from B. Braun Surgical, S.A.U., Spain), knitted with different pore sizes, in between two wet BNC films. The size of the BNC layers was larger than the PP meshes to allow the self-adhesion between BNC films to occur during drying.

### 2.2 Scanning electron microscopy (SEM)

For the SEM characterization of the native wet BNC structure, BNC hydrogels were supercritically dried (SC). For that, the as-obtained BNC films were placed within filter paper sheets and were subjected to a water-to-ethanol solvent exchange process. After two transfers of 3 h in absolute ethanol, the films were moved to a fresh ethanol bath, kept overnight and the resulting alcogel was dried by SC drying. SC drying was performed on a 300 mL capacity autoclave filled with ethanol which was pressurized to 100 bar at room temperature. Liquid CO<sub>2</sub> was dispensed for 1.5 h with a flow of 1 kg h<sup>-1</sup> to exchange the solvent. Then, the reactor was heated up to 45 °C to reach supercritical conditions and supercritical CO<sub>2</sub> was pumped for 1 h keeping the same flow rate. Finally, the vessel was slowly depressurized to avoid pore collapse and BNC aerogels were obtained. For the SEM analysis of dry films, BNC hydrogels were dried as described in section 2.1.

FEI Magellan 400L XHR SEM under a high vacuum, with an acceleration voltage of 2 kV, current of 0.10 nA and a working distance of 5 mm was used to study the morphology of SC dried and dry BNC. The material was fixed with adhesive carbon tape on top of aluminium SEM holders. Dry BNC was sputtered with 5 nm Pt. BNC fibre diameter was calculated as the mean of 100 measurements obtained using Image-J software.

Cross-section images of multi-layered constructs were obtained with FEI Quanta 650GEG-ESEM under low vacuum conditions, an acceleration voltage of 20 kV, an electron beam spot of 4–5 and a working distance of 10 mm. Samples were cut with a PTFE coated blade (Personna GEM single edge, 3-facet stainless steel, 0.23 mm) and placed on holders with a 90° tilt.



### 2.3 Mechanical studies

Each BNC sheet was cut in  $20 \times 50$  mm pieces and the weight, size and thickness were measured with an Acculab Atilon ATL-244-1 analytical balance, Stanley Millesimal rule and Mitutoyo 543-250B micrometer respectively. Results were computed from five replicas. Surface weight was calculated as the ratio between weight and area. Wet BNC samples were deposited on a filter paper to remove the excess of water and measurements were performed when the material was still wet. The thickness of the films was measured in the middle of the specimens. For wet samples, the plunger of the micrometer was lifted and lowered three times and the thickness was obtained when the value was stable for more than 2 s during the third time.

Zwick Z2.5 dynamometer with a load cell of 2.5 kN was used for tensile experiments. The clamps were metallic with a pneumatic flat rubber part in contact with the sample. The test velocity was  $100 \text{ mm min}^{-1}$ , the pressure of the clamps was 6 bars and the distance between them was 20 mm. The preload applied was 0.05 N. Strain and resistance to tearing ( $F_{\text{max}}$ ) values were acquired.

Multi-layered systems were immersed in a 0.9% NaCl solution for 5 min for rehydration before the tensile study. Excess of liquid was removed as described before and water uptake ( $H_2O_{\text{up}}$ ) percentage was calculated as  $(m_w - m_d)/m_d \times 100$ , where  $m_w$  is the weight of the wet sample after hydration and  $m_d$  is the weight of the dry sample before hydration. Surface weight, calculated as the ratio between dry weight and area, and thickness were obtained before the rehydration.

### 2.4 *In vivo* study

A scheme of the steps to BNC implantation is depicted in Fig. 4A. This study was conducted by FREY-TOX GmbH (Herzberg, Germany), a DAkkS (national accreditation body of Germany) accredited laboratory according to EN ISO/IEC 17025 and European guidelines 93/42/EWG as well as 90/385/EWG.

**2.4.1. BNC implant preparation.** Dry BNC patches were cut to a size of  $7 \times 3$  cm with scissors and sterilized by a routine ethylene oxide (EtOx) cycle from B. Braun Surgical S.A.U. to sterilise non-absorbable meshes. Sterility was confirmed by submerging the EtOx-treated BNC into liquid culture medium for 14 days without detecting the appearance of turbidity. The resistance of the biomaterial to the EtOx cycle was assessed by Fourier-Transform Infrared Spectroscopy (FTIR) (Fig. S1†).

**2.4.2. *In vivo* model.** The *in vivo* implantation study was performed in five female SPF albino rabbits of the stock New Zealand White (Envigo, 58" Venray Netherlands). The animals had a bodyweight from 3.4 to 4.2 kg. An acclimatization period of at least 5 days was allowed. General anaesthesia was induced by intramuscular injection of  $35\text{--}40 \text{ mg kg}^{-1}$  ketamine and  $5\text{--}6 \text{ mg kg}^{-1}$  xylazine (Serumwerke Bernburg AG, Bernburg, Germany). This rabbit species was chosen because of its convenient body proportion and proved suitability for studying hernia repair materials including meshes.<sup>28</sup>

In the literature, it is described that most post-surgical adhesion formation takes place approximately until day 8 post-

implantation.<sup>29</sup> Hence, the follow-up time was set at 21-days based on our previous work endorsing it as a sufficient period to observe mature adhesions in an advanced healing process as well as to infer the integration of the biomaterial within the abdominal wall.<sup>30</sup>

**2.4.3. Surgical procedure.** The operation field was shaved, disinfected and the abdomen was covered in a sterile manner. A median laparotomy was performed and the patches were carefully applied onto the left native abdominal wall between the peritoneum and the visceral organs, avoiding folding of the implants. Subsequently, the BNC patches were fixed by 6 suture stitches with polypropylene (Optilene, B. Braun Surgical, S.A.U., USP 3-0) sutures. The wound was closed with a continuous muscle suture and continuous intracutaneous sutures. The skin was glued with Histoacryl®, a cyanoacrylate-based tissue glue (B. Braun Surgical, S.A.U., Spain). After the follow-up time of 21 days, the rabbits were anaesthetized (Ketamine  $40 \text{ mg per kg}$  body weight and Xylazine  $6 \text{ mg per kg}$  body weight) and subsequently euthanized (T61 intravenously).

Once the animals were sacrificed, tissue integration and adhesion formation were macroscopically examined. During explantation, the application site, as well as the abdomen *in toto*, were macroscopically evaluated. Possibly occurring adhesions were evaluated after dissection regarding their area extension in relation (%) to the total abdominal wall area implanted ( $7 \times 3$  cm). Furthermore, adhesions were defined to the following categories following the Zühlke scores as follows:<sup>31</sup>

Score I: String adhesions that are easy to separate (blunt detachment).

Score II: Adhesions being partially vascularized causing blunt to sharp detachment.

Score III: Adhesions having distinct vascularization, with sharp detachment only.

Score IV: Tight adhesions requiring sharp detachment causing damage to the organs.

The tissue integration was judged descriptively: no integration; mild integration = slight pull for uplifting the patch from the abdominal wall; and distinct integration = distinct pull uplifting from the abdominal wall with visible adhesion and vascularization.

### 2.5. Histological analysis

The central area of the implant (size approximately  $1 \times 3$  cm) was extirpated and fixed on 4% buffered formalin for histological examination. Tissue sections were cut with a microtome and processed following standard procedures.<sup>32</sup> Haematoxylin/eosin (HE) was used as a general staining for judgment of tissue integration.

### 2.6 Statistical analysis

Quantitative data were analysed with GraphPad Prism 8.0.2 software using ordinary one-way ANOVA followed by Tukey's multiple comparison test. Statistical significance was accepted



at 0.05 and data are represented as means  $\pm$  standard deviation.

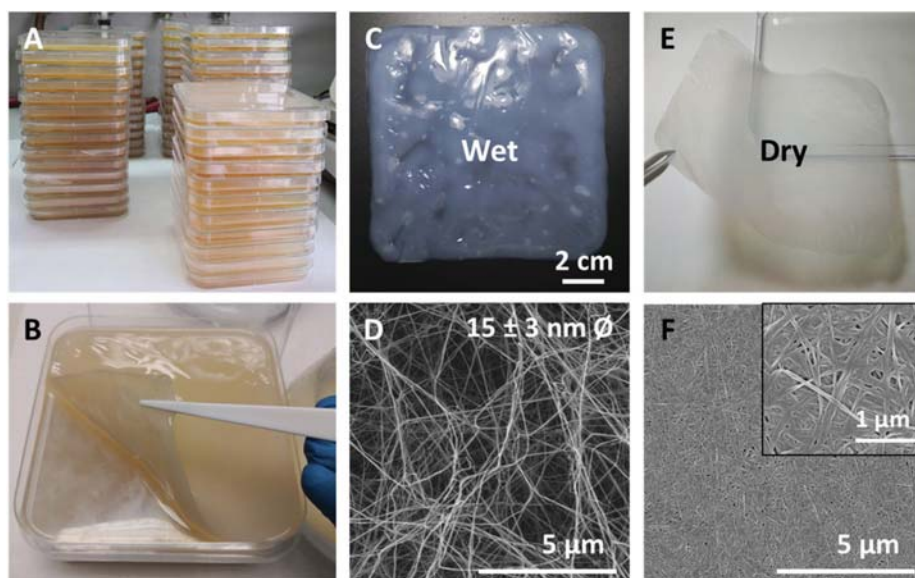
### 3. Results

#### 3.1 Single layered BNC patches

Firstly, single-layer BNC patches intended for hernioplasty applications were produced and characterized in terms of their macroscopic features, thickness and mechanical properties. Fig. 1A displays the simultaneous production of seventy-two  $12 \times 12$  cm-BNC films summing up  $>1$  m<sup>2</sup> of the biomaterial as a venue to attain increased amounts of BNC at a laboratory level. After 6 days at 30 °C, continuous BNC pellicles formed at the surface of the liquid culture (Fig. 1B). Upon cleaning and removing organic residues, a change in colour (from yellowish to translucent white) was appreciated (Fig. 1C).

Macro and microstructure of BNC in wet and dry conditions are depicted in Fig. 1(C, D) and (E, F) respectively. Since the morphology of wet as-synthesized BNC samples could not be observed with enough resolution using SEM, a supercritical (SC) dried film was used as this drying method maintains with high-reliability the architecture of native samples.<sup>33</sup> As exposed in Fig. 1D, SC-dried BNC films are highly porous and composed of entangled cellulose nanofibers of  $15 \pm 5$  nm in diameter. Upon drying at 60 °C, BNC films become more transparent and thinner while the fibres compact and the porosity decreases (see inset in Fig. 1F).

High tensile stress is a basic demand for a biomaterial proposed for soft tissue reinforcement applications. Tensile stress  $\geq 16$  N cm<sup>-1</sup> has been used as a benchmark for safe reinforcement of the abdominal wall.<sup>34</sup> Accordingly, tensile strength experiments were conducted to test the mechanical properties of BNC films using this value as a threshold. Fig. 2 shows the mean values obtained from five BNC samples in dry (pink) and wet (blue) conditions. Before mechanical characterization, the original BNC films ( $12 \times 12$  cm) were cut in  $20 \times 50$  mm samples and their thickness and surface weight (weight per area) were measured in both wet and dry forms. The surface weight is approximately 60 times higher for wet films than for its dried counterparts ( $654 \pm 153$  g m<sup>-2</sup> wet film;  $11 \pm 1$  g m<sup>-2</sup> dry film). Upon drying, 98% of the surface weight is lost as the water is removed, indicating that cellulose nanofibers account for only 2% of the wet BNC mass. These results are in agreement with the thickness measurement as BNC films experience a decrease in thickness of more than 96% when dehydrated (from  $445 \pm 91$   $\mu$ m wet film; to  $16 \pm 8$   $\mu$ m dry film). For the mechanical characterization, the  $20 \times 50$  mm BNC pieces were clamped with metallic clips containing a pneumatic flat rubber part to prevent the sliding of the samples (see the image in Fig. 2). The resistance to tear ( $F_{\max}$ ) of wet BNC is approximately 60% than that of dry BNC ( $5 \pm 1$  N cm<sup>-1</sup> and  $8 \pm 3$  N cm<sup>-1</sup> respectively). On the contrary, the maximum strain increases 12-fold in wet conditions ( $24 \pm 2\%$  in comparison to  $2.1 \pm 0.5\%$  for dry BNC). These data indicate that our single-layer BNC films (neither in wet nor in the dry state) do not meet the minimum mechanical resistance requirements of  $16$  N cm<sup>-1</sup> to be used as a PP mesh substitute.



**Fig. 1** BNC synthesis, wet and dry states and microstructure. (A) Numbering up BNC production at laboratory level. (B) A native wet BNC pellicle. (C) Wet form of BNC after cleaning and autoclaving. (D) SEM image of an SC dried BNC sample mimicking the microstructure of a wet BNC film. (E) Dry BNC film. (F) SEM image of the compact nanofiber conformation for dry BNC. Inset: higher magnification to better visualize the nanofibers arrangement.



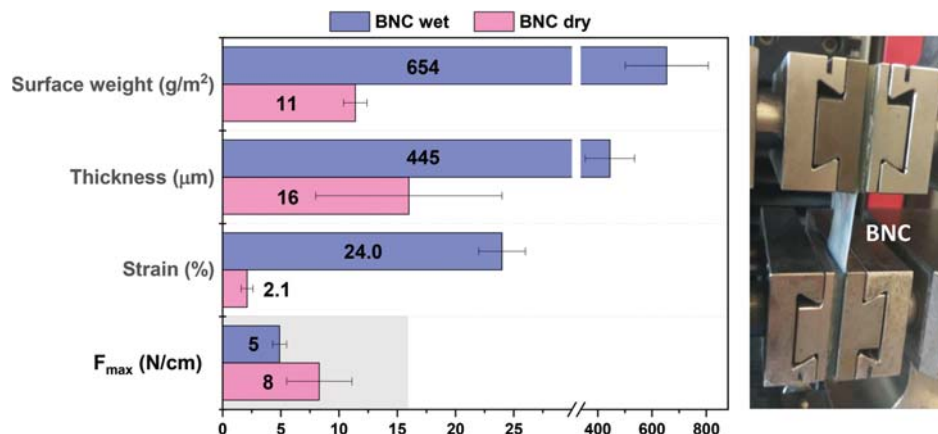


Fig. 2 Mechanical properties of single-layer BNC patches in wet and dry conditions and the experimental setup. Single-layered BNC implants did not meet the acceptance criteria of tensile stress resistance set at  $F_{\max} = 16 \text{ N cm}^{-1}$  (grey area). Statistically significant differences between dry and wet BNC samples were found for all the studied parameters except for the  $F_{\max}$  ( $P$ -values  $< 0.001$ ) ( $n = 5$ ).

### 3.2 Laminated BNC patches and hybrids

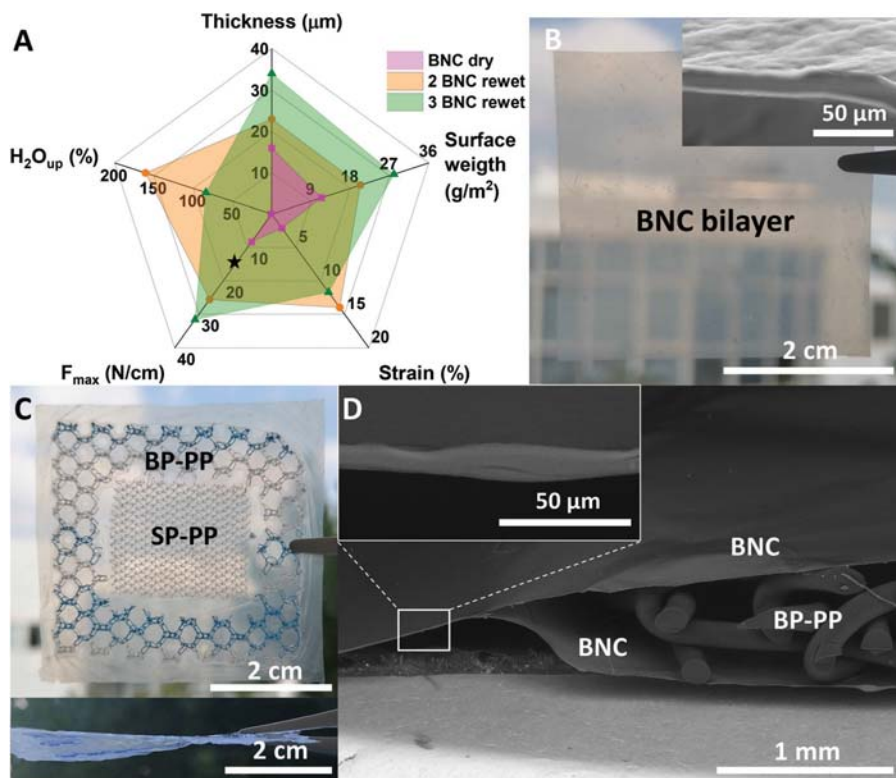
To increase the mechanical resistance of the BNC patches, two strategies were followed: (i) preparation of multi-layered BNC meshes and (ii) combination of BNC with standard PP meshes. Our previous work showed that robust BNC stacks that endure hard manipulation even upon rehydration can be created by pilling up and drying together (*i.e.* applying weight) several wet BNC films. Upon drying, hydrogen bonding between the fibres of two films confers stability to the stack. The multilayers do not suffer delamination even when immersed in a liquid solution.<sup>27</sup> Accordingly, laminated patches were created by assembling 2 or 3 wet BNC films and subjected to the same mechanical characterization as the single BNC layers. Fig. 3A depicts the results of 2 and 3 layers of BNC (mean values of  $n = 5$ ). All the obtained values were substantially higher than those of a single layer. As expected, thickness and surface weight increased as more layers were added. More precisely, thickness raised from  $16 \pm 8 \mu\text{m}$  (1 layer) to  $23 \pm 2 \mu\text{m}$  (2 layers) and  $34 \pm 6 \mu\text{m}$  (3 layers); and surface weight from  $11 \pm 1 \text{ g m}^{-2}$  (1 layer) to  $20 \pm 1 \text{ g m}^{-2}$  (2 layers) and  $28 \pm 2 \text{ g m}^{-2}$  (3 layers). The multilayers were then rehydrated in a 0.9% NaCl solution for 5 min before performing mechanical studies to better simulate the physiological conditions. As shown in Fig. 3A, the laminate BNC presents a maximum strain of  $14 \pm 1$  and  $12 \pm 3\%$  and resistance to tearing of  $26 \pm 6$  and  $32 \pm 9 \text{ N cm}^{-1}$  for 2 and 3 layers respectively. For the double-layered BNC, the maximum strain increased almost 7-fold compared to a single BNC layer (dry form) while, the resistance to tear increased more than 3-fold. As expected, the triple-layer renders an even higher improvement in mechanical resistance (4-fold compared to a dry single layer). Note that the values of both the double and triple-layer laminates are above the set threshold of  $16 \text{ N cm}^{-1}$  for abdominal wall reinforcement applications. Improvements

in mechanical properties (both the % of strain and the max force tolerated) of the stacked-BNC are statistically significant ( $P$ -values  $< 0.001$ ) when compared to the BNC single-layer. Remarkably, during the tensile test, no peeling or separation of the layers was observed. This feature is also exemplified in Fig. 3B where a bi-layered sturdy BNC patch is shown. Both images –the macrostructure image and the cross-section SEM picture (inset)– illustrate the homogeneous adhesion between two BNC films. Moreover, the original transparency was maintained without macroscopic air bubbles trapped in the interface and the boundary area between the two BNC films could not be identified by SEM. Fig. S2† gathers the values obtained for the mechanical properties of all the studied systems for a clearer comparison.

Finally, BNC hybrid constructs incorporating commercial PP meshes were considered. Fig. 3C shows frontal and lateral pictures of a preliminary prototype of a sandwich-like multi-layer composite. The construct was prepared by taking advantage of the above-mentioned self-adhesion property of BNC. Note that the BNC-PP composite firmly incorporates PP meshes with different pore sizes. The thickness of the dry composites varied depending on the incorporated PP material between the BNC layers. That is, for a PP mesh with small pores (named SP-PP) a thickness of  $332 \pm 8 \mu\text{m}$  was obtained, while when a PP mesh with bigger pores was employed (BP-PP) thickness increased up to  $589 \pm 23 \mu\text{m}$ . An SEM cross-section study (Fig. 3D) showed good integration of the BP-PP mesh in between the BNC layers. Although the synthetic material did not adhere to the BNC layers, it was immobilized in an envelop-like structure due to the BNC self-adhesion in the contact areas in between the pores of the PP mesh and at the composite's contour (inset Fig. 3D). The stability of the hybrid structure was tested by rehydration in water. After 5 days, the moist envelope-like structure was flexible and easily handled without noticeable delamination as depicted in Fig. S3.†







**Fig. 3** Composite alternatives to increase the mechanical resistance of BNC-based implants. (A) Mechanical study of BNC multilayers comprised of 2 or 3 films. ( $n = 5$ )  $\star$  indicates the resistance to tear threshold for tissue reinforcement materials ( $16 \text{ N cm}^{-2}$ ). (B) Picture of a BNC multilayer formed by 2 dry BNC films. Inset: SEM cross-section image where the interface between the two BNC layers is undetectable. (C) Preliminary BNC bilayer combination with PP meshes with different pore sizes. Upper panel: frontal view. Lower panel: a lateral image of the BNC-PP mesh composite. (D) SEM cross-section image of the BNC-PP composite. Inset: higher magnification of the cross-section to appreciate the continuous adhesion between BNC layers.

### 3.3 *In vivo* studies

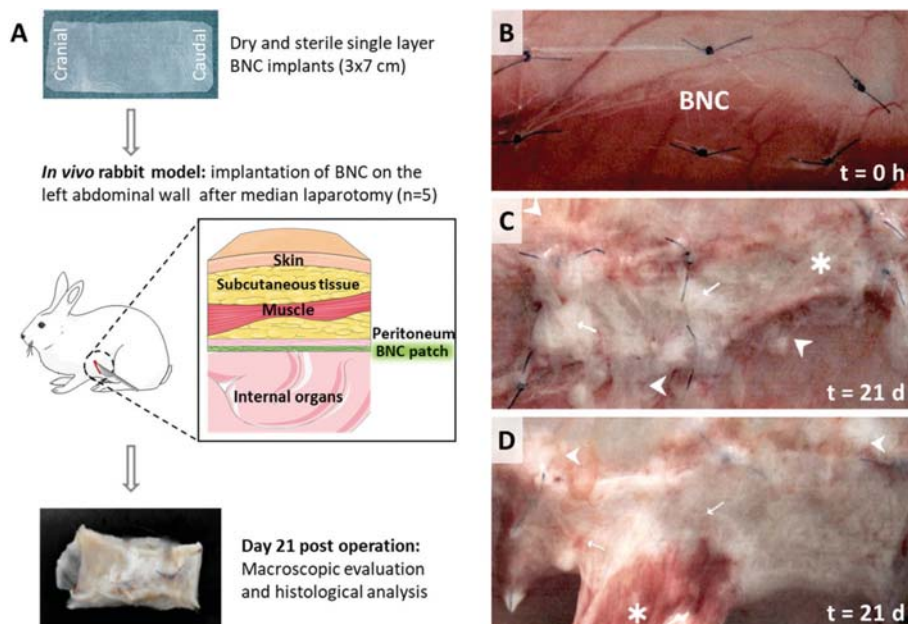
Besides mechanical validation, a key characteristic required from soft tissue repair materials is their proficiency in minimizing adhesion-related complications and integration by surrounding tissues. Therefore, the next step was to assess the anti-adhesion properties of BNC with an *in vivo* rabbit model following the implantation process shown in Fig. 4A.

**3.3.1 Macroscopic evaluation.** Dry and sterile single layer BNC patches of  $3 \times 7 \text{ cm}$  were selected for the *in vivo* study as being the ones with weaker mechanical characteristics and imposing the most stringent conditions. Single-layer BNC patches could be easily handled under operation-room settings, fold-free placing was readily achieved and fixation by suture was performed without complications (Fig. 4B). The semi-transparency of BNC was also convenient to avoid unintentional puncturing of blood vessels while suturing. During the application of the BNC patch, careful handling was necessary, nonetheless, the BNC patch allowed the secure application on the abdominal wall; no fracturing of the suture puncture

holes was observed and the BNC patches were removable with instruments and repositioned if needed. During the postoperative phase, all animals presented swift recovery. Analgesic treatment was only administered in the first postoperative days and a slight body weight gain was detected.

After the implantation period of 21 days, tissue integration was evaluated using observational criteria during the autopsy. The BNC patches displayed a general good integration to the abdominal wall whereas only marginal areas were not integrated. Adhesion level was examined and scored macroscopically considering prevalence (quantity) and type (quality) of the detected adhesions among BNC implants and the internal organs. In 4/5 animals adhesions were detected involving approximately 8% of the overall BNC surface. Although some fibrin accumulation and distinct vascularization were observed in all animals, only one rabbit presented a significant adhesion area (20%) as depicted in Fig. 4D. Three animals presented adhesions to the greater omentum and one animal to the cecum. Notably, one animal was completely free of adhesions (Fig. 4C). The implanted BNC patches were dominated





**Fig. 4** Experimental design, macroscopic evaluation and adhesion assessment for two of the five animals studied. (A) Sketch showing the prepared BNC implant, the employed *in vivo* model and the evaluations performed. (B) Time 0: BNC patches were applied onto the left abdominal wall and fixed with six suture stitches (C) A2 explanted analysis after 21 days (best case scenario). → indicates fibrin accumulation, ► adjacent abdominal wall without adhesions and \* marks vascularization. (D) A4 explanted analysis after 21 days (worst case scenario). → indicates vascularization, ► fibrin accumulations and \* corresponds to adhesion.

by only one visible layer of fibrin. These macroscopic observations are gathered in Fig. S4† and Tables 1 and 2.

**3.3.2. Histological evaluation.** The central area of the implant (size  $\sim 1 \times 3$  cm) was extirpated and used for histological examinations. Representative HE-stained tissue sections from the five studied animals are shown in Fig. 5. The area surrounding the BNC patches presented a severe diffuse to granulomatous immune cell infiltration involving lymphocytes, heterophilic granulocytes, macrophages and solitary

multinucleated giant cells. Also, a moderate active fibroplasia on the implanted zone was noted, as well as a good integration onto the abdominal wall and moderate neovascularization.

## 4. Discussion

We have investigated BNC patches for soft tissue reinforcement applications by dealing with two clinically relevant para-

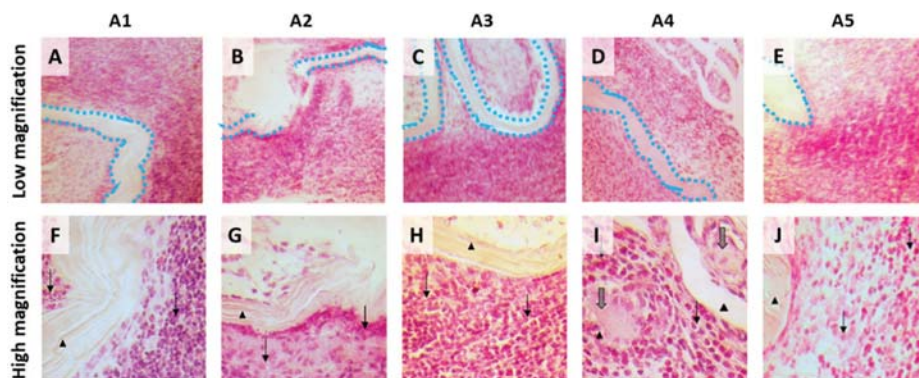
**Table 1** Individual adhesion observations. Results of the area free of adhesions, adhesion area, adhesion score and tissue integration for each studied animal

Animal number	6501	6507	6527	6564	6574
Code	A1	A2	A3	A4	A5
Area free of adhesions approx.	95%	100%	95%	80%	90%
Adhesion area approx.	5% to greater omentum	0%	5% to greater omentum	20% to greater omentum	10% to cecum
Adhesion score (Zühlke scores)	II – blunt to sharp detachment	No adhesions	II – blunt to sharp detachment	IV – sharp detachment	IV – sharp detachment
Tissue integration	Mild integration	Distinct integration	Distinct integration	Mild integration	Mild integration

**Table 2** Overall adhesion observations. Summary of the macroscopic evaluation of adhesions between BNC implants and internal organs

No. of animals affected by adhesions	Area (%) free of adhesions	Adhesions area (%)	Organs involved in adhesion processes
4/5	92	8	Greater omentum (3 animals) Cecum (1 animal)





**Fig. 5** HE-stained tissue sections of the BNC-implanted abdominal walls. A–E: Low magnification images of the five operated rabbits where the BNC implants have been highlighted with a blue dotted line to facilitate interpretation. For all cases, a good integration of the BNC patch together with an inflammatory reaction can be observed. F–J: Zoom-in to better appreciate the BNC implant (▶) and the presence of diverse inflammatory cells (lymphocytes, heterophilic granulocytes and macrophages) surrounding the implant (→). Solitary multinucleated giant cells were observed on A4 (I) (⇒).

meters; the mechanical resistance of constructs comprising one to three BNC layers and the *in vivo* anti-adherence properties of BNC. Before that, we characterized the BNC patches and present an increased BNC production (up to  $\sim 1 \text{ m}^2$ ) under laboratory settings to illustrate the feasibility of an up-scaled fabrication. However, to achieve an industrial manufacturing process, a more advanced system should be implemented such as the pilot-scale production processes reported by Kralisch *et al.*<sup>35</sup> and Beekmann *et al.*<sup>36</sup>

The mechanical characterization of as-synthesized BNC films (wet films) and after drying showed that wet BNC patches are thicker, more brittle but more stretchable than dry BNC patches. This confers to the wet-BNC a higher strain but, at the same time, makes the material less resistant to tear. After drying, the water content of BNC decreases drastically and the cellulose nanofibers condense, reducing their porosity<sup>15</sup> and their ability to rearrange upon tensile stress application. Thus, the dried form of BNC is stiffer and less stretchable than wet-BNC, making it more suitable for hernioplasty. Although the here studied single-layered BNC did not fulfil the mechanical resistance requirements to be used as a PP mesh substitute, thicker single layer BNC films grown for longer periods (>6 days) are expected to present sufficient mechanical support. We have previously reported that BNC fibres condense upon drying and form strong bonds among the cellulose nanofibers, this characteristic allowed us to arrange robust BNC multilayer laminates consisting of 2 or 3 layers.<sup>24</sup> The mechanical studies of those rehydrated BNC laminates have shown that the resistance to tear can be easily improved beyond the required  $16 \text{ N cm}^{-1}$  threshold for abdominal wall reinforcement applications. Even though previous studies confirmed the stability of BNC films in physiological conditions for up to 30 days,<sup>37</sup> the mechanical results of the laminates presented here were obtained after a 5 min-immersion in a saline solution and therefore, we cannot discard that the

mechanical properties of the films could be affected by longer hydration times.

Seeking to expand the library of BNC-based configurations for hernia repair patches, a composite patch integrating both BNC films and PP meshes was fabricated. This preliminary proof-of-concept demonstrates the possibility to, not only tune the mechanical properties of BNC but also to combine BNC films and PP meshes with different pore sizes. The sandwich-like BNC-PP structure was easy to prepare and exhibited robustness and good manageability both in dry and rehydrated conditions. This hybrid material shows the potential of BNC in the development of on-demand hybrid biomaterials for reinforcement of the abdominal wall but still requires further validation. The durability of the BNC-PP composites under physiological conditions is unknown at the moment and the need for additional strengthening of the composite (*i.e.* glueing with a cyanoacrylate-based biocompatible adhesive) could be considered in the future.<sup>38</sup>

We have recently validated BNC in diverse biological scenarios providing data on its cytocompatibility, lack of endotoxins ( $0.04 \pm 0.01$  Endotoxin Units per mL) after its biosynthesis as well as suturability and manageability in preclinical settings.<sup>37,39</sup> These findings, combined with the appealing mechanical properties reported here, positioned BNC as a suitable candidate for soft tissue repair patches and therefore *in vivo* studies were conducted. The anti-adhesion behaviour, biocompatibility and tissue integration characteristics of the BNC patches have been evaluated with a pilot animal study. BNC presented favourable surgical properties for this specific application in terms of suturability, manageability and accommodation to the implantation site. Moreover, the semi-transparent character of BNC was beneficial to avoid unintentional puncturing of underlying tissues. A general fold-free integration of the BNC material to the abdominal wall was detected in all the rabbits. Regarding adhesions between BNC



patches and internal organs, the overall area of the 5 implanted patches free of adhesions in this study is about 92%. Only a few adhesions were found after BNC implantation in the rabbit model, mostly involving the greater omentum which can be assessed as almost physiological since this organ is typically active in any post-surgical process. We hypothesize that the nanofibrillar microstructure of BNC, similar to that of the collagen networks on the extracellular matrix, favours the non-adherent characteristics of the BNC implants in accordance with the anti-fibrotic effect reported for cardiac implants wrapped with BNC.<sup>20</sup> The macroscopic evaluation showed that only a few adhesion strands were detected (overall at about 8% of the implant area) originated mainly on the suture stitches and at the border of the patches. For this pilot test, the BNC patches were fixed with sutures, even though sutures can cause foreign body responses and adhesions; indicating that suture-free administration methods could be worth exploring to diminish the adhesions even more. Overall, the macroscopic observation showed that good biocompatibility can be assumed for the BNC patches *in vivo* and the results indicate that BNC patches might act as a sufficient barrier to prevent adhesions in this rabbit sidewall model. Systemic tolerability of BNC can also be supposed from the good post-operative recovery of the test animals that occurred without notable complications.

On the histological analysis, all BNC implants appeared to be well integrated onto the abdominal wall, in good agreement with the macroscopic observations. An inflammatory response was observed at the *peri*-implanted area presenting fibroplasia and infiltration of diverse cell types (lymphocytes, heterophilic granulocytes, macrophages and solitary multinucleated giant cells) indicating a tissue reaction upon BNC. In a similar work, oxidized and laser-perforated BNC was employed in experimental surgery using a rabbit model.<sup>40</sup> One week after subcutaneous suture-free BNC implantation on the animal's back a positive integration of the BNC implants with the surrounding tissues was reported following our observations. Interestingly, Lai and co-workers stated a very low inflammatory response contrasting with the here presented histological analysis. Possibly, the distinct tissue responses arise from the different experimental protocols used (*i.e.* implantation site, use of sutures and longer implantation time, in our case) or the modifications of BNC. On the other hand, the previously cited work from Rauchfuß and colleagues<sup>26</sup> describes an inflammatory infiltration on the BNC patches judged to be of minimal clinical significance. We endorse that it could also apply to our *in vivo* study based on the witnessed lack of systemic toxicity. Besides, the good integration of the BNC implants –which were only indistinctly noticeable on the surrounding tissue– strengthens this reasoning. Nevertheless, the heterogeneous responses of the host immune system towards BNC implants indicate a need for future work.

Finally, the observation that a single layer of BNC could be sufficient to achieve low adhesions rates further emphasizes the attractiveness of BNC composites. Since a strong mechanical resistance is required for hernioplasty, composite BNC

patches (either as multilayers or in combination with PP meshes) should be the mainstay of our future work.

## 5. Conclusions

In summary, BNC was investigated as a biomaterial for soft tissue reinforcement applications to tackle the long-lasting challenge of reducing adhesions between implants and internal organs after hernia surgery. While single-layer BNC does not present favourable mechanical properties, BNC laminates with 2 or 3 films are resistant enough to reach the minimal acceptance criteria for abdominal wall reinforcement applications. Notably, this simple stacking methodology supported the integration of commercial PP meshes between the BNC sheets opening future perspectives on BNC-PP hybrid biomaterials. Finally, an *in vivo* study revealed that BNC exhibits favourable surgical features in terms of suturability, manageability and accommodation to the implantation site. Besides, mild adhesion scores involving low percentages of the implant's area together with excellent integration capability on the *peri*-implant zone could be demonstrated. BNC elicited an inflammatory response that needs to be further investigated. Overall, our work proves that bio-based BNC possesses attractive mechanical and anti-adherent properties that could be valuable in the development of innovative hernia repair solutions.

## Ethical statement

All animal procedures were performed according to Good Laboratory Guidelines and were carried out in accordance with the guidelines of EN ISO/IEC 17025 and European guidelines 93/42/EWG and 90/385/EWG as accredited by the national accreditation body of Germany (DAkkS, accreditation scope of records: D-PL-20600-01-00).

## Author contributions

Irene Anton-Sales: conceptualization, methodology, validation, formal analysis, writing – original draft. Soledad Roig-Sanchez: conceptualization, methodology, validation, formal analysis, writing – original draft. Kamelia Traeger: methodology, validation, writing – review & editing. Christine Weis: conceptualization, resources, project administration, supervision, writing – review & editing. Anna Laromaine: conceptualization, funding acquisition, supervision, writing – review & editing. Pau Turon: conceptualization, resources, supervision, writing – review & editing. Anna Roig: conceptualization, project administration, funding acquisition, supervision, writing – review & editing.

## Conflicts of interest

There are no conflicts to declare.



## Acknowledgements

Authors acknowledge financial support from the Spanish Ministry of Science and Innovation through the RTI2018-096273-B-I00 project, the 'Severo Ochoa' Programme for Centres of Excellence in R&D (CEX2019-000917-S) and the Generalitat de Catalunya 2017SGR765 grant. Authors are also grateful for the PhD scholarships of I. A-S. (BE-2017-076734) and S. R-S. (BES-2016-077533) and the 2019LLAV00046 project. The ICMAB members participate in the CSIC Interdisciplinary Platform for Sustainable Plastics towards a Circular Economy, SUSPLAST, and in the Aerogels COST ACTION (CA 18125). This work has been performed within the framework of the doctoral program in materials science of UAB (I. A-S. and S. R-S.). We acknowledge the support by the CSIC Open Access Publication Support Initiative through its Unit of Information Resources for Research (URICI) to cover the publication fee.

## References

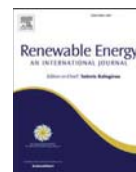
- 1 A. S. Kashyap, K. P. Anand and S. Kashyap, Inguinal and incisional hernias, *Lancet*, 2004, **363**(9402), 84.
- 2 R. Bittner, M. E. Arregui, T. Bisgaard, M. Dudai, G. S. Ferzli, R. J. Fitzgibbons, *et al.*, Guidelines for laparoscopic (TAPP) and endoscopic (TEP) treatment of inguinal hernia, *Surg. Endosc.*, 2011, **25**(9), 2773–2843.
- 3 F. Köckerling, R. Bittner, D. Adolf, R. Fortelny, H. Niebuhr, F. Mayer, *et al.*, Seroma following transabdominal preperitoneal patch plasty (TAPP): incidence, risk factors, and preventive measures, *Surg. Endosc.*, 2018, **32**(5), 2222–2231.
- 4 S. Muller, T. Langø, R. Brekken and B. Ystgaard, Degree of Adhesions After Repair of Incisional Hernia, *J. Soc. Laparoendosc. Surg.*, 2010, **14**, 399–404.
- 5 E. Chelala, Y. Debardemaeker, B. Elias, F. Charara, M. Dessily and J. L. Allé, Eighty-five redo surgeries after 733 laparoscopic treatments for ventral and incisional hernia: Adhesion and recurrence analysis, *Hernia*, 2010, **14**(2), 123–129.
- 6 M. Mirjavan and A. Asayesh, Asgharian Jeedi AA. The effect of fabric structure on the mechanical properties of warp knitted surgical mesh for hernia repair, *J. Mech. Behav. Biomed. Mater.*, 2017, **66**, 77–86.
- 7 C. Hollinsky, T. Kolbe, I. Walter, A. Joachim, S. Sandberg, T. Koch, *et al.*, Tensile strength and adhesion formation of mesh fixation systems used in laparoscopic incisional hernia repair, *Surg. Endosc.*, 2010, **24**(6), 1318–1324.
- 8 S. Lanzalaco, L. J. del Valle, P. Turon, C. Weis, F. Estrany, C. Alemán, *et al.*, Polypropylene mesh for hernia repair with controllable cell adhesion/de-adhesion properties, *J. Mater. Chem. B*, 2020, **8**(5), 1049–1059.
- 9 P. J. Emans, M. H. F. Schreinemacher, M. J. J. Gijbels, G. L. Beets, J. W. M. Greve, L. H. Koole, *et al.*, Polypropylene meshes to prevent abdominal herniation. Can stable coatings prevent adhesions in the long term?, *Ann. Biomed. Eng.*, 2009, **37**(2), 410–418.
- 10 S. Lanzalaco, P. Turon, C. Weis, C. Mata, E. Planas, C. Alemán, *et al.*, Toward the New Generation of Surgical Meshes with 4D Response: Soft, Dynamic, and Adaptable, *Adv. Funct. Mater.*, 2020, **2004145**, 1–9.
- 11 N. Udpa, S. R. Iyer, R. Rajoria, K. E. Breyer, H. Valentine, B. Singh, *et al.*, Effects of Chitosan Coatings on Polypropylene Mesh for Implantation in a Rat Abdominal Wall Model, *Tissue Eng., Part A*, 2013, **19**(23), 2713–2723.
- 12 F. Pomilio Di Loreto, A. Mangione, E. Palmisano, J. I. Cerda, M. J. Dominguez, G. Ponce, *et al.*, Dried human amniotic membrane as an antiadherent layer for intraperitoneal placing of polypropylene mesh in rats, *Surg. Endosc.*, 2013, **27**(4), 1435–1440.
- 13 F. Basile, A. Biondi and M. Donati, Surgical approach to abdominal wall defects: History and new trends, *Int. J. Surg.*, 2013, **11**(S1), S20–S23.
- 14 I. Anton-Sales, U. Beekmann, A. Laromaine, A. Roig and D. Kralisch, Opportunities of Bacterial Cellulose to Treat Epithelial Tissues, *Curr. Drug Targets*, 2019, **20**(8), 808–822.
- 15 M. Zeng, A. Laromaine and A. Roig, Bacterial cellulose films: influence of bacterial strain and drying route on film properties, *Cellulose*, 2014, **21**(6), 4455–4469.
- 16 S. Wang, F. Jiang, X. Xu, Y. Kuang, K. Fu, E. Hitz, *et al.*, Super-Strong, Super-Stiff Macrofibers with Aligned, Long Bacterial Cellulose Nanofibers, *Adv. Mater.*, 2017, **29**(35), 1702498.
- 17 S. Q. Chen, P. Lopez-Sanchez, D. Wang, D. Mikkelsen and M. J. Gidley, Mechanical properties of bacterial cellulose synthesised by diverse strains of the genus *Komagataeibacter*, *Food Hydrocolloids*, 2018, **81**, 87–95.
- 18 H. Ullah, F. Wahid, H. A. Santos and T. Khan, Advances in biomedical and pharmaceutical applications of functional bacterial cellulose-based nanocomposites, *Carbohydr. Polym.*, 2016, **150**, 330–352.
- 19 D. Klemm, E. D. Cranston, D. Fischer, M. Gama, S. A. Kedzior, D. Kralisch, *et al.*, Nanocellulose as a natural source for groundbreaking applications in materials science: Today's state, *Mater. Today*, 2018, **21**(7), 720–748.
- 20 L. Bacakova, J. Pajorova, M. Bacakova, A. Skogberg, P. Kallio, K. Kolarova, *et al.*, Versatile Application of Nanocellulose: From Industry to Skin Tissue Engineering and Wound Healing, *Nanomaterials*, 2019, **9**(2), 164.
- 21 F. M. Lima, F. C. M. Pinto, B. L. Andrade-da-Costa, J. G. Silva, O. Campos Júnior and J. L. Aguiar, Biocompatible bacterial cellulose membrane in dural defect repair of rat, *J. Mater. Sci.: Mater. Med.*, 2017, **28**(37).
- 22 F. C. A. Silveira, F. C. M. Pinto, S. Caldas Neto Sda, M. de C. Leal, J. Cesário and J. L. Aguiar, Treatment of tympanic membrane perforation using bacterial cellulose: a randomized controlled trial, *Braz. J. Otorhinolaryngol.*, 2016, **82**(2), 203–208.
- 23 F. Robotti, I. Sterner, S. Botta, J. M. Monné Rodríguez, G. Pellegrini, T. Schmidt, *et al.*, Microengineered biosynthesized cellulose as anti-fibrotic in vivo protection for cardiac implantable electronic devices, *Biomaterials*, 2020, **229**, 119583.
- 24 K. Ludwicka, M. Kolodziejczyk, E. Gendaszewska-Darmach, M. Chrzanowski, M. Jedrzejczak-Krzepkowska, P. Rytczak,



- et al.*, Stable composite of bacterial nanocellulose and perforated polypropylene mesh for biomedical applications, *J. Biomed. Mater. Res., Part B*, 2019, **107**(4), 978–987.
- 25 A. N. Zharikov, V. G. Lubyansky, E. K. Gladysheva, E. A. Skiba, V. Budaeva, E. N. Semyonova, *et al.*, Early morphological changes in tissues when replacing abdominal wall defects by bacterial nanocellulose in experimental trials, *J. Mater. Sci. Mater. Med.*, 2018, **29**(7).
- 26 F. Rauchfuß, J. Helble, J. Bruns, O. Dirsch, U. Dahmen, M. Ardel, *et al.*, Biocellulose for incisional hernia repair—an experimental pilot study, *Nanomaterials*, 2019, **9**(2), 1–11.
- 27 S. Roig-Sanchez, E. Jungstedt, I. Anton-Sales, D. C. Malaspina, J. Faruado, L. A. Berglund, *et al.*, Nanocellulose films with multiple functional nanoparticles in confined spatial distribution, *Nanoscale Horiz.*, 2019, **4**, 634–641.
- 28 J. C. Y. Chan, K. Burugapalli, Y. S. Huang, J. L. Kelly and A. Pandit, A clinically relevant in vivo model for the assessment of scaffold efficacy in abdominal wall reconstruction, *J. Tissue Eng.*, 2017, **8**, 1–11.
- 29 G. S. DiZerega and J. D. Campeau, Peritoneal repair and post-surgical adhesion formation, *Hum. Reprod. Update*, 2001, **7**(6), 547–555.
- 30 R. A. Lang, P. M. Grüntzig, C. Weisgerber, C. Weis, E. K. Odermatt and M. H. Kirschner, Polyvinyl alcohol gel prevents abdominal adhesion formation in a rabbit model, *Fertil Steril*, 2007, **88**(4 suppl.), 1180–1186.
- 31 H. Kataria and V. P. Singh, Liquid Paraffin vs Hyaluronic Acid in Preventing Intraperitoneal Adhesions, *Indian J. Surg.*, 2017, **79**(6), 539–543.
- 32 J. F. Kukleta, C. Freytag and M. Weber, Efficiency and safety of mesh fixation in laparoscopic inguinal hernia repair using n-butyl cyanoacrylate: Long-term biocompatibility in over 1, 300 mesh fixations, *Hernia*, 2012, **16**(2), 153–162.
- 33 M. E. El-Naggar, S. I. Othman, A. A. Allam and O. M. Morsy, Synthesis, drying process and medical application of polysaccharide-based aerogels, *Int. J. Biol. Macromol.*, 2020, **145**, 1115–1128.
- 34 U. Klinge, B. Klosterhalfen, J. Conze, W. Limberg, B. Obolenski, A. P. Öttinger, *et al.*, Modified mesh for hernia repair that is adapted to the physiology of the abdominal wall, *Eur. J. Surg.*, 1998, **164**(12), 951–960.
- 35 D. Kralisch, N. Hessler, D. Klemm, R. Erdmann and W. Schmidt, White biotechnology for cellulose manufacturing—the HoLiR concept, *Biotechnol. Bioeng.*, 2010, **105**(4), 740–747.
- 36 U. Beekmann, L. Schmölz, S. Lorkowski, O. Werz, J. Thamm, D. Fischer, *et al.*, Process control and scale-up of modified bacterial cellulose production for tailor-made anti-inflammatory drug delivery systems, *Carbohydr. Polym.*, 2020, 116062.
- 37 I. Anton-Sales, J. C. D'Antin, J. Fernández-Engroba, V. Charoenrook, A. Laromaine, A. Roig, *et al.*, Bacterial nanocellulose as a corneal bandage material: A comparison with amniotic membrane, *Biomater. Sci.*, 2020, **8**(10), 2921–2930.
- 38 R. Jain and S. Wairkar, Recent developments and clinical applications of surgical glues: An overview, *Int. J. Biol. Macromol.*, 2019, **137**, 95–106.
- 39 I. Anton-Sales, S. Roig-Sanchez, M. J. Sánchez-Guisado, A. Laromaine and A. Roig, Bacterial nanocellulose and titania hybrids: cytocompatible and cryopreservable cell carriers, *ACS Biomater. Sci. Eng.*, 2020, **6**(9), 4893–4902.
- 40 C. Lai, K. S. Hu, Q. L. Wang, L. Y. Sheng, S. J. Zhang and Y. Zhang, Anti-Adhesion Mesh for Hernia Repair Based on Modified Bacterial Cellulose, *Starch/Staerke*, 2018, **70**(11–12), 1–10.







# Carbons derived from alcohol-treated bacterial cellulose with optimal porosity for Li–O<sub>2</sub> batteries



Wenhai Wang<sup>a</sup>, Siavash Khabazian<sup>b</sup>, Soledad Roig-Sanchez<sup>a</sup>, Anna Laromaine<sup>a</sup>,  
Anna Roig<sup>a</sup>, Dino Tonti<sup>a,\*</sup>

<sup>a</sup> Institut de Ciència de Materials de Barcelona, ICMAB-CSIC, Campus UAB, 08193, Bellaterra, Spain

<sup>b</sup> Nanomaterials Group, Department of Materials Science and Engineering, Tarbiat Modares University, Tehran, Iran

## ARTICLE INFO

### Article history:

Received 10 February 2021

Received in revised form

22 April 2021

Accepted 9 May 2021

Available online 26 May 2021

### Keywords:

Bacterial cellulose

Solvent exchange

Porous carbons

Electrochemical surface area

Li–O<sub>2</sub> batteries

## ABSTRACT

Porous carbons are important cathode materials for metal-air batteries, but the most usual methods to prepare these porous structures are complex and of high cost. We have prepared porous carbons from bacterial cellulose (BC) hydrogels by a simple water-alcohol solvent exchange before carbonization. Alcohol treatment facilitates looser and more open structures than untreated BC, resulting in porous carbon structures with high surface area, appropriate for electrochemical applications. Used as cathodes in lithium-oxygen batteries, the carbon derived from 1-butanol treated BC has excellent discharge capacity (5.6 mA h cm<sup>-2</sup>) and good cycle life. This work presents a sustainable, straightforward and fast way to prepare porous carbon materials from BC.

© 2021 The Author(s). Published by Elsevier Ltd. This is an open access article under the CC BY license (<http://creativecommons.org/licenses/by/4.0/>).

## 1. Introduction

With the development of society, the demand for energy becomes an urgent need. Many aspects of energy-storage technologies have been explored to facilitate the use of sustainable energy sources [1,2]. Among these technologies, Li–O<sub>2</sub> battery has been regarded as one of the most promising, because of its high theoretical energy density of ~3500 Wh kg<sup>-1</sup> [3]. But there are still numerous issues impeding the utilization of Li–O<sub>2</sub> batteries in practical use [4,5]. Owing to their sluggish kinetics, the oxygen reduction reaction (ORR) and the oxygen evolution reaction (OER) show large overpotentials, low energy and coulombic efficiency [6,7]. The performance of a Li–O<sub>2</sub> battery relies on the reaction between lithium ion and oxygen. A good cathode should allow the diffusion of lithium ions and oxygen, and also favor the reversible Li<sub>2</sub>O<sub>2</sub> formation and storage during the process of discharge [8,9]. Porous carbons are the most widely used platform for air cathodes [10,11], as they generally offer good conductivity, light weight, large surface area, tunable porosity, and low cost and abundant, often renewable, sources for its production [12,13].

Bacterial cellulose (BC) is a bio-based polymer produced from a microbial fermentation process [14,15], which is employed in a wide range of applications from health to electronics [16,17]. BC as carbon source has raised great attention, owing to its sustainability, relative low cost, three-dimensional structure, high surface area and accessible porosity [18,19], which are ideal for electrodes in energy storage devices. As-prepared BC is a hydrogel, thus thermal carbonization requires a drying step. The drying route applied considerably modifies the morphology, surface area and porosity of the BC, therefore it can influence the properties of the resulting carbons [20,21]. In fact, when the gel is dried by simple water evaporation in air at room or oven temperature, the strong capillary forces collapse the pores of the cellulose network, which induces fibril aggregation known as hornification, resulting in a low porosity material. Freeze-drying, spray-drying and supercritical drying are often used to hinder hornification [22,23], increasing the surface area of cellulose and producing porous structures.

Such porous cellulose has been successfully employed to produce carbons with a nanofibrous structure that replicates the nanocellulose network [18,24]. However, the drying methods applied are generally time- and energy-consuming and require expensive facilities than simple oven drying. Therefore these methods do not represent a remarkable advantage over more conventional methods to introduce and control porosity of

\* Corresponding author.

E-mail address: [dino.tonti@csic.es](mailto:dino.tonti@csic.es) (D. Tonti).



biomass-derived carbons, as it is the case of chemical activation by corrosive compounds [25,26], addition of templating agents [27], or hydrothermal synthesis [28]. On the other hand, some authors reported that using compatible solvents with low surface tension, such as alcohols, could relieve the occurrence of a compacted structure's cellulose [29,30].

We show here a facile and low-cost method to prepare porous carbons from food store commercial BC after a simple alcohol treatment. The obtained carbon microstructure is not a replica of the cellulose and suggests some intermediate melting step in the pyrolysis process. Nevertheless, the porosity of carbon derived from alcohol-treated BC is remarkable and used as oxygen cathodes in Li–O<sub>2</sub> batteries showed an outstanding capacity and good cycle life. These results not only show a more economic and sustainable route for the preparation of porous carbons, but the striking variations of carbon porosities and electrochemical performance obtained from the same cellulose modified just by controlling fiber aggregation also provide an interesting insight into the carbonization process.

## 2. Experimental

### 2.1. Materials

Bacterial cellulose (BC, Q-Phil Products International), methanol (Scharlau), ethanol (99%, Panreac), 1-propanol (99.7%, Sigma Aldrich), 1-butanol (99.5%, Labkem), 1-hexanol (≥99.9%, Sigma Aldrich), 1-octanol (≥99.9%, Sigma Aldrich), ether (≥99.9%, Sigma Aldrich), acetone (99%, Panreac), Tetraethylene glycol dimethyl ether ether (TEGDME, ≥97.0%, Sigma Aldrich), N-methylpyrrolidone (NMP, Sigma Aldrich), lithium triflate (99.95%, Sigma-Aldrich), bis(2-methoxy ethyl)ether (Diethylene glycol dimethyl ether, DEGDME, 99.95%, Sigma-Aldrich), polyvinylidene fluoride (PVDF, Sigma-Aldrich), carbon black (Super P, Timcal), lithium foil (Sigma-Aldrich, 0.4 mm thick), carbon paper (Freudenberg, H2315, 210 μm thick), glass fibre filter (PRAT DUMAS, 270 μm thick).

### 2.2. Preparation of carbons

BC processing: Food-grade BC was in the form of cubes (approx. size 15 × 15 × 15 mm<sup>3</sup>) immersed in sucrose syrup. Cubes were drained and placed in Milli-Q water under stirring for 3 h, this process was repeated twice to remove the absorbed syrup and a final step of 12 h. Then, the BC cubes were autoclaved at 120 °C for 20 min. To replace water with other solvents, one piece of BC was pressed by a Teflon cylinder (150 g) for 10 min. The squeezed BC was then soaked in a beaker with 10 mL of a given solvent and stirred for 2 h at room temperature. Afterward, the soaked BC was briefly drained of excess solvent and placed without pressing in an oven to dry (60 °C, 24 h). Finally, dried BC was carbonized in a tubular furnace under an Ar flow of 100 mL min<sup>-1</sup> with a ramp of 10 °C min<sup>-1</sup> to 900 °C and kept there for 1 h.

### 2.3. Characterization

The water and alcohol-soaked BCs, were tested by Fourier transform infrared spectroscopy with attenuated total reflectance (FTIR-ATR). The measurements were carried out by Spectrophotometer Jasco 4700 equipment. The scan range was 400–4000 cm<sup>-1</sup>. All scanning electron microscopy (SEM) images were obtained by FEI Quanta 200 FEG-ESEM equipment at 15 kV acceleration voltage, 10 mm working distance. Cross-sections were obtained by dipping samples in liquid nitrogen and then, cutting them with a blade. All samples were placed on an aluminum holder with adhesive carbon tape. For transmission electron microscopy (TEM) analysis, samples were sonicated in ethanol for a few

seconds and dropped on carbon-coated copper grids. TEM images were obtained by JEOL JEM1210 TEM with an ORIUS 831 SC 600 (Gatan camera) at 120 kV. N<sub>2</sub> adsorption/desorption measurements were conducted by Micromeritics ASAP 2020 equipment. The outgas conditions were at 120 °C for 12 h. The thermal properties of dried BCs were investigated by a TGA-DSC/DTA analyzer (NETZSCH STA 449 F1 Jupiter). The thermal conditions were 10 °C min<sup>-1</sup> (ramp), 1000 °C (final temperature) and Ar atmosphere. The X-ray diffraction (XRD) patterns of all samples were performed by Siemens D-5000 equipment with Cu K<sub>α</sub> radiation. Tests were carried out in a 2θ range of 10–90°. The crystallinity index (CI) of BCs was calculated by the following equation:

$CI = (I_{110} - I_{am}) / I_{110}$  (1) where  $I_{110}$  is the intensity of the peak at 22.5° for the crystalline part of cellulose type I and  $I_{am}$  is the intensity of the peak at about 18° for the amorphous part [31].

### 2.4. Electrochemical performance

A slurry was prepared by gently grinding carbon samples in a mortar and mixing with PVDF (8:2 carbon/PVDF w/w) and few drops NMP. The slurry was then casted on a 10 mm diameter carbon paper (Freudenberg H2315). Then, the coated carbon paper was put in a vacuum oven at 80 °C for 24 h to remove NMP. The mass loading of air cathode is about 1 mg cm<sup>-2</sup>. The Li–O<sub>2</sub> battery is composed of 3 parts, carbon paper, glass fibre filter and Li foil. A 1 M lithium triflate solution in DEGDME was used as the electrolyte. The Li–O<sub>2</sub> batteries were assembled in an Ar filled glove box (H<sub>2</sub>O < 0.1 ppm, O<sub>2</sub> < 0.1 ppm). All the tests were carried out in 1 atm dry O<sub>2</sub> to avoid the effect of CO<sub>2</sub> and humidity. The cycle voltammetry measurements were conducted at a scan rate of 20 mV s<sup>-1</sup> in the range of 2.0–4.5 V (versus Li/Li<sup>+</sup>) by a Bio-logic VMP3 multichannel potentiostat. Galvanostatic discharge/charge tests were performed by a battery cycling equipment (MTI BST8-WA).

The estimation of the electrochemical surface area (ECSA) was based on the evaluation of the electrochemical double-layer capacitance and performed in a three-electrode system with a 1 M lithium triflate in DEGDME electrolyte after Ar bubbling. Carbon-coated carbon paper prepared as described above, with a mass loading of about 0.2 mg was used as the working electrode. Platinum wires were used as the counter and the reference electrode. The measurements were conducted at 2 mV s<sup>-1</sup> in a narrow potential range. The electrochemical double-layer capacitance  $C_{EDL}$  was obtained by the following equation [32]:

$$C_{EDL} = \int iVdV / (2vm \Delta V) \quad (2)$$

where  $i$  is the current,  $V$  is the potential,  $m$  is the mass of carbons,  $v$  is the scan rate,  $\Delta V$  is the potential range. The ECSA is given by the [33]:

$ECSA = C_{EDL} / C^*$  (3) where  $C^*$  is the specific capacitance (F m<sup>-2</sup>) of a bare glassy carbon electrode in the same electrolyte. A  $C^*$  value of 14.06 μF cm<sup>-2</sup> was determined by electrochemical impedance spectroscopy (EIS, Fig. S5).

## 3. Results and discussion

As reported by previous literature [29,30], alcohol treatments contribute to better preserve porous structures in dried cellulose reducing the degree of hornification. We tested several solvents as water replacement of the bacterial cellulose hydrogel, focusing in particular on aliphatic alcohols of different chain lengths, carbonized and tested as electrodes in Li/O<sub>2</sub> batteries. As summarized in Table S1, the poorest results are obtained with water, which seems

to confirm the effect of the high surface tension. Other parameters, such as solvent volatility may also play a role in the pore formation and could help explaining differences between alcohols. To better understand the impact that the replacement of water in the hydrogel for an organic solvent we focused on the characterization of the preparative steps of the carbons obtained from untreated (BC-w), ethanol (BC-e) as a reference alcohol treatment and 1-butanol treated cellulose (BC-b) which present the best electrochemical results. The cleaned, cubic-shaped BC hydrogels were pressed to about 10% of the original height to remove the majority of the entrapped water. Pressed BCs were then soaked in the different alcohols and stirred for 2 h. During this time, the BC cubes swelled to recover more than 90% of the original size in ethanol and more than 70% in the case of 1-butanol. FTIR spectra of soaked BC are similar to those of the pure solvents, which is consistent with complete solvent substitution (Fig. S1a and Figure S1c-d). The alcohol treatment does not chemically alter BCs, according to FTIR spectroscopy of dried BCs (Fig. S1b and Fig. S1c-d). In fact, dried BCs show typical cellulose peaks, which can respectively be ascribed to the stretching vibration of O–H ( $3350\text{ cm}^{-1}$ ), H–C–H ( $2900\text{ cm}^{-1}$ ), C–O–C ( $1427\text{ cm}^{-1}$ ) [34], with no apparent difference between them, which also proves the quantitative solvent removal in the three cases.

The SEM image (Fig. S2) of BC-w shows a smooth surface, which demonstrates that fibrils have compacted. The cross-section SEM images (Fig. 1a–c) show that the layers of BC-w are more densified in comparison with BC-e and BC-b. This confirms that the treatment of ethanol and 1-butanol reduce interfibrillar contraction. The morphology differences between BC-w, BC-e can be attributed to the following factors. On the one hand, the much smaller surface tensions of ethanol and 1-butanol (Table S1), which decrease the capillary force effects as compared to water during the solvent evaporation [29,35]. Low surface tensions of ethanol and 1-butanol

result in weaker capillary forces during the process of drying. The fibrils under weak capillary forces move less than under stronger capillary forces resulting from water, barely changing the distance between fibrils. On the other hand, ethanol and 1-butanol can attach to the surface of fibrils via hydrogen-bond [36,37]. As a consequence, the self-association behavior of fibrils can be limited by the steric hindrance of the aliphatic chains of ethanol and 1-butanol, which act as a spacer. Initially weaker and finally repulsive forces will be present among fibrils, preventing their cohesion. Therefore, highly porous structures can be achieved by ethanol and even more by 1-butanol treatment for BC.

The porous structures of dried BCs were further verified by nitrogen adsorption-desorption measurements (Fig. 1d). All three isotherms present hysteresis and could be considered of mixed type II and IV. Pore size distributions (Fig. 1e) mainly range in the mesoporous region, with a macropore contribution in the case of alcohol-treated samples, while micropores are scarce in all three samples. Dried BC-w presents small area and porosity (BET specific surface area  $21\text{ m}^2\text{ g}^{-1}$  and cumulative pore volume  $0.11\text{ cm}^3\text{ g}^{-1}$ , Table 1). In contrast, BC-e and BC-b have respectively over four and five times larger surface areas and pore volumes. These increments agree with the textured structure observed by SEM in BC-e and BC-b. The pore size distributions (Fig. 1e) of all dried BCs are dominated by mesopores, but BC-e and BC-b have larger predominant pore sizes than BC-w.

Powder X-ray diffraction (XRD) was used to study the effect of alcohols on the crystallinity of BCs. Fig. 1g depicts that all BCs show typical pattern peaks ( $14.5^\circ$  and  $22.5^\circ$ ) of cellulose type I, which correspond to the (100) and (110) lattice planes respectively [39]. Comparing with the crystallinity of BC-w (78%), the crystallinity of BC-e (66%) and BC-b (70%) decreases slightly. The decrease in crystallinity suggests that the cellulose becomes more disordered and loosen, which can be attributed to the effect of dissociation of

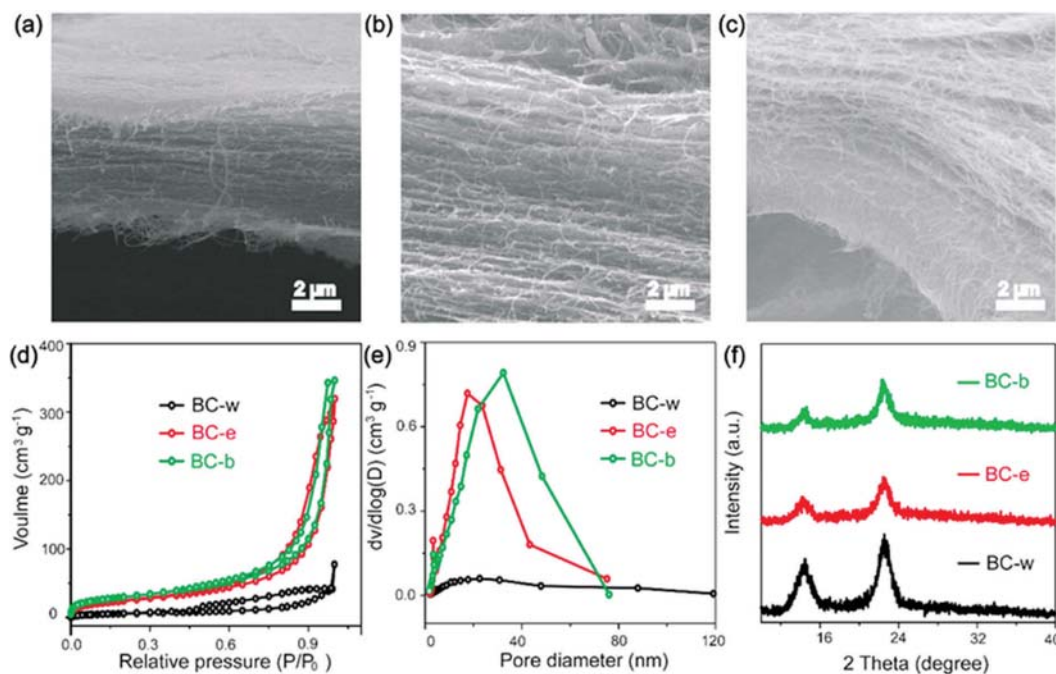


Fig. 1. Characterization of different dried BCs. SEM cross-section images of BC-w (a), BC-e (b) and BC-b (c), nitrogen adsorption–desorption of dried BCs (d), pore size distribution (e), XRD (f).

**Table 1**  
Textural data of samples and the electrochemical surface area (ECSA) of carbons.

Samples	BET surface area (m <sup>2</sup> g <sup>-1</sup> )	External surface area (m <sup>2</sup> g <sup>-1</sup> )	Pore Volume (cm <sup>3</sup> g <sup>-1</sup> )	Predominant pore size (nm)	ECSA (m <sup>2</sup> g <sup>-1</sup> )
Dried	21	18.29	0.11	14	/
BC-w					
Dried BC-e	88	91.83	0.44	17	/
Dried BC-b	107	102.51	0.54	32	/
Carbon-w	1009	153.44	0.19	16	33
Carbon-e	848	142.26	0.41	27	99
Carbon-b	669	237.42	1.25	85	180
Super P [38]	67	70	0.14	40	115

the hydrogen bonds between cellulose [40].

To explore the effect of the fiber aggregation on the carbonization process, all dried BCs were subjected to Thermogravimetric Analysis (TGA) under Ar (Fig. S3a). There are two major mass losses during the temperature ramp. The first small mass loss step (25–100 °C) can be attributed to the evaporation of residual absorbed water [41]. The loss is larger for BC-w (2.5%) than for alcohol-treated samples (0.9% for BC-e and 0.1% for BC-b). This can be considered a proof that a large part of the most tightly bound water molecules was removed during the alcohol treatment. The second mass loss step occurred at 200–400 °C, corresponding to BC decomposition and carbonization. During this step cellulose depolymerizes and fragments on variable molecular weight forms, giving place to char, tar, and volatile compounds (such as water, carbon dioxide and monoxide, acetic acid, and different saccharides) [42]. The yield of these solid, liquid and gaseous fractions has a strong influence on the subsequent carbonization process. The DSC curves (Fig. S3b) indicated that the temperatures for the first major decomposition peaks of BC-e (286 °C) and BC-b (297 °C) are lower than BC-w (322 °C). This can be related to the lower crystallinity of BC-e and BC-b, which can facilitate the degradation process of BCs [43]. In addition, carbon yields (Fig. S3a) of BC-e (9%) and BC-b (10%) are lower than BC-w (14%), probably because of the smaller pores of BC-w. These smaller pores retain more strongly the pyrolysis liquid intermediates, which are also involved in cross-linking and char formation [44]. The impregnation of a less porous system implies a smaller liquid-gas interface and a stronger liquid-solid interaction, reducing the intermediate volatilization and increasing char production, resulting in a larger carbon yield [42,44].

The presence of liquid intermediates is evident from the textures observed after carbonizing dried BCs at 900 °C in Ar. Carbon originated from water-treated BC (carbon-w) presents a compact vitreous morphology (Fig. 2a), which implies that their pores only correspond to narrow gaps between components of carbon-w. In contrast, carbons derived from ethanol (carbon-e) and 1-butanol (carbon-b) present evident porous structures (Fig. 2b and c), although the original fibrous structure is not retained. The disappearance of fibrous structure probably can be ascribed to the melting of nanofibers during the high temperature treatment. The TEM images of carbons (Fig. S4) show that particularly carbon-b possesses more developed and open porous structures, while carbon-w appears denser than carbon-e and carbon-b. This indicates that ethanol and, particularly, 1-butanol treatments are beneficial to obtain porous carbons from BC. The porous structure properties of carbons were further studied by nitrogen adsorption-desorption measurements (Fig. 2c and Table 1). Although the BET surface area of carbon-w results larger than other carbons, its pore structure mainly consists of micropores (Fig. 2d). Instead, the pore structure of carbon-b is dominated by macropores and mesopores, resulting in a larger external area. Therefore, the more open

structure of BC-e and BC-b seems to be beneficial for forming a broader porous structure during pyrolysis. The XRD patterns of carbons are shown in Fig. 2e. The broad peak at around 23° present in the three cases can be attributed to the (002) plane of graphitic carbon [45].

The electrode architecture has a dramatic effect on the discharge capacity of Li–O<sub>2</sub> batteries, as shown by several previous studies [38,46], which are useful to understand the behavior of our materials in this application. Therefore, the electrochemical surface area (ECSA) was determined to gain textural insights from the electrochemical point of view of the porous carbons [47,48], in the same electrolyte used in Li–O<sub>2</sub> battery tests. The values were obtained from capacitive currents in cyclic voltammetry (CV) of the different carbons coated on a carbon paper support (Fig. 3a). The ECSA of bare carbon paper is very small (0.14 m<sup>2</sup> g<sup>-1</sup>), which means that it has little contribution to the electrochemical interface. The ECSA of carbon-b (180 m<sup>2</sup> g<sup>-1</sup>) is the largest among the carbons derived from BCs, as carbon-e provided 99 m<sup>2</sup> g<sup>-1</sup> and carbon-w 33 m<sup>2</sup> g<sup>-1</sup> (Fig. 3b and Table 1). Thus, the largest BET area of BC-w translates into the smallest electrochemically effective area, showing that the smallest micropores are not accessible for our electrolyte, similarly to what we previously demonstrated with ionic liquid electrolytes [46]. Instead, the larger pores of alcohol-treated carbons offer a better ion-accessible surface area, and show larger ECSA values.

ECSA seems a more significant parameter to predict effectiveness as Li–O<sub>2</sub> cathode than BET area. Fig. 3c displays cyclic voltammetry curves of our carbons in O<sub>2</sub> atmosphere at a scan rate of 20 mV s<sup>-1</sup>. There are one reduction peak and one oxidation peak, which can be respectively ascribed to the formation and the decomposition of Li<sub>2</sub>O<sub>2</sub> [49]. Compared with carbon-w, alcohol-treated carbons display higher currents for both reduction and oxidation peaks. This shows that carbon-e and carbon-b provide better oxygen redox activities thanks to their more suitable pore structure. Galvanostatic discharge-charge profiles of Li–O<sub>2</sub> batteries were operated at the current density of 0.1 mA cm<sup>-2</sup> (Fig. 3d). The contribution of bare carbon fiber support is negligible (Fig. S6). Carbon-b and carbon-e provide discharge capacities of 5.58 and 1.36 mA h cm<sup>-2</sup>, while carbon-w only gives capacity similar to that of the support alone (0.14 mA h cm<sup>-2</sup>). Carbon-b also has the highest discharge voltage (~2.75 V), which can be attributed to its larger ECSA. The larger area significantly decreases overpotentials in Li–O<sub>2</sub> batteries and in effect correlation between specific area and discharge potential has been shown previously [38,50]. These capacities clearly show that not only the larger pore volume, but also the larger pore sizes favor the more abundant discharge of Li<sub>2</sub>O<sub>2</sub> [51]. The poor capacity of carbon-w can be attributed to its small pore size. This is reflected by the low ECSA and is consistent with our previous observation that only pores larger than a certain size, in the order of 10 nm, significantly contribute to the cathode capacity [46,52]. Besides, small pores will be easily blocked, which hinders the diffusion of oxygen [53]. Instead, the other carbons

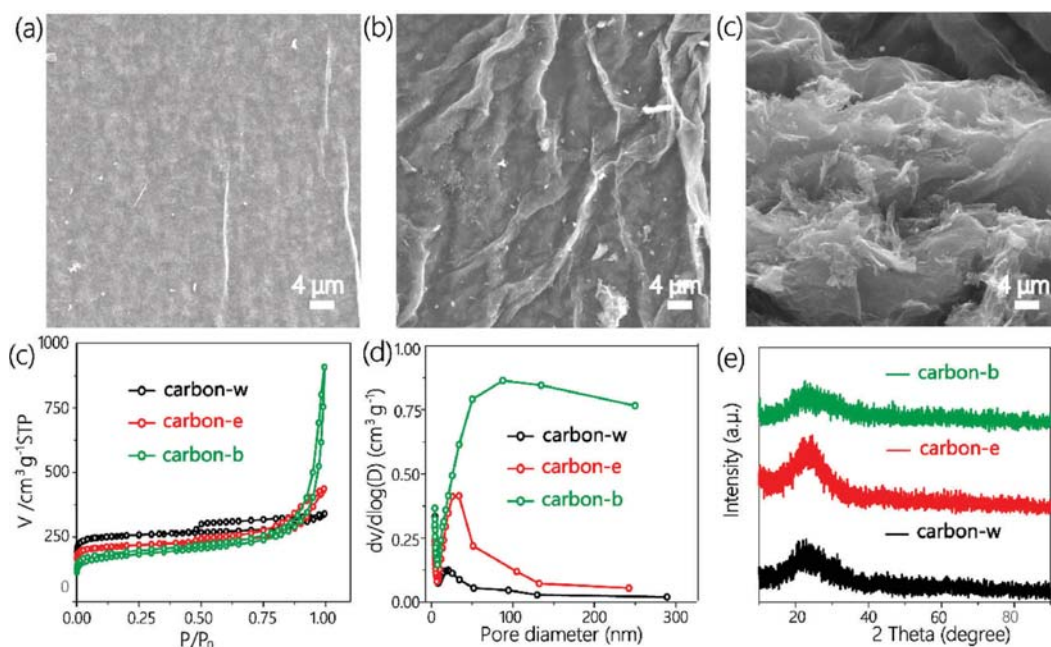


Fig. 2. SEM images of dried carbon-w (a), carbon-e (b) and carbon-b (c), nitrogen adsorption–desorption (d), pore size distribution (e), XRD (f) of carbons obtained from alcohol-treated bacterial cellulose.

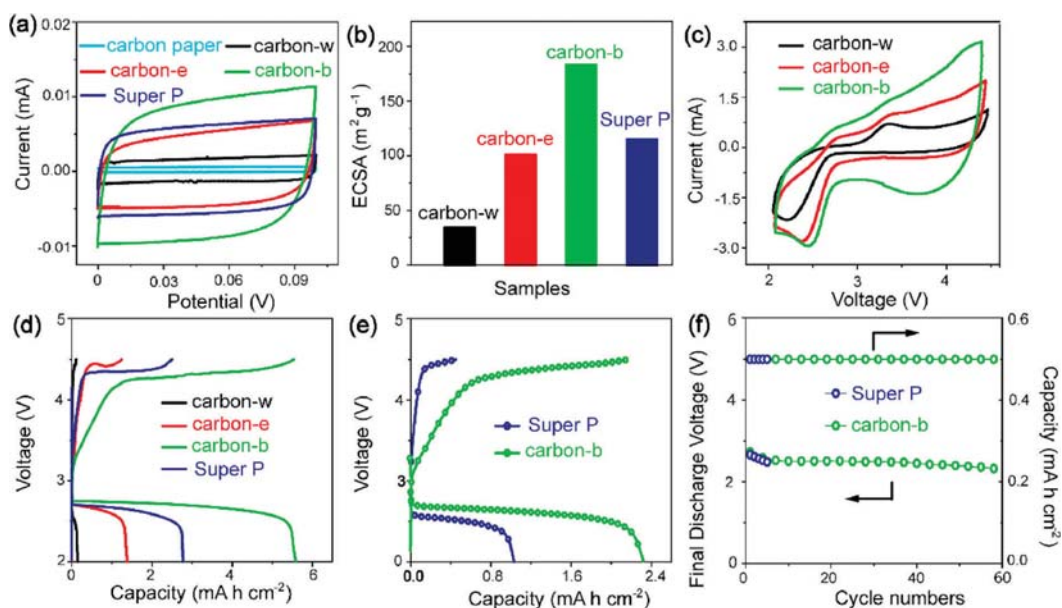


Fig. 3. Electrochemical properties of carbons: (a) CV curves of carbons in Ar-saturated 1 M lithium triflate in DEGDM; (b) comparison of ECSAs; (c) CV curves of Li–O<sub>2</sub> batteries with carbon cathodes; (d) full discharge-charge profiles within the voltage range of 2.0–4.5 V at 0.1 mA cm<sup>-2</sup>; (e) full discharge-charge profiles at 0.4 mA cm<sup>-2</sup>; (f) cycle life of carbon-b tested at 0.1 mA cm<sup>-2</sup>.

show a much more suitable pore structure, in particular carbon-b which outperforms Super P, a carbon black with a very open structure that typically offers large capacity [38,52]. The capacity difference between carbon-b and Super P can be attributed to the

different architecture of carbon-b which offers wider pores and larger surface area that allows for a better distribution of discharge products (Table 1 and Table S2). In addition, BC treated with 1-butanol for 24 h showed similar morphologies and discharge

capacities (Fig. S7), confirming that 2 h soaking is sufficient for quantitative water removal. Compared to other reported carbons, carbon-b exhibits outstanding discharge capacity properties as it can be observed in Table S4.

The rate capabilities of carbon-b and Super P cathodes were compared at the increased current density of  $0.4 \text{ mA cm}^{-2}$  (Fig. 3e). With the increment of the current density, the discharge capacity descended, discharge voltage decreased and charge voltage increased in all cases, but more severely for Super P. This better rate capability can be attributed to larger ECSA, demonstrating again the optimal texture of alcohol-treated carbons as Li–O<sub>2</sub> cathodes. Carbon-b cathodes, displayed nearly 100% coulomb efficiency at  $0.1 \text{ mA cm}^{-2}$ , and still 90% at  $0.4 \text{ mA cm}^{-2}$ . However, due to the larger overpotentials, Super P exhibited poorer figures (92% at  $0.1 \text{ mA cm}^{-2}$ , 43% at  $0.4 \text{ mA cm}^{-2}$ ). In line with this behavior, the cycling stability of carbon-b was far superior to that of Super P. In a test at  $0.1 \text{ mA cm}^{-2}$  with a capacity limitation of  $0.5 \text{ mA h cm}^{-2}$  (Fig. 3f and Fig. S8), the Super P electrode only sustained 4 cycles against more than 58 cycles for carbon-b. Table S3 depicts a comparison of the electrochemical performance for several reported cathodes. The outstanding number of cycles that carbon-b can withstand makes it an attractive material for Li–O<sub>2</sub> batteries.

To prove the specificity of the bacterial cellulose texture, cotton linters and agarose were also treated with water and 1-butanol, but the improvement from water to 1-butanol was not large (Fig. S9 and Fig. S10). This can be probably because the fibers of cotton linters and the bulk of agarose are much thicker and densified than the fiber structure of dried BCs. Other alcohols (such as methanol, 1-propanol, 1-hexanol and 1-octanol) and some non-alcohol solvents (acetone, ether and TEGDME) were also used to treat BCs with the same preparation method. All carbons derived from BCs treated with these solvents exhibit better capacities for Li–O<sub>2</sub> batteries than carbon-w (Fig. S11 and Table S1) but lower than carbon-b. This shows that 1-butanol has optimal affinity for cellulose, probably due to its mixed hydrophobic-hydrophilic character [54,55]. However, in general it can be affirmed that the treatment of solvents with low surface tensions on BCs can promote excellent carbons for Li–O<sub>2</sub> batteries.

#### 4. Conclusions

Porous carbons employed as cathodes in Li–O<sub>2</sub> batteries have been successfully synthesized by using alcohols to treat BC. The much higher porosity compared to that of carbon originated from water-treated BC, seems to correspond to the more open structure of the intermediate dried cellulose, even if in all cases the fiber network is lost during carbonization. The structure obtained by treatment of BC with 1-butanol shows optimal properties as a cathode in a Li–O<sub>2</sub> battery, with much higher capacity ( $5.58 \text{ mA h cm}^{-2}$ ), lower overpotentials and longer cycling life than the water treated equivalent material. This performance is superior even to a reference commercial cathode material such as Super P, demonstrating a clear interest as a practical material for application in metal-air batteries, as well as metal-sulphur, supercapacitors and all systems that require efficient transport properties.

#### CRedit authorship contribution statement

**Wenhai Wang:** Conceptualization, Methodology, Investigation, Formal analysis, Writing – original draft. **Siavash Khabazian:** Methodology. **Soledad Roig-Sanchez:** Methodology, Writing – review & editing. **Anna Laromaine:** Writing – review & editing. **Anna Roig:** Writing – review & editing. **Dino Tonti:** Resources, Conceptualization, Writing – review & editing, Supervision.

#### Declaration of competing interest

The authors declare that they have no known competing financial interests or personal relationships that could have appeared to influence the work reported in this paper.

#### Acknowledgments

This research was supported by the Spanish Government, through the “Severo Ochoa” Programme for Centers of Excellence in R&D (CEX2019-000917-S), the projects MAT2017-91404-EXP and RTI2018-096273-B-I00 and the PhD scholarships of S. R. (BES-2016-077533) with FEDER co-funding. W.W. gratefully acknowledges the support from the China Scholarship Council (CSC No.:201808340076). The authors participate in the SusPlast and FLOWBAT 2021 platforms promoted by the Spanish National Research Council (CSIC) and in the Aerogels COST ACTION (CA 18125). They also acknowledge the Generalitat de Catalunya (2017SGR765 and 2017SGR1687 grants). This work has been performed within the framework of the doctoral program in materials science of UAB (W. W. and S.R.–S.)

#### Appendix B. Supplementary data

Supplementary data to this article can be found online at <https://doi.org/10.1016/j.renene.2021.05.059>.

#### References

- [1] C. Xia, C.Y. Kwok, L.F. Nazar, A high-energy-density lithium-oxygen battery based on a reversible four-electron conversion to lithium oxide, *Science* 361 (2018) 777–781.
- [2] P. Salimi, O. Norouzi, S.E.M. Pourhoseini, P. Bartocci, A. Tavasoli, F. Di Maria, S.M. Pirbazari, G. Bidini, F. Fantozzi, Magnetic biochar obtained through catalytic pyrolysis of macroalgae: a promising anode material for Li-ion batteries, *Renew. Energy* 140 (2019) 704–714.
- [3] J.J. Xu, Q.C. Liu, Y. Yu, J. Wang, J.M. Yan, X.B. Zhang, In situ construction of stable tissue-directed/reinforced bifunctional separator/protection film on lithium anode for lithium-oxygen batteries, *Adv. Mater.* 29 (24) (2017) 1606552.
- [4] E. Wang, S. Dey, T. Liu, S. Menkin, C.P. Grey, Effects of atmospheric gases on Li metal cyclability and solid-electrolyte interphase formation, *ACS Energy Lett* 5 (4) (2020) 1088–1094.
- [5] Y. Qiao, Q. Wang, X. Mu, H. Deng, P. He, J. Yu, H. Zhou, Advanced hybrid electrolyte Li–O<sub>2</sub> battery realized by dual superhydrophobic membrane, *Joule* 3 (12) (2019) 2986–3001.
- [6] C.M. Burke, R. Black, I.R. Kochetkov, V. Giordani, D. Addison, L.F. Nazar, B.D. McCloskey, Implications of 4 e<sup>−</sup> oxygen reduction via iodide redox mediation in Li–O<sub>2</sub> batteries, *ACS Energy Lett* 1 (4) (2016) 747–756.
- [7] I. Landa-Medrano, I. Lozano, N. Ortiz-Vitoriano, I. Ruiz de Larramendi, T. Rojo, Redox mediators: a shuttle to efficacy in metal–O<sub>2</sub> batteries, *J. Mater. Chem. A* 7 (2019) 8746–8764.
- [8] J. Lu, Y.J. Lee, X. Luo, K.C. Lau, M. Asadi, H.H. Wang, S. Brombosz, J. Wen, D. Zhai, Z. Chen, D.J. Miller, R.Y.S. Jeong, J.B. Park, Z.Z. Fang, B. Kumar, A. Salehi-Khojin, Y.K. Sun, L.A. Curtiss, K. Amine, A lithium-oxygen battery based on lithium superoxide, *Nature* 529 (7586) (2016) 377–382.
- [9] W.J. Kwak, Rosy, D. Sharon, C. Xia, H. Kim, L.R. Johnson, P.G. Bruce, L.F. Nazar, Y.K. Sun, A.A. Frimer, M. Noked, S.A. Freunberger, D. Aurbach, Lithium-oxygen batteries and related systems: potential, status, and future, *Chem. Rev.* 120 (2020) 6626–6683.
- [10] M. Olivares-Marín, P. Palomino, J.M. Amarilla, E. Enciso, D. Tonti, Effects of architecture on the electrochemistry of binder-free inverse opal carbons as Li–air cathodes in an ionic liquid-based electrolyte, *J. Mater. Chem. A* 1 (45) (2013) 14270–14279.
- [11] L. Ma, T. Yu, E. Tzoganakis, K. Amine, T. Wu, Z. Chen, J. Lu, Fundamental understanding and material challenges in rechargeable nonaqueous Li–O<sub>2</sub> batteries: recent progress and perspective, *Adv. Energy Mater.* 8 (22) (2018) 1800348.
- [12] D.M. Itkina, D.A. Semenenko, E.Y. Kataev, A.I. Belova, V.S. Neudachina, A.P. Sirotnina, M. Havecker, D. Teschner, A. Knop-Gericke, P. Dudin, A. Barinov, E.A. Goodilin, Y. Shao-Horn, L.V. Yashina, Reactivity of carbon in lithium-oxygen battery positive electrodes, *Nano Lett.* 13 (10) (2013) 4697–4701.
- [13] M. Kim, E. Yoo, W.-S. Ahn, S.E. Shim, Controlling porosity of porous carbon cathode for lithium oxygen batteries: influence of micro and meso porosity, *J. Power Sources* 389 (2018) 20–27.
- [14] S. Roig-Sanchez, E. Jungstedt, I. Anton-Sales, D.C. Malaspina, J. Farauto,

- L.A. Berglund, A. Laromaine, A. Roig, Nanocellulose films with multiple functional nanoparticles in confined spatial distribution, *Nanoscale Horiz* 4 (3) (2019) 634–641.
- [15] A. Alonso-Díaz, J. Floriach-Clark, J. Fuentes, M. Capellades, N.S. Coll, A. Laromaine, Enhancing localized pesticide action through plant foliage by silver-cellulose hybrid patches, *ACS Biomater. Sci. Eng.* 5 (2) (2019) 413–419.
- [16] G. Fei, Y. Wang, H. Wang, Y. Ma, Q. Guo, W. Huang, D. Yang, Y. Shao, Y. Ni, Fabrication of bacterial cellulose/polyaniline nanocomposite paper with excellent conductivity, strength, and flexibility, *ACS Sustain. Chem. Eng.* 7 (9) (2019) 8215–8225.
- [17] D. Abol-Fotouh, B. Dorling, O. Zapata-Arteaga, X. Rodriguez-Martinez, A. Gomez, J.S. Reparaz, A. Laromaine, A. Roig, M. Campoy-Quiles, Farming thermoelectric paper, *Energy Environ. Sci.* 12 (2) (2019) 716–726.
- [18] X. Hao, J. Wang, B. Ding, Y. Wang, Z. Chang, H. Dou, X. Zhang, Bacterial-cellulose-derived interconnected meso-microporous carbon nanofiber networks as binder-free electrodes for high-performance supercapacitors, *J. Power Sources* 352 (2017) 34–41.
- [19] L. Zuo, W. Fan, Y. Zhang, Y. Huang, W. Gao, T. Liu, Bacterial cellulose-based sheet-like carbon aerogels for the in situ growth of nickel sulfide as high performance electrode materials for asymmetric supercapacitors, *Nanoscale* 9 (13) (2017) 4445–4455.
- [20] E. Jazaeri, L. Zhang, X. Wang, T. Tsuzuki, Fabrication of carbon nanofiber by pyrolysis of freeze-dried cellulose nanofiber, *Cellulose* 18 (6) (2011) 1481–1485.
- [21] N. Pircher, L. Carbajal, C. Schimper, M. Bacher, H. Rennhofer, J.M. Nedelec, H.C. Lichtenegger, T. Rosenau, F. Liebner, Impact of selected solvent systems on the pore and solid structure of cellulose aerogels, *Cellulose* 23 (3) (2016) 1949–1966.
- [22] Y. Peng, D.J. Gardner, Y. Han, Drying cellulose nanofibrils: in search of a suitable method, *Cellulose* 19 (1) (2011) 91–102.
- [23] A.A. Alhwaige, H. Ishida, S. Qutubuddin, Carbon aerogels with excellent CO<sub>2</sub> adsorption capacity synthesized from clay-reinforced biobased chitosan-polybenzoxazine nanocomposites, *ACS Sustain. Chem. Eng.* 4 (3) (2016) 1286–1295.
- [24] Y. Li, Y. Liu, M. Wang, X. Xu, T. Lu, C.Q. Sun, L. Pan, Phosphorus-doped 3D carbon nanofiber aerogels derived from bacterial-cellulose for highly-efficient capacitive deionization, *Carbon* 130 (2018) 377–383.
- [25] D.Y. Chung, Y.J. Son, J.M. Yoo, J.S. Kang, C.Y. Ahn, S. Park, Y.E. Sung, Coffee waste-derived hierarchical porous carbon as a highly active and durable electrocatalyst for electrochemical energy applications, *ACS Appl. Mater. Interfaces* 9 (47) (2017) 41303–41313.
- [26] C. Wang, D. Wu, H. Wang, Z. Gao, F. Xu, K. Jiang, A green and scalable route to yield porous carbon sheets from biomass for supercapacitors with high capacity, *J. Mater. Chem. A* 6 (3) (2018) 1244–1254.
- [27] L. Hu, Q. Zhu, Q. Wu, D. Li, Z. An, B. Xu, Natural biomass-derived hierarchical porous carbon synthesized by an in situ hard template coupled with NaOH activation for ultrahigh rate supercapacitors, *ACS Sustain. Chem. Eng.* 6 (11) (2018) 13949–13959.
- [28] L. Zhang, T. You, T. Zhou, X. Zhou, F. Xu, Interconnected hierarchical porous carbon from lignin-derived byproducts of bioethanol production for ultrahigh performance supercapacitors, *ACS Appl. Mater. Interfaces* 8 (22) (2016) 13918–13925.
- [29] A. Tejado, W.C. Chen, M.N. Alam, T.G.M. van de Ven, Superhydrophobic foam-like cellulose made of hydrophobized cellulose fibres, *Cellulose* 21 (2014) 1735–1743.
- [30] J. Li, T. Song, H. Xiu, M. Zhang, R. Cheng, Q. Liu, X. Zhang, E. Kozliak, Y. Ji, Foam materials with controllable pore structure prepared from nanofibrillated cellulose with addition of alcohols, *Ind. Crop. Prod.* 125 (2018) 314–322.
- [31] E. Alonso, M. Faria, F. Mohammadkazemi, M. Resnik, A. Ferreira, N. Cordeiro, Conductive bacterial cellulose-polyaniline blends: influence of the matrix and synthesis conditions, *Carbohydr. Polym.* 183 (2018) 254–262.
- [32] L. Zhang, H. Gong, Improvement in flexibility and volumetric performance for supercapacitor application and the effect of Ni–Fe ratio on electrode behaviour, *J. Mater. Chem. A* 3 (14) (2015) 7607–7615.
- [33] H. Peng, B. Yao, X. Wei, T. Liu, T. Kou, P. Xiao, Y. Zhang, Y. Li, Pore and heteroatom engineered carbon foams for supercapacitors, *Adv. Energy Mater.* 9 (19) (2019) 1803665.
- [34] H. Zhang, X. Sun, M.A. Hubbe, L. Pal, Highly conductive carbon nanotubes and flexible cellulose nanofibers composite membranes with semi-interpenetrating networks structure, *Carbohydr. Polym.* 222 (2019) 115013.
- [35] Z. Hanif, H. Jeon, T.H. Tran, J. Jegal, S.-A. Park, S.-M. Kim, J. Park, S.Y. Hwang, D.X. Oh, Butanol-mediated oven-drying of nanocellulose with enhanced dehydration rate and aqueous re-dispersion, *J. Polym. Res.* 24 (3) (2017) 191–201.
- [36] Z. Lu, Z. Su, S. Song, Y. Zhao, S. Ma, M. Zhang, Toward high-performance fibrillated cellulose-based air filter via constructing spider-web-like structure with the aid of TBA during freeze-drying process, *Cellulose* 25 (1) (2017) 619–629.
- [37] J. Juntaro, S. Ummartyotin, M. Sain, H. Manuapiya, Bacterial cellulose reinforced polyurethane-based resin nanocomposite: a study of how ethanol and processing pressure affect physical, mechanical and dielectric properties, *Carbohydr. Polym.* 87 (4) (2012) 2464–2469.
- [38] M. Olivares-Marín, M. Aklalouch, D. Tonti, Combined influence of meso- and macroporosity of soft-hard templated carbon electrodes on the performance of Li–O<sub>2</sub> cells with different configurations, *Nanomaterials* 9 (6) (2019) 810–822.
- [39] M. Zeng, A. Laromaine, A. Roig, Bacterial cellulose films: influence of bacterial strain and drying route on film properties, *Cellulose* 21 (6) (2014) 4455–4469.
- [40] H. Chen, J. Chen, N. Teng, H. Na, J. Zhu, Controlling the status of corn cellulose solutions by ethanol to define fiber morphology during electrospinning, *Cellulose* 24 (2) (2016) 863–870.
- [41] L. Wang, M. Ago, M. Borghi, A. Ishaq, A.C. Papageorgiou, M. Lundahl, O.J. Rojas, Conductive carbon microfibers derived from wet-spun lignin/nanocellulose hydrogels, *ACS Sustain. Chem. Eng.* 7 (6) (2019) 6013–6022.
- [42] Z. Wang, B. Pecha, R.J.M. Westerhof, S.R.A. Kersten, C.-Z. Li, A.G. McDonald, M. Garcia-Perez, Effect of cellulose crystallinity on solid/liquid phase reactions responsible for the formation of carbonaceous residues during pyrolysis, *Ind. Eng. Chem. Res.* 53 (8) (2014) 2940–2955.
- [43] Z. Wang, A.G. McDonald, R.J.M. Westerhof, S.R.A. Kersten, C.M. Cuba-Torres, S. Ha, B. Pecha, M. Garcia-Perez, Effect of cellulose crystallinity on the formation of a liquid intermediate and on product distribution during pyrolysis, *J. Anal. Appl. Pyroly.* 100 (2013) 56–66.
- [44] P.C. Lewellen, W.A. Peters, J.B. Howard, Cellulose pyrolysis kinetics and char formation mechanism, *Symp. (Int.) Combust.* 16 (1) (1977) 1471–1480.
- [45] P.P. Ghimire, M. Gao, M. Jaroniec, Amino acid-assisted synthesis of porous graphitic carbon spheres with highly dispersed Ni nanoparticles, *Carbon* 153 (2019) 206–216.
- [46] M. Olivares-Marín, P. Palomino, E. Enciso, D. Tonti, Simple method to relate experimental pore size distribution and discharge capacity in cathodes for Li/O<sub>2</sub> batteries, *J. Phys. Chem. C* 118 (36) (2014) 20772–20783.
- [47] H. Wang, J. Wang, Y. Pi, Q. Shao, Y. Tan, X. Huang, Double perovskite LaFe<sub>x</sub>Ni<sub>1-x</sub>O<sub>2</sub> nanorods enable efficient oxygen evolution electrocatalysis, *Angew. Chem. Int. Ed.* 58 (8) (2019) 2316–2320.
- [48] S.D. Ghadge, O.I. Velikokhatnyi, M.K. Datta, P.M. Shanthi, S. Tan, K. Damodaran, P.N. Kumta, Experimental and theoretical validation of high efficiency and robust electrocatalytic response of one-dimensional (1D) (Mn, Ir)<sub>2</sub>O<sub>7</sub>:10F nanorods for the oxygen evolution reaction in PEM-based water electrolysis, *ACS Catal.* 9 (3) (2019) 2134–2157.
- [49] P. Wang, C. Li, S. Dong, X. Ge, P. Zhang, X. Miao, Z. Zhang, C. Wang, L. Yin, One-step route synthesized Co<sub>2</sub>P/Ru/N-doped carbon nanotube hybrids as bifunctional electrocatalysts for high-performance Li–O<sub>2</sub> batteries, *Small* 15 (30) (2019) 1900001.
- [50] K.-H. Xue, T.-K. Nguyen, A.A. Franco, Impact of the cathode microstructure on the discharge performance of lithium air batteries: a multiscale model, *J. Electrochem. Soc.* 161 (8) (2014) E3028–E3035.
- [51] M. Benoit, A. Rodrigues, K. De Oliveira Vigier, E. Fourré, J. Barrault, J.-M. Tatibouët, F. Jérôme, Combination of ball-milling and non-thermal atmospheric plasma as physical treatments for the saccharification of microcrystalline cellulose, *Green Chem.* 14 (8) (2012) 2212–2215.
- [52] M. Aklalouch, M. Olivares-Marín, R.C. Lee, P. Palomino, E. Enciso, D. Tonti, Mass-transport control on the discharge mechanism in Li–O<sub>2</sub> batteries using carbon cathodes with varied porosity, *ChemSusChem* 8 (20) (2015) 3465–3471.
- [53] N. Ding, S.W. Chien, T.S.A. Hor, R. Lum, Y. Zong, Z. Liu, Influence of carbon pore size on the discharge capacity of Li–O<sub>2</sub> batteries, *J. Mater. Chem.* 2 (31) (2014) 12433–12441.
- [54] H.-M. Kao, C.-C. Cheng, C.-C. Ting, L.-Y. Hwang, Phase control of cubic SBA-1 mesostructures via alcohol-assisted synthesis, *J. Mater. Chem.* 15 (29) (2005) 2989–2992.
- [55] C. Calero, J. Faraudo, D. Bastos-Gonzalez, Interaction of monovalent ions with hydrophobic and hydrophilic colloids: charge inversion and ionic specificity, *J. Am. Chem. Soc.* 133 (38) (2011) 15025–15035.





## Bio and soft-imprinting lithography on bacterial cellulose films

S. Roig-Sanchez<sup>a</sup>, C. Fernández-Sánchez<sup>b, c</sup>, A. Laromaine<sup>a, \*</sup>, A. Roig<sup>a, \*\*</sup>

<sup>a</sup> Institute of Materials Science of Barcelona (ICMAB-CSIC), Campus UAB, 08193, Bellaterra, Catalonia, Spain

<sup>b</sup> Instituto de Microelectrónica de Barcelona (IMB-CNM), CSIC, Campus UAB, Bellaterra, 08193, Barcelona, Spain

<sup>c</sup> CIBER de Bioingeniería, Biomateriales y Nanomedicina (CIBER-BBN), Jordi Girona 18-26, 08034, Barcelona, Spain



### ARTICLE INFO

#### Article history:

Received 28 May 2021

Received in revised form

9 July 2021

Accepted 11 July 2021

Available online xxx

#### Keywords:

Bacterial cellulose

Bio-lithography

Soft-imprint

Nanocellulose

Polydimethylsiloxane

### ABSTRACT

Bacterial cellulose (BC) is a biocompatible polysaccharide produced by bacteria currently used in packaging, cosmetics, or health care. A highly attractive feature of BC is the possibility of patterning the BC pellicle during its biosynthesis, a concept coined as bio-lithography. BC-patterned films have demonstrated improved properties for cellular-guided growth, implant protection, or wound dressing. However, aspects such as the diversity and size of the features patterned, how those features withstand post-processing steps, or if large areas can be patterned remain unanswered. Gathering knowledge on these characteristics could extend the use of patterned cellulose-based materials in emerging fields such as transient devices, nanogenerators, or microfluidics. Here, we show that bio-lithographed BC films present good-quality micropatterned features for various motifs (wells, pillars, and channels) in a wide range of sizes (from 200 to 5  $\mu\text{m}$ ) and areas as large as 70  $\text{cm}^2$ . Besides, we have studied the fidelity of the motifs and the fiber organization for wet, supercritical, and oven-dried films. When wells and pillars were patterned, the x and y dimensions were faithfully replicated in the wet and dried samples, but only wet and supercritically dried films afforded mold accuracy in the z-direction. In addition, x/z ratio should be carefully considered for obtaining self-standing pillars. Finally, we compared bio-lithography and soft-imprint lithography. In the latter case, fiber alignment was not observed and the depth of the resulting features dramatically decreased; however, this technique allowed us to produce submicron features that remain after the rewetting of the BC films.

© 2021 The Author(s). Published by Elsevier Ltd. This is an open access article under the CC BY-NC-ND license (<http://creativecommons.org/licenses/by-nc-nd/4.0/>).

## 1. Introduction

Bio-based polymers with a high degree of complexity and added value are securing a place in non-traditional sectors by adapting processing approaches from the semiconductor and synthetic polymers technologies. Among them, bacterial cellulose (BC) is drawing attention as it is a natural polysaccharide produced by bacteria such as *Agrobacterium*, *Komagataeibacter*, *Pseudomonas*, or *Salmonella*. BC grows at the interface between the bacterial broth and the air, generating a continuous film of intertwined nanocellulosic fibers. BC properties, namely, porosity, crystallinity, water-holding capacity, biocompatibility, and outstanding mechanical properties [1–3], have promoted this material to be used in diverse fields as food [4,5], packaging [6], cosmetics [7], or health

care [8–10]. Furthermore, the application landscape of BC is constantly expanding fostered by the versatility and easy fabrication of novel composite BC materials [11,12], BC-based scaffolds [13], and self-standing 3D structures [14,15]. Besides all those aspects, an attractive feature of BC is the possibility to pattern the pellicles at the same time that they are biosynthesized, a concept that has been coined as bio-lithography. This process uses an elastomeric stamp/mold placed on top of the bacterial culture media, which induces the bacteria to produce a cellulose pellicle replicating the pattern of the stamp. The mold is usually made of polydimethylsiloxane (PDMS) as this material shows high oxygen diffusion and can be easily patterned. This one-step and low-cost strategy was first proposed by Guang et al. [16] and further expanded by other groups [17–20]. More complex bio-lithography approaches have also been described, such as the fabrication of BC implants mimicking vascular networks using PLA sacrificial templates [21] or silicone tubes [22] as well as the growth of complex BC films using superhydrophobic molds [23].

Interestingly, recent studies reported on the medical benefits for bio-lithographed BC. Specifically, patterned BC was used as a substrate for cellular-guided growth [24], antifibrotic protection of

Abbreviations: BC, bacterial cellulose; S-BC, structured bacterial cellulose; HS, Hestrin–Schramm; MQ, MilliQ water; PDMS, Polydimethylsiloxane; OD, oven dried; FD, freeze-dried; SCD, supercritically dried; I, soft-imprint lithography.

\* Corresponding author.

\*\* Corresponding author.

E-mail addresses: [alaromaine@icmab.es](mailto:alaromaine@icmab.es) (A. Laromaine), [roig@icmab.es](mailto:roig@icmab.es) (A. Roig).



implantable devices [25], scar inhibition of wound dressings [26], to accelerate wound healing [27], or to reduce biofilms fouling [28]. In general, those studies use channels and trenches as motifs; however, scarce information is found on BC with well or pillars. Gathering data on the different types of features and sizes that can be patterned and how those features withstand postprocessing will certainly expand the uses of bio-lithographed BC to other emerging fields such as transient devices [29], particularly, separators for transient batteries, cellulose nanogenerators based on piezoelectric, triboelectric, or thermoelectric effects [30–32] or single-use recyclable microfluidic platforms [33].

Here, we provide more insight on the bio-lithography process as a one-step, template-induced growth technique to create structured BC (S-BC) films. For that, we have bio-lithographed large areas of the BC films with wells, pillars, and channels, and we have studied the fidelity of the mold replication in a wide range of sizes. Particular efforts have been conducted on the characterization of wells and pillars since they have been identified to influence the expansion, proliferation, and homogeneity of stem cell culture [34]. We have also investigated how the drying method influences the micropatterned BC films' integrity. Finally, we have used the conventional soft-imprinting technology to modify the BC films after biosynthesis and compared both approaches.

## 2. Materials and methods

### 2.1. Materials

*Komagateibacter xylinus* (NCIMB 5346) bacterial strain was obtained from CECT (Valencia, Spain). Glucose, peptone, yeast extract, agar (Conda Lab), disodium hydrogen phosphate dodecahydrate, and citric acid monohydrate (Sigma-Aldrich) were used to prepare Hestrin–Schramm (HS) culture medium. 0.1 M NaOH (Sigma-Aldrich) solution was prepared for the cellulose cleaning process. Sodalime antireflective chrome mask was purchased from DELTA MASK B.V. SU-8 (2005 and 2050) and developer were purchased from Micro Resist Technology GmbH (Berlin, Germany). PDMS Sylgard 184 elastomer kit was purchased from Dow Corning (Midland, MI, USA).

### 2.2. Production of polydimethylsiloxane stamps

The fabrication of the patterned PDMS stamps consists of two main steps: first, the definition of a master using SU-8 negative photoresist and second the replication of the master using PDMS. Masters were fabricated on 4-inch silicon wafers at the IMB-CNM Clean Room facilities. Briefly, the process was, first, a 5- $\mu$ m thick seed layer of SU-8 2005 was spun-coated, prebaked at 95 °C for 2 min, exposed to UV and postbaked at 120 °C for 90 min. Then a layer of SU-8 2050 was spun-coated, prebaked at 95 °C for 120 min, exposed to UV through a mask containing the desired patterns for 26 s, postbaked at 95 °C for 16 min, developed by immersion in the developer solution for 2.5 min, rinsed with isopropanol, and eventually hard-baked at 120 °C for 160 min.

PDMS stamps were obtained by vigorously mixing Sylgard 184 resin and curing agent at a 10:1 ratio. The mixture was then poured onto the master, and vacuum was applied to remove air bubbles entrapped into the PDMS solution and in the master surface. After curing (80 °C, 20 min), the PDMS stamp was peeled off the master. The master was then cleaned with EtOH and the process was repeated if needed.

The PDMS stamp with submicron motifs used for soft-imprinting was kindly provided by the NANOPTO group (ICMAB).

A list and description of the molds used is included in Table S1 and S2.

### 2.3. Production of structured bacterial cellulose films. Bio-lithography

HS liquid medium was prepared by mixing 5 g of yeast, 5 g of peptone, 1.15 g of citric acid, and 6.8 g disodium hydrogen phosphate dodecahydrate in 800 mL of water. 20 g of dextrose was diluted in 200 mL of water, and both solutions were autoclaved. Dextrose was autoclaved separately to avoid a reaction between the monosaccharides and the proteins. After the autoclave step, both solutions were mixed under sterile conditions and kept inside the fridge until further use.

Bacteria were grown in several steps. First, a colony was expanded in 6 mL of HS fresh liquid medium for 7 days at 30 °C. Then, 0.5 mL of bacteria broth was transferred to 4.5 mL of fresh medium and incubated for another 3 days. Subsequently, a solution 1:14 inoculum:HS medium was prepared and transferred to different plates filling two-thirds of the volume. A PDMS mold was placed on top with the patterned side facing the liquid solution. After 3 days of incubation at 30 °C, the PDMS was removed, and the S-BC films were harvested and cleaned. To achieve a BC-structured film of 71 cm<sup>2</sup>, 6 days of incubation were needed.

After harvesting the samples, the films were soaked for 10 min in an EtOH:Milli-Q (MQ) water 1:1 solution. Then, they were washed twice with boiling MQ water for 20 min and another two times for 20 min with a NaOH 0.1 M solution at 90 °C. Finally, the films were rinsed with MQ water until neutralization of the pH and were stored in water at room temperature.

### 2.4. Drying of structured bacterial cellulose films

#### 2.4.1. Oven drying (OD)

BC films were dried between two Teflon plates at 60 °C.

#### 2.4.2. Freeze-drying (FD)

S-BC films were immersed in the smallest amount of MQ water needed (~2 mL) to fully cover the sample inside a vial. Then, the vial was sealed with pierced aluminum paper and placed inside the lyophilizer (LYOQUEST-85 from Telstar) at 0.05 mbar and –80 °C for 48 h until complete ice water sublimation.

#### 2.4.3. Supercritical drying (SCD)

Samples were distributed on a paper accordion, each fold containing one sample. The accordion was soaked twice in ethanol for 30 min and left overnight (12 h) in fresh ethanol for complete solvent exchange. Samples were then placed on a 300 mL vessel filled with the solvent (SCF 300-mL plant). The system was pressurized to 100 bars, and the drying process took place in two steps. First, ethanol was exchanged with liquid CO<sub>2</sub> at a flow rate of 1500 mL/h for 1.5 h. Then, the reactor was heated at 45 °C with a CO<sub>2</sub> flow of 1500 mL/h for 1 h.

### 2.5. Production of structured bacterial cellulose films. Soft-imprint

A solution 1:14 inoculum:HS medium was transferred to different plates filling two-thirds of the volume and after 3 days incubation at 30 °C, a flat BC pellicle (no patterned) was harvested and cleaned. Then, a PDMS stamp was placed above the wet BC with the patterned side facing the film, and both were sandwiched between two Teflon plates for drying:

#### 2.5.1. OD

The setup was allocated inside an oven at 60 °C for 12 h with a 1 kg weight placed on top to ensure a successful transfer of the patterning during drying.

### 2.5.2. SCD

The setup was fastened with two clamps, and the sample was subjected to the solvent exchange and drying process, as described above.

## 2.6. Characterization

### 2.6.1. Scanning electron microscopy and fiber alignment study

Samples were fixed on top of an aluminum SEM holder with adhesive carbon tape. FEI Quanta 200FEG FEG-ESEM under low-vacuum conditions (40–60 Pa) was used to study the replica molding on BC films. An acceleration voltage of 10 kV, an electron beam spot of 3 mm and a working distance of 10 mm were used to study x and y values from 4 to 15 patterns. The samples were tilted under the same conditions to study z values. Fiber orientation was analyzed by OrientationJ package from ImageJ software. An orientation color map was obtained where the hue describes the fiber orientation and the saturation the coherency of the alignment.

### 2.6.2. Optical microscope

Samples were placed on a microscope glass slide and observed through 5x, 20x, 50x, and 100x magnifications (Olympus B×51 and Nikon SMZ2800 N with a XM Full HD camera, MicroscopiaDigital). Size values of the patterns were calculated by analyzing from 4 to 15 features with ImageJ software.

### 2.6.3. Confocal microscope

Soft-imprint topographic studies were done by a LEICA DCM 3D dual-core 3D measuring microscope. Samples were allocated on a microscope glass slide, and images were obtained with 10x and 50x magnifications. Stacks of images covering the z deviation of the surface were acquired. 3D reconstructions and 2D profiles were analyzed with MountainsMap 8.2 software by analyzing three replicas.

### 2.6.4. Atomic force microscopy

Before performing the soft-imprint, BC films were placed over a cover glass to reduce the intrinsic roughness of the BC films on drying. A Keysight 5100 atomic force microscope was employed on

tapping mode to acquire topographic images. The images were analyzed with MountainsMap 8.2 software.

## 3. Results and discussion

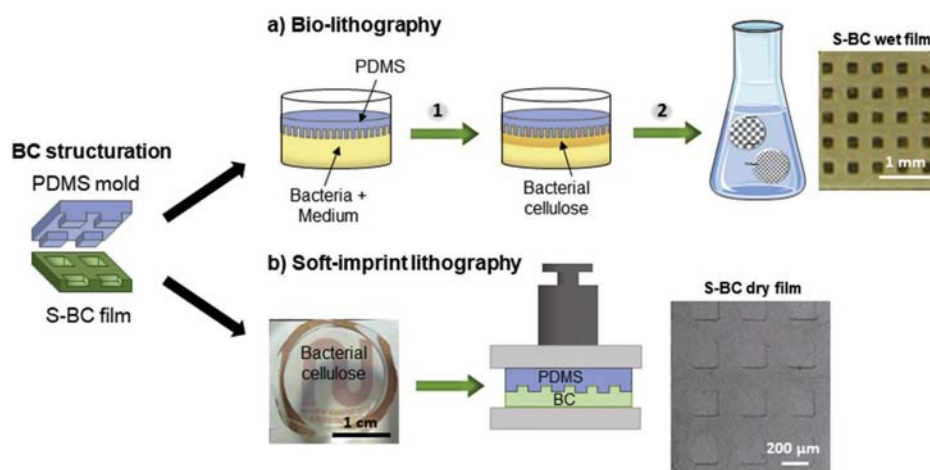
### 3.1. Bacterial cellulose film structuration

S-BC films employing stamps with wells, pillars as motifs were obtained by two different approaches. Molds used are described in Table S1. In the first method, BC was biosynthesized guided by a patterned PDMS template (Fig. 1A). Since PDMS allows oxygen diffusion and has a lower density than water, it sits at the interface between air and bacteria broth. The stamp does not hinder the growth of the BC pellicle but forces the bacteria to produce a film that follows the topology of the template. This process is often referred to as bio-lithography. The second patterning method consisted of the soft imprinting of BC films after the biosynthesis (Fig. 1B). A patterned PDMS mold was placed on a wet BC film and dried together between Teflon plates at 60 °C for 12 h under 1 kg weight pressure. By this soft-imprint lithography, the patterning is performed concomitantly during the drying of the film, resulting in dried S-BC films. In contrast, the bio-lithography method produces wet-patterned BC films that could be used as obtained or be later dried allowing a larger diversity of materials.

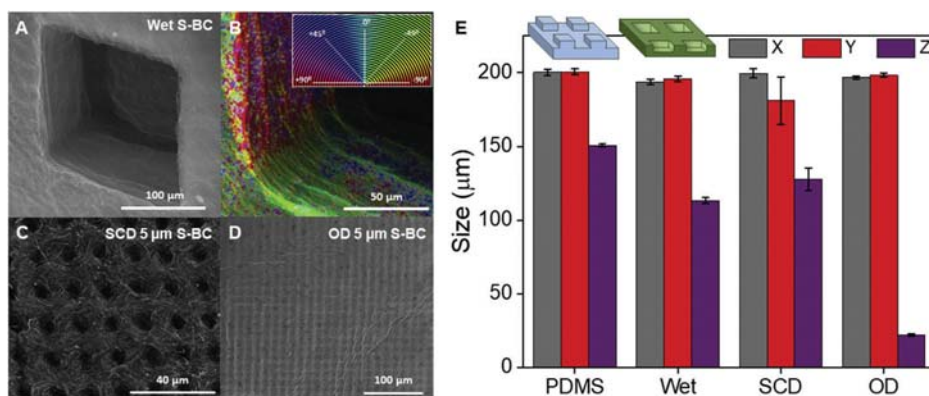
### 3.2. Bio-lithography

Bio-lithography of wells, pillars, and channels or the combination of them were obtained as wet-patterned BC films in a single and reproducible step. In addition, after harvesting, the motifs hold the cleaning BC process and were stable over time. However, to examine more precisely the fidelity of the patterns, the films were dried using different drying processes. In particular, we study the influence of SCD and OD at 60 °C. SCD is the method that mimics more faithfully the fibrillar arrangement and porosity of the native wet BC hydrogel, whereas OD reduces considerably the thickness and porosity of the final film [2].

S-BC film with bio-lithographed square wells of 200, 50, 20, and 5 μm size in the x and y-axis were evaluated. The initial stamp of



**Fig. 1. Scheme of the processes to produce structured bacterial cellulose films (S-BC).** a) Bio-lithography. Step 1: incubation of the bacterial broth for 3 days at 30 °C with the patterned polydimethylsiloxane (PDMS) on top. Step 2: removal of the PDMS and cleaning of BC with boiling water and NaOH 0.1 M solution to obtain wet and transparent S-BC films (image). b) Soft-imprint lithography: harvest and clean the BC film from the culture, and let it dry in contact with a patterned PDMS mold for 12 h at 60 °C and applying pressure (1 kg weight). A dry S-BC film is obtained (image).

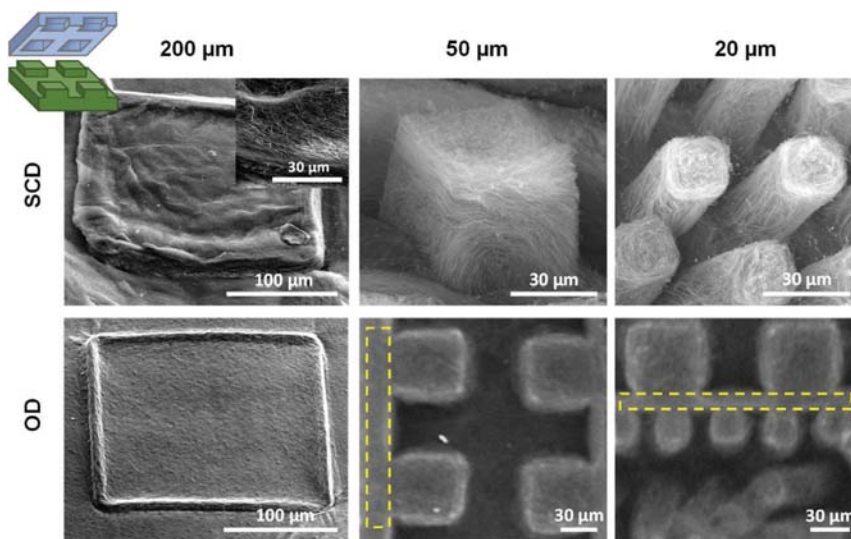


**Fig. 2. Structured bacterial cellulose (S-BC) square well dimension depending on drying conditions.** A) SEM image of a wet S-BC showing a defined feature contour and the alignment of the fibers. B) High-magnification SEM image where the two directions of the aligned fibers are highlighted in a different color. C) S-BC with wells of 5  $\mu\text{m}$  dried under supercritical drying conditions. D) S-BC with wells of 5  $\mu\text{m}$  dried under oven drying conditions. E) Dimension fidelity study of square structures replicated with PDMS mold dimensions of 200  $\mu\text{m}$  length (x, y-axis) and 140  $\mu\text{m}$  depth (z-axis).

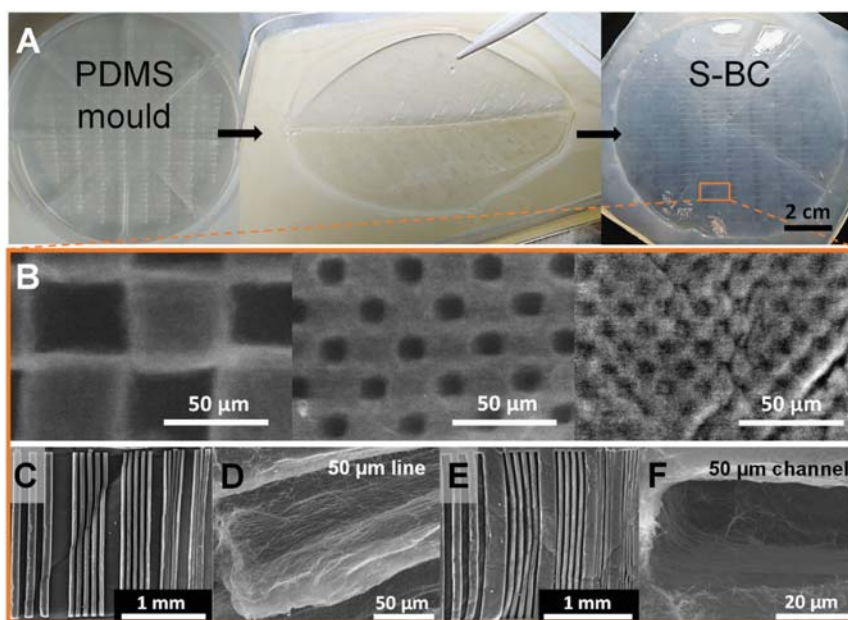
200  $\mu\text{m}$  wells had 140  $\mu\text{m}$  depth (z-axis), whereas the smaller ones all had 50  $\mu\text{m}$  on the z-axis. We compared the dimensions of the patterned features of wet, SCD and OD S-BC with the original PDMS stamp. FD was also tested; however, the square shape of the wells was not maintained with enough fidelity, and the method was discarded. (Fig. S1). Fig. 2 and S2 depict the patterned areas of the films. For the 200- $\mu\text{m}$  well, the wet S-BC presents an extremely good replication of the stamp with well-defined structures (Fig. 2A). A closer look at the fiber disposition of the wet S-BC indicates an alignment of the fibers at the interior of the well. Fig. 2B shows a color map of an area of the well at high magnifications where colors are assigned to different orientations and higher saturation levels indicate high fiber alignment. Two areas with different colors are more prominent, indicating an ordered fiber arrangement at a 90-degree angle, corresponding to the orthogonal

well side. This result suggests that when a bacterium encounter the PDMS mold with the motifs, it surrounds the obstacle producing the cellulose nanofibers in the process. Similar behavior was also reported for PDMS stamps with channels [24]. Interestingly, smaller wells with x, y-axis down to 5  $\mu\text{m}$  could also be well replicated (Fig. 2C) and although OD strongly decreases the depth of the wells (Fig. 2D), fiber-ordered arrangement can also be observed. Note that sharp edges of the square motifs disappeared for features smaller than 20  $\mu\text{m}$  since the used PDMS molds loses the square resolution at those sizes. Fig. S2 includes a more detailed comparison of 50 to 5  $\mu\text{m}$  features of SCD and OD S-BC.

For the 200- $\mu\text{m}$  wells, the replication of the x-, y-, and z-dimensions was studied in detail, and results are summarized in Fig. 2E. The x- and y-dimensions were faithfully replicated in the wet and dried samples while size changes were computed in the



**Fig. 3. Structured films with columns of 50  $\mu\text{m}$  depth (z-value) and square base of 200, 50, and 20  $\mu\text{m}$  dried by supercritical drying or oven drying (lines). Inset: higher magnification SEM image showing the alignment of fibers at the column wall.**



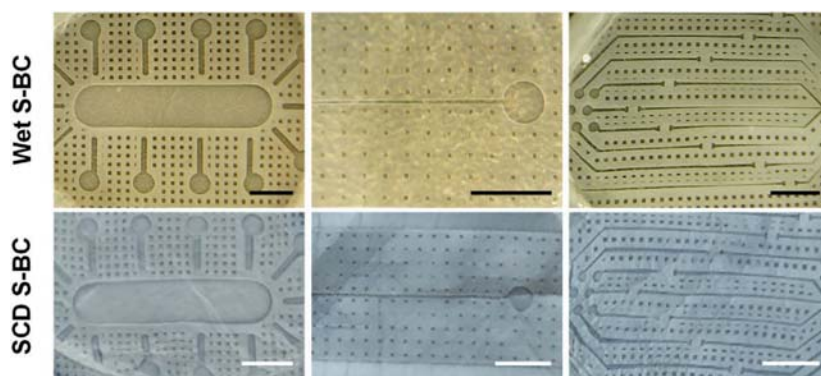
**Fig. 4.** A) Bio-lithography process of a 9.5-cm diameter PDMS mold, which contains 567 patterns with channels, lines, wells, and pillars ranging from 100 to 1  $\mu\text{m}$ . B–F) SEM images of areas of the 9.5-cm structural bacterial cellulose film: B) Zig-zag display of well and pillars of 50, 20, and 10  $\mu\text{m}$ , respectively. C) Lines ranging from 100 to 30  $\mu\text{m}$ . D) Line of 50  $\mu\text{m}$  where the fiber alignment is seen. E) Grooves ranging from 100 to 30  $\mu\text{m}$ . F) Groove of 50  $\mu\text{m}$  where the fiber alignment is seen.

z-dimension. Compared with the initial PDMS stamp, a decrease in z of  $\sim 15\%$  was measured for wet and SCD S-BC films, whereas an 85% reduction was found for the OD samples. As a consequence of the large reduction in the depth of the motifs for the OD samples and the feature compaction, the cellulose fraction increases and results in bright areas surrounding the features in the SEM images (Fig. S3A) and double edges at the borders of the wells (Fig. S3B).

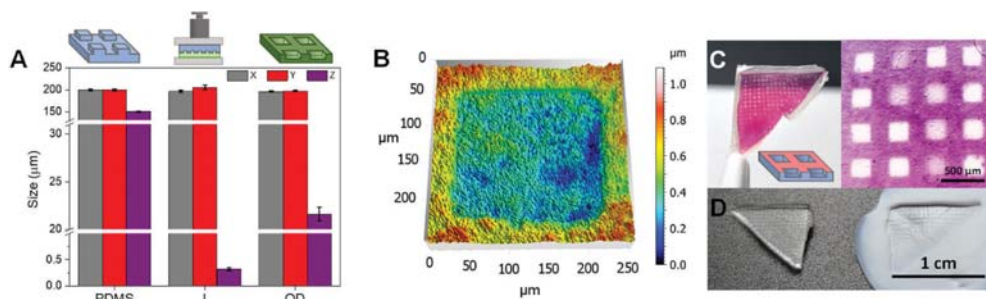
Next, the bio-lithography process of pillars is described. Fig. 3 and Fig. S5 show columns with different base dimensions (200, 50, and 20  $\mu\text{m}$ ) and z (height) of 50  $\mu\text{m}$ . Interestingly, by SCD, it was possible to obtain standing pillars for all the sizes investigated and while decreasing the x/z ratio, those pillars become thinner, longer, and wavier. The alignment of the fibers can again be observed, especially for small x/z ratio structures. In addition, as previously

observed in the case of wells, OD induces pillars' collapse or bending, as seen in the 200- $\mu\text{m}$ -wide pillars and Fig. S4. However, when the pillar is in contact with another cellulosic structure supporting it (Fig. 3 lower row, highlighted as a dashed rectangle), well-defined standing pillars can be obtained even by OD.

Finally, a large micropatterned PDMS mold of 70  $\text{cm}^2$  containing 567 replicas of a particular pattern, which includes channels, lines, wells and pillars ranging from 100 to 1  $\mu\text{m}$  in size (x, y-axis) was used as a template (Fig. 4A). After an incubation period of 6 days, a structured film was obtained. Fig. 4B depicts features with dimensions of 50, 20, and 10  $\mu\text{m}$  present in the S-BC film. For sizes below 20  $\mu\text{m}$ , the square structure replicates as a circular as we reach the square-resolution limit of our PDMS mold. Note that a good replication of channels and lines ranging from 100 to 30  $\mu\text{m}$  could be achieved (Fig. 4C and E). In both cases, the



**Fig. 5.** Wet and supercritical drying structured bacterial cellulose films with combinations of channels and wells. Scale bar: 2 mm.



**Fig. 6.** A) Dimensions of 200- $\mu\text{m}$  well-squares obtained from soft-imprint lithography (I) vs. bio-lithography (OD). B) Topographic confocal image of structured bacterial cellulose (S-BC) with 200  $\mu\text{m}$  squares obtained from soft-imprint lithography. C) Proof-of-concept of BC functionalization during soft-impression. D) Image of an S-BC structured during the supercritical drying process.

cellulose fibers are templated, and an alignment can be easily observed (Fig. 4D and F).

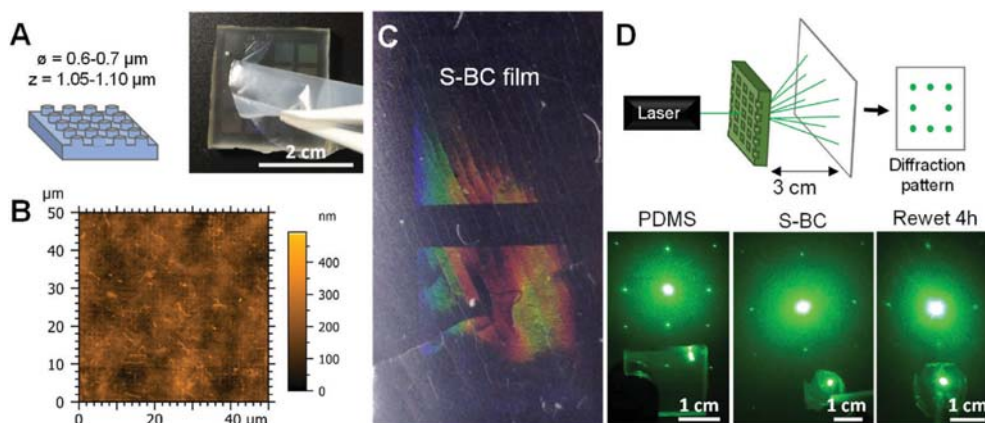
The same process can be used to obtain more intricate shapes as shown in Fig. 5, which displays examples of wet S-BC films combining channels and wells. These films can withstand OD and SCD, maintain the structure even after 5 h rehydration (Fig. S6) and could be ideal to structure microfluidic devices in a single step. For that, a proof-of-concept of their channel diffusion was tested showing capillarity, although more optimization is needed (Fig. S7).

### 3.3. Soft-imprint lithography

Soft-imprint lithography (Fig. 1B) was used to imprint features below 1  $\mu\text{m}$  that could not be achieved with the bio-lithography approach. First, a PDMS mold with square columns of 200  $\mu\text{m}$  base size and 140  $\mu\text{m}$  depth was used for that purpose. As shown in the graph of Fig. 6A, while the x and y dimensions are maintained, the z is considerably reduced (~99%), which is a much larger reduction than for OD S-BC obtained by bio-lithography. Fig. 6B shows a topographic image of a 200- $\mu\text{m}$  well from a soft-imprinted BC film with a depth of  $0.33 \pm 0.03 \mu\text{m}$ . Interestingly, this approach also offers the opportunity to functionalize particular areas of the BC film just by a simple transference from the PDMS mold to the BC. Fig. 6C shows an S-BC film dyed with Safranin-O, which was previously added to the PDMS mold. Besides, as this technique struc-

tures the BC during drying, we tried to soft-imprint under SCD conditions, allowing us to obtain a good pattern transfer (Fig. 6D).

The soft-imprint technique has been previously used to structure films made of cellulose nanocrystals derived from wood pulp [35,36]. Espinha et al. applied soft lithography to hydroxypropyl cellulose using PDMS stamps and reported photonic cellulose-based architectures [37]. Here, aiming to obtain photonic BC, a PDMS mold with circular pillars of 0.6–0.7  $\mu\text{m}$  of diameter and a pitch of 1.05–1.10  $\mu\text{m}$  was soft-imprinted in a BC film (Fig. 7A). AFM image depicted in Fig. 7B shows that the structure was correctly transferred to the BC film reaching the point where cellulose fiber bundles became comparable with the feature sizes, making it difficult to visualize in the AFM image. Since the dimensions of the patterned geometry are similar to the visible light wavelengths, we were able to produce colorful BC films as shown in Fig. 7C. The grating behavior of our BC films was also tested passing a green laser through the sample and analyzing the diffraction pattern observed. Fig. 7D shows the diffraction pattern obtained for the PDMS mold and the S-BC after the soft-imprint process. It can be observed that the diffraction pattern, although less intense, corresponds to the square array configuration also found on the PDMS mold. The S-BC was submerged in water for 4 h and re-analyzed, obtaining the same pattern. Therefore, this technique offers the possibility to obtain BC films with optical properties that remains even if the sample is rehydrated.



**Fig. 7.** A) Polydimethylsiloxane (PDMS) mold scheme and image showing the peeling process of bacterial cellulose (BC) after the soft-imprint. B) Atomic force microscopy image showing the structuration of BC after soft-imprint lithography. C) Structured bacterial cellulose (S-BC) showing optical birefringence. D) Top: scheme of how the diffraction pattern was obtained and analyzed. Bottom: diffraction pattern images comparison of PDMS mold, S-BC, and S-BC after being immersed in water for 4 h.

#### 4. Conclusions

S-BC films with wells and self-standing pillars of different dimensions have been obtained through two different processes: bio-lithography and soft-imprint lithography. Both techniques allow expanding the scope and versatility of BC in fields such as bioengineering, transient sensors and batteries, and cellulosic nanogenerators or microfluidic devices by simple and scalable processes.

In the first case, patterns have been attained in a wide size range (from 200 to 5  $\mu\text{m}$ ). Those structures can withstand different drying processes such as SCD or OD although the final height of the pattern is reduced by 15% in SCD and 85% in OD. SCD has proved to prevent z-dimension collapse while maintaining a porosity similar to that of the never-dried hydrogels and allowed to visualize the fiber alignment. FD was tested, but the shape of the pattern was adversely affected. For structures with a z of 50  $\mu\text{m}$  or higher, an ordered arrangement of the fibers is easily observable. Besides, large replication areas up to 70  $\text{cm}^2$  with a mixture of different features (lines, groves, wells, and pillars) have been successfully bio-synthesized and films with intricate shapes, which withstand rewetting processes have been obtained with applicability in the microfluidic sector as bio-based platforms. Finally, it has been observed that the PDMS mold resolution is key to obtain well-defined features. In our particular case, squared structures showing widths below 20  $\mu\text{m}$  gradually change into circular-shaped features. The PDMS replicates the pattern photolithographed on the silicon wafer used as a master [38]. In the future, the process would be optimized.

On the other hand, a two-step, soft-imprint lithography arises as a versatile technique as it allows to easily and locally functionalize the BC films, a characteristic hard to achieve by bio-lithography. However, the depth of the features obtained is dramatically decreased, and no alignment of the fibers is observed compared with bio-lithography. Even though, submicron features can be patterned and present stability even in rehydrated conditions with sufficient depth to obtain S-BC films with optical properties.

#### CRedit authorship contributions

**Soledad Roig-Sanchez:** Methodology, Validation, Formal analysis, Investigation, Visualization, Writing—Writing – original draft, Writing—review and editing. **Cesar Fernández-Sánchez:** Resources, Methodology, Writing—editing. **Anna Laromaine:** Conceptualization, Resources, Funding acquisition, Supervision, Writing—review and editing. **Anna Roig:** Conceptualization, Resources, Funding acquisition, Supervision, Writing—original draft, Writing—review and editing.

#### Declaration of competing interest

The authors declare that they have no known competing financial interests or personal relationships that could have appeared to influence the work reported in this article.

#### Acknowledgments

Authors acknowledge financial support from the Spanish Ministry of Science and Innovation through the RTI2018-096273-B-I00 project, the ‘Severo Ochoa’ Programme for Centres of Excellence in R&D (CEX2019-000917-S) and the PhD scholarship of S.R.-S. (BES-2016-077533). The Generalitat de Catalunya projects, 2017SGR765 and 2017SGR1771 are also acknowledged. The authors also express their gratitude to the technical services of ICMAB (SC facilities, SEM, AFM), UAB (microscopy facilities) and ICN2 (electron microscopy).

This work used the Spanish ICTS Network MICRONANOFABS, which is partly supported by the Spanish Ministry of Science and Innovation. The authors participate in the CSIC Interdisciplinary Platform for Sustainable Plastics toward a Circular Economy, SUSPLAST and in the Aerogels COST ACTION (CA 18125). The authors very much appreciate the critical revision of A. Mihi (ICMAB) and the stamp provided by his group. This work has been performed within the framework of the doctoral program in materials science of UAB.

#### Appendix A. Supplementary data

Supplementary data to this article can be found online at <https://doi.org/10.1016/j.mtchem.2021.100535>.

#### References

- [1] S.-S. Wang, Y.-H. Han, Y.-X. Ye, X.-X. Shi, P. Xiang, D.-L. Chen, M. Li, Physico-chemical characterization of high-quality bacterial cellulose produced by *Komagataeibacter* sp. strain W1 and identification of the associated genes in bacterial cellulose production, *RSC Adv.* 7 (2017) 45145–45155, <https://doi.org/10.1039/c7ra08391b>.
- [2] M. Zeng, A. Laromaine, A. Roig, Bacterial cellulose films: influence of bacterial strain and drying route on film properties, *Cellulose* 21 (2014) 4455–4469, <https://doi.org/10.1007/s10570-014-0408-y>.
- [3] A. Retegi, N. Gabilondo, C. Peña, R. Zuluaga, C. Castro, P. Gañan, K. de la Caba, I. Mondragon, Bacterial cellulose films with controlled microstructure-mechanical property relationships, *Cellulose* 17 (2010) 661–669, <https://doi.org/10.1007/s10570-009-9389-7>.
- [4] Z. Shi, Y. Zhang, G.O. Phillips, G. Yang, Food hydrocolloids utilization of bacterial cellulose in food, *Food Hydrocolloids* 35 (2014) 539–545, <https://doi.org/10.1016/j.foodhyd.2013.07.012>.
- [5] Y. Guo, X. Zhang, W. Hao, Y. Xie, L. Chen, Z. Li, B. Zhu, X. Feng, Nano-bacterial cellulose/soy protein isolate complex gel as fat substitutes in ice cream model, *Carbohydr. Polym.* 198 (2018) 620–630, <https://doi.org/10.1016/j.carbpol.2018.06.078>.
- [6] S. Bandyopadhyay, N. Saha, U.V. Brodnjak, P. Saha, Bacterial cellulose and guar gum based modified PVP-CMC hydrogel films: characterized for packaging fresh berries, *Food Packag. Shelf Life.* 22 (2019) 100402, <https://doi.org/10.1016/j.foodpsl.2019.100402>.
- [7] T. Amnuakitt, T. Chusuit, P. Raknam, P. Boonme, Effects of a cellulose mask synthesized by a bacterium on facial skin characteristics and user satisfaction, *Med. Dev. Evid. Res.* 4 (2011) 77–81, <https://doi.org/10.2147/MDER.S20935>.
- [8] C. Fey, J. Betz, C. Rosenbaum, D. Kralisch, M. Viereicher, O. Friedrich, M. Metzger, D. Zdzieblo, Bacterial nanocellulose as novel carrier for intestinal epithelial cells in drug delivery studies, *Mater. Sci. Eng. C* 109 (2020) 110613, <https://doi.org/10.1016/j.msec.2019.110613>.
- [9] I. Anton-Sales, J.C. D’Antin, J. Fernández-Engroba, V. Charoenrook, A. Laromaine, A. Roig, R. Michael, Bacterial nanocellulose as a corneal bandage material: a comparison with amniotic membrane, *Biomater. Sci.* 8 (2020) 2921–2930, <https://doi.org/10.1039/d0bm00083c>.
- [10] H.G. De Oliveira Barud, R.R. Da Silva, H. da S. Barud, A. Tercjak, J. Gutierrez, W.R. Lustrí, O.B. De Oliveira Junior, S.J.L. Ribeiro, A multipurpose natural and renewable polymer in medical applications: bacterial cellulose, *Carbohydr. Polym.* 153 (2016) 406–420, <https://doi.org/10.1016/j.carbpol.2016.07.059>.
- [11] T.R. Stumpf, X. Yang, J. Zhang, X. Cao, In situ and ex situ modifications of bacterial cellulose for applications in tissue engineering, *Mater. Sci. Eng. C* 82 (2018) 372–383, <https://doi.org/10.1016/j.msec.2016.11.121>.
- [12] S. Roig-Sanchez, E. Jungstedt, I. Anton-Sales, D.C. Malaspina, J. Faraudo, L.A. Berglund, A. Laromaine, A. Roig, Nanocellulose films with multiple functional nanoparticles in confined spatial distribution, *Nanoscale Horizons* 4 (2019) 634–641, <https://doi.org/10.1039/c8nh00310f>.
- [13] P.A. Rühls, F. Storz, Y.A. López Gómez, M. Haug, P. Fischer, 3D bacterial cellulose biofilms formed by foam templating, *Npj Biofilms Microbiomes* 4 (2018) 1–6, <https://doi.org/10.1038/s41522-018-0064-3>.
- [14] A. Laromaine, T. Tronser, I. Pini, S. Parets, P.A. Levkin, A. Roig, Free-standing three-dimensional hollow bacterial cellulose structures with controlled geometry via patterned superhydrophobic-hydrophilic surfaces, *Soft Matter* 14 (2018) 3955–3962, <https://doi.org/10.1039/c8sm00112j>.
- [15] M. Schaffner, P.A. Rühls, F. Coulter, S. Kilcher, A.R. Studart, 3D printing of bacteria into functional complex materials, *Sci. Adv.* 3 (2017), ea66804, <https://doi.org/10.1126/sciadv.a66804>.
- [16] G. Wang, X.F. Chen, X.D. Shi, L.J. Yu, B.F. Liu, G. Yang, Bio-fabrication of patterned cellulose nano-fibers, *Adv. Mater. Res.* 47–50 (2008) 1359–1362, <https://doi.org/10.4028/www.scientific.net/AMR.47-50.1359>.
- [17] Y. Uraki, Y. Tamai, T. Hirai, K. Koda, H. Yabu, M. Shimomura, Fabrication of honeycomb-patterned cellulose material that mimics wood cell wall formation processes, *Mater. Sci. Eng. C* 31 (2011) 1201–1208, <https://doi.org/10.1016/j.msec.2010.11.009>.
- [18] S. Bottan, F. Robotti, P. Jayathissa, A. Hegglin, N. Bahamonde, J.A. Heredia-Guerrero, I.S. Bayer, A. Scarpellini, H. Merker, N. Lindenblatt, D. Poulikakos,

- A. Ferrari, Surface-structured bacterial cellulose with guided assembly-based biolithography (GAB), *ACS Nano* 9 (2015) 206–219, <https://doi.org/10.1021/nn5036125>.
- [19] S. Zang, R. Zhang, H. Chen, Y. Lu, J. Zhou, X. Chang, G. Qiu, Z. Wu, G. Yang, Investigation on artificial blood vessels prepared from bacterial cellulose, *Mater. Sci. Eng. C* 46 (2015) 111–117, <https://doi.org/10.1016/j.msec.2014.10.023>.
- [20] R. Prathapan, A.K. Ghosh, A. Knapp, A. Vijayakumar, N.N.J. Bogari, B.D. Abraham, A. Al-Ghabkari, A. Fery, J. Hu, In situ alignment of bacterial cellulose using wrinkling, *ACS Appl. Bio Mater.* 3 (2020) 7898–7907, <https://doi.org/10.1021/acsabm.0c01030>.
- [21] S. Sämfors, K. Karlsson, J. Sundberg, K. Markstedt, P. Gatenholm, Biofabrication of bacterial nanocellulose scaffolds with complex vascular structure, *Biofabrication* 11 (2019), <https://doi.org/10.1088/1758-5090/ab2b4f>, 04510.
- [22] L. Bao, F.F. Hong, G. Li, G. Hu, L. Chen, Improved performance of bacterial nanocellulose conduits by the introduction of silk fibroin nanoparticles and heparin for small-caliber vascular graft applications, *Biomacromolecules* 22 (2021) 353–364, <https://doi.org/10.1021/acs.biomac.0c01211>.
- [23] I.G. Greca, M. Rafiee, A. Karakoç, J. Lehtonen, B.D. Mattos, B.L. Tardy, O.J. Rojas, Guiding bacterial activity for biofabrication of complex materials via controlled wetting of superhydrophobic surfaces, *ACS Nano* 14 (2020) 12929–12937, <https://doi.org/10.1021/acsnano.0c03999>.
- [24] N. Geisel, J. Clasohm, X. Shi, L. Lamboni, J. Yang, K. Mattern, G. Yang, K.H. Schäfer, M. Saumer, Microstructured multilevel bacterial cellulose allows the guided growth of neural stem cells, *Small* 12 (2016) 5407–5413, <https://doi.org/10.1002/sml.201601679>.
- [25] F. Robotti, I. Sterner, S. Bottan, J.M. Monné Rodríguez, G. Pellegrini, T. Schmidt, V. Falk, D. Poulikakos, A. Ferrari, C. Starck, Microengineered biosynthesized cellulose as anti-fibrotic in vivo protection for cardiac implantable electronic devices, *Biomaterials* 229 (2020) 119583, <https://doi.org/10.1016/j.biomaterials.2019.119583>.
- [26] M. Jin, W. Chen, Z. Li, Y. Zhang, M. Zhang, S. Chen, Patterned bacterial cellulose wound dressing for hypertrophic scar inhibition behavior, *Cellulose* 25 (2018) 6705–6717, <https://doi.org/10.1007/s10570-018-2041-7>.
- [27] Y. Cao, M. Liu, Z. Xue, Y. Qiu, J. Li, Y. Wang, Q. Wu, Surface-structured bacterial cellulose loaded with hUSCs accelerate skin wound healing by promoting angiogenesis in rats, *Biochem. Biophys. Res. Commun.* 516 (2019) 1167–1174, <https://doi.org/10.1016/j.bbrc.2019.06.161>.
- [28] S.L. Arias, M.K. Cheng, A. Civantos, J. Devorkin, C. Jaramillo, J.P. Allain, Ion-induced nanopatterning of bacterial cellulose hydrogels for biosensing and anti-biofouling interfaces, *ACS Appl. Nano Mater.* 3 (2020) 6719–6728, <https://doi.org/10.1021/acsnam.0c01151>.
- [29] N. Mittal, A. Ojanguren, M. Niederberger, E. Lizundia, Degradation behavior, biocompatibility, electrochemical performance, and circularity potential of transient batteries, *Adv. Sci.* (2021) 2004814, <https://doi.org/10.1002/advs.202004814>.
- [30] P.K. Annamalai, A.K. Nanjundan, D.P. Dubal, J.B. Baek, An overview of cellulose-based nanogenerators, *Adv. Mater. Technol.* 6 (2021) 2001164, <https://doi.org/10.1002/admt.202001164>.
- [31] D. Abol-Fotouh, B. Dörfling, O. Zapata-Arteaga, X. Rodríguez-Martínez, A. Gómez, J.S. Reparaz, A. Laromaine, A. Roig, M. Campoy-Quiles, Farming thermoelectric paper, *Energy Environ. Sci.* 12 (2019) 716–726, <https://doi.org/10.1039/c8ee03112f>.
- [32] M. Li, L. Zong, W. Yang, X. Li, J. You, X. Wu, Z. Li, C. Li, Biological nanofibrous generator for electricity harvest from moist air flow, *Adv. Funct. Mater.* 29 (2019) 1901798, <https://doi.org/10.1002/adfm.201901798>.
- [33] T. Akyazi, L. Basabe-Desmonts, F. Benito-Lopez, Review on micro fluidic paper-based analytical devices towards commercialisation, *Anal. Chim. Acta* 1001 (2018) 1–17, <https://doi.org/10.1016/j.aca.2017.11.010>.
- [34] K. Kolind, K.W. Leong, F. Besenbacher, M. Foss, Biomaterials guidance of stem cell fate on 2D patterned surfaces, *Biomaterials* 33 (2012) 6626–6633, <https://doi.org/10.1016/j.biomaterials.2012.05.070>.
- [35] T.H. Zhao, R.M. Parker, C.A. Williams, K.T.P. Lim, B. Frka-Petesic, S. Vignolini, Printing of responsive photonic cellulose nanocrystal microfilm arrays, *Adv. Funct. Mater.* (2018) 1804531, <https://doi.org/10.1002/adfm.201804531>.
- [36] Y. Zhou, Y. Li, F. Dundar, K.R. Carter, J.J. Watkins, Fabrication of patterned cellulose film via solvent-assisted soft nanoimprint lithography at a sub-micron scale, *Cellulose* 25 (2018) 5185–5194, <https://doi.org/10.1007/s10570-018-1920-2>.
- [37] A. Espinha, C. Dore, C. Matricardi, M.I. Alonso, A.R. Goñi, A. Mihi, Hydroxypropyl cellulose photonic architectures by soft nanoimprinting lithography, *Nat. Photonics* 12 (2018) 343–348, <https://doi.org/10.1038/s41566-018-0152-1>.
- [38] Q.M. Chen, J.Y. Zhou, Y.M. Hu, Q. Zheng, Tradeoff control of multi-exposure lithography for SU-8 photochemical reaction channel formation, *Biochip J* 14 (2020) 369–380, <https://doi.org/10.1007/s13206-020-4405-y>.





